

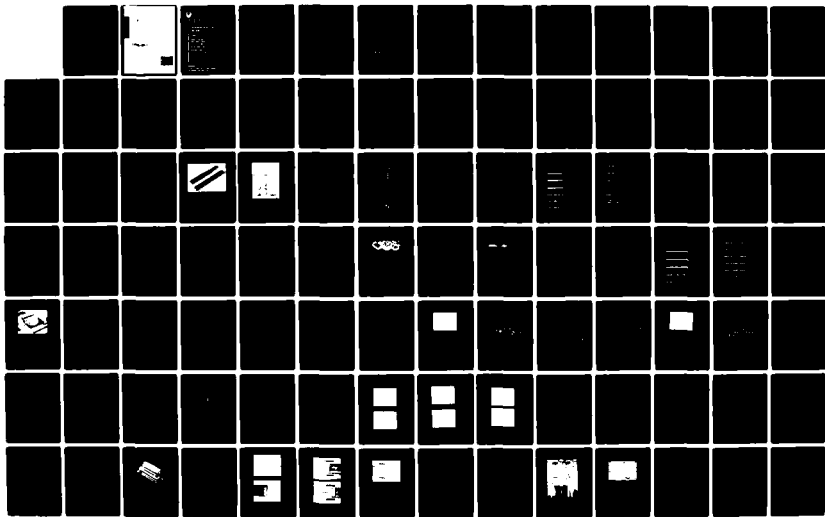
UNCLASSIFIED

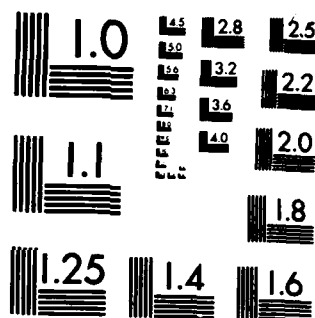
DELET-TR-80-0281-1 DAAK20-80-C-0281

 $\frac{1}{2}$ 

F/G 9/1

NL





MICROCOPY RESOLUTION TEST CHART  
NATIONAL BUREAU OF STANDARDS-1963-A

AD A 1 2 9 36

DECEMBER 1982

DTIC  
ELECTE  
JUN 30 1983  
S B



**Research and Development Technical Report,  
DELET-TR-80- 0281-1**

## **SAW RESONATOR AND REFLECTIVE ARRAY DEVICES**

**J. Thoss  
D. Pennuneri  
S. Ricca**

**GROUND SYSTEMS GROUP  
HUGHES AIRCRAFT COMPANY  
FULLERTON, CALIFORNIA 92634**

**DECEMBER 1982**

**Interim Report : Engineering Phase  
for Period 1 July 1980 - 31 May 1982**

**DISTRIBUTION STATEMENT:**

**Approved for public release, distribution unlimited.**

**ERADCOM**

**US ARMY ELECTRONICS AND DEVELOPMENT COMMAND  
FORT MONMOUTH, NEW JERSEY 07703**

## **N O T I C E S**

### **Disclaimers**

The citation of trade names and names of manufacturers in this report is not to be construed as official Government indorsement or approval of commercial products or services referenced herein.

### **Disposition**

Destroy this report when it is no longer needed.  
Do not return it to the originator.

UNCLASSIFIED

SECURITY CLASSIFICATION OF THIS PAGE (When Data Entered)

REPORT DOCUMENTATION PAGE		READ INSTRUCTIONS BEFORE COMPLETING FORM
1. REPORT NUMBER DELET-TR-80-0281-1	2. GOVT ACCESSION NO. AD-A129926	3. RECIPIENT'S CATALOG NUMBER
4. TITLE (and Subtitle)  SAW Resonator and Reflective Array Devices		5. TYPE OF REPORT & PERIOD COVERED 1st Interim 1 July 80 - 31 May 82
		6. PERFORMING ORG. REPORT NUMBER
7. AUTHOR(s)  J. Herold, et al		8. CONTRACT OR GRANT NUMBER(s)  DAAK20-80-C-0281
9. PERFORMING ORGANIZATION NAME AND ADDRESS Hughes Aircraft Company Ground Systems Group Fullerton, CA 92634		10. PROGRAM ELEMENT, PROJECT, TASK AREA & WORK UNIT NUMBERS  5297 OH 9897
11. CONTROLLING OFFICE NAME AND ADDRESS U. S. Army Electronics Research & Development Cnd ATTN: DELET-MA-M(Heinzman) Fort Monmouth, NJ 07703		12. REPORT DATE December 1982
14. MONITORING AGENCY NAME & ADDRESS (if different from Controlling Office)		13. NUMBER OF PAGES
		15. SECURITY CLASS. (of this report)  UNCLASSIFIED
15a. DECLASSIFICATION/DOWNGRADING SCHEDULE		
16. DISTRIBUTION STATEMENT (of this Report)  Approved For Public Release; Distribution Unlimited.		
17. DISTRIBUTION STATEMENT (of the abstract entered in Block 20, if different from Report)		
18. SUPPLEMENTARY NOTES  None		
19. KEY WORDS (Continue on reverse side if necessary and identify by block number) Surface Acoustic Waves SAW Resonators SAW Reflective Array Compressor (RAC) Filter		
20. ABSTRACT (Continue on reverse side if necessary and identify by block number) This report documents the engineering effort applied during this Manufacturing Methods and Technology (MM&T) contract on two distinct SAW devices using grooved reflective arrays on two different piezoelectric substrate materials. One device is 60 MHz by 60 microsecond down chirp linearly-dispersive filter operating at 200 MHz using lithium niobate and the second device is a two-part, 100 KHz bandwidth resonator operating at 400 MHz using quartz. The reflective is formed by an ion beam etch process. The degree of time-linearity on the RAC filter was achieved by use of metallic phase correction patterns. With		

DD FORM 1473

JAN 73

EDITION OF 1 NOV 68 IS OBSOLETE

UNCLASSIFIED

SECURITY CLASSIFICATION OF THIS PAGE (When Data Entered)

UNCLASSIFIED

SECURITY CLASSIFICATION OF THIS PAGE(When Data Entered)

a common pattern, the phase error was reduced to about 18 degrees (RMS); with a second correction pattern designed for each individual RAC, the phase error was further reduced to about 7 degrees (RMS). The corresponding sidelobe levels in the time-domain pulse compression loop using an ideal matched filter were 25 and 32 dB, respectively.

Accession For	
NTIS GMA&I	<input checked="" type="checkbox"/>
DTIC TAB	<input type="checkbox"/>
Unannounced	<input type="checkbox"/>
Justification	
<b>PER CALL JC</b>	
By	
Distribution/	
Availability Codes	
Dist	Avail and/or Special
<b>A</b>	



UNCLASSIFIED

SECURITY CLASSIFICATION OF THIS PAGE(When Data Entered)

## TABLE OF CONTENTS

	Page
1.0 OVERVIEW	1
2.0 ELECTRICAL DESIGN	3
2.1 Introduction	3
2.2 Design of RAC	5
2.3 Design of Resonator	9
3.0 DEVICE FABRICATION	19
3.1 RAC Device	19
3.1.1 Device Description	19
3.1.2 Crystal Description	22
3.1.3 Detailed Process Specification	25
3.1.4 Reflective Array Etch Development	29
3.1.5 Reflective Array Depth Control	32
3.2 Resonator Device	35
3.2.1 Device Description	36
3.2.2 Crystal Description	38
3.2.3 Detailed Process Description	41
3.2.4 Reflective Array Etch Development	46
4.0 ELECTRICAL EVALUATION OF ENGINEERING SAMPLES	48
4.1 RAC Device	48
4.1.1 General Considerations	48
4.1.2 Test Results	48
4.2 Resonator Device	59
4.2.1 General Considerations	59
4.2.2 Evaluation of Phase I Devices	60
4.2.3 Evaluation of Phase II Devices	69
4.2.4 Comparison of Specification Requirements Versus Measured Performance	70
5.0 PRODUCTION RAC PACKAGE DEVELOPMENT	74
5.1 Introduction	74
5.2 Signal Feedthrough Evaluation	74
5.3 Proposed Housing Changes	80
6.0 RAC UP-CHIRP (TEST-LINE) DEVELOPMENT	84
6.1 Introduction	84
6.2 Design	84
6.3 Evaluation	88
6.4 Scattering Loss Considerations	92



## TABLE OF CONTENTS (Continued)

	Page
7.0 RESONATOR TRIM DEVELOPMENT AND EVALUATION	97
7.1 Introduction	97
7.2 Wafer Probe Evaluation	97
7.3 Laser Trim Technique	100
8.0 CONCLUSIONS AND RECOMMENDATIONS	103
8.1 RAC Device	103
8.2 Resonator Device	104
APPENDIX A. TEST DATA FOR ENGINEERING PHASE RAC FILTERS	106
APPENDIX B. WAFER LEVEL FREQUENCY PROBE RESULTS FOR ENGINEERING PHASE RESONATORS	176
REFERENCES	vi

## LIST OF ILLUSTRATIONS

<u>Figure</u>		<u>Page</u>
2.1	Theoretic Frequency Response of RAC Filter Transducers	7
2.2	Loss Contributions of Downchirp Expansion Line	10
2.3	Groove Depth Profile of Downchirp Expansion Line	11
2.4	Resonator Design Schematic	18
3.1	Photograph of Assembled RAC Filter	20
3.2	Processed RAC Crystal	23
3.3	RAC Device Fabrication Flow for Engineering Samples	26
3.4	Schematic Arrangement for Depth Profile Etching	30
3.5	Steps in Achieving Desired Etch Depth Profile	31
3.6	Automatic Etch Depth Sensor	33
3.7	Cross Section Detail of Etch Depth Sensor	34
3.8	Assembled Resonator	37
3.9	Processed Resonator Die	39
3.10	Resonator Fabrication Flow	42
3.11	Probe Station with Card Assembly	45
4.1	Measured Frequency Response of the S/N1 RAC Line	50
4.2	Phase Response of S/N1 RAC Line	51
4.3	Wideband Frequency Response of S/N1 RAC Line	52
4.4	Recompressed Pulse Characteristic of S/N1 RAC Line	53
4.5	Amplitude Response of S/N5 RAC Line	54
4.6	Phase Response of S/N5 RAC Line	55
4.7	Wideband Frequency Response of S/N5 RAC Line	56
4.8	Recompressed Pulse Characteristic of S/N5 RAC Line	57
4.9	Frequency Response of Untuned Resonator	62
4.10	Expanded Frequency Response of Untuned Resonator	63
4.11	Wideband Response of Untuned Resonator	65
4.12	Wideband Response of Tuned Resonator	66
4.13	Wideband Response of Tuned Resonator with Secondary Response	67
4.14	Simulation of Secondary Resonance Effect	68
4.15	Typical Response of Packaged Resonator	71
5.1	Package Developed for Feedthrough Evaluation Study	75
5.2	Feedthrough Study Configurations	77
5.3	Detailed View of Packaged, Unnotched Crystal	82
5.4	Package Used for Confirmatory Sample Phase	83
6.1	Amplitude Response of Upchirp RAC Filter Transducer	85
6.2	Loss Contributions of Upchirp Comparison Line	86
6.3	Groove Depth Profile of Upchirp Comparison Line	87
6.4	Amplitude Response Composition of Upchirp Line and Ideal Hamming Weighted Line	89
6.5	Insertion Loss Variation of Measured Performance and Ideal Hamming Weighted Response (Overetched sample)	90
6.6	Insertion Loss Variation of Measured Performance and Ideal Hamming Weighted Response (correctly etched sample)	91
6.7	Modified Groove Depth Profile of Upchirp Compression Line	93

### LIST OF ILLUSTRATIONS (Continued)

<u>Figure</u>		<u>Page</u>
6.8	Amplitude Response Comparison of Modified Upchirp Line and Ideal Hamming Weighted Line	94
6.9	Insertion Loss Variation of Measured Performance (Modified Design) and Ideal Hamming Weighted Response	95
6.10	Slanted Grating Section for Upchirp Filter	96
7.1	Wafer Level Center Frequency Probe Results	98
7.2	Fractional Frequency Shift as a Function of Opened Electrodes	102

## LIST OF TABLES

<u>Table</u>		<u>Page</u>
1.1	Device Specifications	2
2.1	Performance Characteristics of the 60 MHz, 60 Microsecond RAC Filter	6
2.2	Resonator Design Parameter Values	15
2.3	Resonator Loss Performance Parameters	16
3.1	RAC Crystal Data	24
3.2	Resonator Crystal Die Specifications	40
4.1	Test Results of Engineering Phase Devices (RAC filters)	49
4.2	Test Results of Engineering Phase Devices (Resonators)	61
4.3	Results for Assembled Lot of Phase I Resonators	69
4.4	Results for Assembled Lot of Phase II Resonators	70
5.1	RAC Filter Signal Feedthrough Results	76
7.1	Wafer Probe Results for Engineering Phase Resonators	100
AI.1	Engineering Phase I RAC Filter Test Data	107
AI.2	Engineering Phase II RAC Filter Test Data	108

## 1.0 OVERVIEW

The objective of this Manufacturing Methods and Technology program (MM&T) is the establishment of a production capability for surface acoustic wave (SAW) devices (i.e., two-port resonators and reflective array compressors, RACs) which use acoustically reflective arrays etched into the substrate surface. Furthermore, the developed capability must meet military needs for a period of two years after the completion of the contract, and it must establish a base and plans to meet expanded requirements.

To accomplish the above objectives, the MM&T program has been divided into four distinct phases: Engineering Development Phase, Confirmatory Sample Phase, Pilot Line Production, and the Capability Demonstration. The first phase will establish the precise design, fabricate and test ten of each of the devices, and accomplish the preliminary production planning efforts. The second, or Confirmatory Sample Phase, will test the manufacturing techniques on an unbalanced production line and assess yield figures and preliminary device costs. The final hardware phase is the Pilot Production Run. During this period, the throughput capacity of the line is demonstrated and final yield figures and device costs established. At the conclusion of the pilot production, an on-site capability demonstration will be conducted to provide a means for transfer of the technology developed during the program to interested members of the industrial community. In addition, engineering analysis and planning will be developed for expansion of the manufacturing capability to accommodate high device production rates. This analysis and planning will be provided in a General Report.

This program addresses the production of two distinct SAW devices using grooved reflective gratings on two different piezoelectric substrate materials. The first device is a 60 MHz by 60 microsecond linearly-dispersive (downchirp) filter operating at 200 MHz. This reflective array compressive filter (RAC), fabricated on lithium niobate, employs ion beam etch techniques to form the reflective groove structure. The second device is a precision, low loss, 100 KHz bandwidth, two-port resonator centered at 400 MHz. This device is fabricated on quartz and, similarly, the grooved array grating is formed using the highly controlled ion beam etch process. The electrical specifications required to be met for both device types are summarized in Table 1.1.

This interim report details the developments of the engineering phase for both devices. The specific electrical design and test results for both the RAC and resonator are presented. In addition, the process and assembly procedures planned for the Pilot Production Line have been developed and are also discussed in the sections describing the fabrication of both devices. The quality control requirements and electrical test plans will be discussed in separate reports. Finally, this report addresses several engineering tasks that still require technical resolution and will be resolved during the Confirmatory Sample Phase.

TABLE 1.1. DEVICE SPECIFICATIONS

Parameter	Requirement	
	RAC	Resonator
Substrate Composition	YZ - Lithium Niobate	ST - Quartz
Die per Wafer	$\geq 3$	$\geq 50$
Passband Insertion Loss	$\leq 40$ dB	$\leq 5$ dB
3 dB Bandwidth	$60 \pm 1$ MHz	$100 \pm 5$ kHz
Center Frequency	$200 \pm 2$ MHz	$400 \pm .01$ MHz
Group Time Delay Dispersion	$60 \pm .5$ $\mu$ sec	N/A
Ideal Phase-Frequency Characteristic	Second Order Quadratic	Linear
Adjacent Side-lobe Suppression Measurement Domain	$> 25$ dB Time	$> 20$ dB Frequency
Feedthrough Suppression	$\geq 50$ dB	$\geq 50$ dB
Spurious Echo Suppression	$\geq 40$ dB	$\geq 35$ dB

## 2.0 ELECTRICAL DESIGN

2.1 Introduction. Reflective array compressors (RACs) are rather unique surface acoustic wave devices that are used in modern radar and communication systems. This program addresses two such devices, namely pulse expansion and pulse compression delay lines. The desired performance for these two devices is achieved by arranging the reflective gratings, which are ion-beam etched to varying groove depths, in two dispersive arrays forming a "chevron" pattern. Acoustic waves are launched by a nondispersive, broadband transducer and are reflected at right angles by the first reflection array at a point where the spacing of the grooves along the direction of propagation is a wavelength. A second array reflects the wave back to the output transducer. Two major advantages of this configuration include large dispersion, since the length of the device is used twice, and very low distortion. In general, reflective arrays introduce minimal distortion effects as the surface waves propagate through them.

The pulse expansion RAC lines fabricated on this program have a flat passband response and exhibit a linear down-chirp time - frequency dispersion characteristic. In particular, the grooves placed near the transducers are closer together permitting the higher frequency components of a signal to be reflected first. As a result, that signal component will have a shorter path to travel and the resulting overall delay will be less than for the lower frequency components. The pulse compression line, on the other hand, employs a Hamming weighted passband response with an up-chirp dispersion characteristic. In this design the grooves with the largest spacing are close to the input and output transducer configuration. The selection of a Hamming weighted envelope response for the up-chirp line will permit the achievement of greater than 25 dB time sidelobes in the recompressed pulse, provided the magnitude of the phase errors for the matched filter pair can also be reduced to some low nominal value (i.e.,  $< 5^\circ$ ).

The design details for the flat passband, down-chirp lines are presented in the next section. In particular, the line's passband response is synthesized based on the performance characteristics of an eight electrode interdigital transducer (for both input and output) containing a phase reversed electrode pair on one end of each transducer, and a shallow groove depth profile developed from the predictions of a reflective array model operating in the weakly-coupled limit.

The design steps for the up-chirp line are similar to those of the down-chirp line and are discussed in detail in Section 6 of this report. To date, a truly Hamming weighted response has not been achieved. A basic weighted depth profile has been developed and evaluated using several modifications. However, the passband response continues to exhibit a relatively large roll-off above center frequency. The onset of a similar degradation in the high frequency portion of the passband has been observed on other up-chirp lines built at Hughes. The effect has not been at all as pronounced on these lines as for the one developed on this program and has

therefore gone relatively undetected. However, this device differs from previously built lines in that it has a very long reflective array containing many grooves. It is presently felt that for up-chirp lines, where the grooves with largest spacing are close to the input transducer, a loss mechanism to bulk waves exists when high frequency component waves pass through these widely spaced grooves. Furthermore, the effect is proportionately enhanced for lines with long arrays containing a high density of widely spaced groove patterns.

Surface acoustic wave resonators have recently emerged from the laboratory and are now receiving wider usage in communication and radar systems. Their applications generally fall into one of two categories: 1) as frequency control elements of stable oscillators requiring high Q, and, 2) as multipole filters for channel control in frequency-multiplexed communication systems. The SAW resonator has the same fundamental resonant properties and basically can be modeled by the same equivalent circuit as the quartz crystal resonator, therefore allowing the development of all oscillator and filter functions now being performed by the bulk crystal. The key advantage is that these functions can be performed readily at much higher frequencies (i.e., from 30 MHz into the low GHz range).

A SAW resonator, configured as a two-port resonator filter, consists of two distributed reflectors placed around a pair of interdigitated transducers. The placement of the reflectors forms a cavity that serves to confine the surface wave while the transducers are instrumental in introducing and transferring the signal energy into and out of the cavity. The resonant condition established is identical to observed resonances in standard microwave and optical Fabry-Perot cavities. However, one main difference exists, namely, the SAW gratings are formed from distributed elements and therefore operate as efficient reflectors only over a narrow relative bandwidth.

A two-port SAW quartz resonator was designed on this program to operate at 400 MHz with a maximum insertion loss of 5 dB. Geometric configurations for the interdigitated transducers, the feedthrough suppression grating and the metal pattern employed to define the reflective array have been selected so standard production photolithographic techniques can be employed. A single mask pattern defines both the transducer and groove configuration. The grooves are etched into the surface of the quartz substrate using the highly controlled ion-beam etch technique. While the center frequency for the resonator is set by the design of the photolithographic mask, post fabrication trimming is required to achieve an overall settability within  $\pm 10$  ppm. Laser trimming (opening) the stripes forming the feedthrough suppression grating between the transducer configuration was investigated on this program. This technique can be highly automated and should prove to be a rapid, low-cost method for achieving final trim in a production environment.



2.2 Design of RAC. The Reflective Array Compressor (RAC) delay lines for this program were designed to operate on lithium niobate at 200 MHz with a dispersive delay of 60  $\mu$ s and an operational bandwidth of 60 MHz. Table 2.1 summarizes the overall filter specifications for these lines. The amplitude response of these down-chirp lines was designed to be flat over the 60 MHz bandwidth with a CW insertion loss not to exceed 40 dB. When operated with its matched Hamming weighted compression line filter, these devices were required to exhibit a minimum 25 dB time - sidelobe suppression relative to the main lobe. The flat amplitude response was achieved using depth- weighted grooves ion-beam milled into the substrate surface.

The correct depth profile for the reflective array grooves was obtained using the design procedure described by Otto and Gerard [1]. In this model the overall filter response is expressed as:

$$H(f) = T(f) + NS(f) + P(f) + \Gamma(f) \quad (1)$$

where each term is defined as follows:

$H(f)$  = overall filter amplitude response

$T(f)$  = combined loss characteristic of the input and output transducers

$NS(f)$  = non-synchronous (bulk) scattering loss

$P(f)$  = propagation loss

$\Gamma(f)$  = combined reflection loss of the grooved grating

The combined theoretical insertion loss of the 8-finger, half-phased-reversed transducer configuration used in these lines is shown in Figure 2.1. The midband loss of the transducers is approximately 19 dB and increases to 23 dB at the upper band edge near 230 MHz.

The expression for the non-synchronous scattering loss is based on an empirical expression derived by Otto [1]:

$$NS(f) = 8.68 A^2 \left( \frac{f}{v} \right)^2 \star \int_0^Z h(Z') \frac{dZ'}{g(Z')} \quad (2)$$

where  $A$  is an empirical constant equal to 2.4,  $h(Z')$  is the groove depth at a point  $Z'$  in the array, and  $g(Z')$  is the local groove period at a point  $Z'$  in the array. As noted by Otto, the non-synchronous scattering effect limits the overall filter performance achievable for a given design. In integrated form, the scattering loss increases as an exponential function of  $h/\lambda$  while the groove reflectivity increases as  $(h/\lambda)^4$ . Once a scattering

TABLE 2.1 PERFORMANCE CHARACTERISTICS OF THE 60 MHz,  
60 MICROSECOND RAC FILTER

Parameter	Specification	Measured Performance
Insertion Loss (max)	40 dB	38 $\pm$ 2 dB
Bandwidth (3 dB)	60 $\pm$ 1 MHz	60.6 $\pm$ .5 MHz
Center Frequency	200 $\pm$ 2 MHz	200.3 $\pm$ 0.3 MHz
Group Time Delay		
Center Frequency Delay	TBD $\mu$ sec	35.98 $\pm$ 0.05 $\mu$ s
Dispersive Delay	60 $\pm$ 0.5 $\mu$ sec	60.4 $\pm$ 0.4 $\mu$ s
Chirp Sense	-1	-1
Phase Deviation (RMS)	TBD	5.5° $\pm$ 3.2°
Sidelobe Suppression (min)	25 dB	33 $\pm$ 4 dB
CW Feedthrough Suppression	50 dB	53 $\pm$ 9 dB
Spurious Echo Suppression (Relative to Peak of Recompressed Pulse)	40 dB	> 60 dB*
VSWR, max	TBD	6.1 $\pm$ 0.9:1.0

\*Spurious echo level was below the 60 dB dynamic range of the experimental test loop.

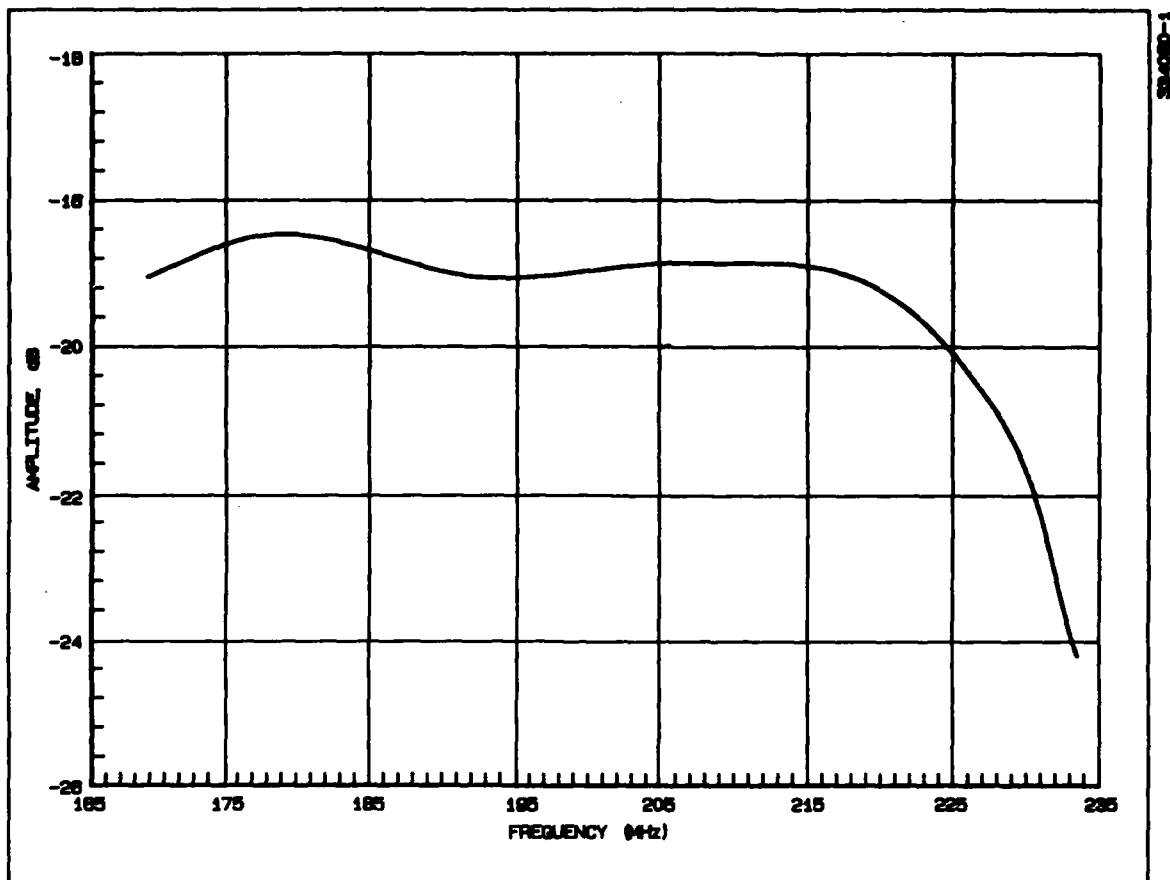


Figure 2.1. Combined Frequency Response (theoretical) of the Input and Output Transducers Used in the 60 MHz, 60 $\mu$  sec RAC Design

loss of 8.6 dB is reached, any further increase in groove depth will cause the scattering loss to increase at a rate faster than the decreasing groove reflection loss can compensate. For this particular design the maximum non-synchronous scattering loss is about 3 dB below the 8.6 dB limit.

The propagation loss is given empirically by

$$P(f) = [.19(f/f_r) + .88(f/f_r)^2] [\tau_0 - (\Delta\tau/\Delta f)(f - f_0)] \quad (3)$$

where  $f_r$  is a reference frequency, namely 1 GHz,  $\tau_0$  is the midband delay,  $\Delta\tau$  the dispersive delay, and  $\Delta f$  is the chirp bandwidth. It is noted that the propagation loss is independent of groove depth.

Using the low reflectivity model, the grating reflection loss is given by

$$\Gamma_L(f) = 10 \log (h/\lambda_0)^2 (f/f_0)^4 (L_a/\lambda_0)^2 a(Y) \quad (4)$$

where

$$(L_a/\lambda_0) = (f_0/2) \sqrt{\Delta\tau/\Delta f} \quad (5)$$

$$a(Y) = Y/[1 + (Y/1.85)^5]^{0.2} \quad (6)$$

and

$$Y = (W/L_a) \tan 46.82^\circ. \quad (7)$$

$W$  is the width of the grating in wavelengths and  $46.82^\circ$  is the angle the individual grooves form with the incident wave propagation direction.

In order to account for multiple reflection losses in the grating area, the low reflectivity model can be modified to yield an effective grating loss. This conversion is given by the expression

$$\Gamma(f) = \frac{\Gamma_L(f)}{2} + \left[ \frac{\Gamma_L(f)}{2}^2 + 17.5 \right]^{1/2}. \quad (8)$$

It can be demonstrated using the equation above that multiple reflection effects add approximately 1 dB of additional loss when  $\Gamma_L(f)$  equals 17 dB and approximately 2 dB when  $\Gamma_L(f)$  is reduced to 6 dB. These are small contributions and the results of the weak coupling model employed in this design accurately describe the reflective array performance.

An interactive design procedure was used in the Engineering phase to determine an overall grating loss that compensated the transducer, scattering and propagation losses to obtain the desired overall filter response. For the lines on this program a flat amplitude response with a nominal insertion loss of 38 dB was specified. The relative loss factors that were computed using the above program are shown in Figure 2.2. At the low frequency (i.e., at the far end of the grating), the transducers contribute approximately 19 dB to the overall loss, the grating reflection 10 dB, and the combined propagation and bulk scattering losses 9 dB.

The optimized groove depth profile required to achieve this design is shown in Figure 2.3. The maximum depth is approximately 1500 Å at the low frequency with a gradual roll-off to 400 Å at the high frequency. The absence of rapid changes in the depth profile greatly simplifies the ion-beam machining operation and each line can therefore be milled to the desired depth in only a few minutes.

**2.3 Design of Resonator.** The key specification parameters which dictate the resonator device design are center frequency, insertion loss, bandwidth (or Q) and adjacent sidelobe (or spurious mode) suppression. Other performance parameters, such as feedthrough suppression, depend primarily on layout and packaging considerations. The nominal center frequency of the resonance (400 MHz) is determined by the effective surface acoustic wave velocity in the reflective grating area. This effective velocity is in turn dependent upon the etched groove depth according to the relationship [2]

$$V_g = V_f [1 - K_v(h/\lambda_0)^2], \quad (1)$$

where  $V_g$  is the effective velocity in the reflective grating and  $V_f$  is the free surface acoustic wave velocity,  $h$  is the groove depth and  $\lambda_0$  is twice the groove periodicity. Experimentally, it has been shown that  $V_f = 3157.6 \pm 0.2$  m/sec and  $K_v = 10.3 \pm 0.5$  for groove depths near  $h = 0.01\lambda_0$ . Therefore, for a groove depth of 1100 Å the effective velocity  $V_g = 3151.3$  m/sec. In order to achieve resonance at 400 MHz a groove periodicity equal to  $\lambda_0/2 = 3.939$  micrometers must therefore be selected.

The insertion loss, bandwidth (or loaded  $Q_L$ ) and unloaded  $Q_U$  for a resonator are related according to equation [3]

$$IL = 10 \log (1 - Q_L/Q_U)^2. \quad (2)$$

This relationship can, in turn, be solved for  $Q_U$  and provide an estimate for the necessary unloaded device Q. In particular,

$$Q_U = Q_L [1 - 10IL/20]^{-1}. \quad (3)$$

For a resonator operating at 400 MHz and with a 100 KHz bandwidth requirement, the loaded Q is determined to be

$$Q_L \geq \frac{400}{0.1} = 4000. \quad (4)$$

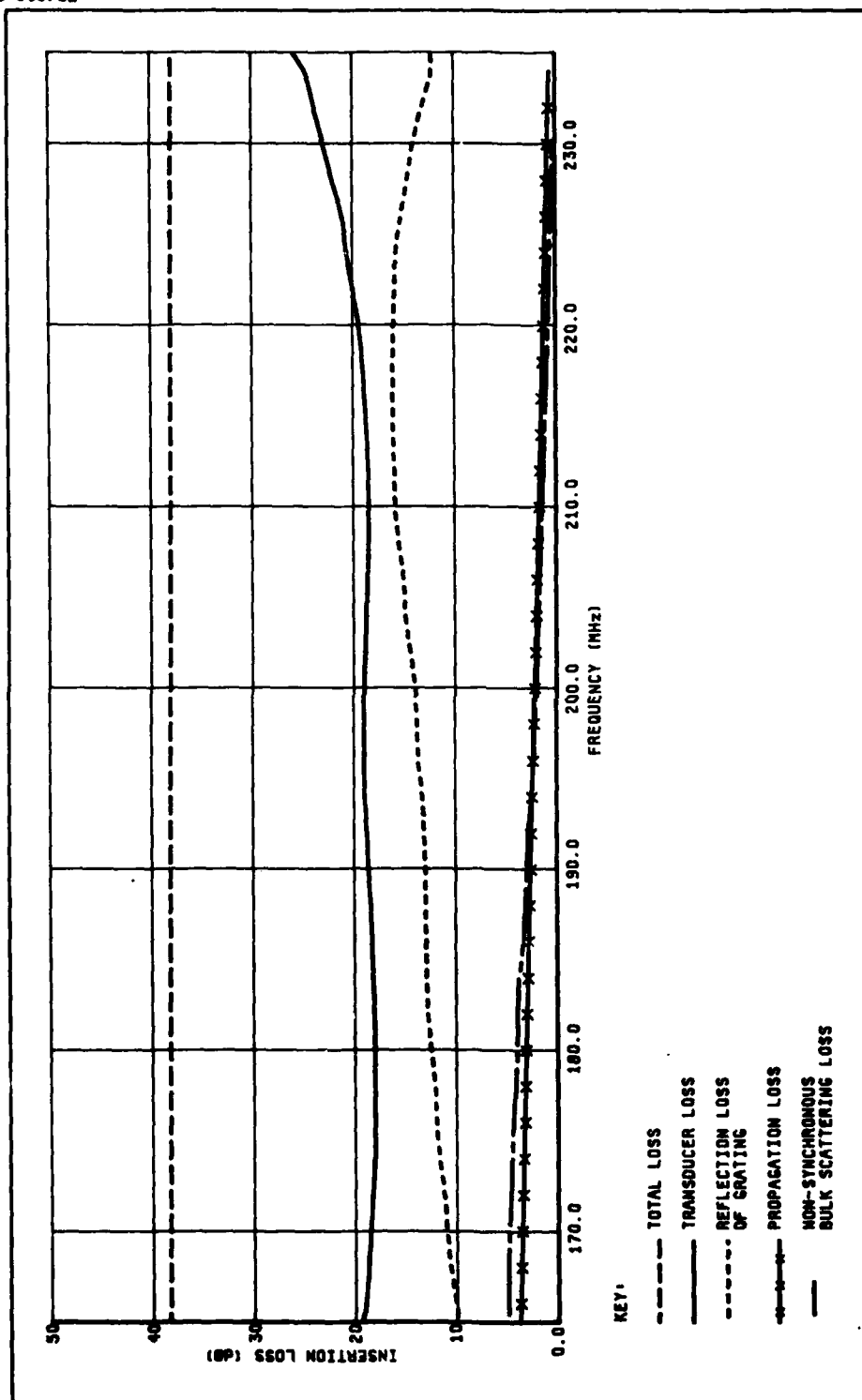
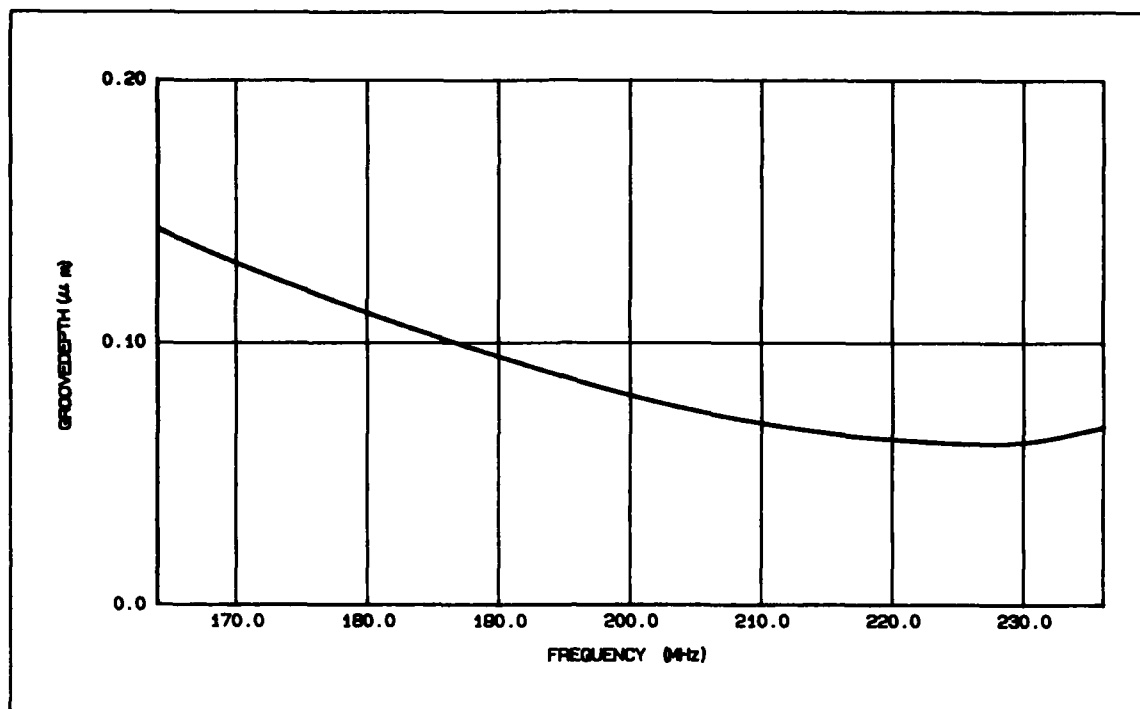


Figure 2.2. Loss Contributions Employed In the Design of the 60 MHz, 60  $\mu$ sec Downchirp Expansion Line



SS-4080-3

Figure 2.3. Groove Depth Profile Employed to Obtain a Flat Passband Response

Since the required insertion loss must satisfy

$$IL \leq 5 \text{ dB}, \quad (5)$$

an unloaded Q value for the resonator of this program can be computed from equation (3) above, i.e.,

$$Q_u \geq 9100.$$

An expression for the total unloaded Q ( $Q_u$ ) of the resonator in terms of all loss factors contributing to its performance limitation is given by the relationship [4]

$$\frac{1}{Q_u} = \frac{1}{Q_R} + \frac{1}{Q_{BG}} + \frac{1}{Q_{BT}} + \frac{1}{Q_M} + \frac{1}{Q_A} + \frac{1}{Q_D} + \frac{1}{Q_\Omega}. \quad (6)$$

A brief discussion of each term in the above expression is presented below and the dependence on the design parameters is outlined.  $Q_R$  is the reflector radiation quality factor and it is given by the equation [4]

$$Q_R = 2\pi N_{CR}/4 \exp(-N_g h/\lambda_0) \quad (7)$$

where

$$N_{CR} = M_{CE} + 4\lambda_0/h. \quad (8)$$

$M_{CE}$  characterizes the edge-to-edge cavity length in wavelengths, and  $N_g$  is the actual number of grooves (after withdrawing grooves if this weighting technique is used).  $Q_{BG}$  describes the bulk mode acoustic radiation loss from the grating and is represented by [5]

$$Q_{BG} = 2\pi N_{CR}/K_{BG} (h/\lambda_0)^2 \quad (9)$$

where  $K_{BG}$  is a material dependent constant. An accurate value is not currently available but it is estimated to be approximately equal to 10 [5]. Similarly,

$$Q_{BT} = 2\pi N_{CR}/K_{BT} (t/\lambda_0)^2 \quad (10)$$

describes the bulk mode acoustic radiation loss from the transducers and shield structures when these are not recessed. According to Cross [8]  $K_{BT}$  has a value approximately equal to 18 for aluminum electrodes on quartz.

The loss associated with viscous damping of the SAW mode within the quartz substrate is given by the relationship [5]

$$Q_M = 1.05 \times 10^{13}/f_0, \quad (11)$$

where  $f_0$  is the resonant center frequency. The value of  $Q_M$  represents a fundamental limitation to device performance on quartz since it describes an



inherent material property and therefore is not adjustable. Air loading losses in turn are given by the term  $Q_A$ , which for quartz is approximately 58,000.

The loss resulting from surface acoustic wave diffraction effects is given by

$$Q_D \approx 20 N_A^2 \quad (12)$$

where  $N_A$  is the aperture width in wavelengths. Finally, the resistive dissipation loss associated with the interdigitated transducers is given by  $Q_\Omega$ , i.e.,

$$Q_\Omega = 1.3 \times 10^{14} N_g N_{CR} h / N_A^2. \quad (13)$$

The starting point of a resonator design is based on first selecting a geometric configuration, determine the various losses identified above, and compare the computed values to the inherent  $Q$  of the material ( $Q_M$ ). A geometrical configuration, in turn, is generally defined by deriving parameter values for the aperture ( $N_A$ ), the transducer length ( $N_T$ ) and the number and depth of the grooves forming the reflective array. In particular, the aperture  $N_A$  selected must be sufficiently small so that transverse spurious modes are suppressed but large enough to provide a practical transducer capacitance. In general,  $N_A$  is chosen to satisfy  $100 \geq N_A \geq 50$ .

The length of the transducers,  $N_T$ , must be large enough to provide good acoustic coupling but small enough to keep the resonator cavity length as short as possible in order to suppress adjacent resonant modes. Usually,  $N_T$  is selected to satisfy  $40 \geq N_T \geq 25$ . In addition, the transducers are generally apodized to provide matching of the transducer beam profile to the lowest order resonant mode. The resonant mode profile has a gaussian cross section so that for optimum coupling the transducer will generate a beam with a similar profile. In practice an approximation due to Haus [6] is used to apodize the transducers and it has been shown to be very effective in suppressing transverse modes.

In order to employ geometries which are compatible with current production capabilities single electrode transducer configurations were selected. At 400 MHz the nominal wavelength is 7.9 micrometers. The width of a single electrode and a groove width is less than 2 micrometers. Alternatively, the width of a double electrode stripe is less than 1 micrometer. Since production processing employing wet etching techniques require geometries to be greater than 1 micrometer, a single electrode transducer configuration is selected. This choice has the added benefit that all minimum geometries (electrode and groove widths) have the same dimension. Therefore any fabrication optimization such as exposure and etch time adjustments are considerably simplified.

Finally, recently reported work [8] suggests that synchronous transducers, i.e., transducers with electrode placement shifted relative to

conventional buried transducers by  $1/4$  wavelength but not buried, offer several advantages. Specifically, the resonant response appears to significantly improve spurious suppression. In addition, this synchronous structure is simpler to fabricate and less sensitive to process variations, a key advantage for devices designed for large volume production. However, this design approach will yield a slightly larger insertion loss. Based on the above considerations, a "surface" transducer as opposed to a "buried" configuration was selected to meet the electrical design requirements for the resonator of this program.

In order to suppress direct electromagnetic feedthrough from input transducer to output transducer, it is desirable to incorporate a shorted transducer configuration as a shield between the active transducer elements. An optimum length ( $N_s$ ) has not been established. However, it is felt that selecting a value for  $N_s$  as large as  $N_s = 20$  (wavelength) will be more than adequate to minimize capacitive coupling, yet, at the same time, will not substantially increase the resonant cavity length.

Finally, the metal thickness,  $t$ , of both transducers and shield configuration must be small in order to minimize any offset in frequency of the fundamental resonance. A value must be selected that is compatible with present production fabrication practices yet reduce overall resistance losses.

The best device performance has been shown to result for resonators with a large number of shallow grooves (as opposed to short gratings with relatively deep grooves). That is, the groove depth should occur in the range  $.015 \geq h/\lambda_0 \geq .005$ . The rationale is that shallow grooves maximize  $Q_B$ , and long gratings maximize  $Q_R$ . In order to effectively suppress reflection coefficient sidelobes, weighting of the reflective elements is required. For this case, the length of each reflector groove (in units of one half wavelengths),  $N_R$ , is related to the actual number of grooves,  $N_G$ , according to the selected weighting function. Two choices of weighting are generally employed, namely cosine and Hamming. Hamming weighting exhibits the best reflector sidelobe suppression characteristic, and it can be shown that the value for  $N_R$  and  $N_G$  are related according to the expression [2]  $N_R = 1.85 N_G$ .

In order to meet the performance requirements of this program, the geometrical parameters depicted in Table 2.2 were selected. The required and predicted performance is seen in Table 2.3. It can be seen that transducer resistive losses and reflector radiation losses are negligible. In fact, the lowest  $Q$  value is the material quality factor. This in turn implies that the parameter selection of Table 2.2 is a good starting point to satisfy the electrical specification requirements. The next largest  $Q$  is that computed for air loading. Both sources of loss are the major contributors to overall resonant loss. This can be demonstrated by comparing

$$Q_{M+A} = 1/(1/Q_M + 1/Q_A) = 1.8 \times 10^4$$

with the value of  $Q_U$  of Table 2.3.

TABLE 2.2. RESONATOR DESIGN PARAMETER VALUES

Parameter	Selected Values
$\lambda_0$ (Micrometers)	7.89
$N_A$	100
$N_T$	30
$N_S$	20
$N_g$	811
$N_r$	1500
$t/\lambda_0$	.019
$h/\lambda_0$	.016
Transducer Apodization	Haus Profile
Reflector Weighting	Hamming

KEY:

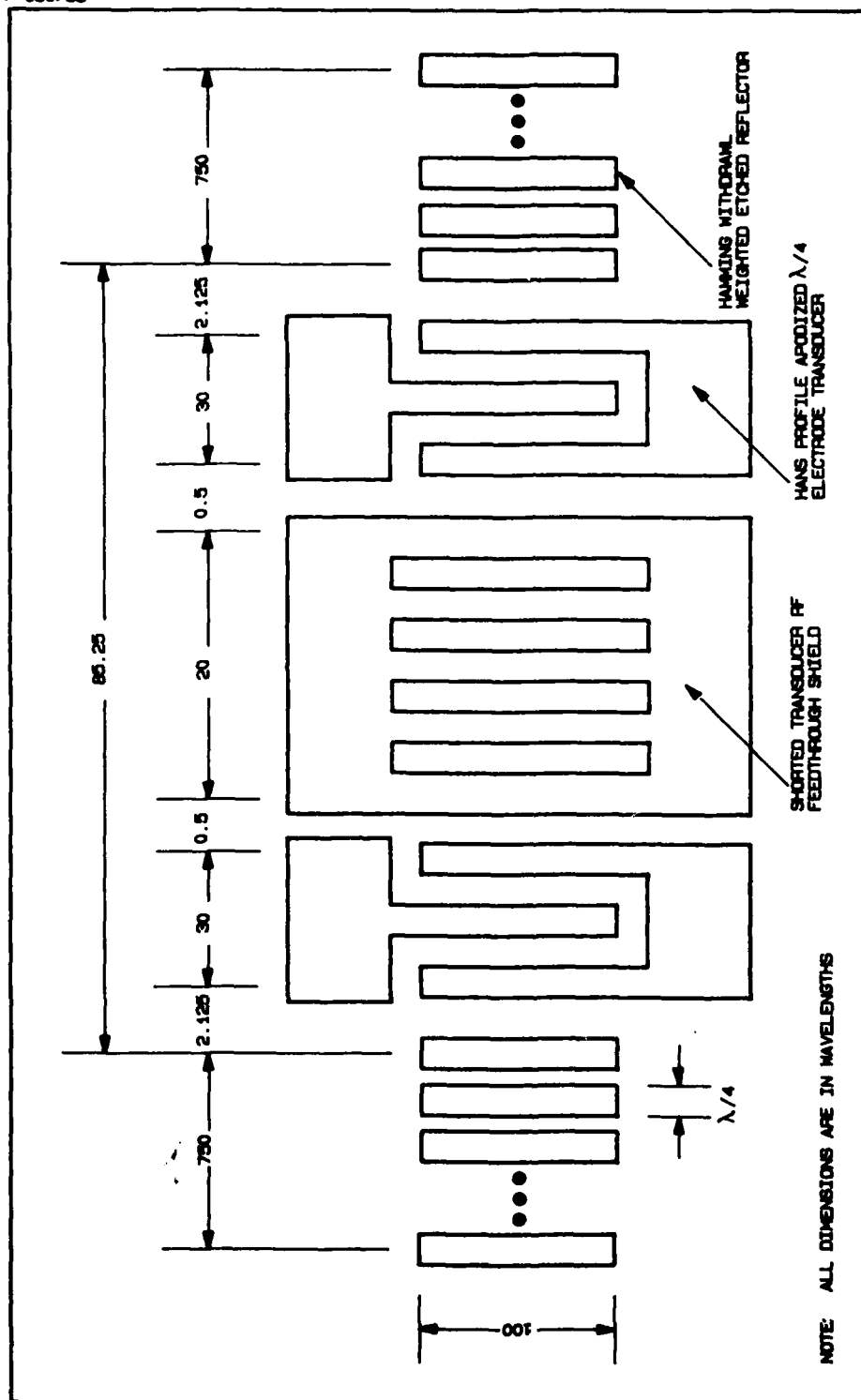
- $N_A$  = Aperture width in wavelengths ( $\lambda$ )
- $N_T$  = Length of the transducers ( $\lambda$ )
- $N_S$  = Length of the shorted transducer (shield) between active transducers ( $\lambda$ )
- $N_g$  = Actual number of reflecting grooves (after weighting)
- $N_r$  = Length of reflector grating ( $\lambda/2$ )

TABLE 2.3. RESONATOR LOSS PERFORMANCE PARAMETERS

<u>Required Performance</u>	
Loaded Q ( $Q_u$ )	$\geq 4000$
Insertion Loss	$\leq 5$ dB
Unloaded Q ( $Q_u$ )	$\geq 9100$
<u>Computed Performance</u>	
$M_{CE}$	$85.5 \lambda_0$
$N_{CR}$	$336 \lambda_0$
$Q_R$	$2.3 \times 10^8$
$Q_{BG}$	$4.1 \times 10^5$
$Q_{BT}$	$3.2 \times 10^5$
$Q_M$	$2.6 \times 10^4$
$Q_A$	$5.8 \times 10^4$
$Q_D$	$2 \times 10^5$
$Q$	$10^9$
$Q_U$	$1.5 \times 10^4$
$Q_L$	6600

In summary, the key factors influencing SAW two port resonator design have been discussed. It was shown that the overall unloaded resonator Q consists of several components. All the loss elements which are design dependent have been minimized to the point where only a material and air loading loss dominate. Air loading loss can be minimized by sealing the packaged die under high vacuum conditions. This sealing technique is costly and its use must be traded off with respect to required device end-of-life performance and anticipated package leak rates.

The 400 MHz design of the resonator developed for this program is presented in Figure 2.4. All dimensions are given in terms of basic wavelength units.



NOTE: ALL DIMENSIONS ARE IN WAVELENGTHS

Figure 2.4. Resonator Design Schematic

### 3.0 DEVICE FABRICATION

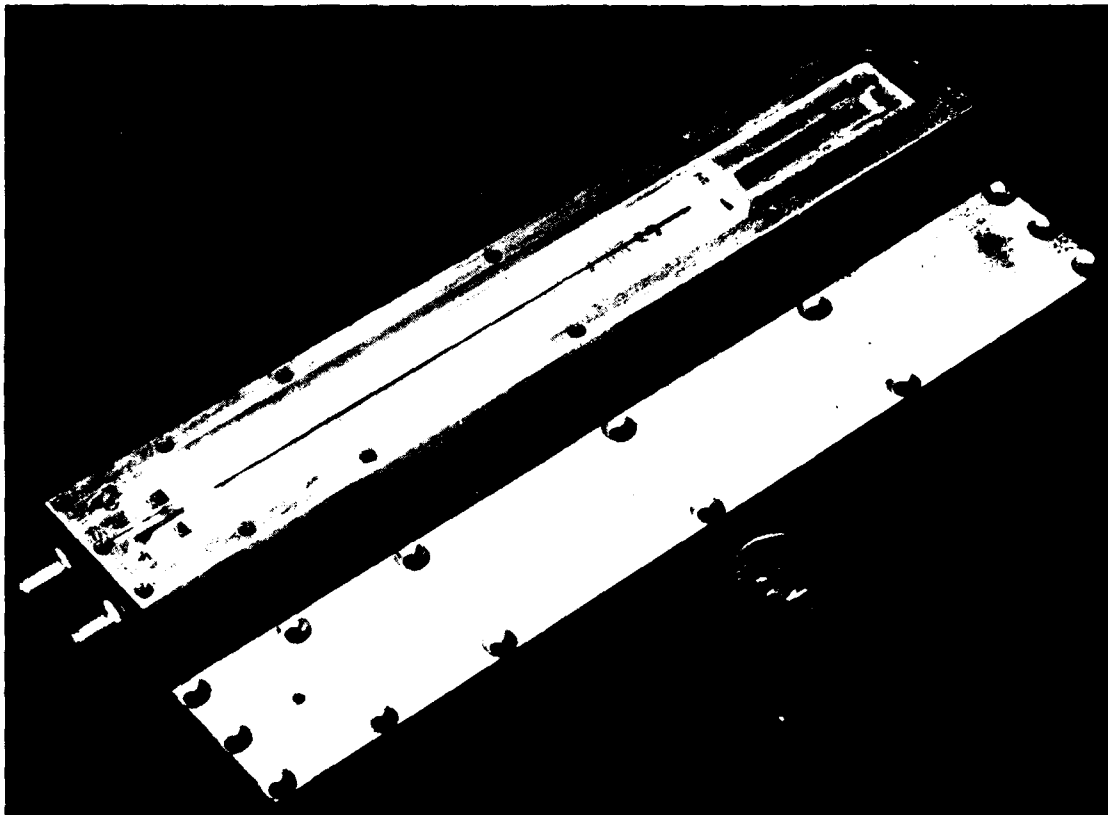
**3.1 RAC Device.** RAC device fabrication uses basically the same photolithographic process and assembly techniques developed for other standard SAW devices. The groove array fabrication step using ion beam etching adds only minor complexity to the existing fabrication process. However, the selection of a production method to form the notch between the input and output transducers was viewed as a key problem from the beginning of the program. Lithium niobate is a relatively fragile material, and all milling and cutting processes investigated could not assure the crystal would remain in a relative stress-free state. Furthermore, the addition of a septum to the package housing severely complicated the development of a hermetic production package with rework capability.

During Phase II of the engineering effort, it was demonstrated that a 50 dB feedthrough level can in essence be achieved without a notched crystal and septum combination. The use of a well grounded shield configuration placed between the transducers and short wire bonds interconnecting the transducers to the feedthrough terminals provided the required signal feedthrough suppression. As a result, the crystal fabrication and packaging approach of the RAC device was significantly simplified. A description of this effort is presented in Section 5.0.

In this section, the details of the photolithographic process and the ion beam etch technique employed to fabricate the RAC crystal are presented. Also described are the package and the overall assembly technique.

**3.1.1 Device Description.** Figure 3.1 shows a completely assembled RAC device, as built during the engineering phase (I) of this program. The nickel plated, machined aluminum package contains three cavities. The upper cavity, or crystal cavity contains the crystal, a metal septum, grounding terminals, and feedthrough terminals which connect to the lower cavities. The lower cavities in turn each contain a series mounted toroid inductor and an SMA connector. All the cavities are non-hermetic, and each cover is simply secured with screws. A common cover is used for both of the lower cavities. In the upper cavity, more screws are used at the end of the package with the septum to assure good contact between the housing wall, septum and lid. It should be observed that one screw actually threads into the septum itself, and furthermore, a wire is pressed into a groove milled into the top of the septum. The overall packaging scheme was originally developed to maximize electromagnetic feedthrough suppression.

Each toroid in the lower cavities is wound with 20 turns of 32 gauge insulated copper wire around a phenolic T16-0 core and soldered in series with the transducer, the SMA connector and the feedthrough terminal. After the final tuning operation, both toroids are secured with the application of RTV 3140 silicone rubber adhesive. The adhesive keeps the wire turns fixed about the core and at the same time supports the toroid as a whole to the package housing.

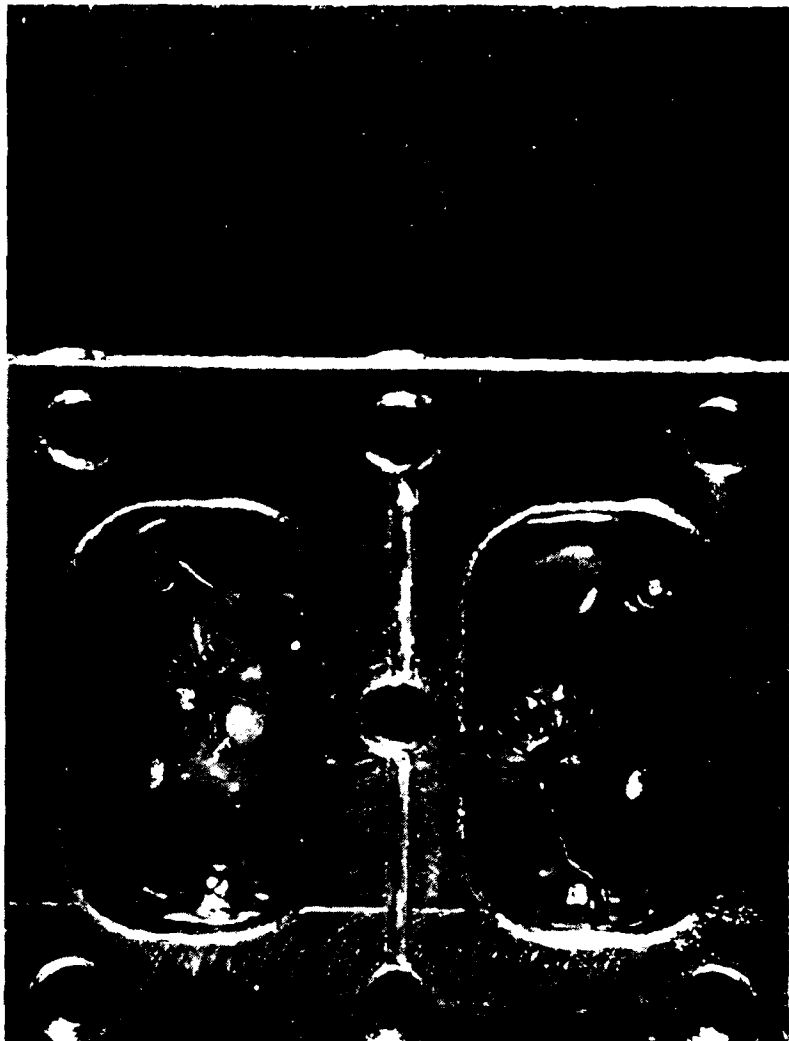


82-08-0228

Figure 3.1a.

Photograph of completely assembled RAC Filter. Figure 3.1a above shows the crystal cavity and septum configuration.





334020-6

Figure 3.16.

Figure 3.1b above shows the two separate input and output cavities containing the series tuned toroids.

3.1.2 Crystal Description. Figure 3.2 is a diagram depicting the overall structure of a fully processed RAC crystal ready for final assembly and electrical test. The various component elements are also labeled in the diagram. Detailed numerical data of the crystal, the photolithographically defined pattern and grooves is given in Table 3.1.

Three pairs of input/output transducers are "printed" on the same crystal in order to minimize crystal level reject and rework. It is also possible to print new transducers without affecting the rest of the crystal processing if the original transducers are damaged, but this rework effort is difficult and a time consuming operation. Alignment is critical and pattern definition is compounded due to photo-resist buildup around the notch and the edges of the crystal. Since these transducers have only eight fingers, nearly perfect delineation is required in order to maintain the insertion loss at an acceptable level. Transducers with open fingers are rejected, however, shorted fingers may be separated with the laser mask repair unit. Photolithographic rework on transducers was successfully performed on three devices fabricated during this phase of the program.

Two pairs of test transducers at the opposite end of the crystal from the input/output transducers are included in the pattern. The purpose of these transducers is to evaluate the transmission characteristic of either reflective grating for time delay measurements and for overall passband evaluation of the transducer configuration. Since these test transducers are not generally used for final measurement purposes and, in addition, must be covered with absorber to prevent strong reflections, they will be eliminated from the photomask for future phases of this work.

The dual phase correction pattern placed between the reflective array is a composite pattern consisting of two individual metallic strips. Each strip has a straight base and a discretely varying edge along its length. The two patterns are placed in opposite direction but share a common base. The extent of base overlap is not critical, provided it does not exceed the minimum width of either single phase correction pattern. The first strip is a generic pattern determined from the average of several phase errors versus frequency plots. The purpose of this generic pattern is to provide data on the repeatability of the device to device phase variation, and to evaluate the effectiveness of using a single pattern on all future devices. This approach will eliminate performing a custom phase correction to each device. The second pattern, however, is a custom pattern applied, based on the performance and subsequent correction of the generic pattern. Both phase correction patterns are applied using the liftoff process. At the present time three separate photolithographic steps must be performed in order to provide a phase-corrected crystal.

The final intent will be to generate an "optimized" generic phase correction pattern and include it in the etch mask containing the transducer configuration and the reflective array geometry. If this can be achieved, crystal processing can be reduced to a one step photolithography operation.

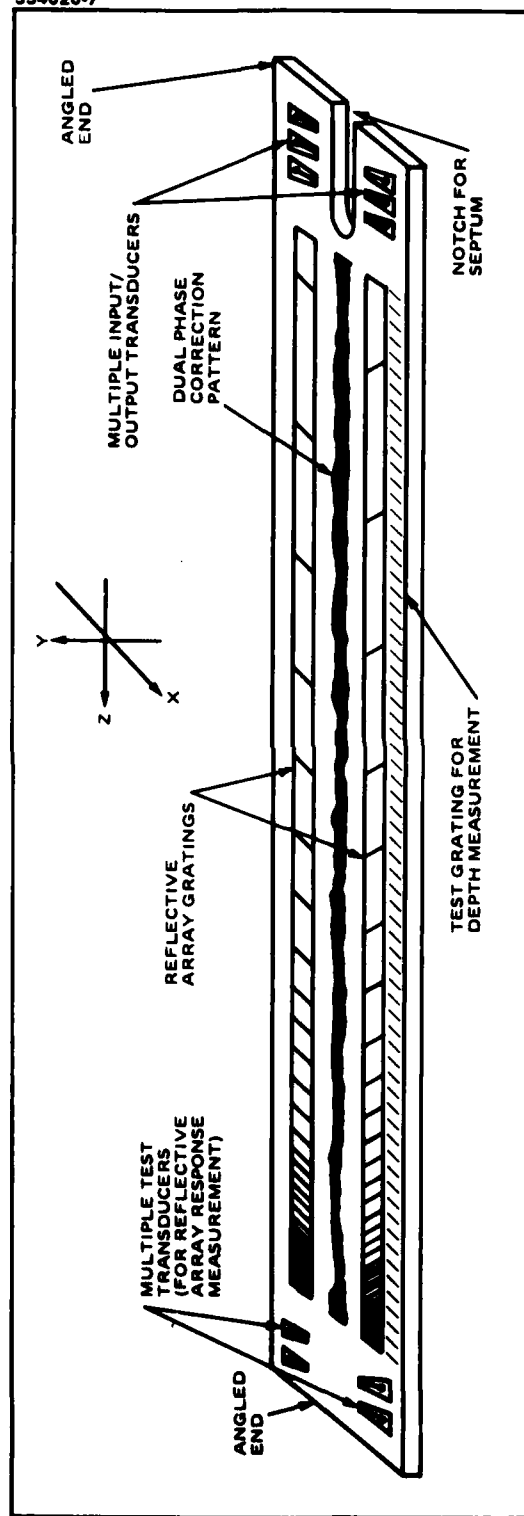


Figure 3.2. Processed RAC Crystal. Notch is sawed into the die after transducer pattern has been etched.

TABLE 3.1. RAC CRYSTAL DATA

<b>I. <u>Substrate</u></b>	
Substrate material	YZ-Lithium Niobate (LiNbO <sub>3</sub> )
Substrate dimensions (approximate)	12.7 x 1.3 x 0.15 cm
Acoustic velocity	3.47954 x 10 <sup>5</sup> cm/sec
Notch dimensions (approximate)	0.65 x 0.30 cm
Angle on ends (approximate)	7-10 degrees
<b>II. <u>Metallization</u></b>	
Material	99.9 percent pure aluminum (Al)
Thickness (Etch Process) (transducers, notch-cutting guide, grating mask)	3500 Å
Thickness (Liftoff Process) (phase correction pattern)	400 Å
<b>III. <u>Transducers</u></b>	
Number	3 input/output pairs, 2 test pairs
Number of fingers per transducer	8
Line/space width	6.74 µm
Overall dimensions (including surrounding ground shield)	2.921 x 1.016 mm
Aperture width	1.778 mm
<b>IV. <u>Phase Correction Pattern</u></b>	
Maximum width of single pattern (approximate)	0.5 mm
Minimum width of single pattern	45.7 µm
Resolution in length (frequency)	162.6 µm (93.4 KHz)
Overlap dimension between single patterns in dual	45.7 µm
<b>V. <u>Reflective Array</u></b>	
Length	10.67 cm
Number of grooves (each side)	6,202
Aperture width (same as for transducers)	1.778 mm
Groove angle (measured from Z-axis)	46.82 degrees
Minimum groove width	7.54 µm
Maximum groove width	10.29 µm
<b>VI. <u>Test Grating</u></b>	
Bar, space width	50.8 µm
Bar height	203.2 µm
Number of bars	1048
Number of tick marks	13 (1 every 5 MHz = 1 every 8.7 mm)

The test grating shown in Figure 3.2 is composed of many rectangular bars and is included in the pattern so that the groove depth profile for each device may be checked. These grooves are much wider than those forming the array to allow for the finite width dimension of the stylus used in the depth measurement equipment. Reference along the array is established by selecting a bar in 5 MHz increments.

To minimize electromagnetic coupling between input and output transducers through the crystal substrate as well as the air space above the crystal, a notch is cut between the transducers at the end of the crystal. This is presently performed using a dicing saw. Lithium niobate is sufficiently fragile that fracture lines have been introduced during this operation. This task is very operator-dependent, and the implementation of a low-cost production method does not appear feasible.

Finally, spurious reflections are suppressed by covering all four edges of the crystal, all unused transducers, and the test grating with acoustic absorber. Photoresist is used as the absorber while performing first electrical test. When the device is prepared for final electrical test, RTV 3140 is applied instead. End reflections are further suppressed by slightly angling the ends of the crystal.

3.1.3 Detailed Process Description. Figure 3.3 presents a summary of all the process and assembly steps required to fabricate the RAC line. In the discussion that follows, a brief review is provided on the key steps employed on the Engineering Phase units, also outlined are the relevant process steps that will be changed in the Production Phase of this program.

All deposition and photolithographic process steps are identical to those used on standard SAW devices. Photoresist application is performed by dipping rather than spinning, but this is the method adopted in general on long SAW crystals.

The ion etch process is discussed in detail in Sections 3.1.4 and 3.1.5 respectively. During this operation the grooves are formed in the array, the metal mask is removed, the depth profile is measured using the bar grating at the edge of the crystal and a uniform oxygen rejuvenation etch is performed to eliminate residual conductivity effects on the crystal surface generated by the ion bombardment process. After ion etching, the dual phase correction patterns are added to the crystal. The two thin aluminum strips are placed in the space between the two rows of grooves forming the "chevron" configuration. The pattern itself is transferred using a standard liftoff process. As already discussed in the previous section, both process steps will be eliminated in the production phase and a single pattern will be incorporated into the photomask and etched along with the transducer configuration.

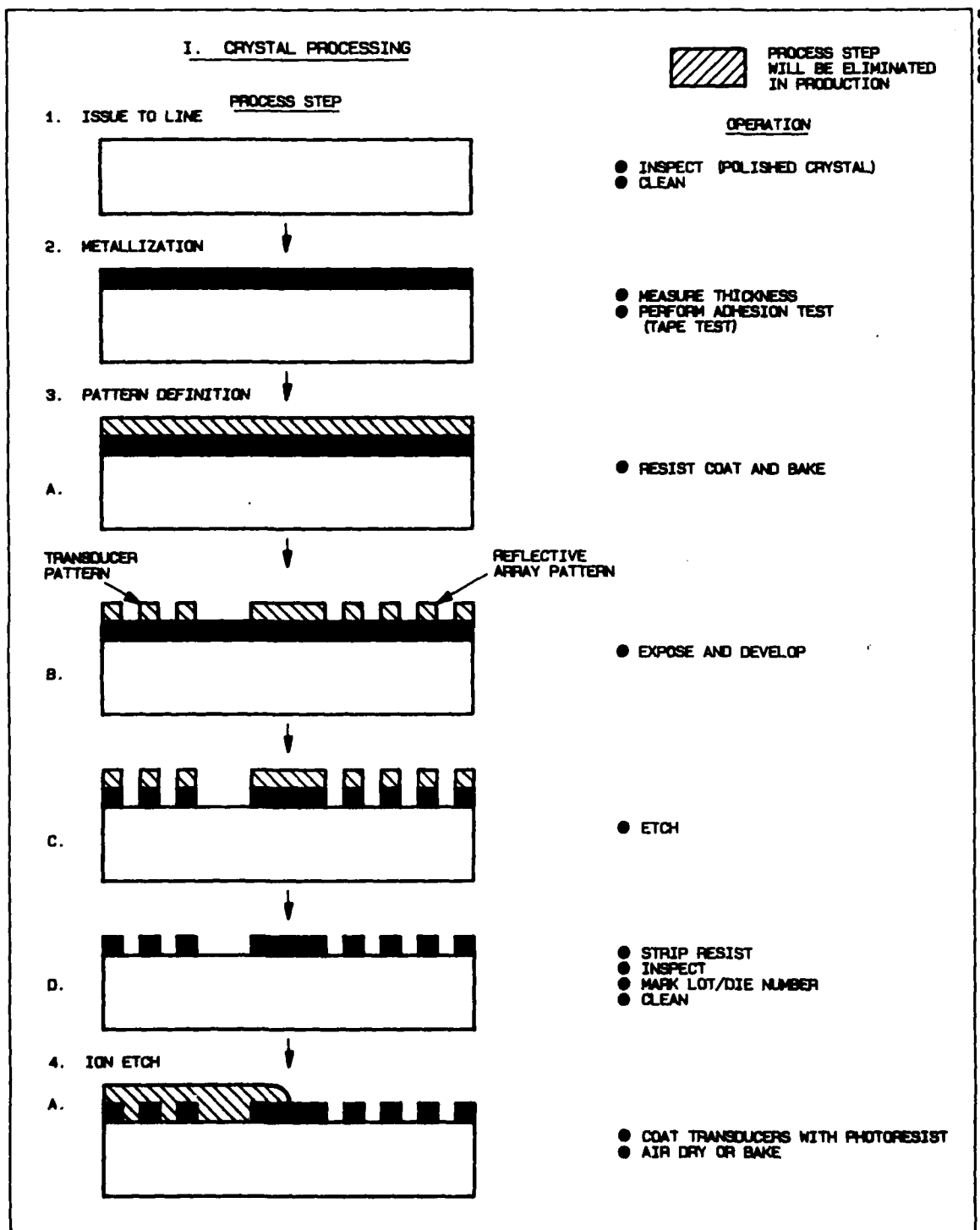


**Figure 3.3. RAC Device Fabrication Flow for Engineering Samples**

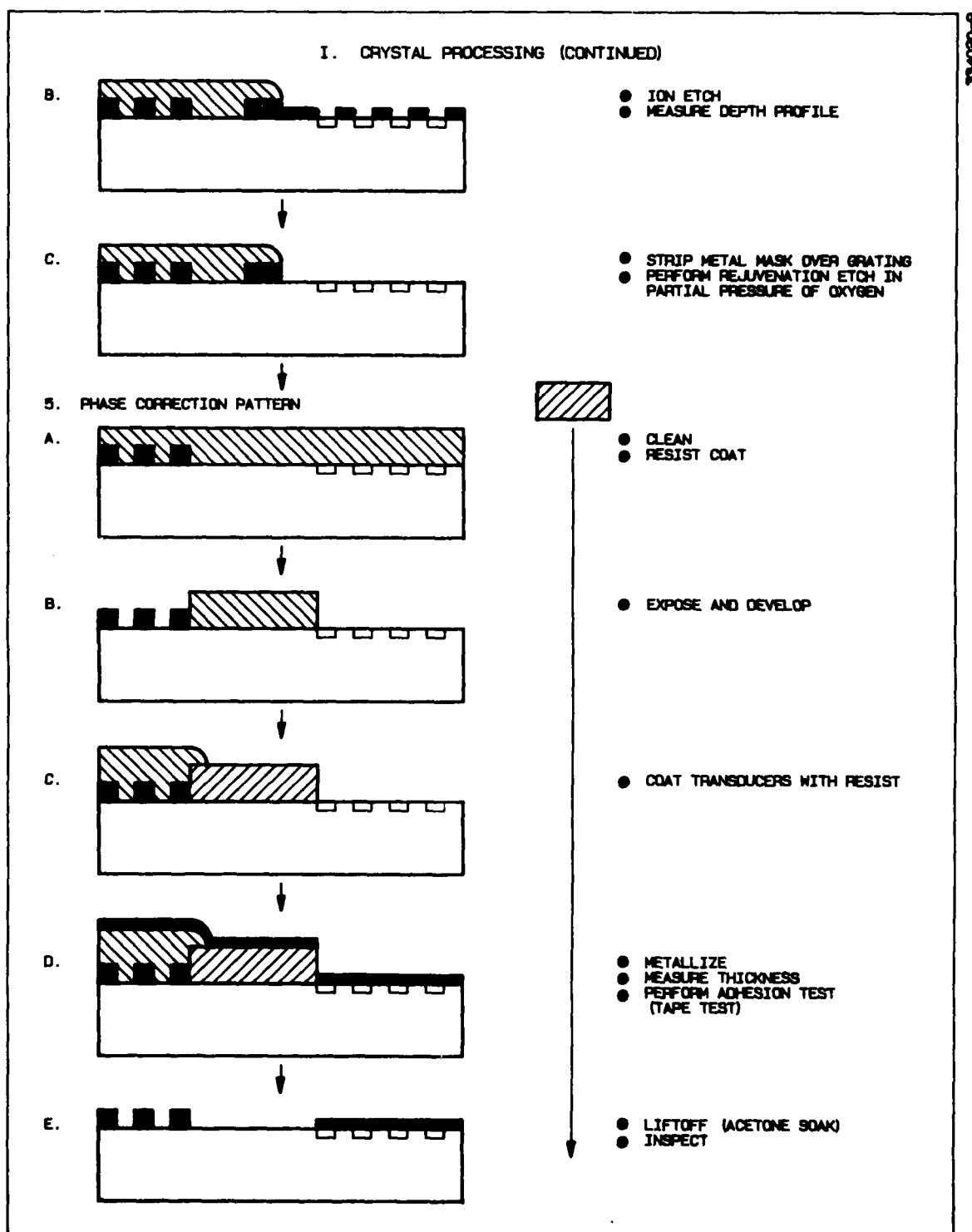
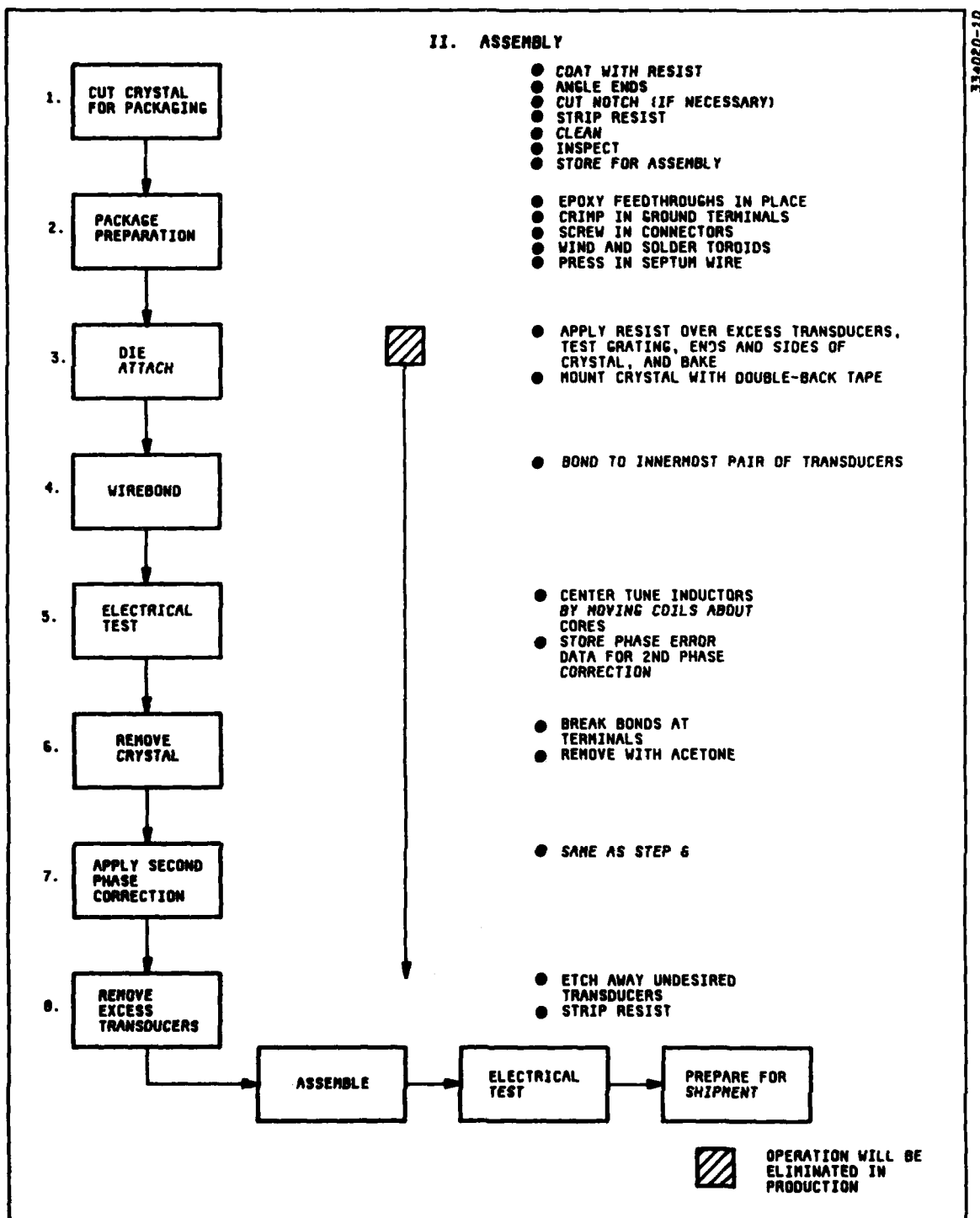


FIGURE 3.3. RAC Device Fabrication Flow for Engineering Samples (Continued)



**Figure 3.3. RAC Device Fabrication Flow for Engineering Samples (Continued)**



The assembly and test operations are generally initiated with the necessary preparations of the package. Connectors, feedthrough and ground terminals, toroids and wire for the septum groove are installed into the housing. Since the cavities are not hermetic, the feedthrough terminals are simply epoxied into place. A hermetic cavity will however require that they be soldered. Hughes/Materials and Processes Department has developed a procedure for hermetically soldering these into place at high yields. The ground terminals are small sections of large diameter wire which are pressed into the housing floor with a crimping tool. In the next phase of the program these terminals will be replaced with gold-plated molytabs welded to a nickel-plated housing base. It has been demonstrated that this is a low resistance interconnection and therefore does not adversely affect the feedthrough performance.

During the combined assembly and test operation, the Engineering Sample Phase devices were subjected to extensive handling. This resulted largely because of the dual phase correction requirement. For each pattern correction and subsequent electrical evaluation the crystal has to be temporarily secured and bonded into the package. The temporary assembly operations were implemented with photoresist as the acoustic mode absorber and with double-backed tape for attachment of the crystal to the housing floor. Final assembly, of course, was performed entirely using RTV.

Extensive handling always introduces the added risk of damaging the metal patterns, introducing foreign matter in the active region or possibly even fracturing the crystal material itself. The latter in particular has occurred several times with the notched crystal configuration. Careful alignment of the crystal has to be exercised when placed into the housing and simultaneously aligned with the septum. The crystal itself is relatively long and any excess torque applied at right angle to its length during mounting risks fracturing the crystal at the notch site. A fully productized version of this design will eliminate both the notch as well as the added highly labor intensive process and assembly steps associated with the phase correction operation. The removal of the crystal from the package should only be required in the event extensive rework, such as replacing a transducer.

3.1.4 Reflective Array Etch Development. Ion beam sputter etching has proven to be the most effective method of etching the reflective grooves in the RAC (as well as the resonator) SAW devices. In our earlier experiences with argon ion beam etching of  $\text{Li NbO}_3$ , we found that the removal rate was sufficiently constant with time that the varying depth of etch (required to optimize the frequency response of the reflective grooves) could be produced by traveling the crystals under an aperture at a time-varying programmed speed. This method permitted us to make delay times with various designs of frequency response by merely varying the paper-tape command to the etching stage. An alternative method was developed to produce a larger number of devices when a constant design of depth profile is to be repeated. In this method (shown schematically in Figure 3.4)

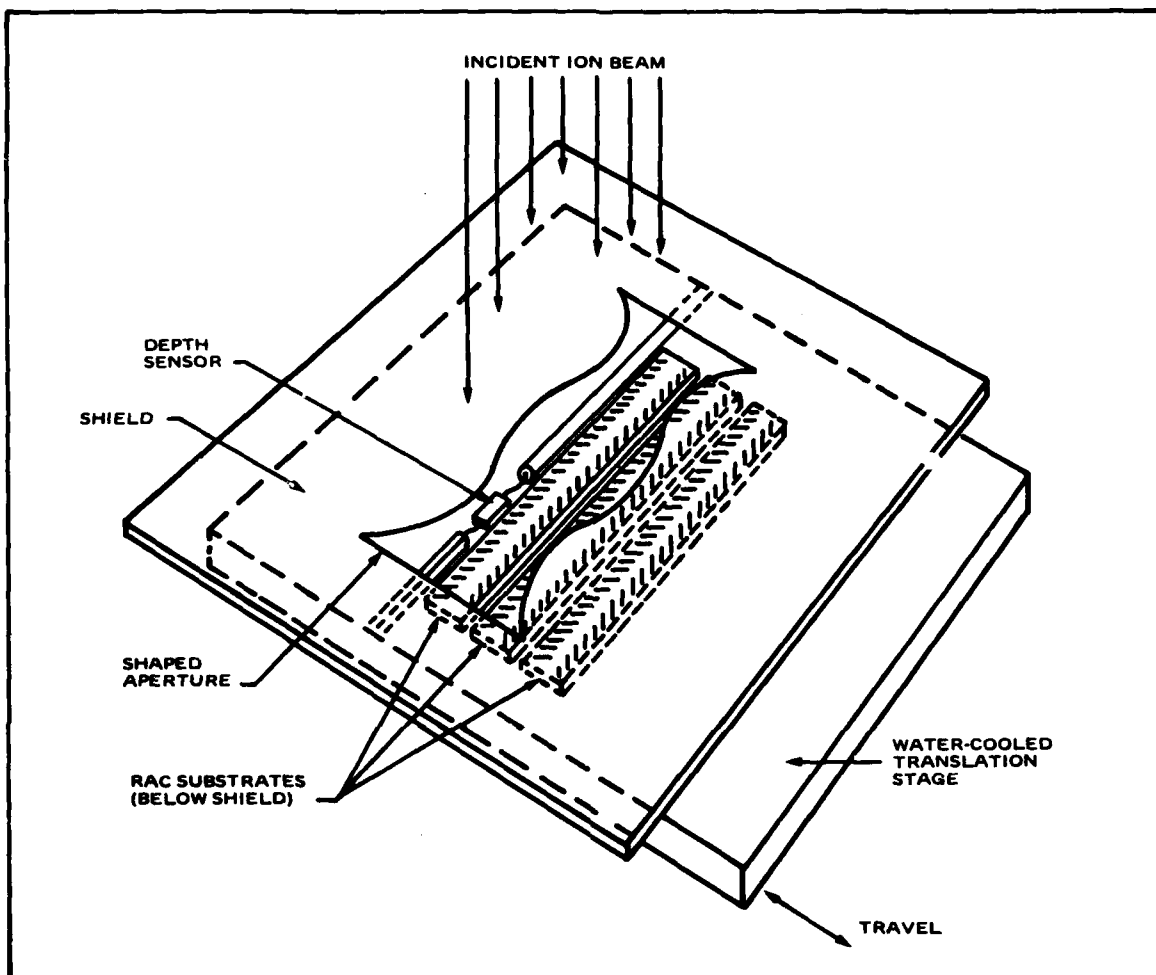


Figure 3.4. Schematic Arrangement for Depth Profile Etching

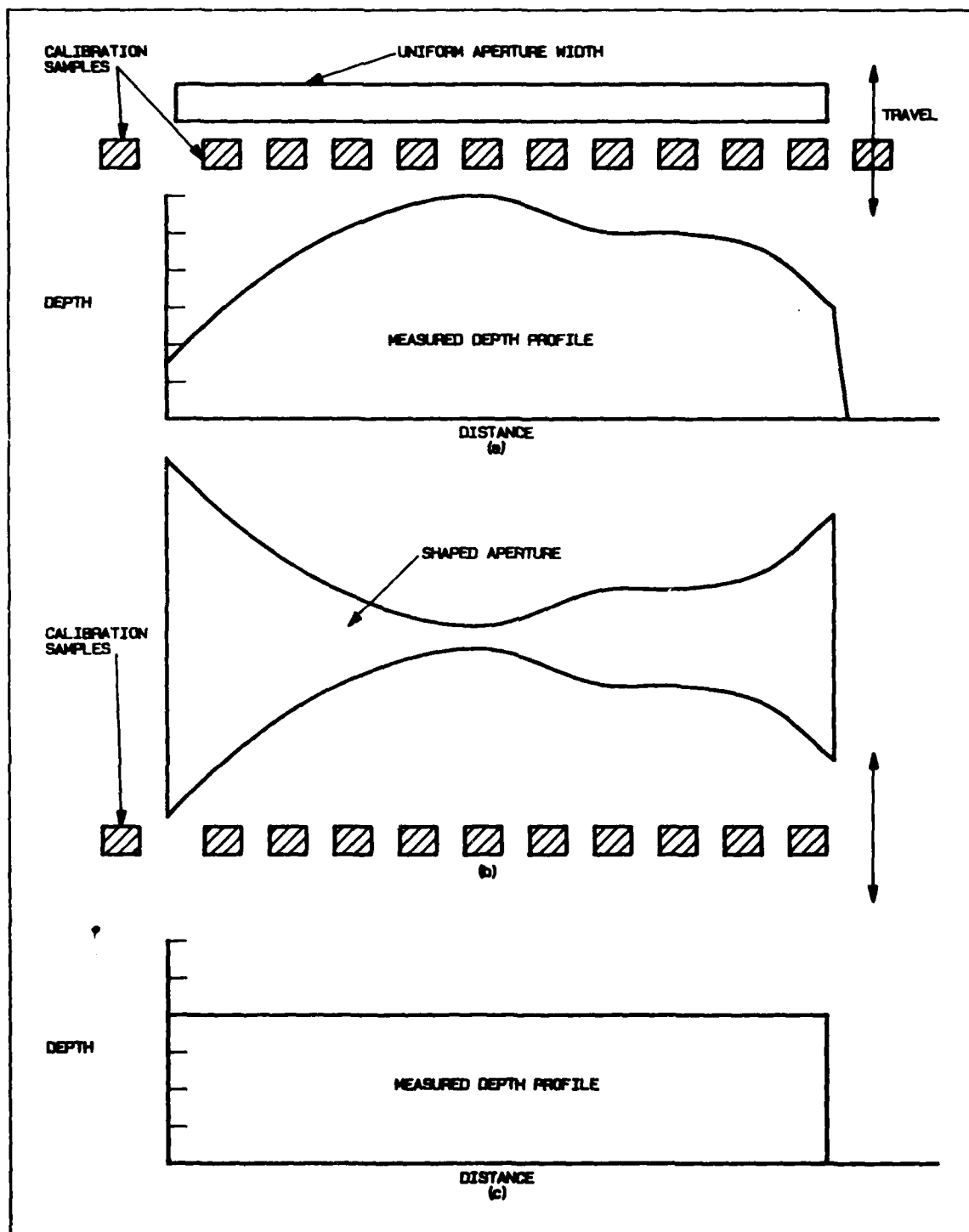


Figure 3.5. Steps in Achieving Desired Etch Depth Profile

an aperture is prepared which is wider where the crystal is to be deeply etched and narrow where it is to be shallow. Thus, a number of patterned crystals can be translated uniformly under the aperture and the same depth profile will be etched simultaneously into all of their surfaces. By this approach we have shown very close control of the etching profile which is repeatable for many RAC lines.

The critical step in this method is the development of the aperture mask to produce the particular depth profile. To illustrate the steps involved in this development consider that a uniform depth is to be produced across the entire crystal surface (as is the case when producing resonator devices). A measurement is made of the ion beam intensity profile by translating calibration samples under a uniform aperture (see Figure 3.5a). These samples may be a gold film with a coarse photoresist grating pattern to permit accurate measurement of the etch depth variation resulting from fall-off of the ion beam intensity at its outer edges. An aperture is then shaped to compensate for this intensity distribution (see Figure 3.5b) and another calibration etch is made on monitoring samples. A uniform depth should now be produced (see Figure 3.5c). If not, minor adjustments are made in the aperture to achieve the final depth profile. We have achieved a depth accuracy of within  $\pm 50$  Å in most profile designs. For non-uniform profiles used in compressive or expansion RAC lines a shaped aperture producing close to the designed profile is used as the starting calibration. Then minor changes are made in preparing a new etching aperture for the new depth profile. All etching apertures are cataloged and retained for subsequent use in device etching.

**3.1.5 Reflective Array Depth Control.** In the previous section we described the technique used to produce the depth distribution in the reflective array devices. The sensor which we have developed provides the capability to simultaneously etch a number (6 to 10) of RAC lines and program their final depth to be controlled automatically. The sensor (shown schematically in Figure 3.6) consists of a very thin conductive film with measured thickness of  $\text{SiO}_2$  deposited over it. During the etching operation of a RAC line (or a resonator wafer) the sensor is placed adjacent to the RAC line at a position where the  $\text{SiO}_2$  thickness will be etched in the same time that the desired depth is etched into the crystalline substrate (see Figure 3.4). (Repeated calibration runs have shown that a constant relationship exists between the etch rate of sputter-deposited  $\text{SiO}_2$  and  $\text{LiNbO}_3$  or crystalline quartz substrates.) Once the  $\text{SiO}_2$  film is penetrated the metal sublayer is etched in seconds, opening a bridge circuit and triggering the end of the etching process. When many substrates are being etched simultaneously they travel back and forth under the shaped aperture many times and thus the sensor is able to control the depth on all substrates to within  $\pm 50$  Å of the desired length.

The accuracy of the system depends upon the precision in preparation of the sensor devices. These are made on clean glass slide substrates. The metal bridge film is a 100 Å of Au with less than 25 Å of Cr deposited above and below it to improve adherence of the  $\text{SiO}_2$  layer. As shown in Figure 3.7, thicker metal (about 0.3  $\mu$ ) is deposited at the ends for contact

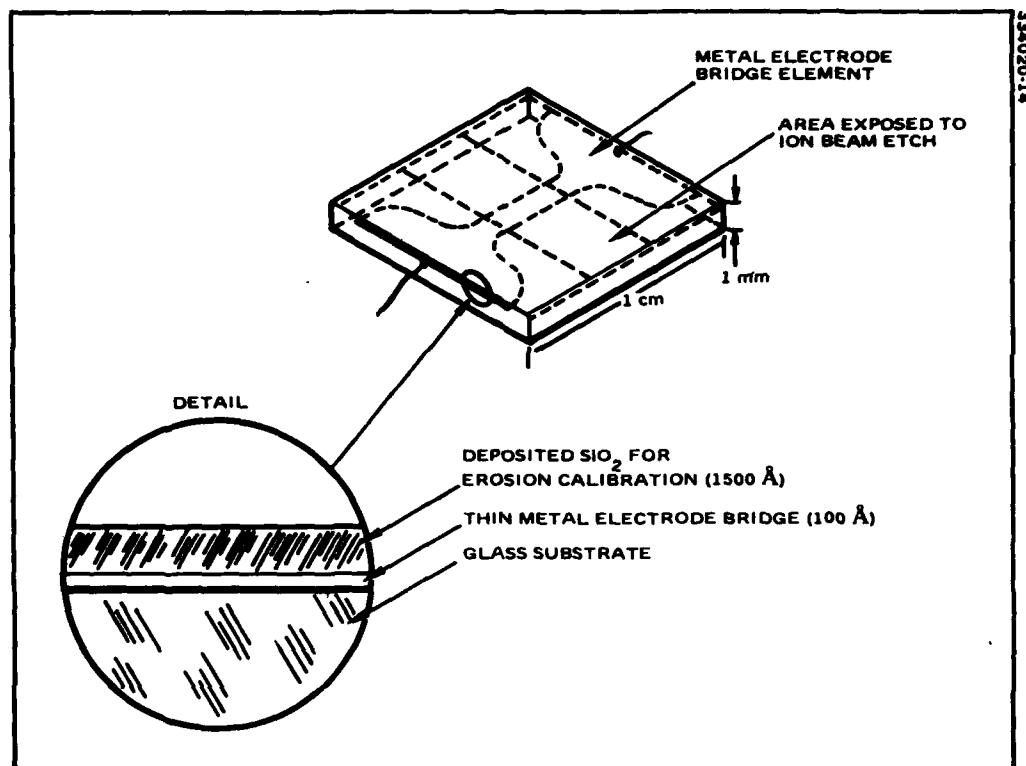


Figure 3.6. Automatic Etch Depth Sensor. Calibration is achieved by relating the rate of sputtering removal of  $\text{SiO}_2$  with that of the bulk material used in the acoustic device.

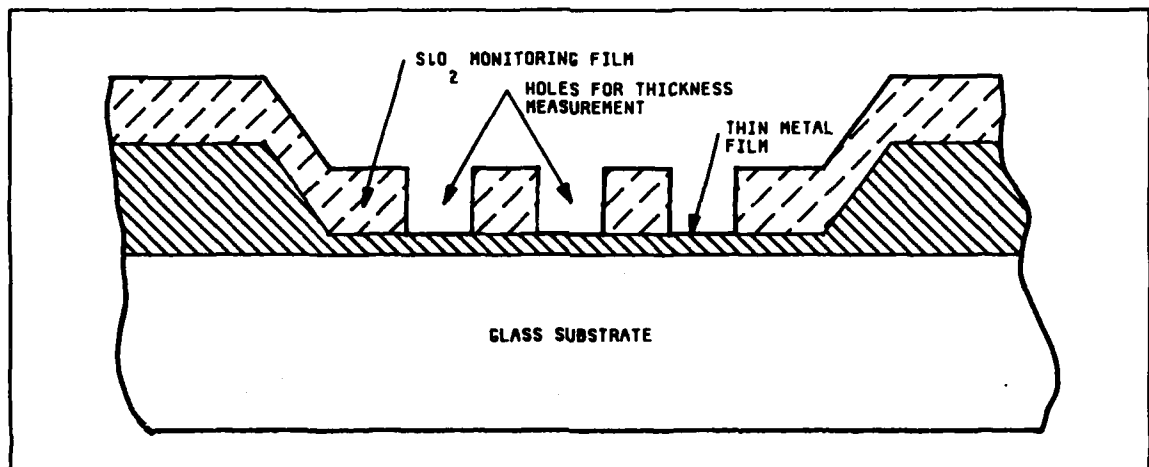


Figure 3.7. Cross Section Detail of Etch Depth Sensor

durability, then a photoresist pattern of dots is applied. The  $\text{SiO}_2$  film is sputter-deposited onto the surface and then the slide is cut into 1/4 inch wide sections. The photoresist is dissolved off leaving a repeated thickness pattern in the  $\text{SiO}_2$  film. A calibrated Dektak surface profilometer is used to measure the local thickness of the  $\text{SiO}_2$  film and this sensor is placed at the appropriate position beside the RAC lines. Although the ion beam intensity has been observed to slowly increase and decrease with time, the sensor integrated the total etching accomplished and in over a dozen tests it has provided accurate end point determination. The single failure which occurred (when 6 RAC lines were being etched) came about because a single vacuum feedthrough carried the instrumental signal to the sensor (the other side was tied to the ground). In the process of etching the lines the single lead was shorted to ground and did not detect the opening of the sensor film. Since that time we have redesigned the circuit to carry both leads out to the instrumentation and have also added a second sensor which will give a preliminary warning signal when the etch is approximately 75 percent complete. This system will allow many substrates to be etched with confidence to the desired depth profile in one etching operation. For quantity production additional substrate holders can be loaded for rapid replacement between etching operations.

3.2 Resonator Device. The resonator uses basically the same photolithographic process and assembly techniques developed for standard SAW devices. The reflective grating, like in the RAC device, is formed using ion beam etching. While other processes such as reactive plasma etching and rf sputter etching can be employed to form a uniformly depth-etched profile, Hughes has elected to go with the ion beam approach since it is highly controllable and potentially provides wafers with a narrow center frequency distribution. In particular, the argon ion beam density and uniformity over the target area in an ion beam system can be more readily controlled than the chemical reaction rates of a plasma system. As a result, overall etch rates are controlled and more reproducible from run to run. While rf-sputter etching can potentially provide etch performance equalling that of an ion beam system, extensive shaping of the electromagnetic fields at the perimeter of the target area has to be performed.

In order to meet the center frequency specification within the required 20 KHz tolerance, a fine frequency trim technique is required. When standard trimming techniques are employed, the individual resonator die is etched in the transducer region prior to final assembly. However, this does not adjust for any frequency shifts which may result from parasitic capacitance effects associated with the package and die attach process. In order to accommodate these shifts, Hughes is developing a frequency trim technique to be employed on a fully assembled and tuned device. In particular, a pulsed laser beam of very small spot size will be used to open the shorted electrodes of grating placed between the input and output transducers; this grounded grating helps improve the device feedthrough suppression. The trim operation can ultimately be performed using an automated laser system and is therefore well suited for large volume production requirements. A technical discussion of the selected frequency trim technique using the shorted feedthrough suppression grating is presented in section 7.3 of this report.

In this section, the details of the photolithographic process and the ion beam etch techniques that are employed to fabricate the resonator die are presented. Also described are the packaging approach and the overall assembly technique.

**3.2.1 Device Description.** Figure 3.8 shows a completely assembled resonator built during the engineering phase of this program. The header is a standard gold-plated, Kovar, dual in-line, hybrid pin package, manufactured by Isotronics, Inc. A common case ground is used, and two pins are used as standoff posts to serve as a transition between a solder connection and a wirebonded pad.

The toroids are connected in series to the transducers, and each is formed using 14 turns of 32 gauge insulated copper wire about a phenolic core element. After tuning, the toroids are secured with RTV 3140 to assure a stable series inductance value.

The resonator die is mounted to the package header with a small bead of RTV 3140 adhesive placed directly underneath its center. It was discovered early in the program that, if RTV is applied along the entire length of the crystal, a large frequency shift is introduced when torque is applied to the package in its test fixture. In addition, a large permanent shift was observed when these devices were sealed using projection welding. The frequency shift in the test fixture was eliminated by minimizing the use of RTV as described above. At the same time the shift during the sealing operation was greatly reduced. However, the small residual frequency shifts still observed after seal are presently still attributed to small header deformations that occur during the impact weld operation. These deformations are in turn transmitted to the crystal die via the adhesive fulcrum.

The inductive elements used to tune the transducers have been the object of considerable experimentation throughout the engineering phase. Because of the small transducer capacitance (approximately 0.7 pF), a relatively large inductance value is required. At the same time, a high-Q value is necessary in order to minimize both insertion loss and resonant bandwidth. The latter requirement in particular suggests the use of a toroid element. In practice, however, the use of a toroid is undesirable because it must be secured to the package with relatively large quantities of an organic adhesive. This in turn may potentially alter the long term device performance due to outgassing of the organic material.

If the inductors are placed in separate cavities, as is done in the RAC design, the parasitic capacitance of the feedthrough pin placed between the inductor and the transducer will in turn severely limit device performance. In addition, it would also greatly increase the overall packaging cost. Planar thin film spiral elements are attractive in terms of repeatability and stability, however, they are a source of resistive loss.



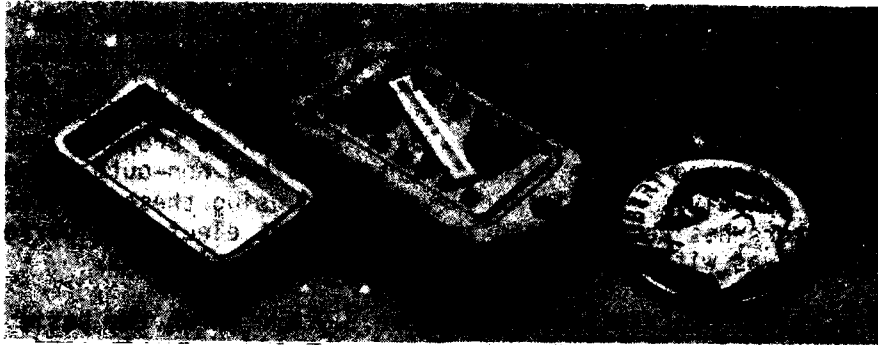


**Figure 3.8. Assembled Resonator.** Crystal is attached with RTV placed only underneath center position of die. Series inductive tuning is achieved using a phenolic toroid core.

During the engineering phase of this program, toroids were used on the ten delivered devices in order to demonstrate die performance. At the same time a parallel effort was undertaken to define an alternate tuning element to be used in the other phases of the program. The best choice to date is a tunable inductor manufactured by Piconics, Inc. This element uses bondable terminations on an alumina substrate base which is in turn connected to a solenoid winding encapsulated with conformal coated epoxy. The desired inductance is established by moving a rod made of a high permeability material inside the solenoid cavity. After the rod is properly positioned, it is rigidly attached to the element housing with a non-outgassing cyanoacrylate adhesive. Preliminary evaluation using these devices in sample resonators has demonstrated that equivalent electrical performance can be achieved as with the resonators using toroid elements.

**3.2.2 Crystal Description.** In Figure 3.9 are shown the basic elements of the resonator die. Detailed data on the overall dimensions of the crystal, the photolithographically defined pattern, and the groove structure forming the reflective array is presented in Table 3.2.

The input and output transducers lie near the center of the crystal, spaced a whole number of wavelengths apart. In order to establish high photolithographic process yields, single electrode transducers are used. The resulting line width is a nominal two micron value versus the required one micron value necessary for the equivalent "split" electrode design. (One micron electrode line width requirements approach the limit in resolution of standard optical photolithographic equipment used in production.) Test results to date indicate some defects in the fingers forming the transducers are tolerable, although specific inspection criteria have not been developed at this point.

Withdrawal weighted reflective arrays are placed symmetrically on both sides of the transducer region. As shown in the figure, the arrays have been stripped of the metal mask used to define the overall array. Since the relative percentage of energy reaching the end of the reflective array is very small, it is not necessary to use an acoustic absorber on top of the crystal or, alternatively, angle the ends of the die as is often done on SAW devices.

A grounded periodic metal grating placed between both the input and output transducers supplies a fine frequency trim structure while simultaneously provides an rf shield to aid in signal feedthrough suppression. Single lines with the same width and periodicity as the transducer fingers are individually opened at both ends from the shorting sum bars with a laser beam during the fine frequency trim operation. The elimination of the shorting effect on velocity for the area under the opened fingers produces a small increase in the overall effective SAW velocity, and, as a result, a shift in the center frequency. It is anticipated that there will exist a tradeoff between the maximum frequency trim capability

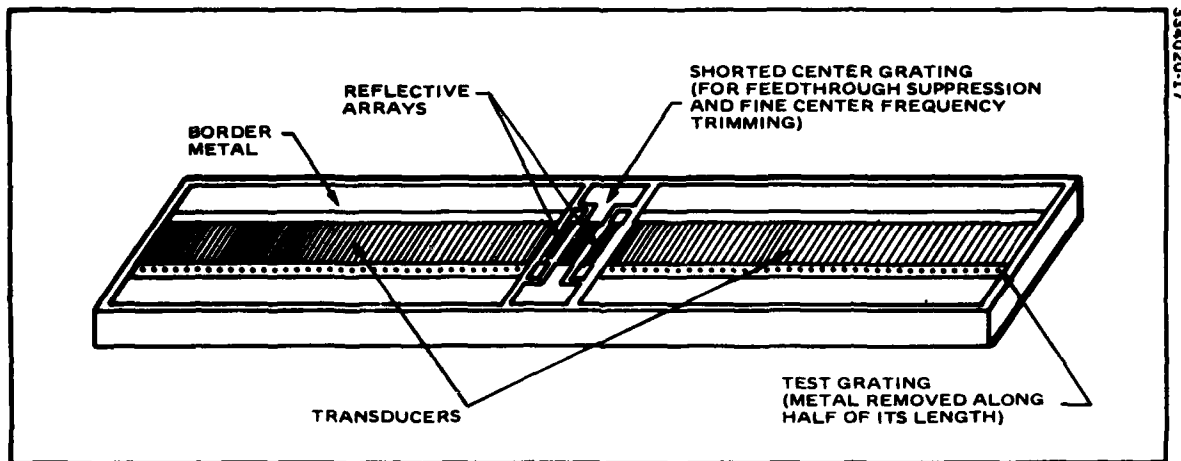


**Figure 3.9. Processed Resonator Die.** All metallization geometries are formed from nominal 2 micron lines providing a high process yield.

TABLE 3.2. RESONATOR CRYSTAL DIE SPECIFICATIONS

<b>I. <u>Substrate</u></b>	
Substrate material	ST-Quartz
Substrate dimensions (approximate)	1.27 x 0.25 x 0.063 cm
Acoustic velocity (reflective arrays, effective)	3152.4 m/sec
<b>II. <u>Metallization</u></b>	
Material	99.9 percent pure aluminum (Al)
Thickness	1500 Å
Resistivity	0.3 ohms/square
<b>III. <u>Transducers</u></b>	
Number of fingers per transducer	61
Line, space width	1.97 µm
Overall dimensions	2.189 x 0.239 mm
<b>IV. <u>Shorted Center Grating</u></b>	
Number of fingers	41
Line, space width	1.97 µm
Overall dimensions	2.189 x 0.641 mm
<b>V. <u>Reflective Arrays</u></b>	
Length	5.89 mm
Number of grooves each	1500
Number of withdrawn grooves each	689
Groove width	1.97 µm
Minimum space between grooves	1.97 µm
Maximum space between grooves	49.3 µm
Aperture width (same as maximum transducer aperture width)	789 µm
<b>VI. <u>Test Gratings</u></b>	
Bar, space width and height	0.300 mm
Number of bars each	97

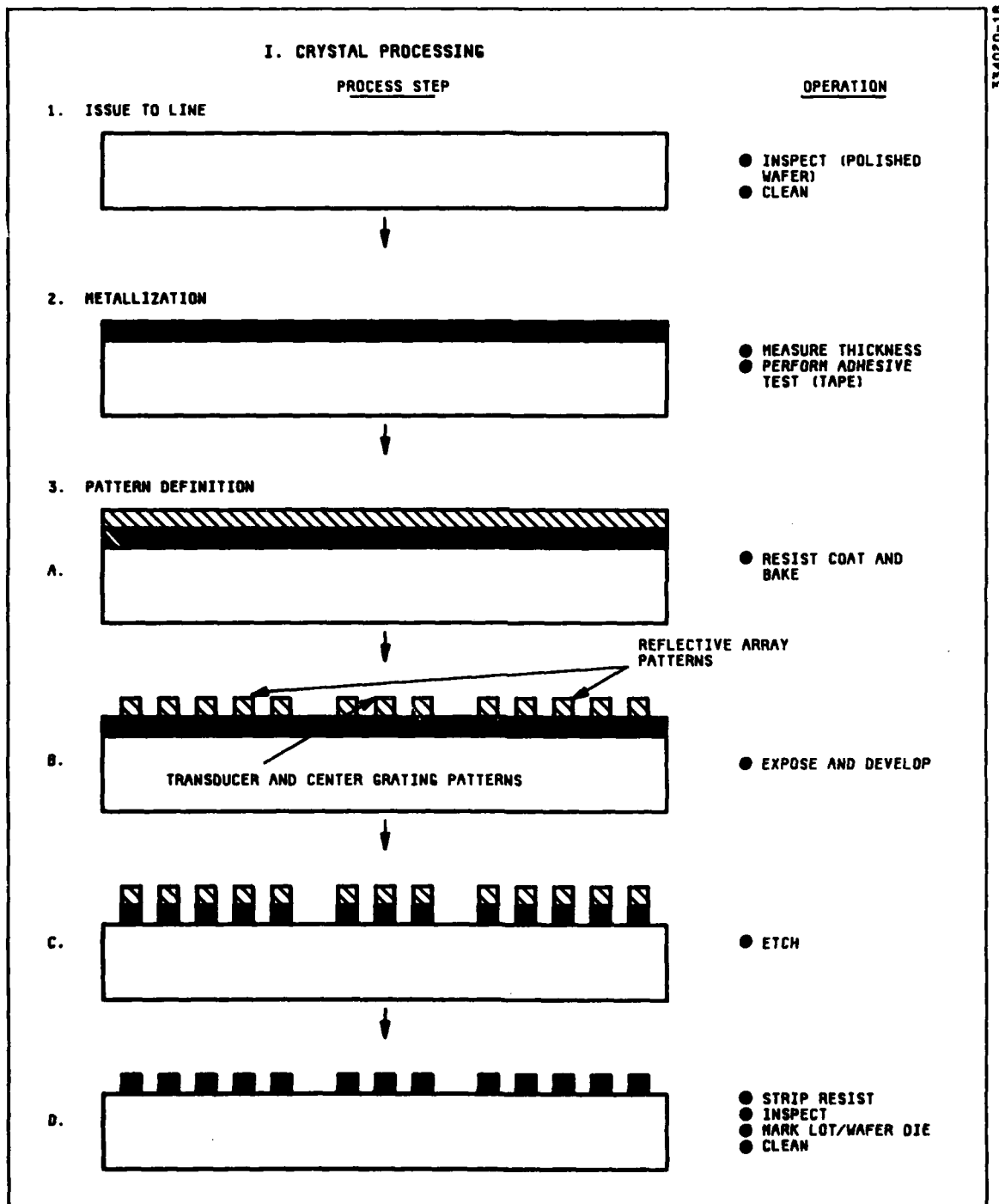
and the level of feedthrough suppression achievable as the number of opened fingers increases. The bonding pads on this center grating are enlarged into a "T" configuration to provide more area in locating the thermocompression ball bond. This eliminates the possibility of shorting the transducer to the grounded center grating during the bonding operation.

A test grating is also included in the die pattern to allow groove depth and transducer metalization thickness measurements on each individual die. The grooves forming the array are too narrow to permit tracking with the normally employed five micron diameter styles used on the depth measurement equipment. When the metal mask is stripped from the reflective grating, some of the metal along the test grating length remains on the die permitting the above measurements to be performed. The width of these grooves are, of course, much wider than those forming the reflective array.

**3.2.3 Detailed Process Description.** Figure 3.10 delineates the detail process steps required to fabricate a resonator. Up to the ion etch step, all processing is identical to that generally employed on standard SAW devices. The addition of the groove etching requires additional photolithography steps. These are described below. It is necessary to protect the transducer configuration during ion etching and assure that grooves are placed only into the reflective grating area.

A protective photoresist layer is first placed over the metal mask delineating the grating area. This assures that during the ion beam etch process the metal is not entirely removed before the required groove depth is reached. This part of the process is discussed further in Section 3.2.4. A separate layer of photoresist is used to coat and protect the transducer area. In order to process the wafer so that the transducer protection pattern and the additional photoresist masking layer over the reflective array can be treated independently, negative developing photoresist is used for the former and positive for the latter. By exposing through the back side of the wafer, the resist pattern duplicating the metal mask pattern is created. The wafer is then subjected to an ion beam etch as described in Section 3.1.4. Both photoresist layers and the metal mask are finally etched off the wafer leaving a stepped and repeated pattern of resonator die, ready for probing.

The wafers are probed to determine the general quality of the frequency response and the distribution of center frequency values. A probe card containing two coaxial probes specifically designed to align with the bonding pads on the resonator die was assembled by Inter-Logic System, Inc. This card fits into a Wentworth probe station, which in turn positions the wafer and probe tips relative to each other. The coaxial probe tip assembly is connected to a network analyzer for the frequency measurements. To achieve the required frequency accuracy, it was also necessary to add a stable frequency counter to the network analyzer source. A photograph of the probe station assembly is presented in Figure 3.11.

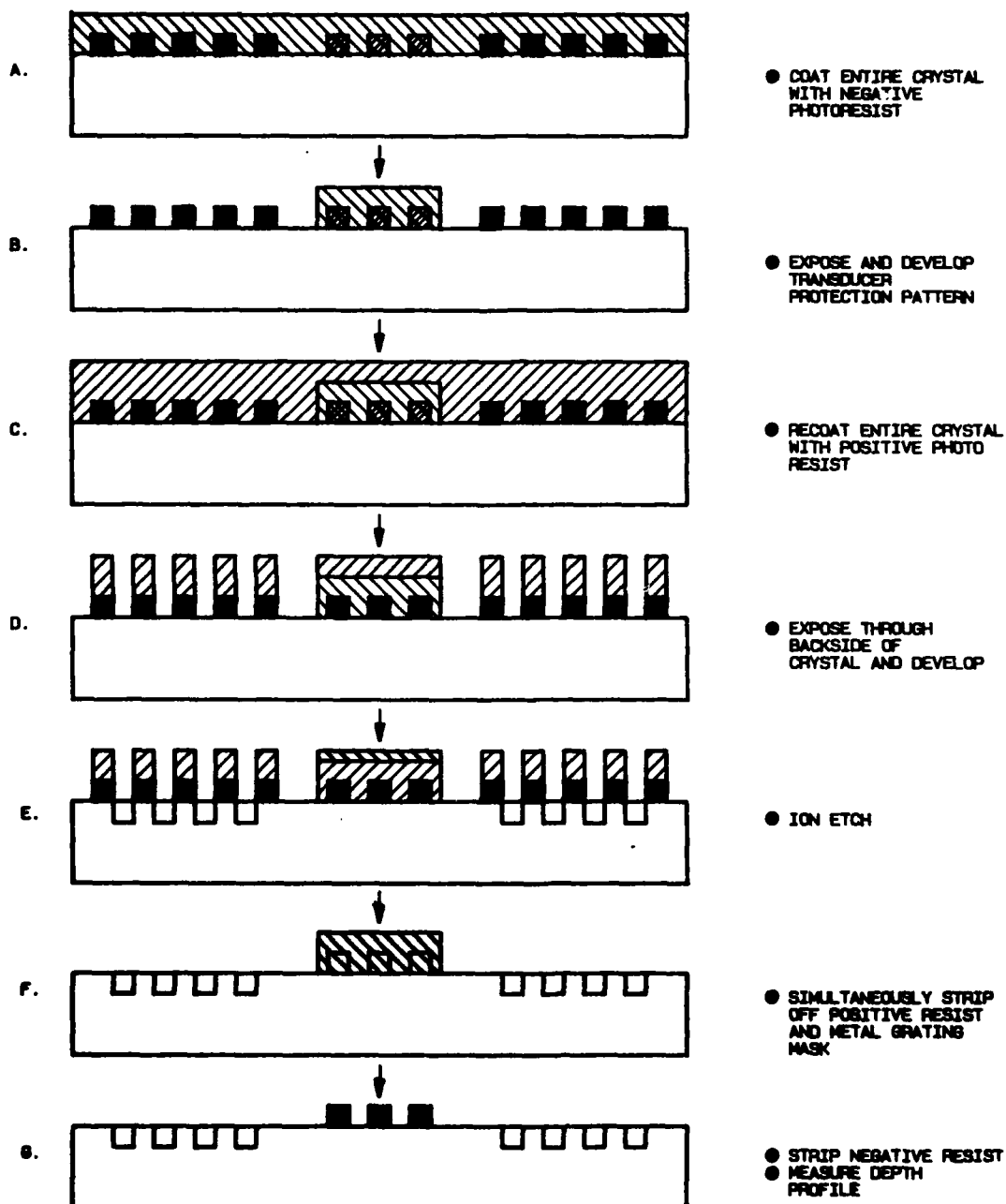


334020-18

Figure 3.10. Resonator Fabrication Flow for Engineering Samples

# CRYSTAL PROCESSING (CONTINUED)

## 4. ION ETCH



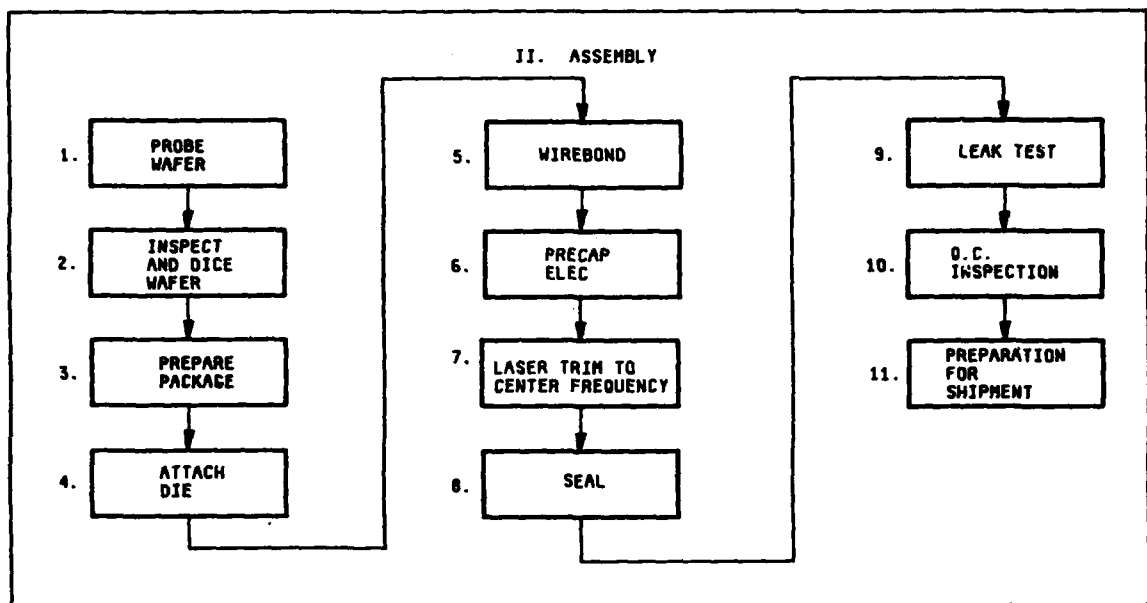
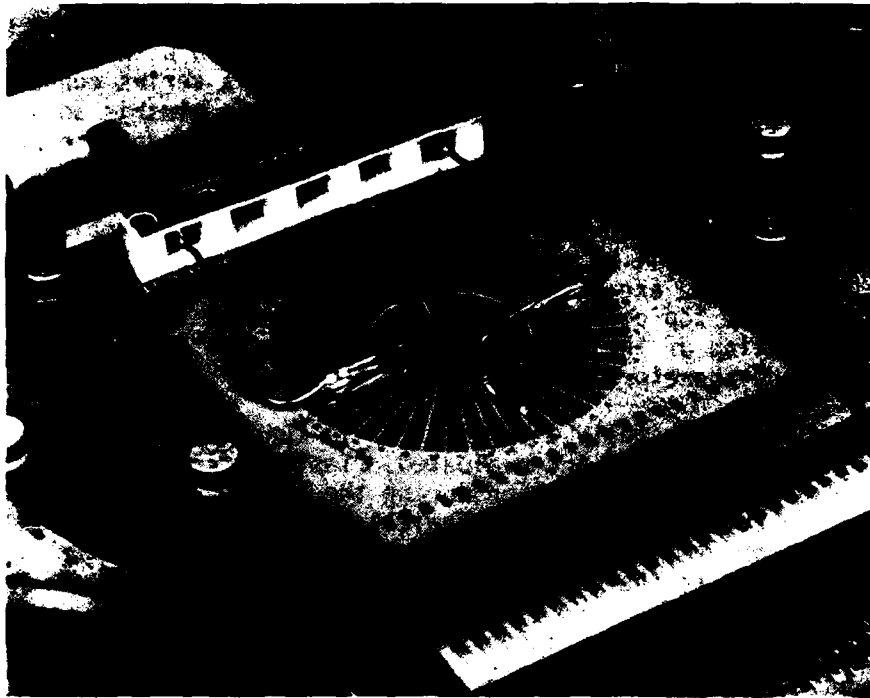


Figure 3.10. Resonator Fabrication Flow for Engineering Samples (Continued)





82-10-0272

Figure 3.11. Probe Station with Card. Coaxial cable configuration is routed directly to wafer in order to minimize stray capacitance effects.

After probing, the wafers are diced, and the acceptable die as determined from the probe data, is submitted to assembly. At this point, the die is mounted into a prepared package and wire bonded to the header floor and appropriate pins. The packages are prepared with two toroids, each soldered between two package pins and forming a series connection with the capacitive transducer configuration. One of the pins is an input or output pin, while the other pin is always used as a standoff to provide a transition from a soldered interconnection to a wire bonded connection. Care must be exercised when soldering to the standoff pin, because solder must be prevented from flowing onto the top surface of the gold plated pin where the wire bond will be placed. In addition, during thermocompression bonding, care must be exercised to assure that the solder does not reflow and migrate to the top of the pin damaging the bonded interface. Plans call for the elimination of the toroid as a tuning element in the latter phase of this program and therefore eliminate this problem.

Once the device is fully assembled, it is tuned by adjusting the turns of wire on the toroid core and evaluated. Testing per the specification has been a completely manual operation during the engineering phase; however, it can be readily automated using the Hewlett Packard 9805A network analyzer system. Although still under development, the tested resonator device is next laser trimmed to the center frequency as described in Section 7.3.

Finally, the tuned and frequency trimmed devices are sealed for hermeticity and submitted to any additional environmental testing that may be required. After final electrical testing and quality control inspection, the devices are prepared for shipment.

3.2.4 Reflective Array Etch Development. The critical aspects in the development of a stable resonator are (1) the production of the metal transducer pattern simultaneous with, and aligned with the reflective groove array, (2) the etching of the reflective array to the optimum depth for the frequency of operation without etching the crystal in the vicinity of the transducer pattern then (3) removing the aluminum mask from the area of the reflective grooves. The mass loading of the transducer metal dictates that the thickness must be no more than 1200 to 1500 Å. This is marginal if it must serve also as an ion beam sputtering mask for etching the reflective array. Thus, a masking procedure was developed to protect the metal transducers and masks. First, a negative photoresist is applied to the surface and a mask is aligned so that exposure (resist hardening) occurs over the transducer area. Then a positive resist film is applied and the wafer is exposed from the back side. This causes the resist to be dissolved away in the open (grooved) portion of the reflective array but leaves the positive mask over the aluminum lines and leaves the negative resist to prevent etching in the transducer area.

The process described in Sections 3.1.4 and 3.1.5 was also used to etch the resonator arrays to the desired depth. After ion beam etching the front of the wafers, they were exposed to an ultraviolet lamp and then immersed in a concentrated positive photoresist developer (a weak sodium hydroxide solution). This dissolved off the positive resist and also etched off the aluminum mask lines in the reflector area. The wafers were then dipped in a negative resist stripper at 100°C to remove the transducer protection. This completed the fabrication of the wafer including the resonator structure and they were then evaluated for center frequency performance as discussed in the previous section.

## 4.0 ELECTRICAL EVALUATION OF ENGINEERING SAMPLES

### 4.1 RAC Device.

4.1.1 General Considerations. The test effort on this portion of the program was divided into two distinct phases. The first engineering phase served to demonstrate basically overall specification compliance, and in addition, to establish optimum sidelobe level performance achievable with the application of a dual phase compensation pattern. During this phase, five devices were fabricated and evaluated. The first phase correction was performed using a single generic pattern on all devices which was based on an average response computed from the uncompensated phase data measured on the first two devices. The second correction, in turn, consisted of an individual compensation applied to each of the 5 lines in order to further reduce the RMS phase error response.

During the second engineering phase, five additional devices were fabricated and dual phase corrected in the same manner as was done in Phase I. A key goal of Phase II was directed toward obtaining a generic phase compensation pattern that would provide greater than 25 time sidelobe suppression in the compressed pulse response with a suitably optimized conjugate filter. To achieve this, a new phase pattern was derived based on additional phase data obtained on the uncompensated Phase II devices. The new pattern was in turn applied to the five devices. The second correction was again applied to each line on an individual basis.

A summary of the test results obtained for all 10 RAC filters is presented in Table 4.1. Included is the measured data for each phase correction as well as the specification requirements established for this device. It can be seen that all the specification parameter values have, in general, been met. Several lines exhibited a slightly larger 3 dB bandwidth and therefore a larger dispersive time delay. A minor adjustment to the length of the reflective array grating has been made, and future devices will readily meet both specification requirements. Specification values for time delay at center frequency, phase error, and VSWR will be determined at the end of the Confirmatory Sample Phase.

Detailed test data on the individual devices is presented in Appendix I. Also included are passband frequency response plots and the recompressed pulse performance after each phase correction step.

4.1.2 Test Results. The typical amplitude and phase error characteristics of the down-chirp RAC filters fabricated on this program are shown for two lines in Figures 4.1 - 4.8. The average insertion loss for all the lines produced during the engineering phase is 38 dB, with a peak-to-peak amplitude variation approximately equal to  $\pm 1.5$  dB. The amplitude response of device No. 1, shown in Figure 4.1, exhibits an insertion loss 3 dB below the design average. This is attributed to deeper grooves in the reflective array. This device was inadvertently ion-beam etched a few hundred Angstroms deeper than the desired depth profile, which

TABLE 4.1. TEST RESULTS OF ENGINEERING PHASE DEVICES

Parameter	Units	Specification Requirement	After One (Generic) Phase Correction		After Two Phase Corrections	
			MIN	MAX	MIN	MAX
Insertion Loss	dB	$\leq 40$	35.5	40.5	36.0	40.0
Center Frequency	MHz	200 $\pm$ 2	200.0	200.7	200.0	200.6
3 dB Bandwidth	MHz	60 $\pm$ 1	60.2	61.0	60.2	61.1
Center Frequency Time Delay	$\mu$ sec	TBD	35.29	35.36	35.93	36.03
Dispersive Delay	$\mu$ sec	60 $\pm$ 0.5	59.6	60.8	60.0	60.8
RMS Phase Error	deg	TBD	4.3	17.7	2.4	8.7
Sidelobe Suppression	dB	$\geq 25$	20	37	29	37
Feedthrough Suppression	dB	$\geq 50$	-	-	44	62
Spurious Echo Suppression	dB	$\geq 40$	-	-	> 55	> 70
VSWR	-	TBD	5.5:1	7.3:1	5.2:1	7.0:1

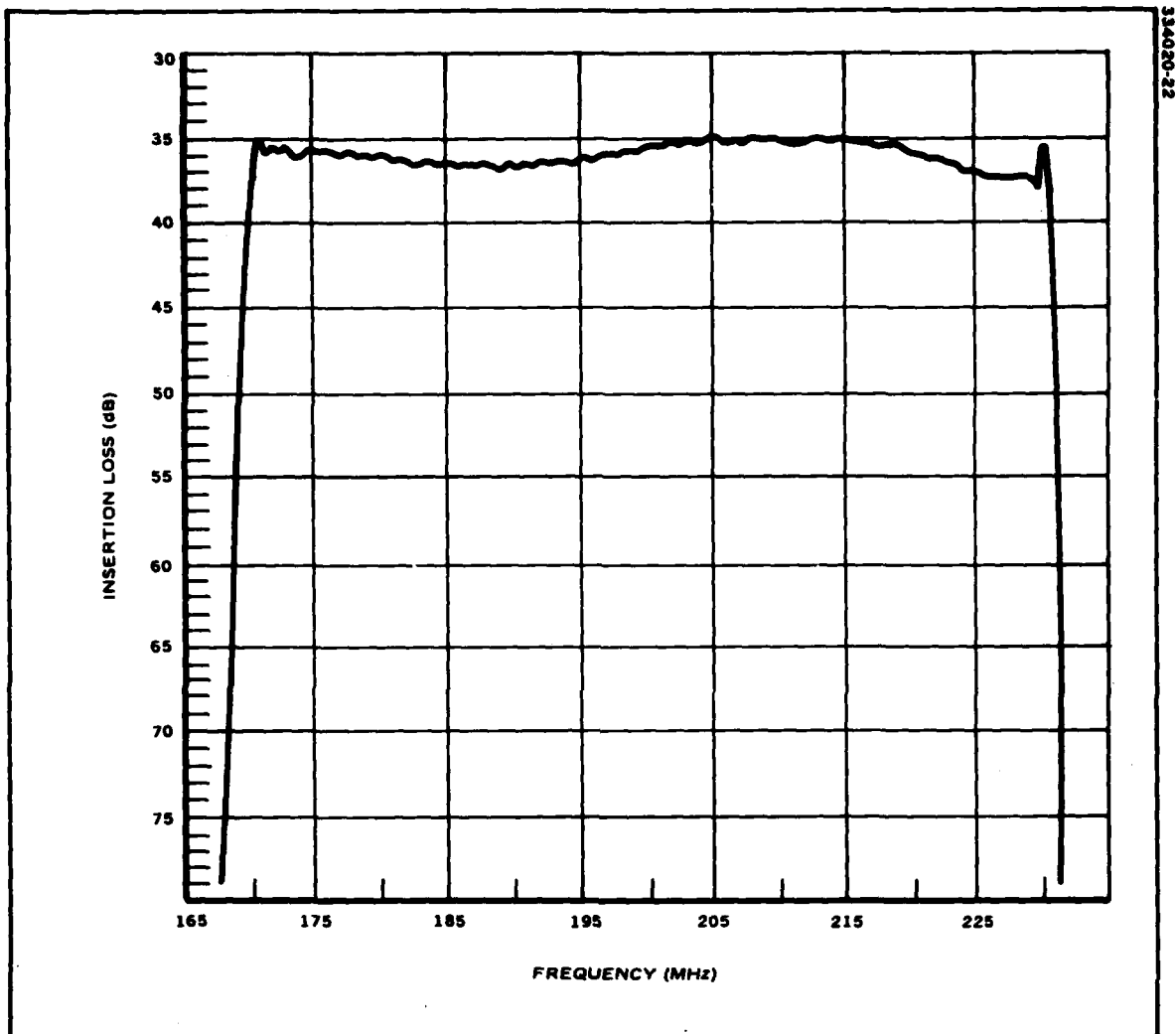


Figure 4.1. Measured Frequency Response of the S/N 1 RAC Line

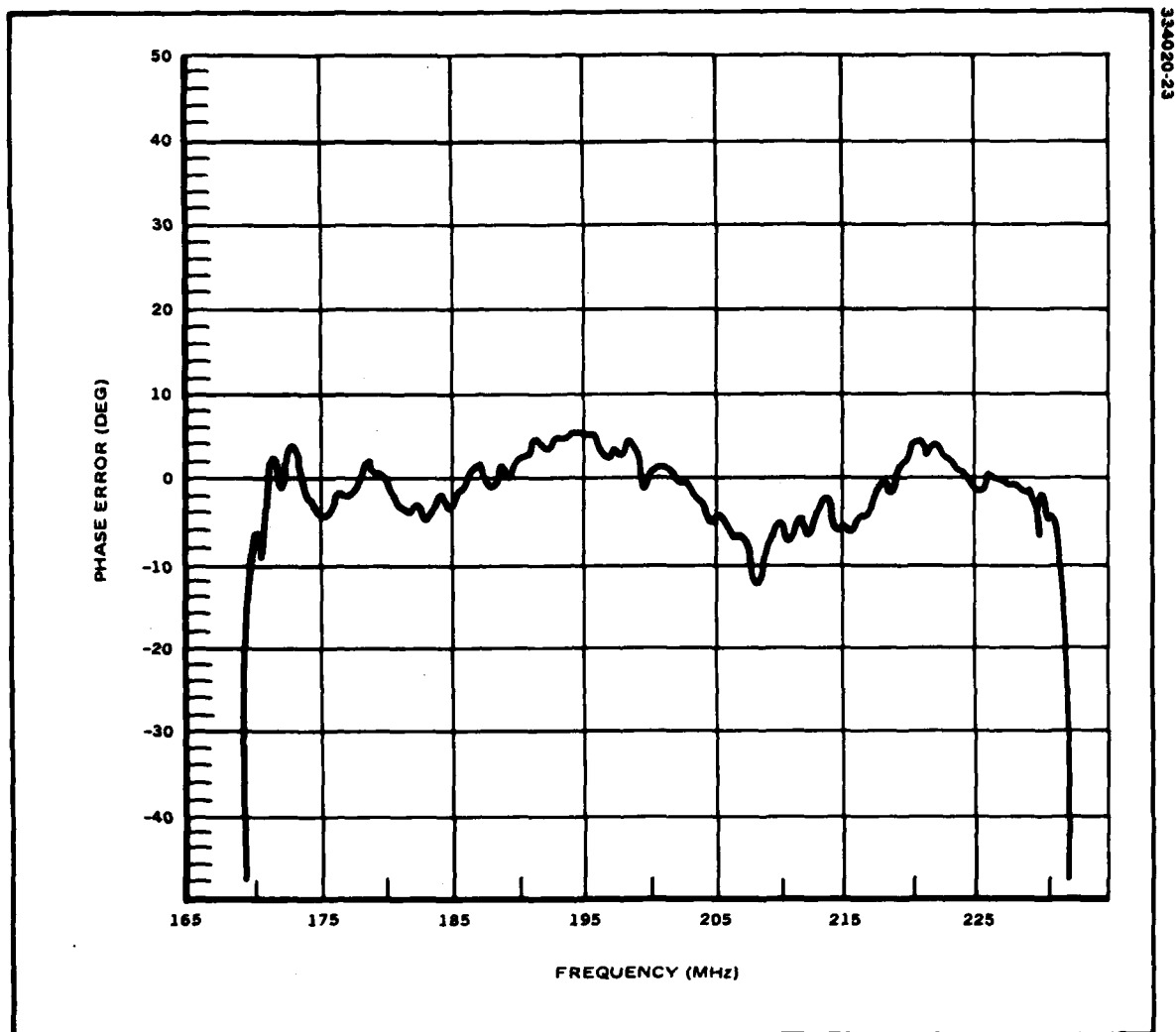
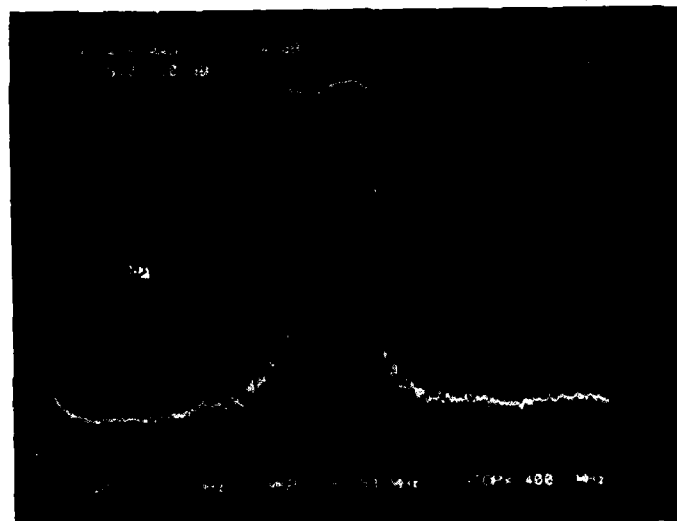
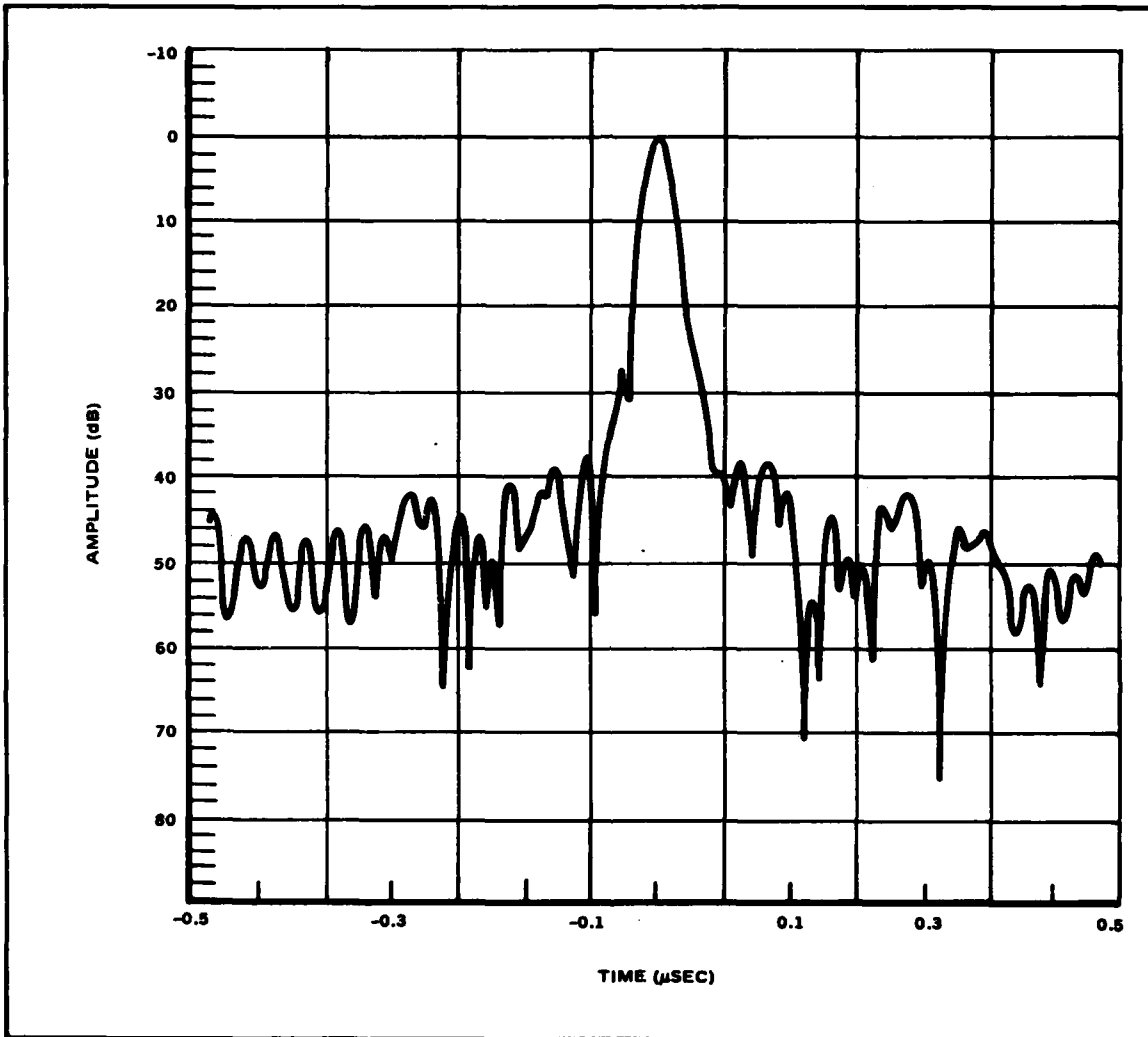


Figure 4.2. Measured Phase Error Response of the S/N 1 RAC Line After Two Phase Corrections.  
(The rms phase error for this line is  $4.1^{\circ}$ .)



**Figure 4.3. Out-of-Band Frequency Response of the S/N 1 RAC Line Showing a Direct Feedthrough Isolation of Approximately 70 dB Using a Septum to Separate Input From Output**





**Figure 4.4. Recompressed Pulse Characteristics Obtained by Correlating the Response of the S/N 1 RAC line with an Ideal Hamming Weighted Compression Line**

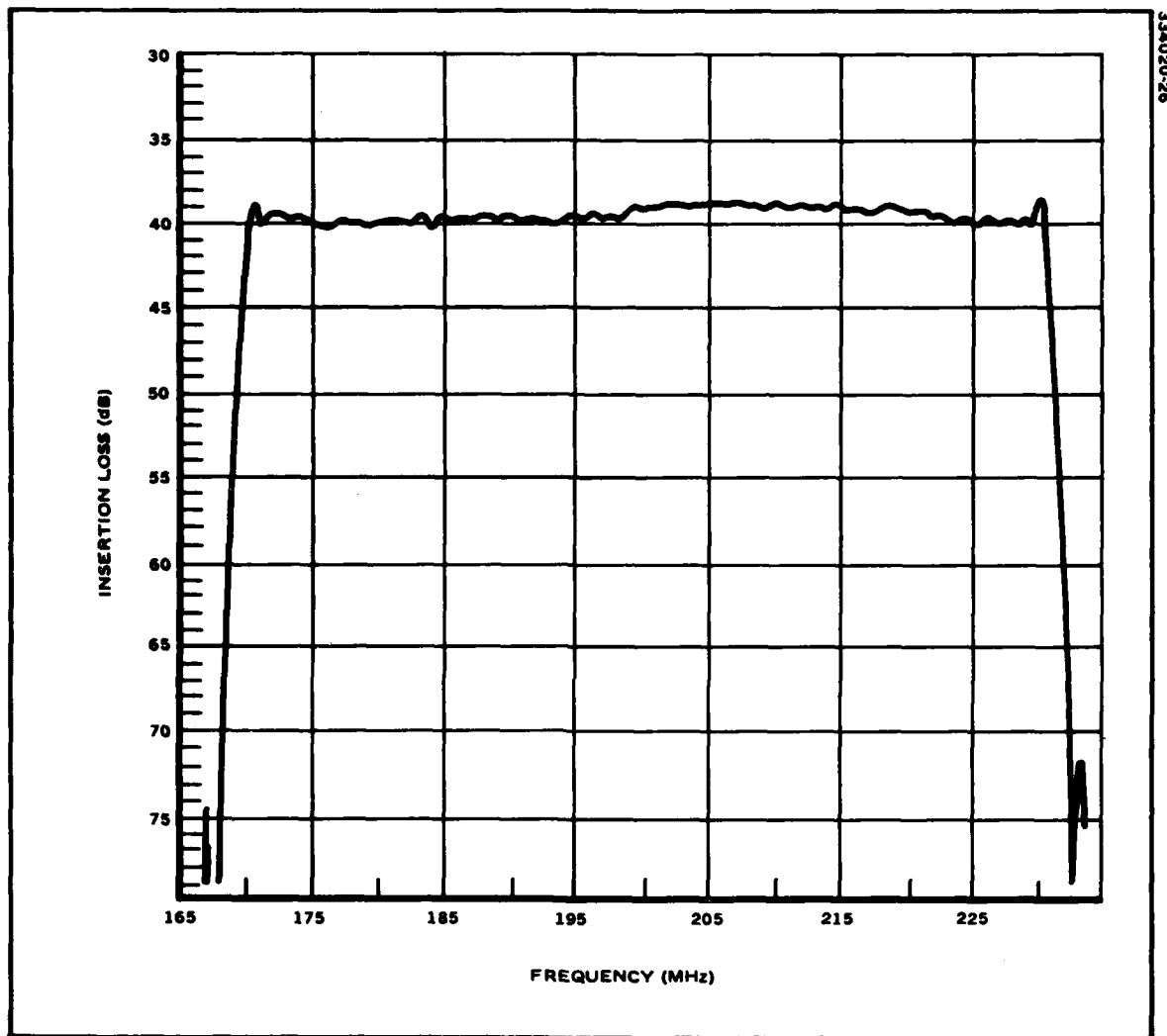


Figure 4.5. Measured Frequency Response of the S/N 5 RAC Line

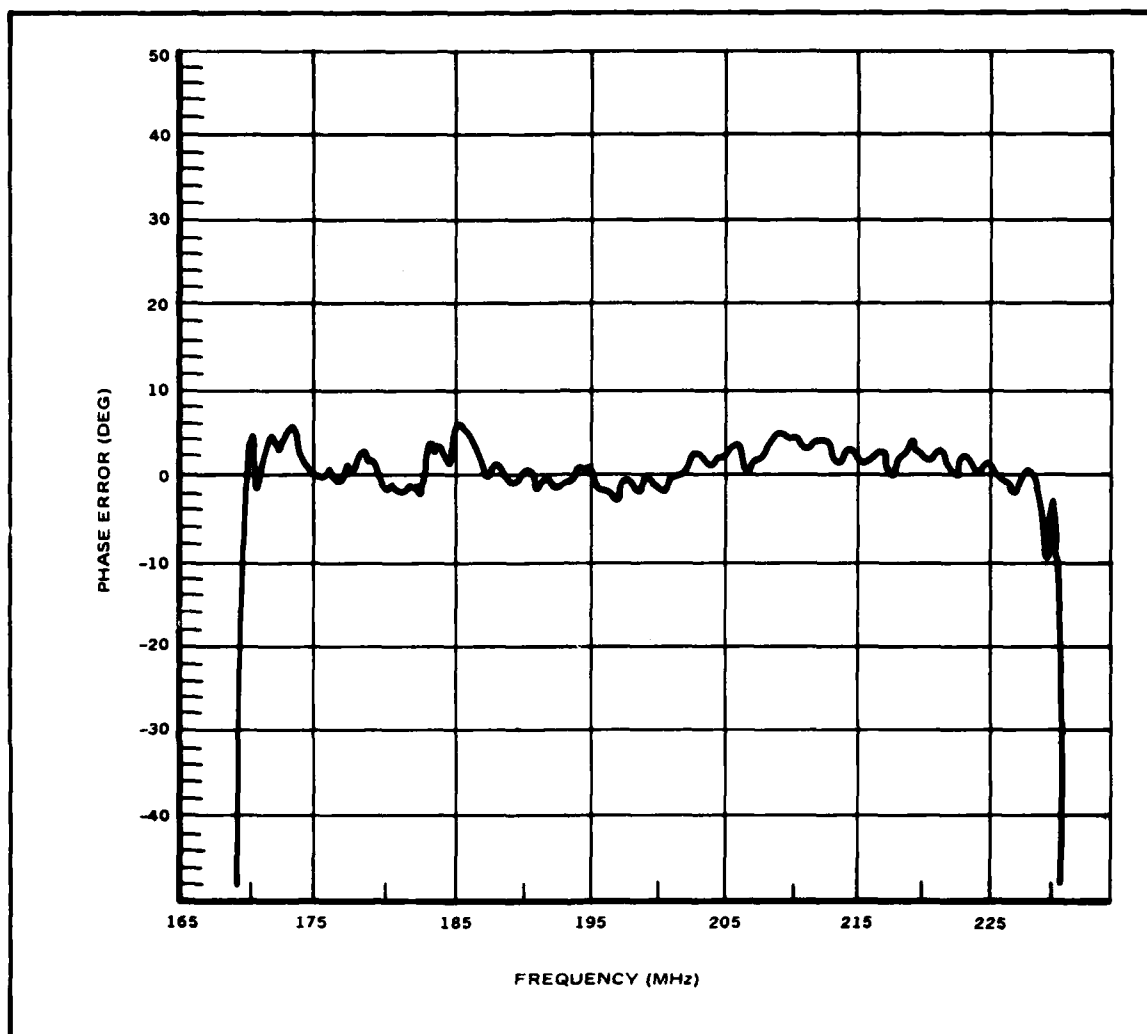


Figure 4.6. Measured Phase Error Response of the S/N 5 RAC Line After Two Phase Corrections. (The rms phase error of this line was  $2.4^{\circ}$ .)

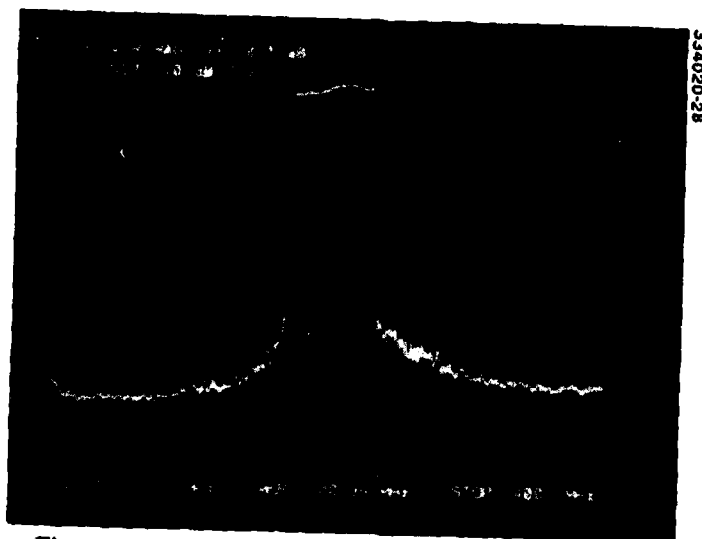


Figure 4.7. Out-of-Band Frequency Response of the S/N 5 RAC Line. The feedthrough isolation for this line is approximately 65 dB with septum.

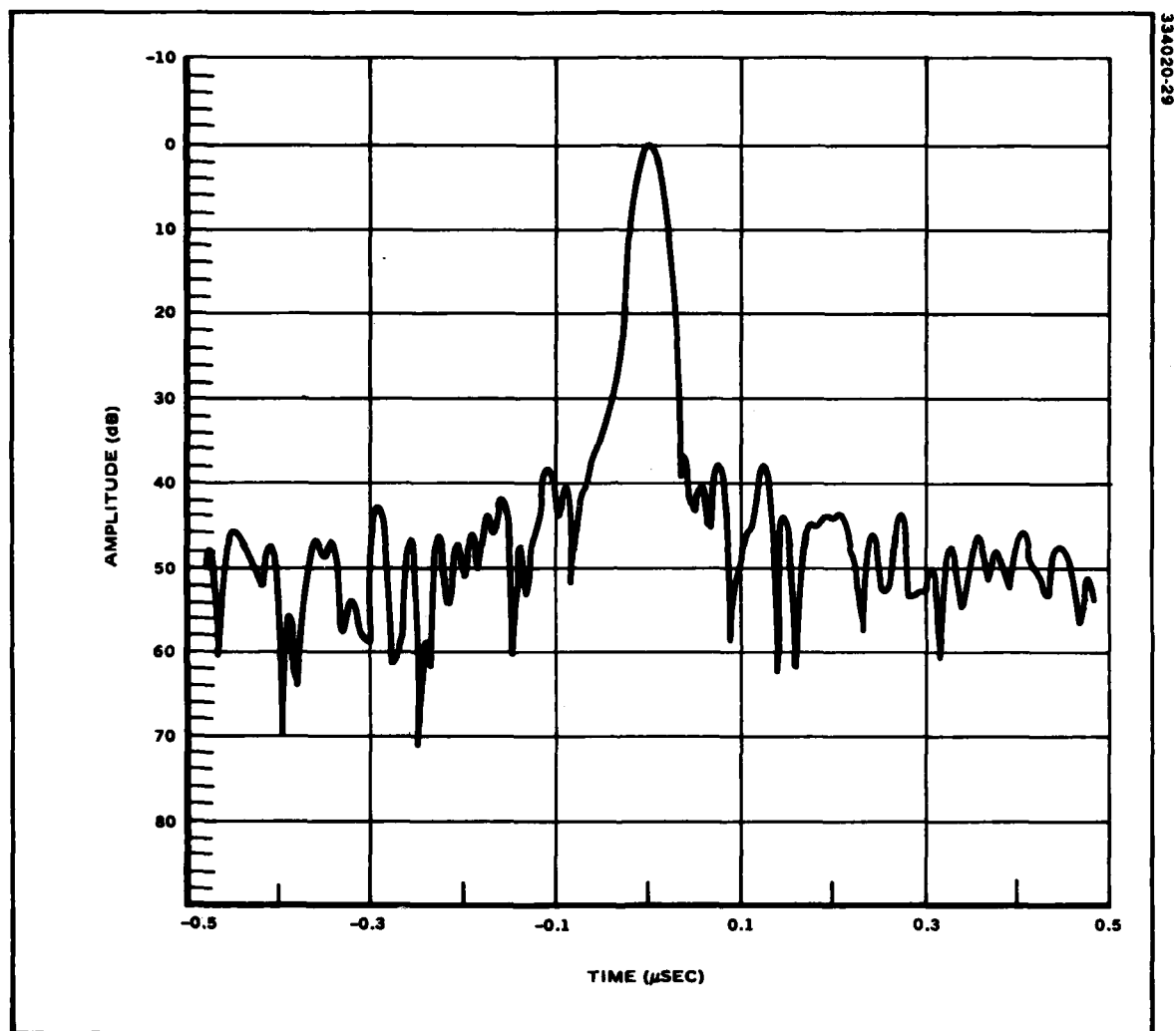


Figure 4.8. Recompressed Pulse Characteristics of S/N 5 with Ideal Hamming Weighted Upchirp Delay Line

in turn reduced its midband loss to a 35 dB value. Figure 4.5 displays the amplitude response for device No. 5 whose grooves were etched to the prescribed array depth and has the designed midband insertion loss of 38 dB. All lines exhibited an approximate cubic ripple in the passband of average 2.5 dB peak-to-peak value.

The nominal center frequency for these lines is  $200.3 \pm 0.3$  MHz. This value falls well within the desired specification of  $200 \pm 2$  MHz. The measured 3 dB bandwidths for these devices is equal to  $60.7 \pm 0.4$  MHz with dispersive delays of  $60.2 \pm 0.4$   $\mu$ S. Both values have been reduced by a minor adjustment in the length of the reflective array; and in future devices, the specification values will be readily met in all cases.

The final RMS phase error for these devices, examples of which are shown in Figures 4.2 and 4.6, respectively, were obtained after the application of the second phase correction pattern to each individual RAC line. The first phase correction (generic) pattern was largely generated from the phase error response of line No. 1 and then applied to all five lines of Phase I. However, it was established later that this line exhibited an uncharacteristically large phase error response in the lower half of its passband, which in turn was incorporated into the generic pattern. Consequently, with the use of this pattern, an optimum response was not achieved on the first five devices after one correction.

A new generic correction pattern was generated based on the uncompensated phase data on two of the five devices for Engineering Phase II. Again an overall improvement in obtaining lower RMS phase values was not achieved. An analysis of the uncompensated data for two filters demonstrated that these lines exhibited 24 degrees and 26 degrees, respectively. As a result, a generic correction reduced the above magnitudes to only 15 degrees and 18 degrees, respectively.

On the average, after the first phase correction, RMS phase errors were measured to be 11 degrees. By individually correcting each line using a second pattern, these phase errors were reduced to 5.5 degrees. By selecting a larger number of devices (6) and averaging their phase response, it should be possible to obtain a generic correction pattern which limits the RMS phase error value to 8 degrees. It is believed that this value will be sufficient to meet the -25 dB sidelobe requirement for the production devices. It is now planned to generate an additional generic pattern based on the performance of the first six units fabricated in the Confirmatory Sample Phase.

The out-of-band frequency performance of the RAC filter design is shown in Figures 4.3 and 4.7. In particular, Figure 4.3 shows the frequency response for line No. 1 from 0 to 400 MHz. It is noted that the response drops quickly to the feedthrough isolation level of -70 dB outside the passband. Line No. 5 exhibits a similar out-of-band performance as seen in Figure 4.7. These photographs demonstrate that the specification feedthrough suppression value of 50 dB can be easily met using a septum between the input and output transducers. Additional measurements in the

time domain also confirmed these results. In Section 5.0 of this report, further discussions on the observed feedthrough characteristics of these devices is presented along with a modified package that will still provide 50 dB of signal suppression performance. The proposed hermetic housing concept will, however, significantly reduce device fabrications costs. It is expected to accomplish this by providing overall higher yields at crystal fabrication, assembly, and perimeter seal.

Bulk mode conversion is highly suppressed in RAC filters. This is also demonstrated in the frequency response plots of Figures 4.3 and 4.7, respectively. These photographs show bulk modes suppressed in general 50-60 dB. In the trailing stopband region near the passband edge, line No. 5 exhibits an increased bulk spurious response not present in line No. 1. While the increased spurious level does not adversely affect the overall filter response, performance identical to line No. 1 can be assured by uniformly sandblasting the back of each crystal. It is presently planned to perform this task for the remaining devices on this program.

The compressed pulse performance for the two sample RAC filters is shown in Figures 4.4 and 4.8, respectively. These results were obtained by using a computer program developed at Hughes which correlates the measured response of the down-chirp expansion lines with an ideal up-chirp Hamming weighted compression line. A fabricated up-chirp delay line was not available during the engineering phase of this program. The compressed pulse performance of line No. 1 (Figure 4.4) shows a close-in sidelobe suppression of 29 dB. Within  $\pm 0.5 \mu\text{s}$  of the peak response, all sidelobes have rolled off to at least 42 dB below the peak response. The improved phase error characteristics obtained for line No. 5 provided close-in sidelobe levels 39 dB below the peak response. Again, at  $\pm 0.5 \mu\text{s}$  away from the main response, both leading and trailing sidelobes are suppressed by at least 48 dB. Both lines, and in fact all 10 lines, should exceed the close-in sidelobe suppression specification requirement of 25 dB by a wide margin.

The 25 dB sidelobe requirement was easily met since all lines were phase compensated with a dual phase correction pattern, and closed loop measurements were performed with a simulated up-chirp line of zero phase error. Results obtained to date on simulations performed using an up-chirp line with expected amplitude and phase errors have not proven conclusive. Based on closed loop tests using measured data from several down-chirp expansion lines, it was observed that both improvement as well as reduction in sidelobe level can be expected. However, it is felt that there is sufficient margin to meet a 25 dB specification for the production units, provided the application of a generic pattern to an uncompensated line can correct large existing RMS phase errors to within an 8 degree value.

#### 4.2 Resonator Device.

4.2.1 General Considerations. The engineering development effort for the resonator was divided into two phases. During the first phase the electrical design was established, a mask fabricated to reflect the design

requirements, and several samples fabricated and evaluated. During the second phase of the development effort several corrections were introduced into the design, a new mask generated, and an additional set of devices were fabricated and evaluated. The measured performance for the ten delivered devices resulting from the overall engineering effort is presented in Table 4.2.

In the following sections, the developments during both phases are discussed along with the details of the test results. A review of the data in Table 4.2 indicates that after two design iterations, specification compliance was not achieved. Therefore, in the final section, a discussion is provided which attempts to explain the deviations observed from the specification requirements.

4.2.2 Evaluation of Phase I Devices. Five wafers were rf probed and the resonator circuits exhibiting the lowest insertion loss resonances of these were diced into individual resonators. Several of these devices were mounted onto 14-pin, dual-in-line, gold plated packages. The crystal itself was attached using Dow Corning 3140 RTV and allowed to cure for 24 hours. At the end of the cure cycle, the devices were thermo-compression bonded using 1 mil gold wire. The rf shield and one side of each transducer was bonded (i.e. grounded) directly to the package header while the opposite pad of each transducer was bonded to an insulated package pin as discussed in detail in Section 3.2.1.

A typical response for a mounted but untuned resonator is seen in Figure 4.9. The frequency sweep width is 100 MHz and therefore shows not only the resonant peak but also the main lobe of the transducer-transducer delay line and its sidelobes. The figure illustrates that greater than 40 dB of feedthrough suppression is possible in this package for an untuned device. Figure 4.10 depicts an expanded plot of the resonance itself. The 3 dB bandwidth is approximately 55 kHz which corresponds to a resonant  $Q$  of 7300. This  $Q$  value is lower than the computed value in Section 2.3 i.e.  $Q = 9100$ . The reduction is attributed totally to the deeper grooves selected for the design (1200 Å). If shallower grooves are etched into the grating, the bulk scattering losses will be reduced, hence the  $Q$  value increased.

Also observed in the response is a slight shoulder in the high frequency portion of the resonance which is attributed to a residual transverse mode. Figure 4.11 displays the resonance over a 6 MHz frequency range. A secondary resonance is observed below the main frequency response. Also shown in the upper traces are the return loss for each transducer. It should be noted that the main response is reflected in the return loss as a dip at the same frequency. It should also be noted that the secondary resonance is reflected in the return loss as a dip for only one of the transducers. The return loss for the other transducer does not appear to dip at the frequency of the secondary resonance even when viewed on the most sensitive amplitude scale of the network analyzer (0.1 dB/cm). This behavior could not be observed during wafer probing because of the presence of very high rf feedthrough levels. It was, however, noted in other devices and therefore has suggested operational differences between the two



TABLE 4.2. TEST RESULTS OF ENGINEERING PHASE DEVICES

Parameter	Units	Spec. Req.	PHASE I						PHASE II					
			No 3	No 4	No 7	No 8	No 11	2A	3A	5A	7A	8A		
Insertion Loss	dB	5.0	8.2	8.9	7.8	9.6	9.6	5.2	5.2	4.8	5.4	5.4		
Bandwidth (3dB)	kHz	100 $\pm$ 5	135	129	163	210	144	135	150	140	138	128		
Center Frequency	MHz	400 $\pm$ .01	400. 0905	400. 0335	400. 1315	400. 046	400. 149	398. 854	398. 820	398. 866	398. 858	398. 792		
Adjacent Side- lobe Suppression	dB	20	18	9	20	9	18	15	13	13	13	16		
Feedthrough Suppression	dB	50	30	32	30	33	38	34	32	36	32	30		

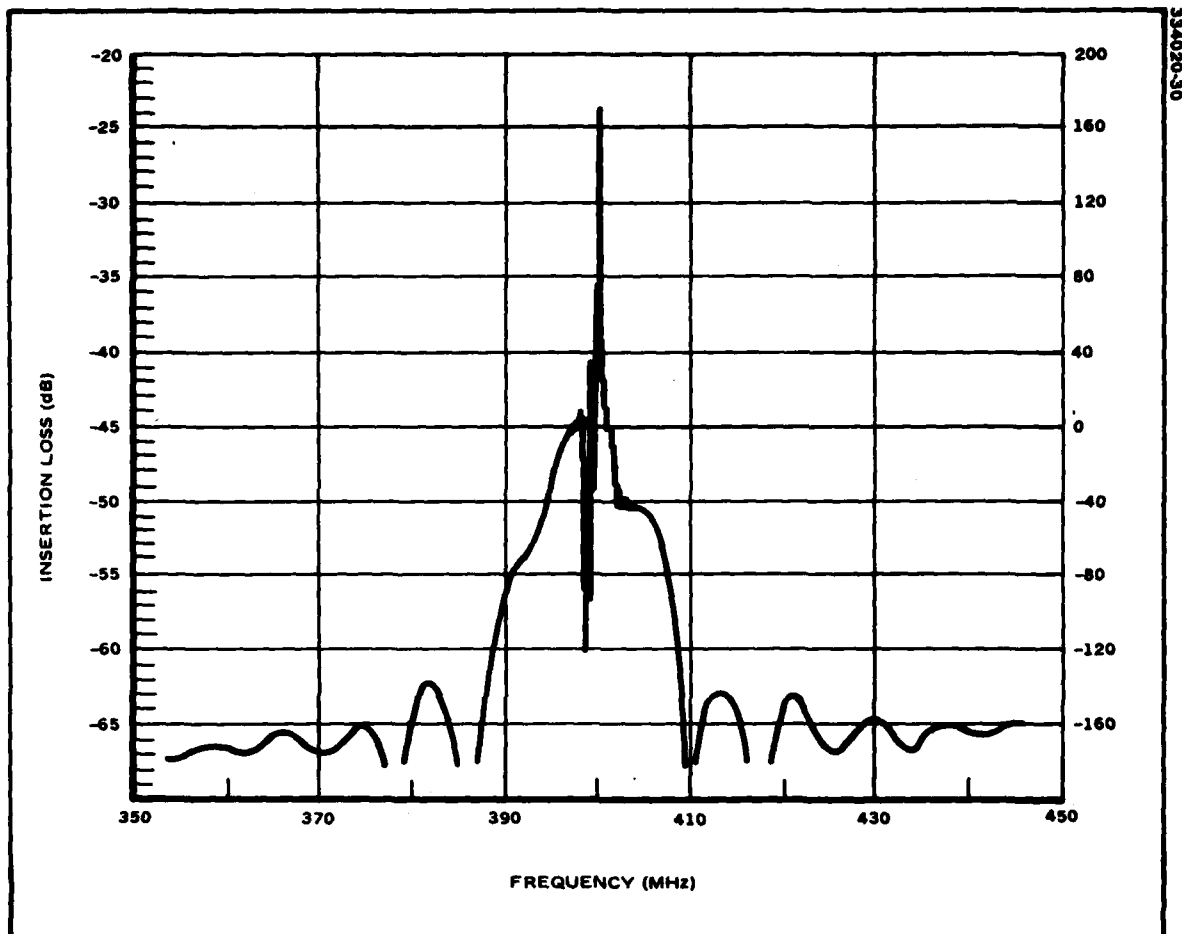


Figure 4.9. Frequency Response of an Untuned Resonator

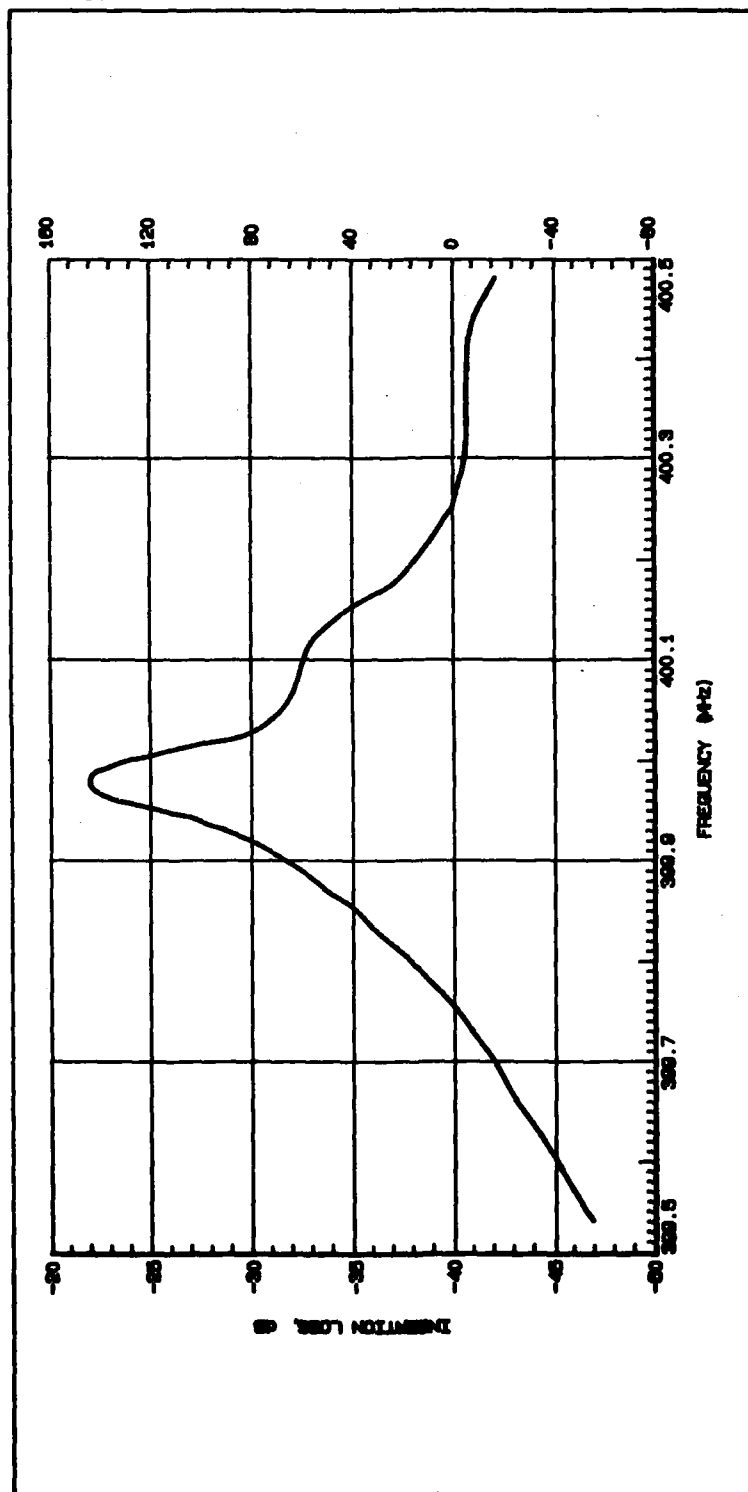


Figure 4.10 Expanded Frequency Response of Untuned Resonator

transducers or possibly an asymmetry in the resonator cavity. This hypothesis resulted in a second careful inspection of the photomask, and the results of this inspection will also be discussed in this section.

Figure 4.11b shows an extremely wide band CW frequency response (350 MHz to 950 MHz) and illustrates that this package is capable of providing very good rf feedthrough suppression (at least 50 dB from the input and 30 dB from the peak resonant output for untuned resonators). Figure 4.12a depicts the response of a tuned resonator exhibiting 6.1 dB of insertion loss. Also observed is an asymmetry in the main and associated return loss resonant response. The wide band response presented in Figure 4.12b also shows very good isolation far from resonance (60 dB at 600 MHz). Near resonance, the rf feedthrough increases to approximately -35 dB, a result which is attributed to crosstalk between the toroidal tuning inductors placed within the package. In Figure 4.13a, the response of another tuned device with 8.1 dB insertion loss is shown. As previously discussed, this device also exhibits an asymmetry in the return loss response of the secondary resonance.

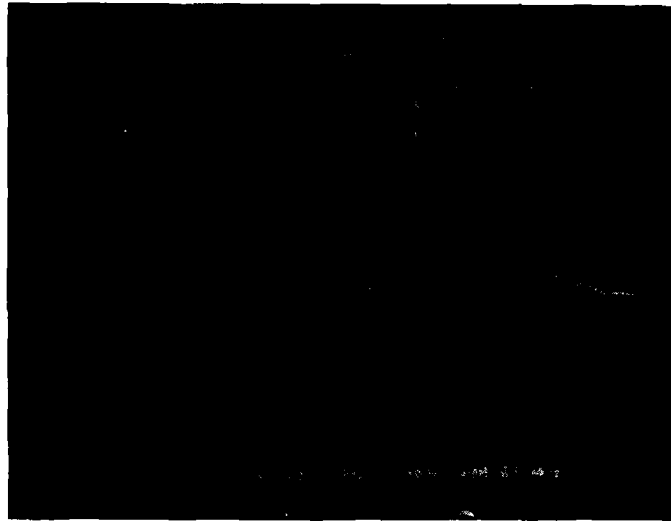
The secondary resonance with asymmetric return loss characteristics suggested a problem with the photomask which was not discovered on previous inspections. A review of the photomask revealed that the alignment of one transducer relative to the reflection grating differed from that of the other transducer relative to its neighboring reflection grating. As a result, the overall periodicity of the combined grating and input/output transducer configuration was disturbed, which in turn acted as a small perturbation on the performance characteristics of the resonant cavity. Since the photomask was stepped from three individual reticles, one for the transducer configuration and two for the individual reflection gratings, a placement error could easily have occurred in the initial overall alignment.

In order to gain confidence that this was the cause of the spurious responses observed experimentally, the placement errors were simulated on the computer. The result of the simulations are presented in Figure 4.14. A secondary resonance is observed below the main response. The alignment was subsequently adjusted in the new photomask for Phase II.

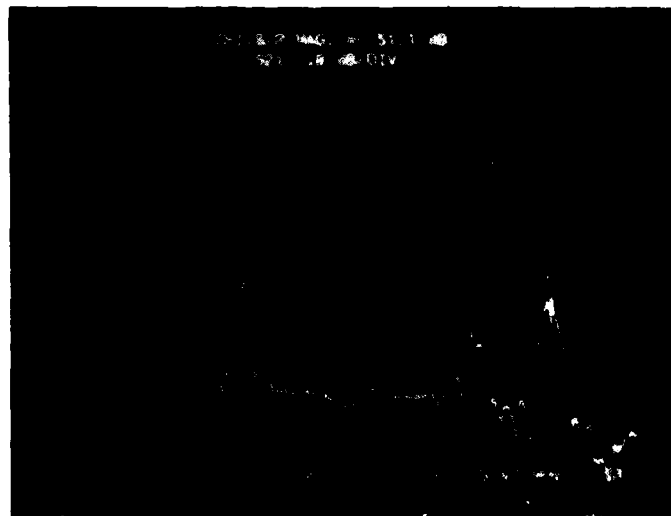
A summary of the measured results for the insertion loss and the center frequency before and after seal is presented in Table 4.3. Large variations in the control of the center frequency were observed. It was noted, in addition, that the frequency measurement itself was sensitive to the pressure exerted on the package while in the test fixture. For the first set of devices, the crystal was mounted with RTV adhesive under its entire length and bonded to the package base. Thus, as the package was forced to flex, the crystal was placed into a strained condition. The problem was resolved by limiting the RTV and placing it only under a small area at the center of the resonator crystal.

A second effect which was observed after sealing the devices was an increase in the overall insertion loss value of the tuned devices. Further evaluation has demonstrated that the toroids employed on these devices were

334020-32

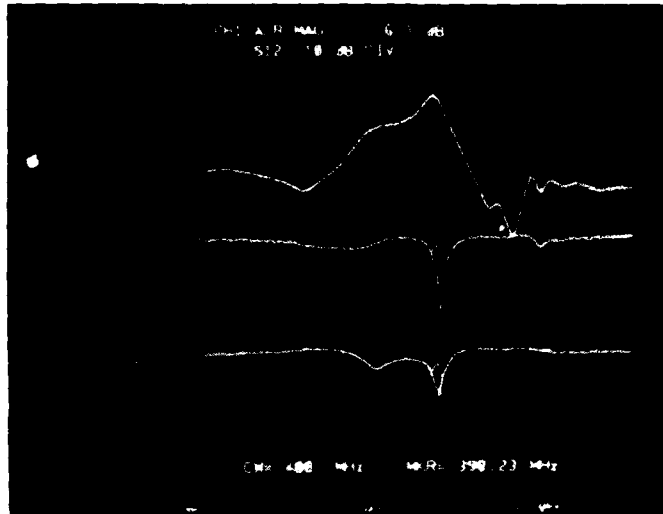


**(A) INSERTION LOSS AND RETURN LOSS OF UNTUNED RESONATOR**

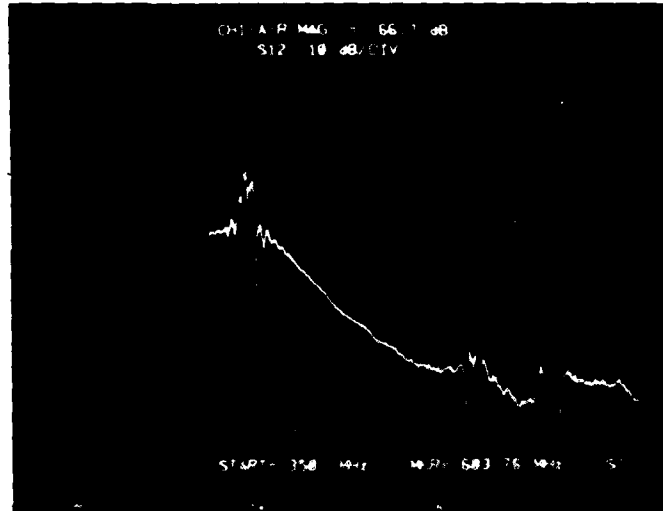


**(B) VERY WIDEBAND RESPONSE SHOWING EXCELLENT ISOLATION**

**Figure 4.11. Frequency Response of Untuned Resonator**

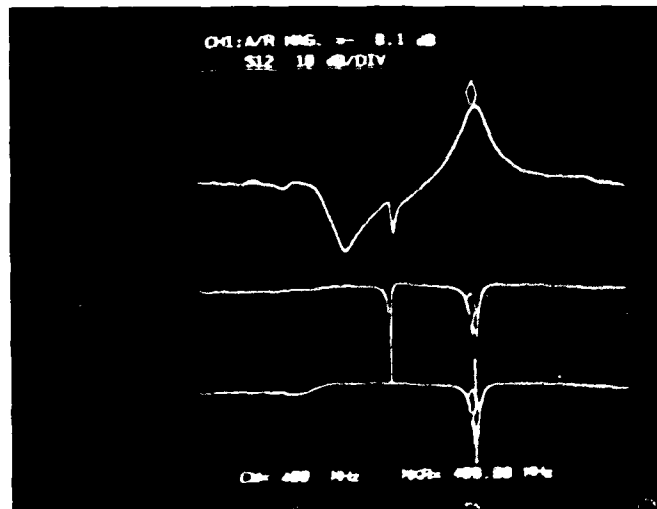


(A) INSERTION LOSS AND RETURN LOSS FOR TUNED RESONATOR

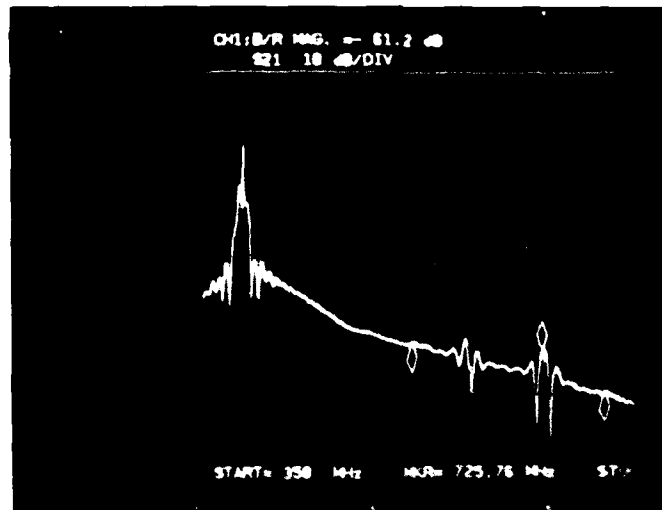


(B) VERY WIDEBAND RESPONSE FOR TUNED RESONATOR

Figure 4.12. Frequency Response of Tuned Resonator



(A) INSERTION LOSS AND RETURN LOSS FOR TUNED RESONATOR



(B) VERY WIDEBAND RESPONSE SHOWING EXCELLENT ISOLATION

Figure 4.13. Frequency Response of Tuned Resonator Exhibiting Secondary Response

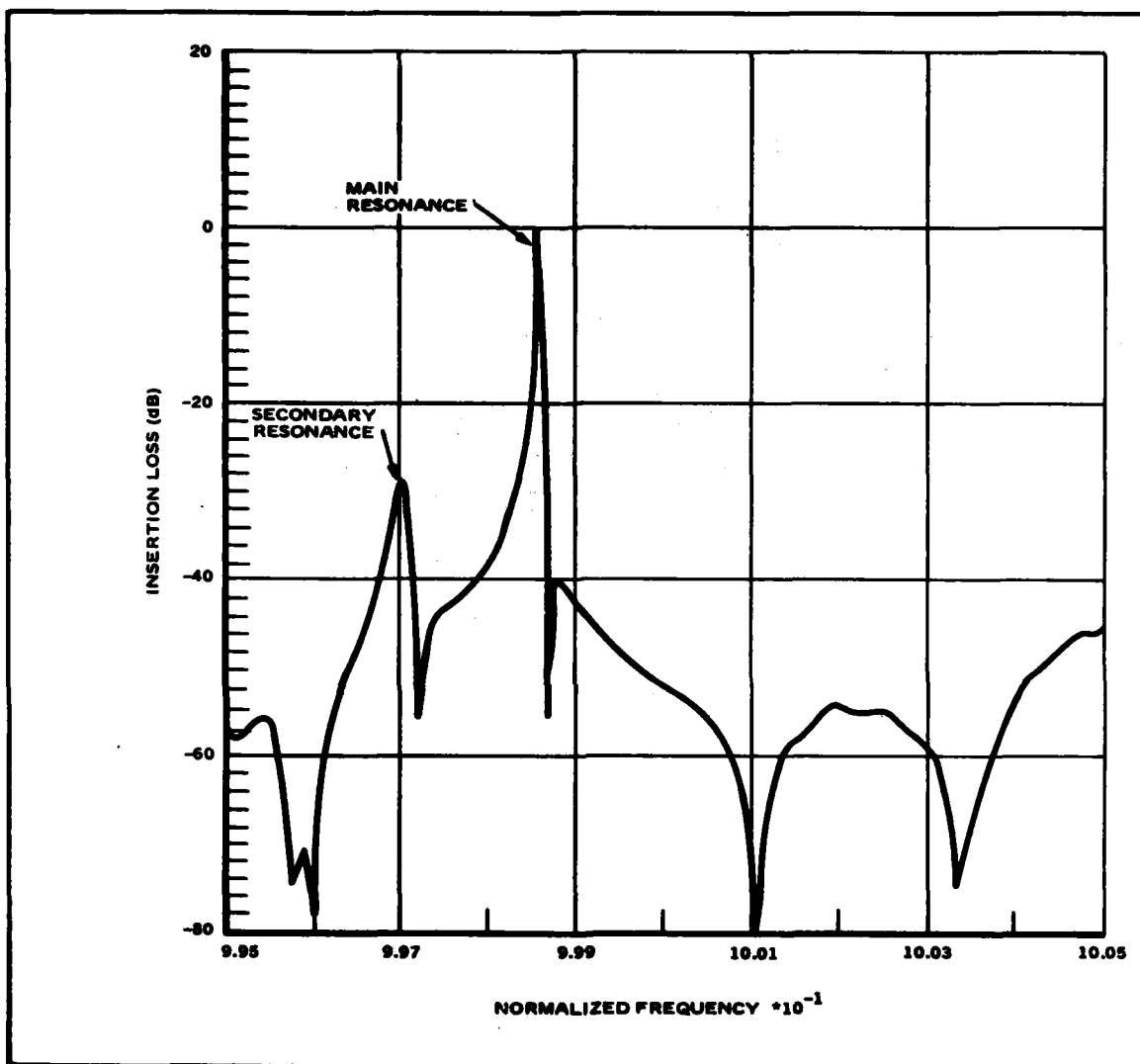


Figure 4.14. Simulation Showing Effect of Reticle Placement Error on the Insertion Loss of the Resonator



TABLE 4.3. RESULTS FOR ASSEMBLED LOT OF PHASE I RESONATORS

Serial Number	Before Seal		After Seal		$\Delta$	$\Delta$
	Freq. (MHz)	IL (dB)	Freq. (MHz)	IL (dB)	Freq. (kHz)	IL (dB)
1	400.174	10.0	400.135	11.5	-40	1.5
2	400.000	9.6	400.009	11.4	9	1.8
3	400.085	6.7	400.091	8.2	6	1.5
4	400.013	7.2	400.034	8.9	21	1.7
7	400.125	6.7	400.132	7.8	7	1.1
8	400.033	7.9	400.046	9.6	13	1.7
11	400.155	8.6	400.149	9.6	-6	1.0
12	400.039	9.2	400.021	10.8	-18	1.6
AVERAGE	400.078		400.077		-1	1.5
STD. DEV. ( $\sigma$ )	.067		.056		20	0.3

formed on a core material containing a powdered magnetic constituent. As a result of the high temperature bake prior to sealing, the permeability characteristic of these elements had shifted and hence the inductance value of the tuning network. For Phase II, toroids wound on a phenolic core were used.

**4.2.3 Evaluation of Phase II Devices.** A new photomask was fabricated which corrected the alignment problem discussed in Section 4.2.2. In addition, a minor adjustment was made in the transducer electrode line width and reflective array spacing in order to target closer to the 400 MHz center frequency requirement. An additional lot of wafers were fabricated and probed for resonant frequency response. All wafers basically exhibited good resonances and one was diced in order to provide the necessary resonators for Phase II. A lot of eight devices (S/N 1A through 8A) were assembled, tuned, and sealed. A summary of the measured performance for the key parameters is presented in Table 4.4. An average insertion loss of 5.5 dB is observed. This value is several dB lower than the value determined for the samples of Phase I. The average center frequency is 398.832 MHz with a  $1\sigma$  (sigma) variation equalling 55 kHz. This value falls short of the specified 400 MHz requirement and an additional adjustment of the line-width and spaces aspect ratio is required. Furthermore, all frequencies were too low in value to attempt adjusting to 400 MHz using the laser.

Finally, Table 4.4 also lists the measured 3-dB bandwidths. Prior to tuning, the observed values ranged from 50 to 60 kHz. After final tuning with the toroid elements, the bandwidth widened to a 136 kHz average value. While these values again do not meet the specification requirement, improvement over previous results has been achieved.

TABLE 4.4. RESULTS FOR ASSEMBLED LOT OF PHASE II RESONATORS

Serial No.	Insertion Loss (dB)	Frequency (MHz)	Bandwidth (kHz)
1A	6.7	398.724	127
2A	5.2	398.854	135
3A	5.2	398.820	150
4A	21.6	-	-
5A	4.8	398.866	140
6A	5.8	398.907	137
7A	5.4	398.858	138
8A	5.4	398.792	128
Average	5.5	398.832	136
STD. DEV. ( $\sigma$ )	0.6	0.055	7

One resonator, serial number 4A, failed during the sealing process. The crystal on this device was scratched during the seal preparation process.

A typical plot of the resonator response in the packaged configuration is depicted in Figure 4.15. A higher order resonance is observed 15 to 20 dB below the main response. On other wafers exhibiting slightly higher wafer level frequencies, the higher order mode does not appear. Therefore, it appears that this spur can be eliminated by adjusting the etch depth and in addition by providing more stringent control on the metallization thickness. Furthermore, a broad spurious spectrum is observed below the main resonant response. It is speculated that this mode is related to anomalies with the input/output transducer configuration and its cause is currently unclear.

In summary, performance improvement has been achieved over the Phase I devices, however the devices still fall short in meeting several of the specification parameters of this program. A net 1.2 MHz shift in center frequency below the desired 400 MHz value is now observed with the updated design. This shift was not predictable and was introduced as a result of the relatively small photomask adjustment made to the previous design in order to optimize the peak resonance response.

**4.2.4 Comparison of Specification Requirements Versus Measured Performance.** In this section, the performance parameters are discussed for which the specification requirement could not be met. An explanation is provided in each case for the existing deviation.

1. **Insertion Loss.** The average insertion loss of the set of tuned resonators was 5.5 dB. The specification requirement is 5 dB, and 4 dB was initially predicted for this device. The following contributions exist which may add nonnegligibly to the predicted value. In particular,

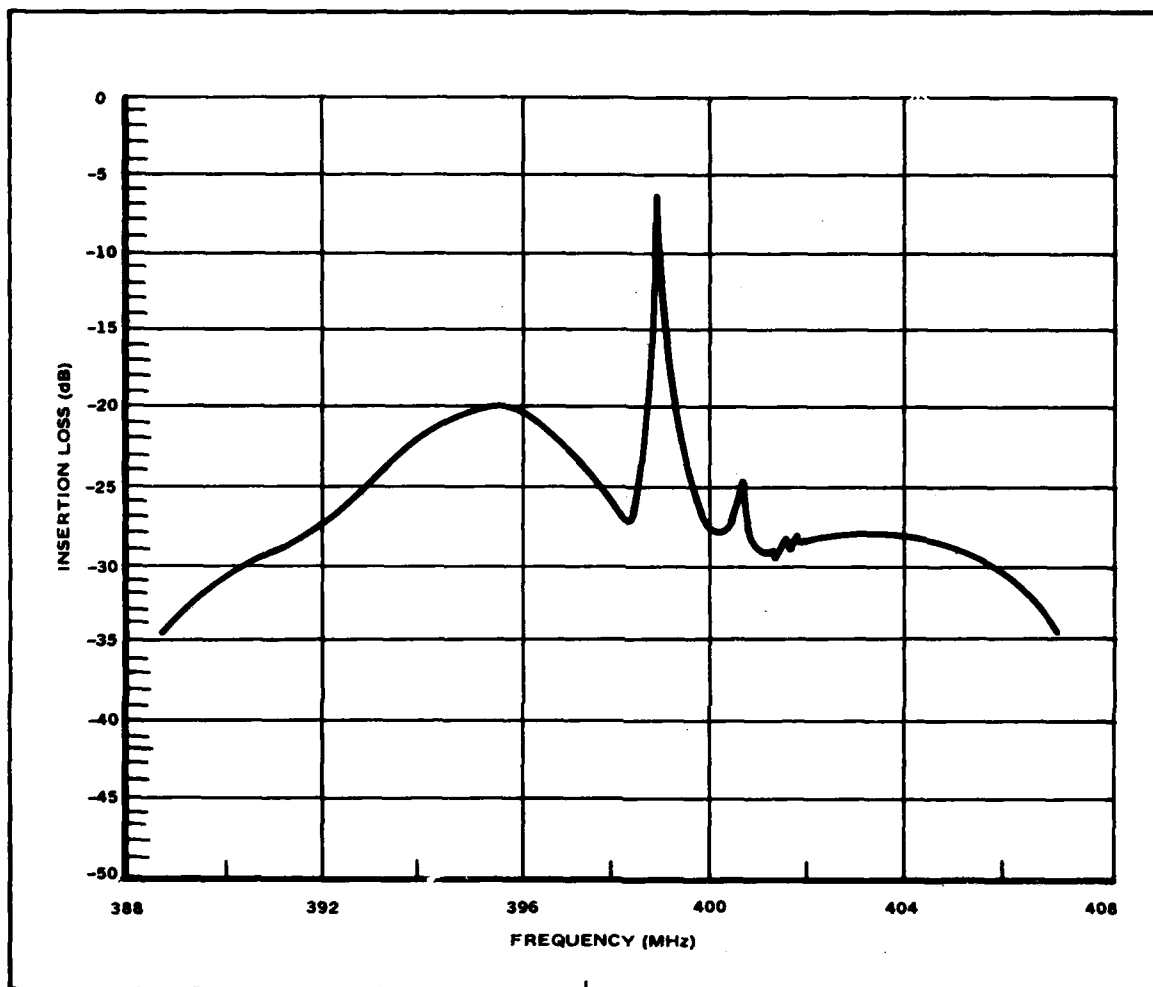


Figure 4.15. Typical Response of Packaged Resonator for Phase II

- a. resistive losses in the transducer and tuning circuit,
- b. parasitic capacitance to ground shunting the transducer,
- c. scattering to bulk waves in the grating region, and
- d. scattering loss in the rf shield.

Since toroid inductors at this frequency typically exhibit circuit Q's of only 50 to 60, the resistive loss of the series tuning inductor could account for 1 to 2 dB of additional insertion loss increase. The other major contributor is scattering loss in the rf shield. Since the rf shield forms a periodic grating, the possibility exists for scattering to bulk waves. Originally, this mechanism was considered to be a second order effect. It is possible, however, that for the thicker metallization and deeper grooves that were used, the scattering into the bulk mode from the rf shield may no longer be negligible. This effect could also possibly explain the distortions observed in the resonant response. The remaining effects, namely contributions b. and c. above, are still considered to contribute negligibly to the overall resonator insertion loss.

2. Bandwidth. The average measured bandwidth for the set of tuned resonators was 136 kHz versus the specification requirement of 100 kHz. The resistive loss mechanism responsible for the insertion loss increase is also suspected to decrease the overall circuit Q and hence increase the bandwidth of the resonator. Since the bandwidth of the untuned resonators was generally in the 50-60 kHz range, it seems to indicate that the additional resistive loss contributions are providing the additional resonance broadening.
3. Center Frequency. The center frequency requirement was  $400 \pm 0.01$  MHz. The first design (Phase I devices) resulted in an average center frequency of 400.076 MHz. Following the photomask modification that properly centered the resonance of the transducer relative to the reflective array, the average center frequency shifted 1.244 MHz downward to the value 398.932 MHz. With the resonant peak now properly centered, it will be a simple matter to scale the device wavelength and shift the average center frequency to the specification value. It is felt that this can be achieved with one additional mask iteration.
4. Adjacent Sidelobe Suppression. The minimum adjacent sidelobe suppression level required 20 dB; however, on the average, only 13 dB was actually obtained. The relatively large deviation is attributed to the highly asymmetric transducer response. This conclusion was verified by applying photoresist over both of the etched reflective gratings. The photoresist acts as an acoustic absorber, and therefore, the reflective properties of the grating is destroyed. What remains is a simple

transducer-to-transducer delay line configuration. It was observed that the asymmetry in the frequency response remained after both gratings were covered with photoresist. Furthermore, the asymmetric response did not occur in the original design. It is therefore concluded that the transducer layout, which was slightly modified for the Phase II devices, is responsible for the asymmetric response. The effect is probably due to diffraction of the smaller transducer apertures which were farther apart for the second iterated design.

5. Feedthrough Suppression. It is now felt that a 50 dB feedthrough value cannot be met for a two port resonator. For untuned resonators as much as 40 dB of signal suppression (measured in the frequency domain as broadband stop band suppression) was obtained. The use of internal tuning inductors, in this case toroids, significantly degrades the feedthrough suppression as a result of direct inductor-to-inductor cross talk. Since in a two port design, both transducers are close together, the input and output tuning inductors will similarly be spaced close to each other. Separation of these elements at high frequency will only add additional unwarranted parasitic capacitance effects.

## 5.0 PRODUCTION RAC PACKAGE DEVELOPMENT

**5.1 Introduction.** The packaged RAC device configuration proposed originally on this program required the use of a notched crystal which in turn was placed inside a housing containing an appropriately sized septum. This configuration was capable of providing 65 dB of signal feedthrough suppression, a value significantly higher than required on this program (50 dB) and in most other applications. Furthermore, it was discovered early in the program that lithium niobate is a fragile material and does not lend itself readily to standard production oriented milling, grinding, and sawing operations. Miniature cracks are easily introduced which can adversely affect the electrical performance of the device after being exposed to the various environmental conditions. In addition, the introduction of a septum to the housing frame significantly increases the complexity for reworking the package to achieve hermeticity and sufficient signal feedthrough suppression.

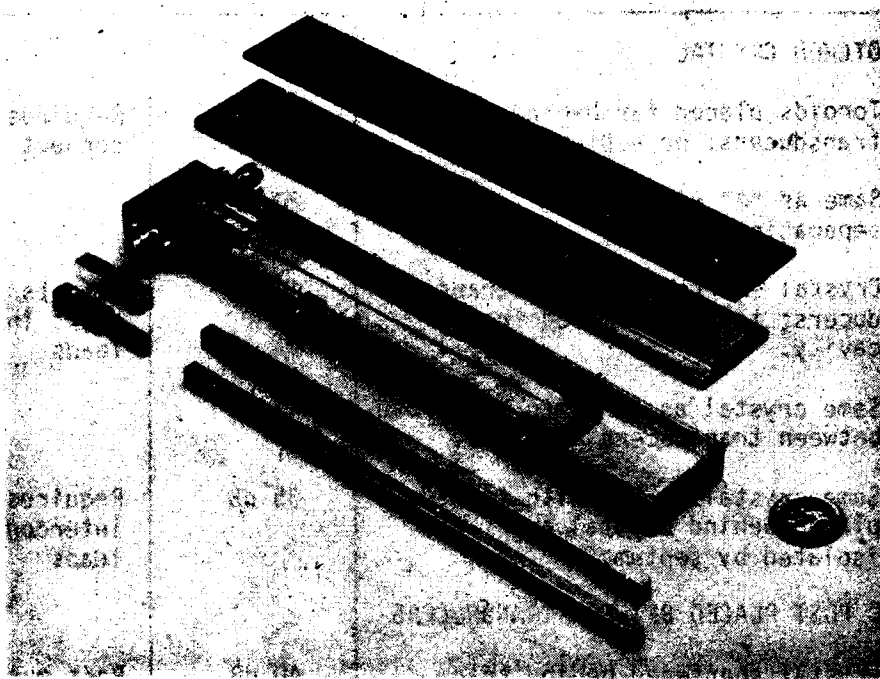
Based on the considerations above, an alternate package design was investigated during the Engineering Development Phase that would eliminate the septum and notched crystal combination. The results obtained, and discussed below, indicate that a 45 dB suppression level can be readily achieved using a simplified crystal cavity design.

**5.2 Signal Feedthrough Evaluation.** A series of configurations were built using a crystal and a specially machined package designed to study the effects of crystal and packaging changes on feedthrough suppression. A photograph of this package is shown in Figure 5.1. Also shown are the inserts machined to permit varying the crystal cavity.

The major elements contributing to feedthrough were identified to be: (1) the inductors, (2) the high permittivity crystal material between the transducers, (3) coupling of fields through the space above the transducers, (4) the length and actual configuration of input/output interconnects, and (5) the quality of the ground connection. The cavity dimension, which was made adjustable by the insertion of the various width spacers and both flat and stepped covers, did not have any effect on the feedthrough level, and were therefore discarded early in the investigation as a key variable.

Table 5.1 summarizes the results for the various configurations and tests performed. Also presented in Figure 5.2 are photographs showing each configuration. All septa used in configurations 1 and 2 were formed from several layers of thin conductive rubber gasket material. The top and bottom layers were pressed firmly against the cover and floor of the package, respectively, to achieve good grounding. The septum used in configuration 3 was machined from aluminum and was located with screws through the package bottom and lid.

The rationale behind the sequence of tests shown in Table 5.1 and the interpretation of the results are described below. Configuration 1A shows the unnotched crystal and the inductors all contained in a single cavity.



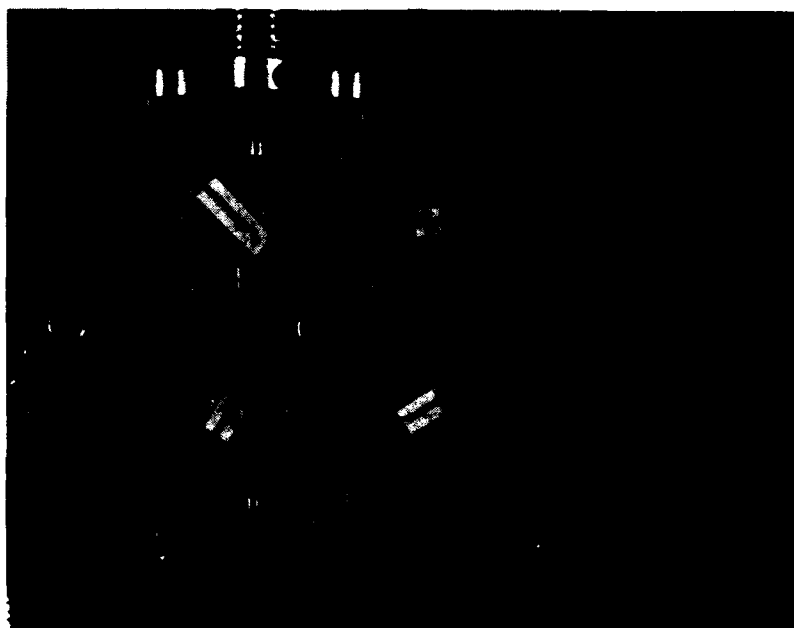
82-10-003

**Figure 5.1. Package Developed to Evaluate Feedthrough Performance for Various Cavity Configurations**

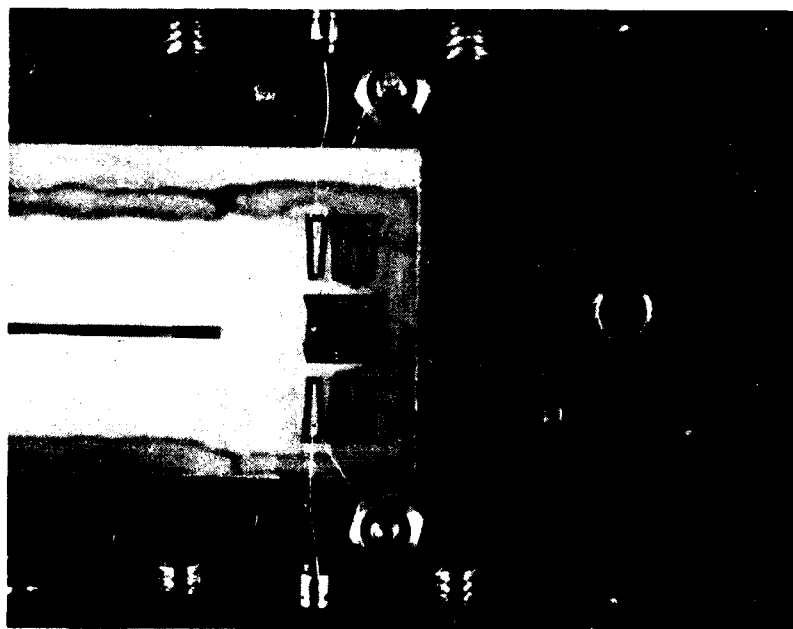
TABLE 5.1. RAC FILTER SIGNAL FEEDTHROUGH RESULTS

CONFIGURATION	NOMINAL FEEDTHROUGH	REMARKS
1. UN-NOTCHED CRYSTAL		
A. Toroids placed far behind transducers; no septum.	15 dB	Requires long interconnect leads
B. Same as "A" with septum separating toroids.	20 dB	
C. Crystal shortened behind transducers; toroids removed from cavity.	40 dB	Permits use of very short interconnect leads
D. Same crystal as "C" with metal pad between transducers grounded.	45 dB	
E. Same crystal as "E" with toroids placed behind crystal and isolated by septum.	35 dB	Requires long interconnect leads
2. METAL POST PLACED BETWEEN TRANSDUCERS		
A. Crystal shortened behind transducers and toroids placed behind crystal; no septum separating toroids.	40 dB	Post must contact package floor and cover
B. Same as "A" with septum placed between toroids.	45 - 50 dB	
3. NOTCHED CRYSTAL		
A. Septum separating toroids only.	50 dB	Septum must contact package floor and cover
B. Septum extending fully into area separating transducers.	55 dB	



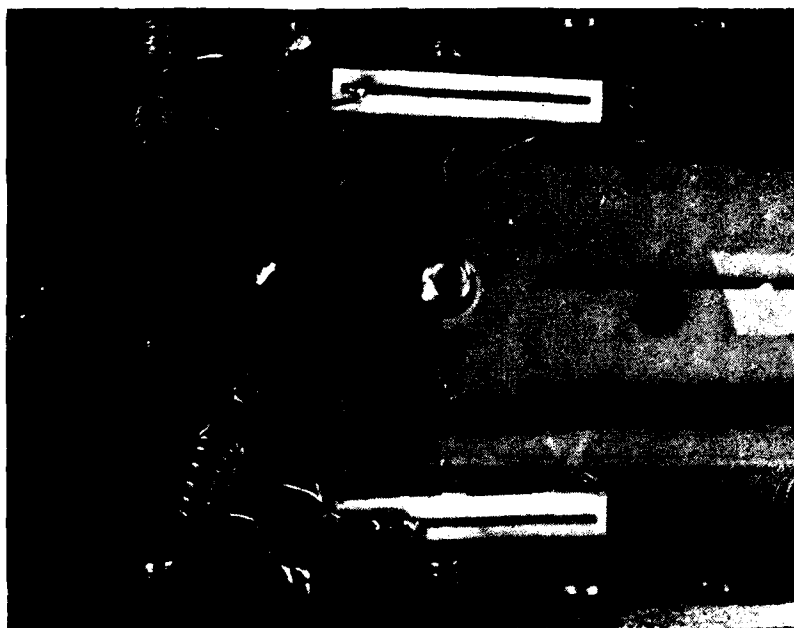


(A) CAVITY CONTAINS UNNOTCHED CRYSTAL WITH TUNING ELEMENTS FAR REMOVED FROM TRANSDUCERS

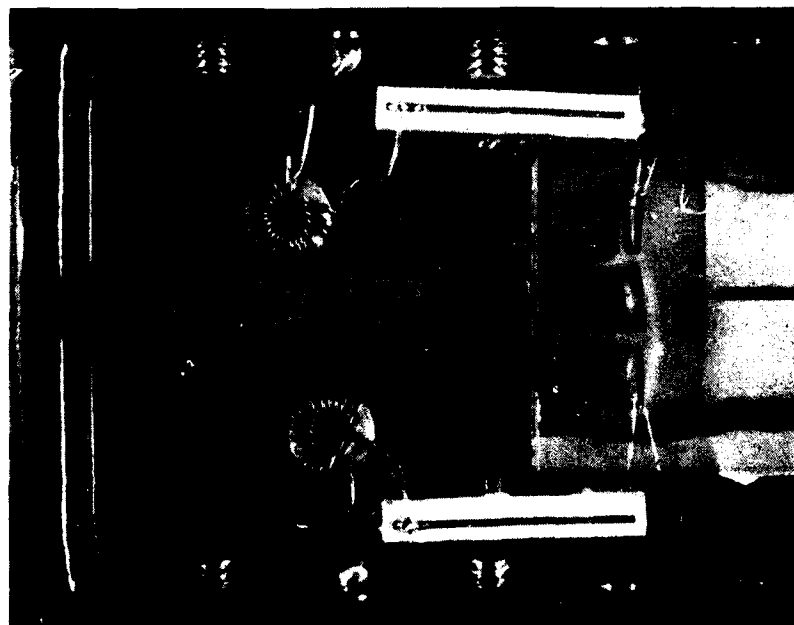


(B) TOROIDS ARE REMOVED FROM THE CAVITY AND INTER-CONNECTS ARE ACHIEVED USING VERY SHORT WIREBONDS

Figure 5.2. Package Configurations Used to Evaluate Signal Feedthrough.



(C) INTERCONNECTS ARE ACHIEVED WITH SHORT WIREBONDS AND A SEPTUM IS PLACED BETWEEN THE TOROIDS



(D) A METALLIC POST IS PLACED BETWEEN THE INPUT AND OUTPUT TRANSDUCERS AND A SEPTUM IS LOCATED TO SEPARATE BOTH TOROIDS

Figure 5.2. Package Configuration Used to Evaluate Signal Feedthrough  
(Continued)

334020-40

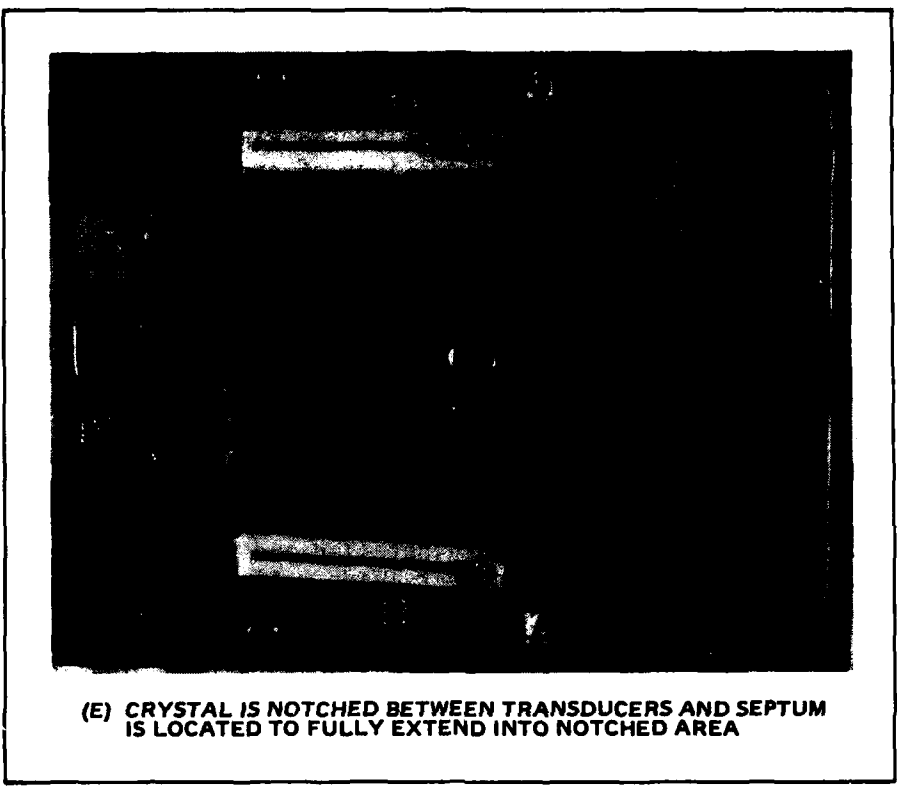


Figure 5.2. Package Configuration Used to Evaluate Signal Feedthrough  
(Continued)

Very short 0.635 mm thick (25 mil) alumina substrates containing 50 ohm impedance lines served as transitions between a wirebond connection and a solder termination. The measured results indicate very poor feedthrough suppression is achieved for this configuration. It was also noted that the actual level is sensitive to the distance between the inductors, but not their relative orientation. The placement of a septum between the toroids provides only a nominal 5 dB improvement in the feedthrough suppression. The toroids were also replaced with sections of short wire; again, with no additional improvement.

In configurations 1C and 1D, the lead lengths are shortened as much as possible. Simultaneously, welded moly tabs instead of crimped-in or screwed-in terminals were introduced for use as grounding structures. It was demonstrated earlier that moly tabs provide a good ground at 200 MHz, and therefore will be used on this program. As a result of this work, moly tabs are already being used on other SAW devices for grounding the transducers and have replaced terminal posts and selective gold plating techniques. Also, at this point in the evaluation, the metal notch-cutting guide located between the transducers was employed as a Faraday shield. As a result, the feedthrough improved from nominally 40 to 45 dB. In configuration 1E, the toroids were reinstalled and care was exercised to minimize the length of the interconnect leads. Also, the metal pad between the transducers was grounded and the toroids were isolated by a septum. Again, it was observed that the feedthrough was sensitive to the distance between the toroids, but not their relative orientation. The lower value (35 dB) achieved in this configuration can be attributed to the longer lead length required to implement the interconnect network.

In configurations 2A and 2B, a hole was drilled in the area separating the input and output transducers. The hole was drilled using a 0.277 cm (0.109 inch) diameter diamond core drill bit. The feedthrough level improved as shown in Table 5.1, but 50 dB was only marginally achieved. It was demonstrated only with a septum placed between the toroids, a conductive post (screw) placed through the hole in the crystal, and both making contact with the package floor and cover. Finally, the hole through the crystal was extended to its end forming a notch as shown in the photograph of Figure 5.2E. Three different septum configurations were used for further evaluation. One configuration separated only the toroids and provided nominally 50 dB of suppression. Of the other two septa, one contained a lip which only extended over the notched area (shown in the photograph), while the other extended entirely into the notched area. Both provided approximately 55 dB of signal suppression.

5.3 Proposed Housing Changes. A review of the data in Table 5.1 indicates that a 45 dB level can be readily achieved without a notched crystal and toroids. This in turn implies that a nominal 50 dB feedthrough suppression level should be attainable using a packaging approach without a septum and notched crystal configuration, but with the input and output toroid elements highly isolated. It was possible to test such a configuration by introducing a simple modification to two of the engineering

units scheduled for delivery to Fort Monmouth. The modifications are shown in Figure 5.3. The wirebond connections are very short and similar in arrangement to Figure 5.2B. The tuning inductors are completely isolated in the separate cavities located underneath the main crystal cavity. A 45 to 55 dB of signal feedthrough suppression level was measured for this configuration. The relatively large variation was attributed to crosstalk between the two inductor cavities, and this in turn was highly dependent on the location and tightness of the toroid cover in one of the two packages. This problem was considered anomalous and can be avoided in future packages, but it does demonstrate a sensitivity to the toroid cavity and cover design.

Since the results obtained on the two devices proved successful, the existing package design was modified and a sample housing was fabricated. A picture of an assembled RAC filter in the new package configuration is shown in Figure 5.4. For this device, 50 dB of signal feedthrough suppression was readily achieved.

It should be noted that the feedthrough terminals are offset relative to each other. The intent is to minimize direct coupling of the electromagnetic fields surrounding the wirebonds. In addition, the offset feedthrough terminals permit bonding to transducer pairs that are similarly offset from one another. This further increases the distance between the input and output port configuration and should therefore provide additional suppression. The only change introduced in the lower cavity configuration is that both connectors are placed on opposite sides rather than the end of the package. This change should further minimize any possible coupling between input and output terminals.

In conclusion, the signal feedthrough suppression performance of a RAC filter using a closely spaced input/output transducer configuration was investigated for various tuning network spatial configurations. Based on the results obtained from this study, it was possible to eliminate the package septum and notched crystal configuration and still obtain the required 50 dB signal suppression level. As a result, the modified engineering phase package depicted in Figure 5.4 will be employed in the Confirmatory Sample Phase and Pilot Production Phase.

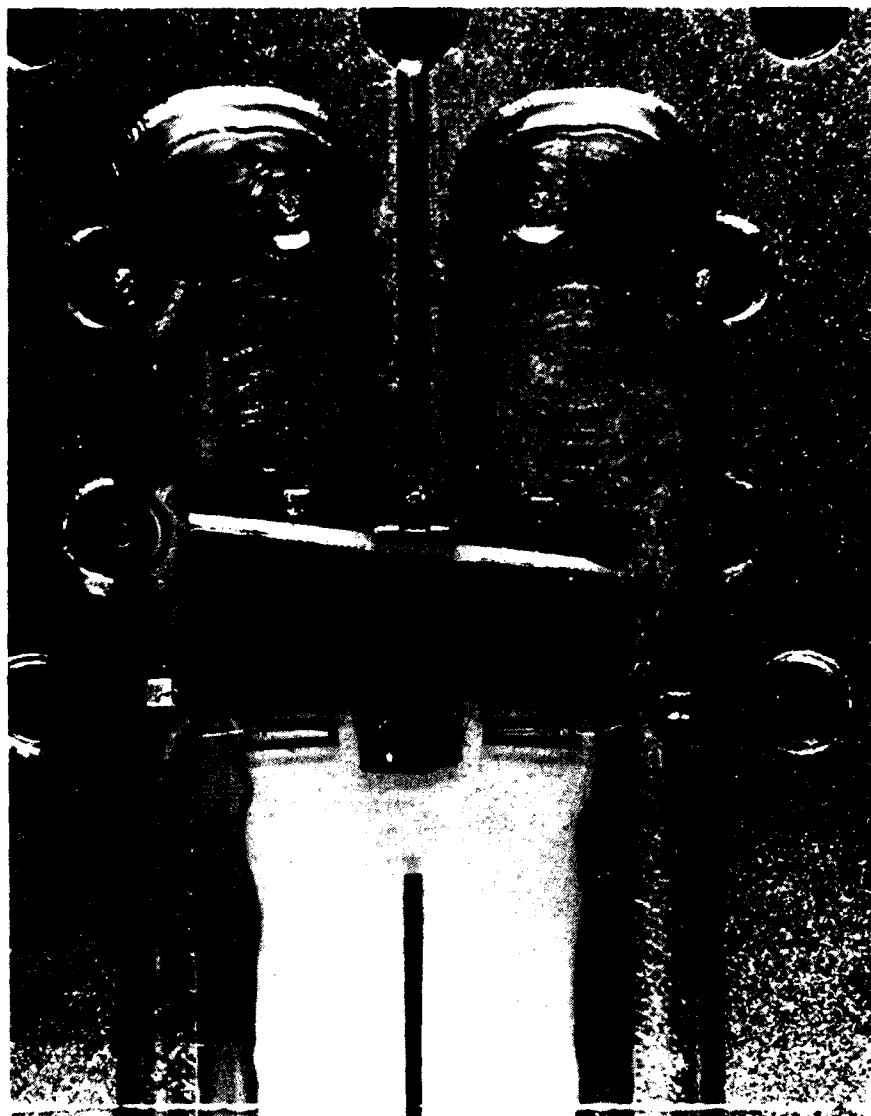
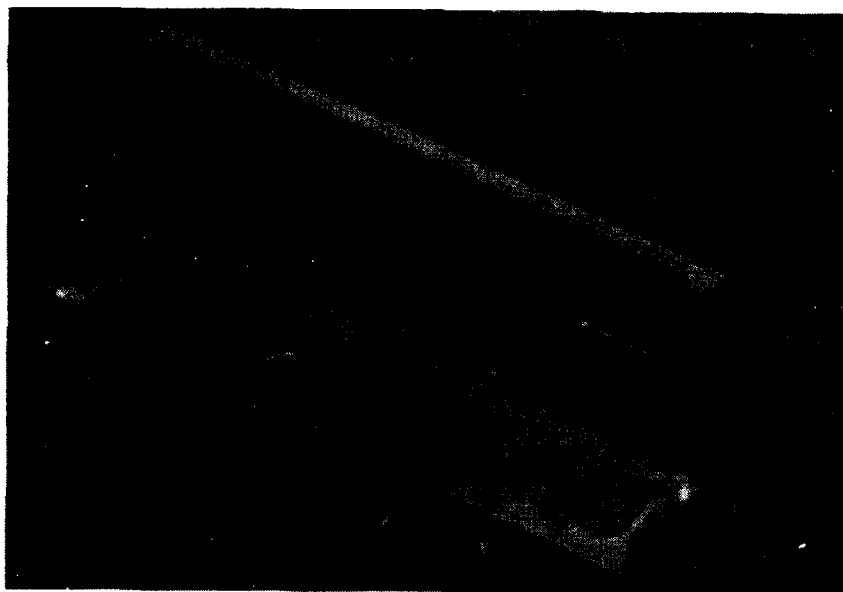


Figure 5.3. Photograph of Experimental Package Used to Demonstrate Performance Without a Notched Crystal. Configuration shows unnotched crystal and relatively short wire bond leads to achieve good grounding and interconnection to posts. Toroids are placed in isolated cavities on opposite side of crystal cavity.



82-10-0002

**Figure 5.4.** Photograph of Package Configuration to be Used for the Confirmatory Sample Phase and Pilot Production RAC Filters. Spectrum has been removed and toroid interconnect posts have been relocated to permit shoft wirebond loops.

## 6.0 RAC UP-CHIRP (TEST-LINE) DEVELOPMENT.

6.1 Introduction. The pulse compression performance of the RAC down-chirp expansion filters can be demonstrated by performing a closed loop test using an up-chirp compression line. This line is also designed to have an operating bandwidth of 60 MHz centered at 200 MHz with a dispersive delay of 60 us. Similarly, this device is fabricated on lithium niobate, and contains depth weighted ion-beam etched grooves to achieve the desired amplitude and phase response. However, unlike the expansion line design, the compression line is weighted using a Hamming window function to provide a theoretical sidelobe suppression of 42 dB. Expected amplitude and phase errors incurred throughout the various manufacturing steps degrade this suppression level, so that actual measured close-in sidelobes may fall between 25 to 30 dB.

6.2 Design. Using the design procedure described in Section 2, the required overall Hamming weighted frequency response was obtained by systematically varying the depth profile of the reflecting grooves until the depth dependent nonsynchronous (bulk) scattering loss,  $NS(d,h)$ , and the grating reflection loss,  $\Gamma(f,h)$ , match the overall filter response,  $H(f)$ . In particular,

$$NS(f,h) + \Gamma(f,h) = H(f) - T(f) - P(f), \quad (1)$$

where  $h$  is the groove depth and  $f$ , the frequency. The terms  $T(f)$  and  $P(f)$  describe the combined loss characteristics of the transducer configuration and the propagation loss, respectively. Both loss terms are groove depth independent.

The passband response of the eleven finger periodic transducer designed for this compression line filter is shown in Figure 6.1. The response is flat over a large portion of the 60 MHz passband and exhibits 14 dB of insertion loss.

The remaining loss terms, in particular nonsynchronous bulk scattering, propagation loss, and grating reflection loss, are calculated as described in Section 2.2 and shown in Figure 6.2. The minimum overall device insertion loss was designed to be 35 dB at the center of the passband. The nonsynchronous bulk scattering loss term contributes approximately 3 dB to the overall loss at the high frequency passband edge, the propagation loss term approximately 6 dB, the grating reflection loss term 8 dB, and the losses from the transducer pair 30 dB. These values all fall within the low reflection loss model limits, and therefore, multiple reflection loss contributions can be ignored.

The groove depth profile developed for this design is shown in Figure 6.3. A relatively broad spectrum of deep grooves (500 to 600 Å) is formed over the center portion of the response with a gradual roll-off taking place to a depth of 350 Å near both edges of the passband. The above profile was implemented by using a stationary apodized slit aperture and moving the



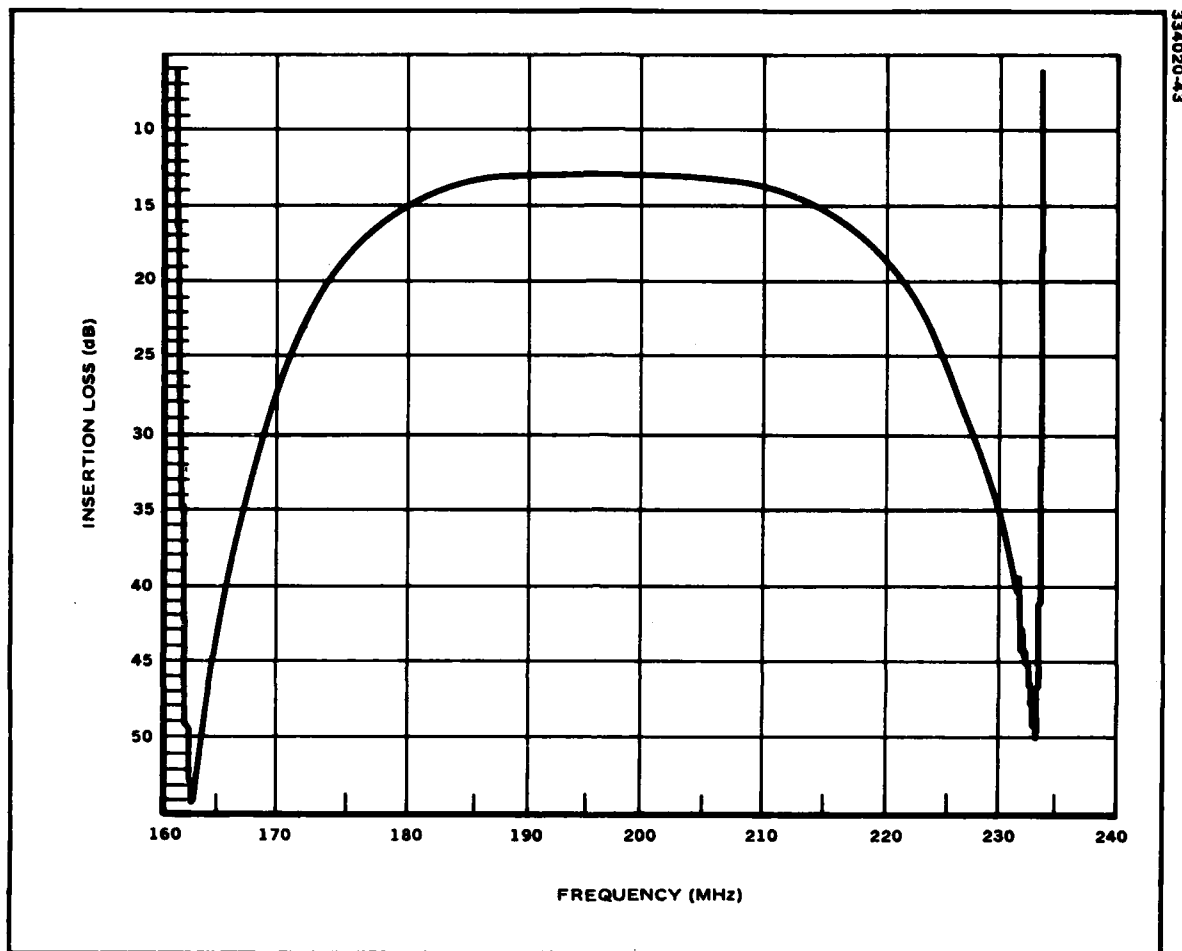


Figure 6.1. The Amplitude Response of the Transducer Design Used on the Upchirp RAC Filter

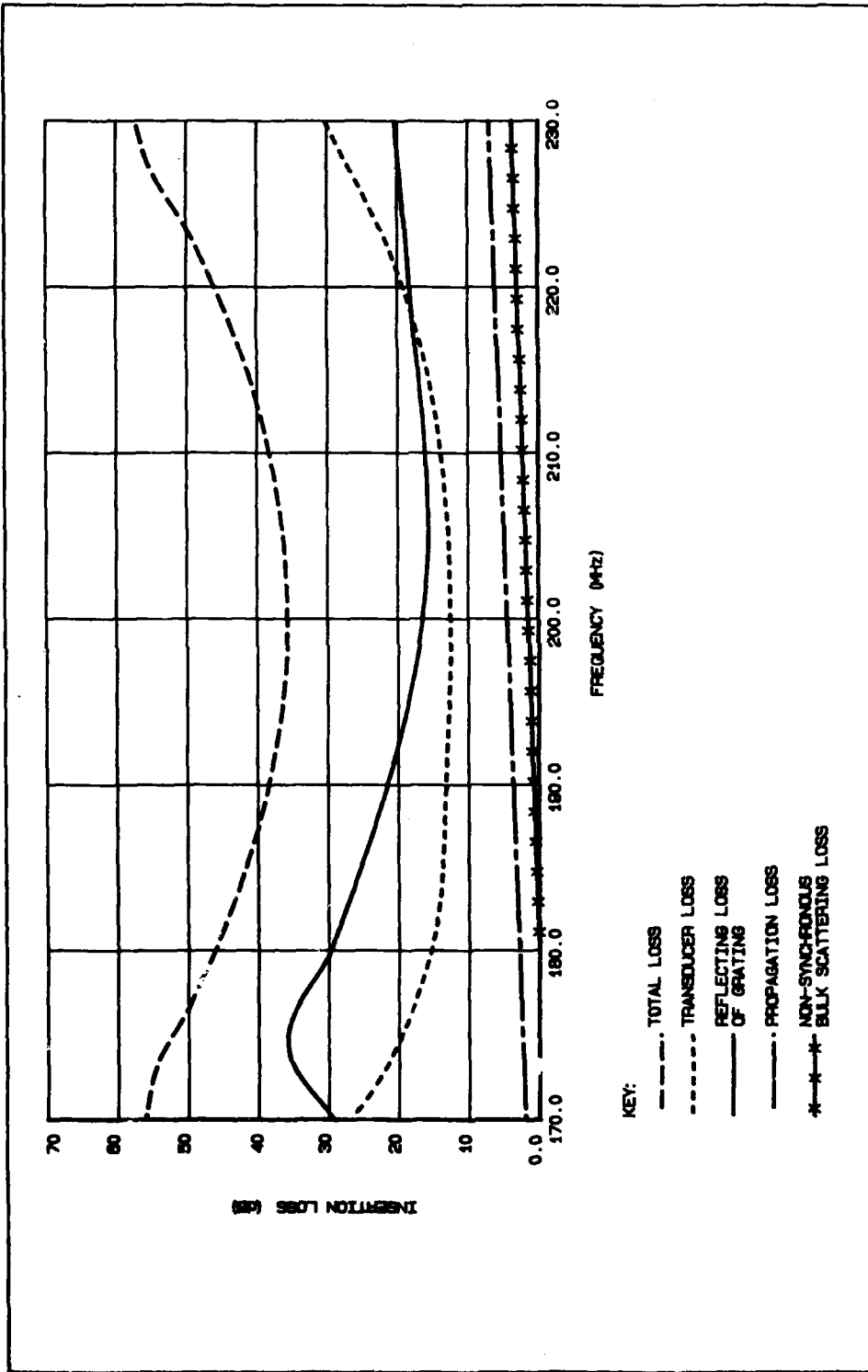


Figure 8.2. Frequency Plots of Loss Terms Contributing to Overall Insertion Loss Characteristic of Hamming Weighted RAC Filter

AD-A129 936

SAW (SURFACE ACOUSTIC WAVE) RESONATOR AND REFLECTIVE  
ARRAY DEVICES(U) HUGHES AIRCRAFT CO FULLERTON CA GROUND  
SYSTEMS GROUP J HEROLD ET AL. DEC 82

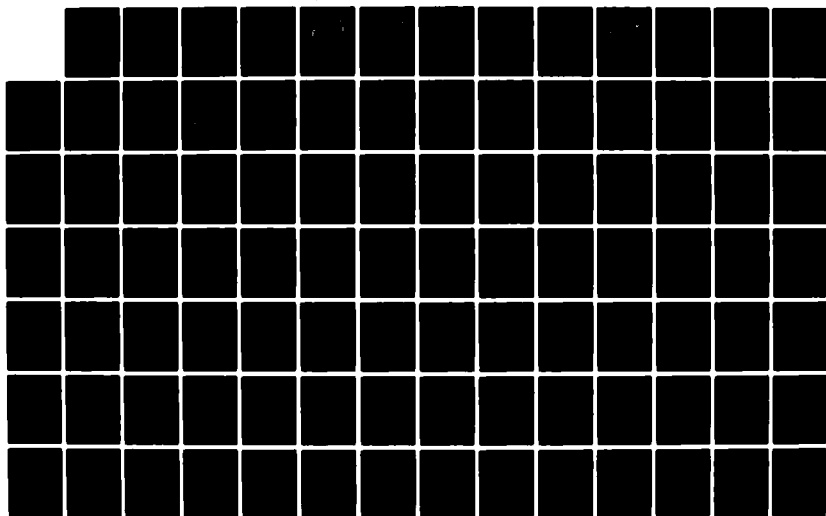
2,2

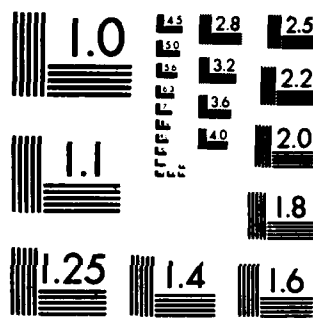
UNCLASSIFIED

DELET-TR-80-0281-1 DAAK20-80-C-0281

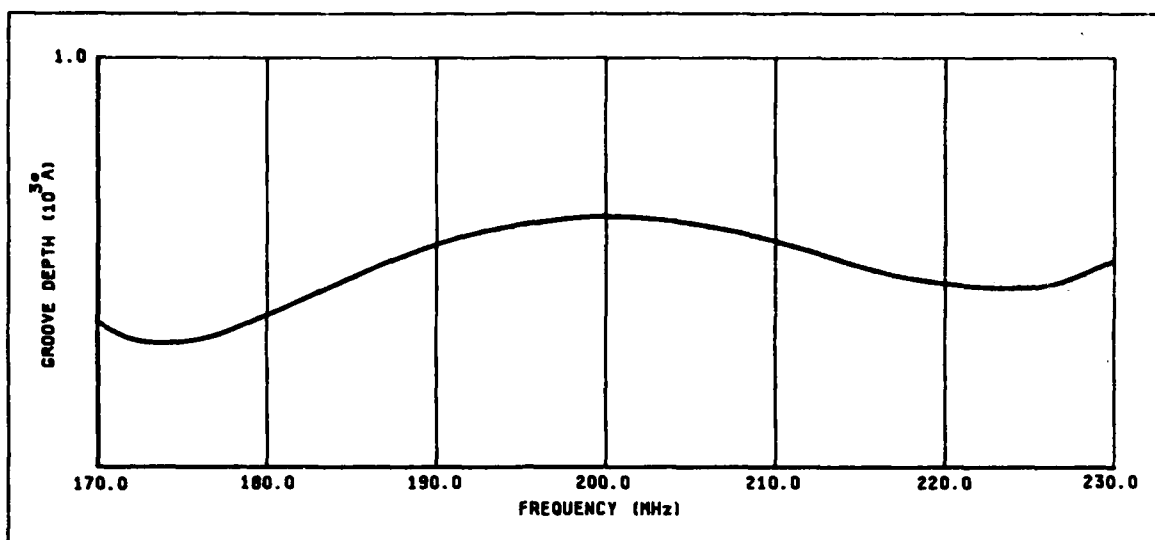
F/G 9/1

NL





MICROCOPY RESOLUTION TEST CHART  
NATIONAL BUREAU OF STANDARDS-1963-A



334020-45

Figure 6.3. Reflective Array Depth Profile Developed for the Hamming Weighted Upchirp Line

crystal in a transverse direction underneath the impinging ion beam. While this profile design exhibits higher rates of change for the etch depth over frequency than required for the down-chirp expansion line, groove depth measurements on sample arrays have shown that the profile can be readily etched within a 50 Å window.

**6.3 Evaluation.** Several up-chirp compression RAC delay lines were fabricated and evaluated during the engineering phase of this program. In Figure 6.4 is shown a typical amplitude passband response for these lines using the reflective array grating profile discussed in the previous section. The response of an ideal Hamming weighted function is superimposed over the measured data.

The average midband insertion loss for these lines is approximately 35 dB, well within the predicted performance of the design model. The overall response is smooth and exhibits the desired Hamming weighted performance up to the center of the passband. At higher frequencies, deviations from ideal weighting are observed. The high frequency roll-off phenomenon narrows the overall response, and therefore, makes accurate measurements of the bandwidth and dispersive delay difficult. However, the phase determined chirp slope still provides a measure of the overall accuracy of the filter design. For example, the measured chirp slope for one line at room temperature (23.5°C) is 0.99582 MHz/us. The derived value is 0.99523 MHz/us, and therefore, the design provides a chirp slope accuracy better than 0.06%.

Figures 6.5 and 6.6 present the plots of the amplitude difference between the ideal Hamming weighted response and the measured performance for two of the fabricated lines. The response in Figure 6.5 shows that this line was slightly overetched, which is highlighted by the deviation at the center of the band. This deviation can be predicted, to first order, from the relationship

$$R = 40(d/d_0), \quad (2)$$

where  $R$  is the relative loss variation in dB,  $d$  is the measured groove depth and  $d_0$  is the design groove depth value. For example, a 50 Å variation in the groove depth gives rise to a 1.3 dB variation in the insertion loss value at a given frequency. The line above was overetched by approximately 100 Å at center frequency which, in turn, provided the additional 3 dB of loss. The response depicted in Figure 6.6 shows a correctly etched line. The large variations observed near the band edges are the Fresnel ripple terms resulting from a truncated Hamming weighted response.

In order to reduce the roll-off observed above center frequency, the grooves in the high frequency portion of the reflective array were deepened. However, the measured amplitude response was not observed. These results strongly suggest that for long time delay up-chirp RAC filters, a coherent scattering process dominates, which in essence removes the high frequency energy component from the total signal in the widely spaced region

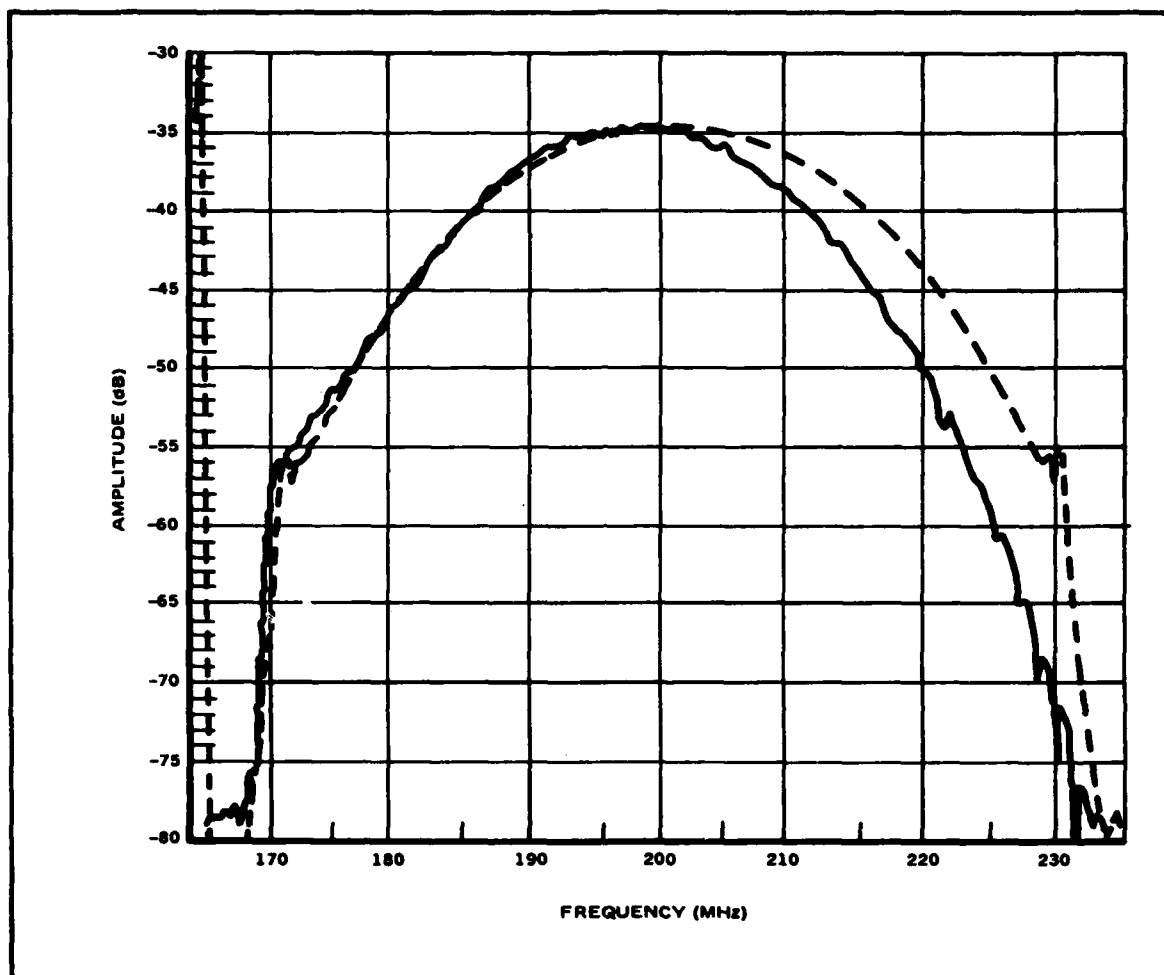


Figure 6.4. Amplitude Responses of Measured Up-Chirp Line (Solid Curve) and Ideal Hamming Weighted Line (Dotted Curve)

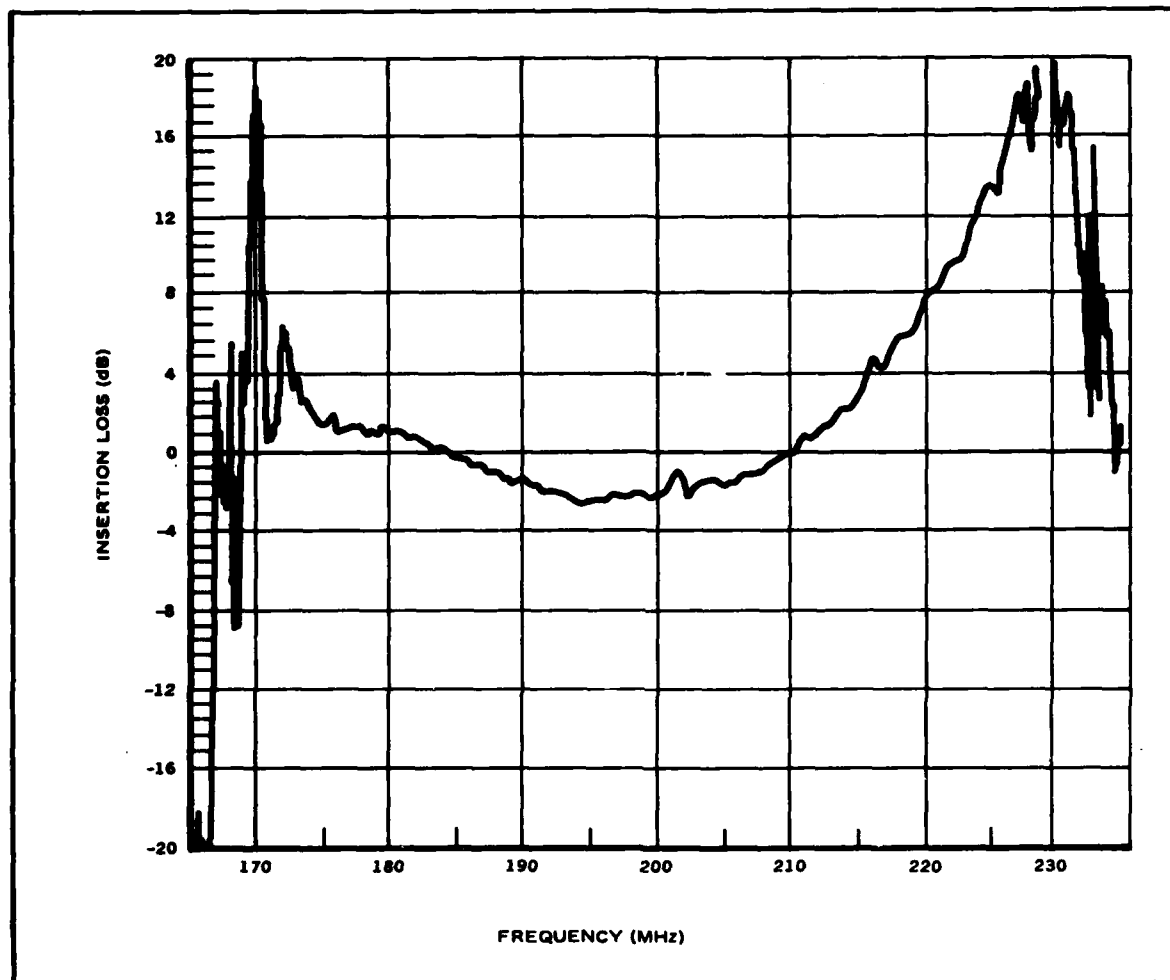
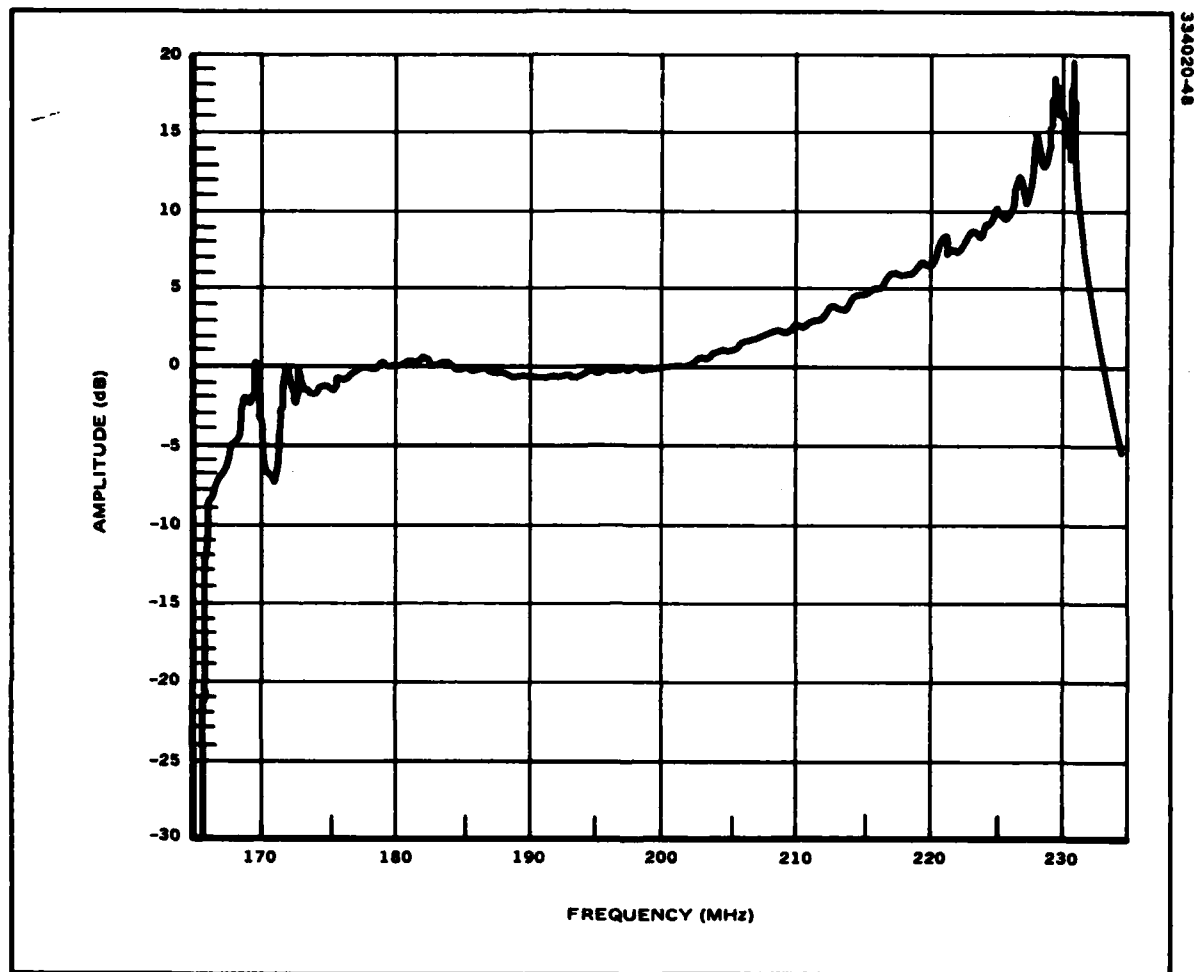


Figure 6.5. Insertion Loss Variation Between an Ideal Hamming Weighted Response and Measured Response of Upchirp Line. The deviation at the center of the passband is due to overetching the array region.





**Figure 6.6** Insertion Loss Variation Between an Ideal Hamming Weighted Response and Measured Response of Correctly Etched Upchirp Line. The large ripple terms near the band edges are Fresnel ripple resulting from the truncated Hamming response.

of the reflective array. In order to obtain a better understanding of the scattering related process, one line was evaluated containing a reflective array formed from very shallow etched grooves. A plot of the groove depth profile used is presented in Figure 6.7. Actual groove depths range from approximately 125 Å near the frequency band edges to a nominal 225 Å depth at center frequency.

The measured amplitude response of the shallow etched line is summarized in the plots of Figures 6.8 and 6.9, respectively. A comparison with the response of Figure 6.4 shows that some improvement in the magnitude of the roll-off above center frequency has been achieved. A comparison of the plots of Figures 6.6 and 6.9 indicates that a shallow profile improves the roll-off approximately 7 dB at the band edge. However, for the new line, the insertion loss value at center frequency has increased from a 35 dB value measured on earlier lines to 50 dB. It is presently felt that the increased loss may pose a dynamic range problem with the available test equipment used for performing closed loop measurements. Furthermore, while improvement in the roll-off has been demonstrated, it cannot be concluded at this time that the performance of the device as a test "standard" is acceptable to perform closed loop testing with the down-chirp lines. Additional evaluations are planned in this area in order to resolve these concerns.

**6.4 Scattering Loss Considerations.** It is presently believed that the large deviation from the ideal Hamming weighted amplitude response observed in the up-chirp RAC filters results from scattering of the z-directed Rayleigh wave into either shear bulk or pseudo-surface wave modes [9,10]. Furthermore, it appears that the scattering loss occurs in the low frequency portion of the grating array where phase coherence between the propagating surface wave, the grating, and the particular scattering mode can be satisfied according to the wave vector relationship

$$\vec{k}_z + \vec{k}_g = \vec{k}_s. \quad (3)$$

In particular, as the high frequency signal components propagate through the array structure, a phase matched condition with the low frequency spaced grooves permits energy to be removed from the beam and transferred to one of the synchronous scattering modes defined above. The resulting loss is observed as a high frequency roll-off in the amplitude response of the device. In down-chirp lines, on the other hand, it is the low frequency signals that propagate the entire length of the grating structure. A similar phase coherence condition cannot be established since the resulting surface wave is characterized by a wavelength always larger than the wavelength of the grating structure it traverses.

Otto [9] has postulated a model describing synchronous bulk scattering in periodic arrays formed from thin metallic stripes on YZ-lithium niobate [10]. An expression for the loss contribution,  $\alpha$ , is presented in terms of two empirical constants  $A_1$  and  $A_2$  as follows:

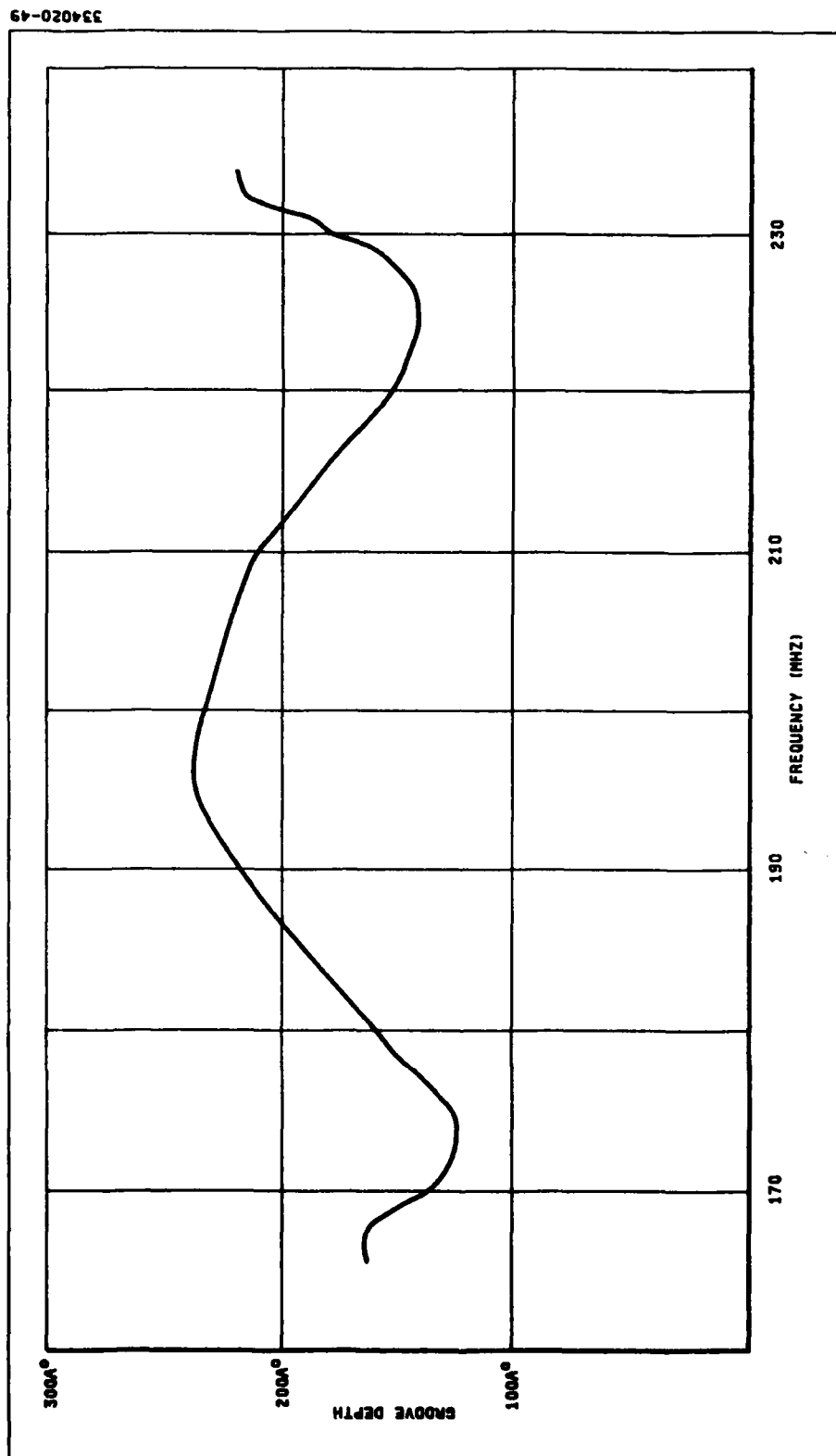
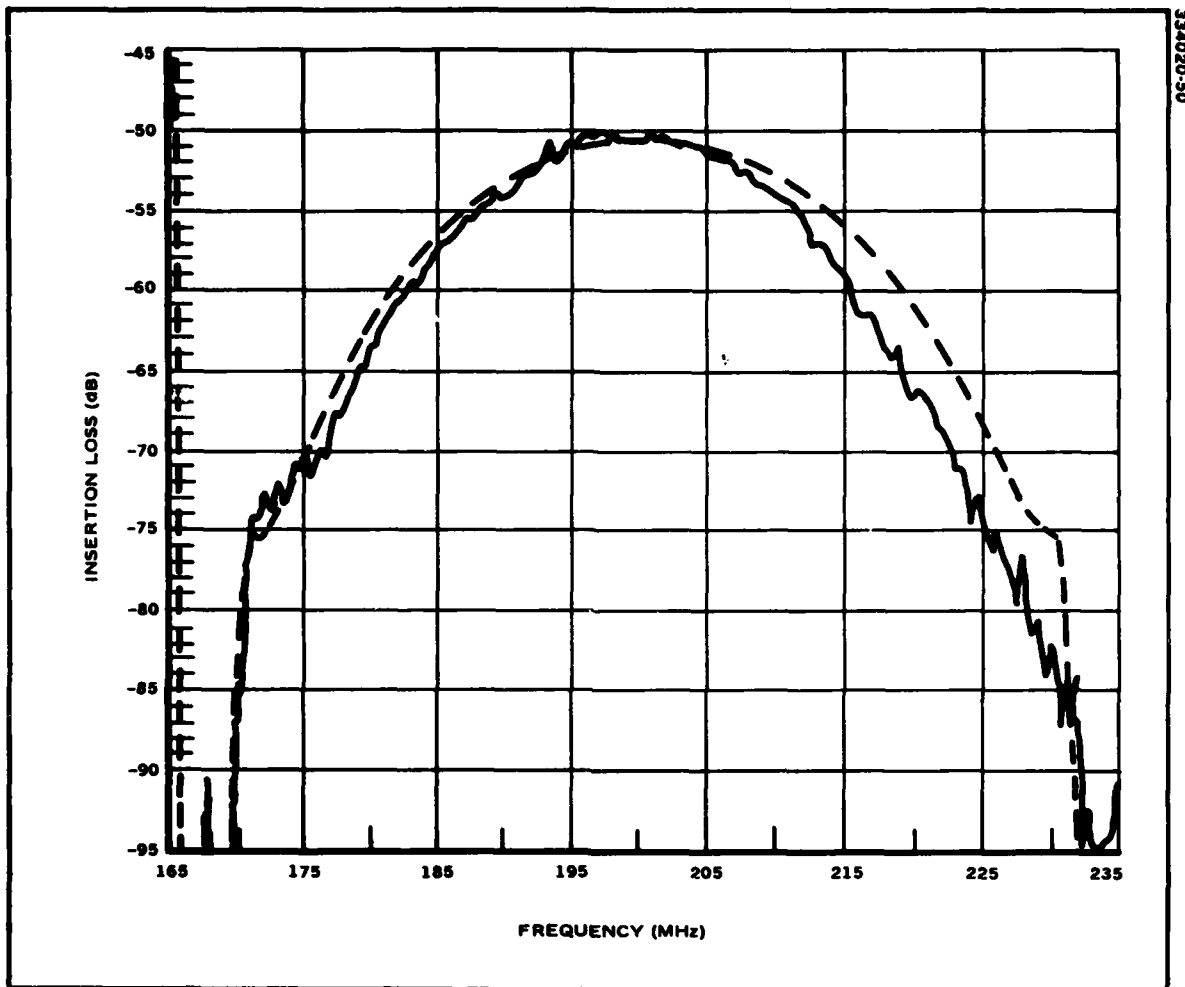
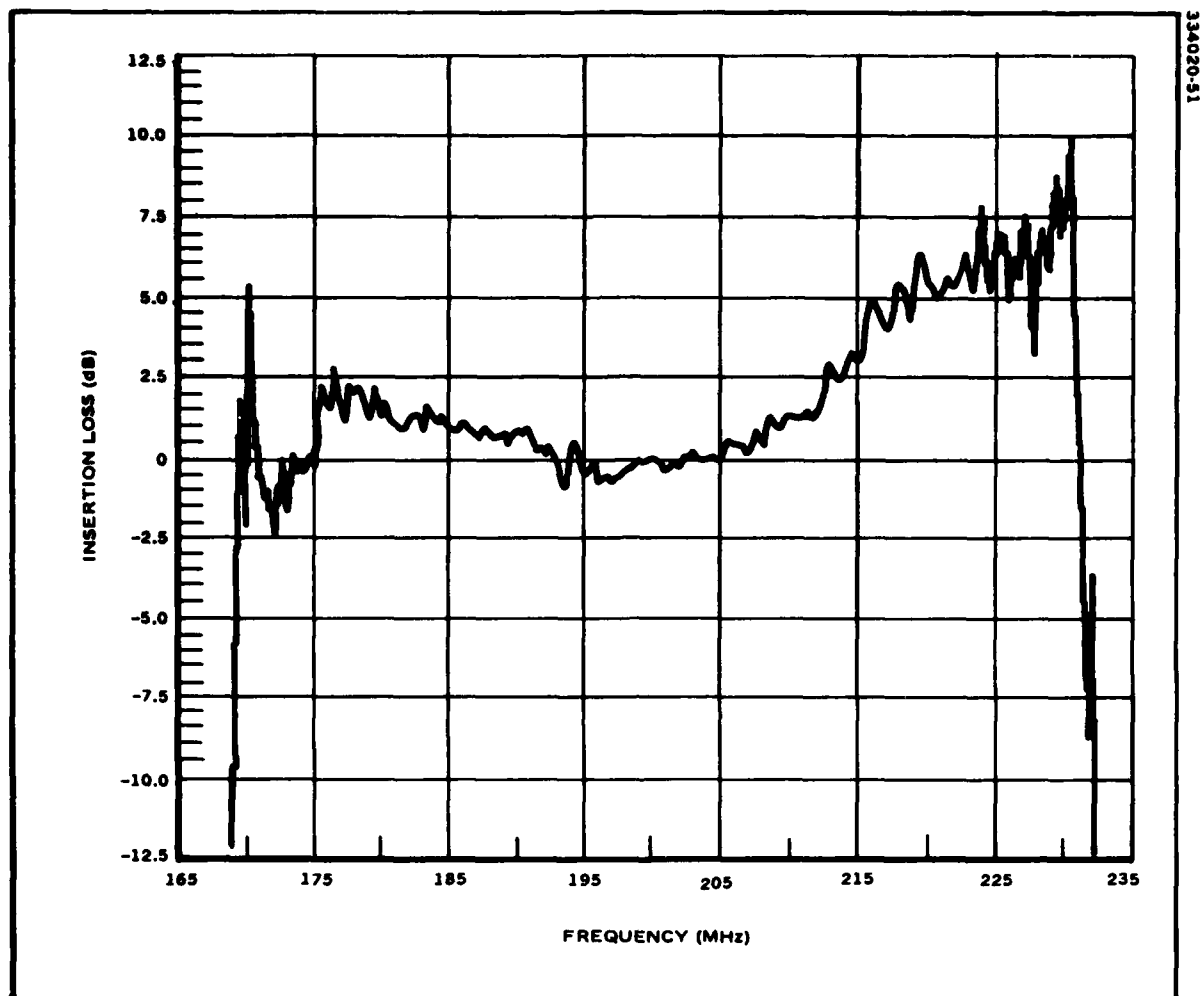


Figure 6.7. Reflective Array Profile for Hamming weighted upchirp line using shallow grooves



**Figure 6.8. Comparison of Measured Amplitude Response with Ideal Hamming Weighted Response for Line With Shallow Etched Groove Profile**



**Figure 6.9. Insertion Loss Variation Between an Ideal Hamming Weighted Response and Measured Response of Upchirp Line with Shallow Groove Profile**

$$\alpha \approx A_1 - A_2 \left( 1 - \frac{f}{1.4f_0} \right)^2 \text{ dB/stripe.} \quad (4)$$

The operating frequency,  $f$ , is constrained to fall within some specified frequency limit which, in turn, depends on the detailed phase matching characteristics with a specific scattering mode. It may be possible to adapt the expression above to ion-beam etched grooves, and therefore, employ the model with new constants to correct for the roll-off condition. The model compensates for the roll-off by increasing the groove depths in the high frequency portion of the array. However, any increase in groove depth in the high frequency portion of the array may increase the nonsynchronous bulk scattering loss contribution above the 8.6 dB value discussed in Section 2.2. In fact, it is speculated that this effect may indeed be happening on this device. As a result, any attempt to provide synchronous scattering compensation by deepening the grooves in the high frequency portion of the reflective array is totally offset by a proportional increase in nonsynchronous bulk scattering.

The selection of a slanted RAC grating design [11] as shown in Figure 6.10 is expected to eliminate the synchronous bulk scattering effect in the grating region. As shown in the diagram, the high frequency surface wave components propagate across the free surface of the crystal within the grating area until they intersect the array region where the groove spacing is identical to the wavelength of the propagating surface wave.

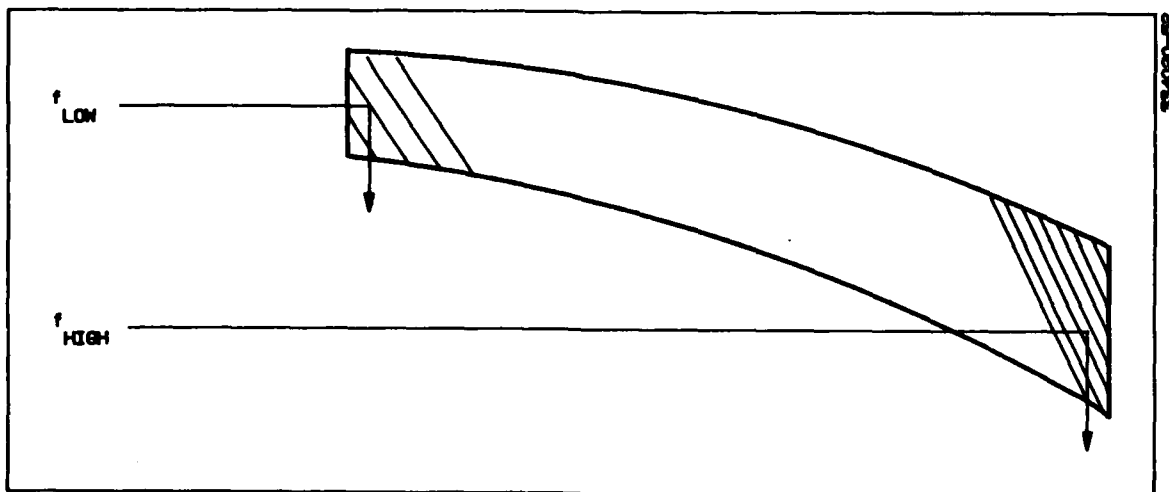


Figure 6.10. Slanted Grating Section for Upchirp Filter Design

Figure 6.10. Slanted Grating Section for Upchirp Filter

## 7.0 RESONATOR TRIM DEVELOPMENT AND EVALUATION

**7.1 Introduction.** In this section, the center frequency probe results obtained at the wafer level are presented. Included in this data will be a discussion of the variations observed in the etched groove depth, metallization thickness and the transducer linewidth, and how these parameter variations affect the spread in resonant frequencies across the individual wafers. Finally, a detailed discussion of the laser trim technique will be presented. The rationale for developing this approach along with the progress made to date will be described.

**7.2 Wafer Probe Evaluation.** During the Engineering Phase, eight wafers were processed and evaluated in order to establish a data base for determining yield figures at the wafer level. In addition to obtaining center frequency data, groove depth, metallization thickness and transducer linewidth and space measurements were also performed. In Figure 7.1 are presented the center frequency probe results obtained for a typical wafer out of the selected lot of eight. Figure 7.1a presents a listing of the actual measurements. On this particular wafer, one die was damaged and this is denoted by the value "zero" entered in the 3A coordinate. For the remaining fifty die values, a center frequency and standard deviation about this frequency was computed and the data ordered into the histogram of Figure 7.1b. This plot in essence presents the number of die in each 20 kHz window over the probed 400 kHz frequency interval. For this particular wafer, the center frequency is established to be 399.020 MHz with a one sigma standard deviation equal to 68 kHz about this value. The probe data and the histograms for the other seven wafers are provided in Appendix II.

The utility of these histograms will be to establish a criteria for determining the need to perform an additional etch at the wafer level. An additional etch across the entire wafer will shift the whole distribution to a lower frequency interval. Final frequency adjustment of the individual die will be accomplished by opening the metal stripes of the rf shield with a laser of very small spot size. This adjustment is, of course, performed on the fully assembled and tuned resonator.

A summary of the measurements performed on all the eight wafers is presented in Table 7.1. Each wafer is characterized in terms of a computed average frequency and the associated standard deviation value. In addition, the average groove depth (h), metallization thickness (t) and the transducer stripe to gap aspect ratio (s) measurements with percent variation across the 2 by 2 inch wafer surface are also included. Different groove depths were initially selected in order to determine the center frequency value and its dependence on total groove depth. The metallization thickness, on the other hand, was fixed with a target value of 1700 Å. Similarly, the stripe to gap aspect ratio is established by the photomask with a value of 1.0 for this design.

A review of the evaluated data indicates that in order to obtain a narrow distribution of frequencies about the average value, i.e. small sigma,

WAFER 38-2

	A	B	C
1	399.005	398.902	398.931
2	398.986	398.902	398.932
3	0.000	398.926	398.946
4	399.025	398.926	398.961
5	399.004	398.926	398.975
6	399.022	398.941	398.944
7	399.014	398.950	398.969
8	399.022	398.954	398.979
9	399.048	398.971	398.989
10	399.074	398.990	398.984
11	399.062	399.015	399.017
12	399.095	399.039	399.049
13	399.109	399.047	399.103
14	399.104	399.048	399.132
15	399.108	399.088	399.133
16	399.094	399.099	399.149
17	399.109	399.035	399.107

PER CENT GOOD DIE	AVRG (MHZ)	STND DEV (MHZ)
98.0	399.0188	.0687

Figure 7.1 Wafer Level Center Frequency Probe Results. Figure 7.1a above presents a tabulation of the individual die measurements. Each 2 x 2 wafer contains three columns containing 17 resonator die.



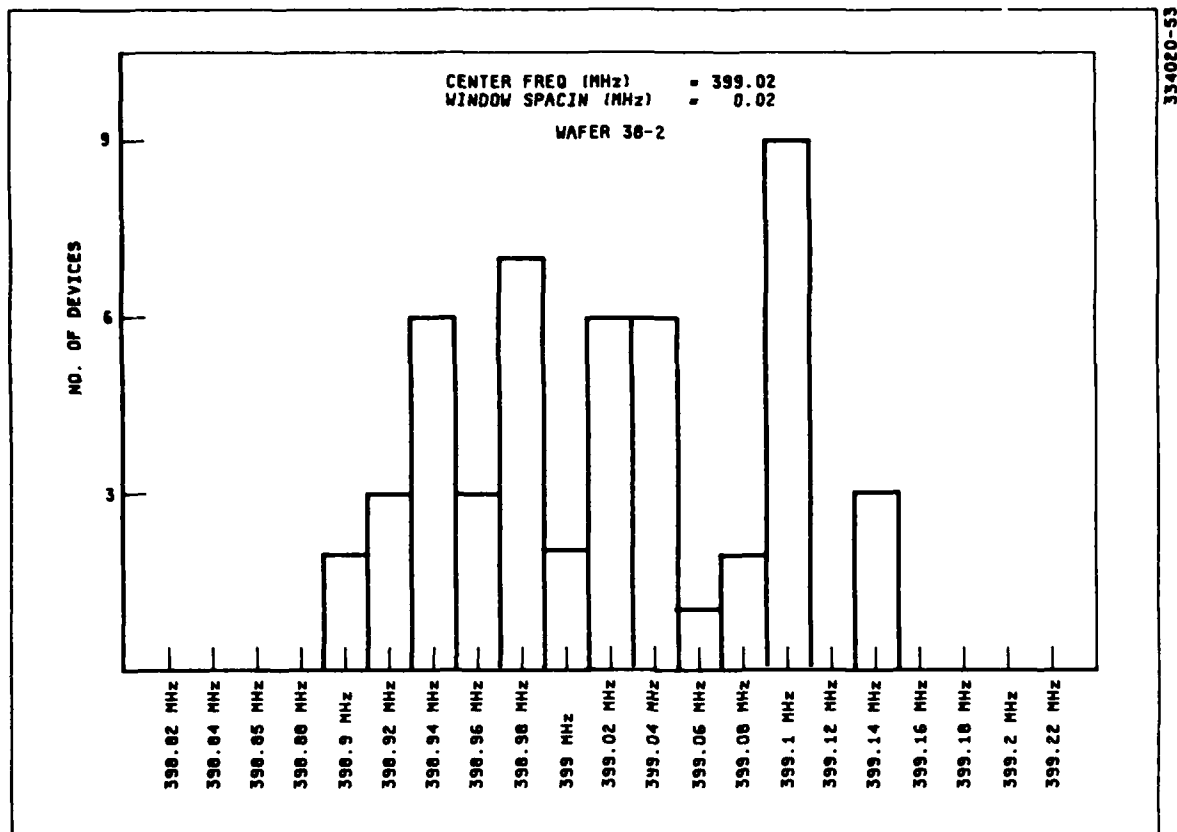


Figure 7.b. The number of die per 20 KHz window over the measured frequency range are presented.

TABLE 7.1. WAFER PROBE RESULTS FOR ENGINEERING PHASE RESONATORS

Wafer No.	Yield ( % )	$\bar{f}_0$ (MHz)	Std. Dev. (kHz)	$\bar{h}$ (Å)	$\Delta h/h$ (%)	$\bar{t}$ (Å)	$\Delta \bar{t}/\bar{t}$ (%)	$\bar{S}$ -	$\Delta \bar{S}/\bar{S}$ (%)
38-1	96	398.689	38	1440	4	1630	12	.93	22
38-3	65	398.788	54	1330	4	1740	7	.84	29
38-2	98	399.019	69	1340	6	1230	16	.93	22
9-7	92	399.049	82	1200	13	1460	20	.57	42
9-5	71	399.146	130	1190	8	1640	16	.34	103
9-8	75	399.153	90	1160	10	1540	6	.42	74
9-9	98	399.164	58	1150	9	1510	7	.43	33
9-11	100	399.201	64	1100	8	1230	15	.58	72

KEY:  $h$  = array groove depth  
 $t$  = metallization thickness  
 $s$  = strip/gap width ratio

$\bar{X}$  = denotes average value  
for designated parameter

the deposition parameter, the photolithography, and the etch processing must be carefully controlled. Wafers 1 and 2 exhibit the smallest frequency deviation about the computed average value, and it is also for these wafers that the etch depth, the metallization thickness and the aspect ratio show the smallest variation across the wafer surface. While still preliminary, it appears that in order to achieve, for example, a one sigma (1) standard deviation of better than 50 kHz, the array groove depth has to be controlled to better than 5%, while the transducer metallization thickness and linewidth require control to at least within 10% and 25%, respectively.

**7.3 Laser Trim Technique.** Ideally, a narrow band surface acoustic wave (SAW) device should be fabricated in a closed-loop system where the device performance is monitored in order to provide real time corrections to the fabrication process parameters. In practice because of the difficulty of making, in situ, RF measurements, SAW devices are typically manufactured open-loop, whereby no corrections are made to the fabrication process. Due to process variations, the SAW performance parameters exhibit total variations up to 400 ppm. Therefore, post-fabrication frequency trimming is generally required for narrow band devices, i.e., devices with bandwidths approaching the process variations.

Several techniques are available for trimming etched groove resonators including the use of deposited thin films<sup>[12]</sup> and realignment of the etch mask over the initial etched grating for use during a correction etch.<sup>[13]</sup> There are some problems associated with the above proposed approaches. The use of a dielectric overlay, first of all, tends to exacerbate aging effects and secondly, modifies the temperature stability of ST-cut, X-propagating quartz.<sup>[14]</sup> The use of additional masking steps results in a significant increase in fabrication difficulty due to the introduction of critical realignment steps. Moreover, it has been shown that etching the transducers of the resonator using reactive plasma etching

in  $\text{CF}_4$  and  $\text{O}_2$  produces frequency shifts which are the result of topological step height changes.[15]

Frequency shifts exceeding 50 ppm were still observed for the devices fabricated on this program following package seal. The cause of these frequency shifts remains to be determined, but it does appear that the thermal and mechanical stresses introduced during resistance welding the dual-in-line packages are transmitted to the SAW crystal. Improved mounting techniques can still be developed to further mechanically decouple the active device from the package header to achieve improved stability. However, a trim technique must ultimately be developed to use in high reliability applications where accurate frequency settability is required; furthermore, it is desirable for such a trim procedure to be compatible with automatic manufacturing techniques. One possibility proposes the use of a laser trimmer to open the shorted electrodes forming the rf shield between the transducer configuration. For the devices developed on this program, the trim capability using a laser will be established and the maximum frequency shift achievable will be assessed. The actual trim operation to final frequency value will be performed just prior to sealing the devices.

The effect of laser trimming (opening electrodes) in the shorted rf shield is estimated by assuming that the main effect is electromechanical coupling via surface shorting so that the fractional frequency shift per electrode opened is

$$\frac{\Delta f}{f} \approx \frac{k^2}{2} \cdot \frac{1}{2L_C}, \quad (1)$$

where  $L_C$  is the length of the resonator cavity.

For the present design, this is approximately 2.5 ppm/electrode. Figure 7.2 shows the result of the initial laser trim experiments performed using samples fabricated during the Engineering Phase. The average slope of the frequency shift observed is approximately 1 ppm for each electrode opened. However, as much as a 60 ppm shift was observed on one particular device. A substantial scatter in the data exists and this is largely attributed to measurement difficulty. These devices were mounted using the adhesive under the entire length of the crystal and therefore the mounted die was subject to stresses imparted to the resonator package.

Additional devices will need to be fabricated in order to better define the expected maximum frequency shift. In addition, it is predicted that the trend in frequency shift will be much more consistent for the samples mounted using only a small quantity of adhesive placed under the center of the die.

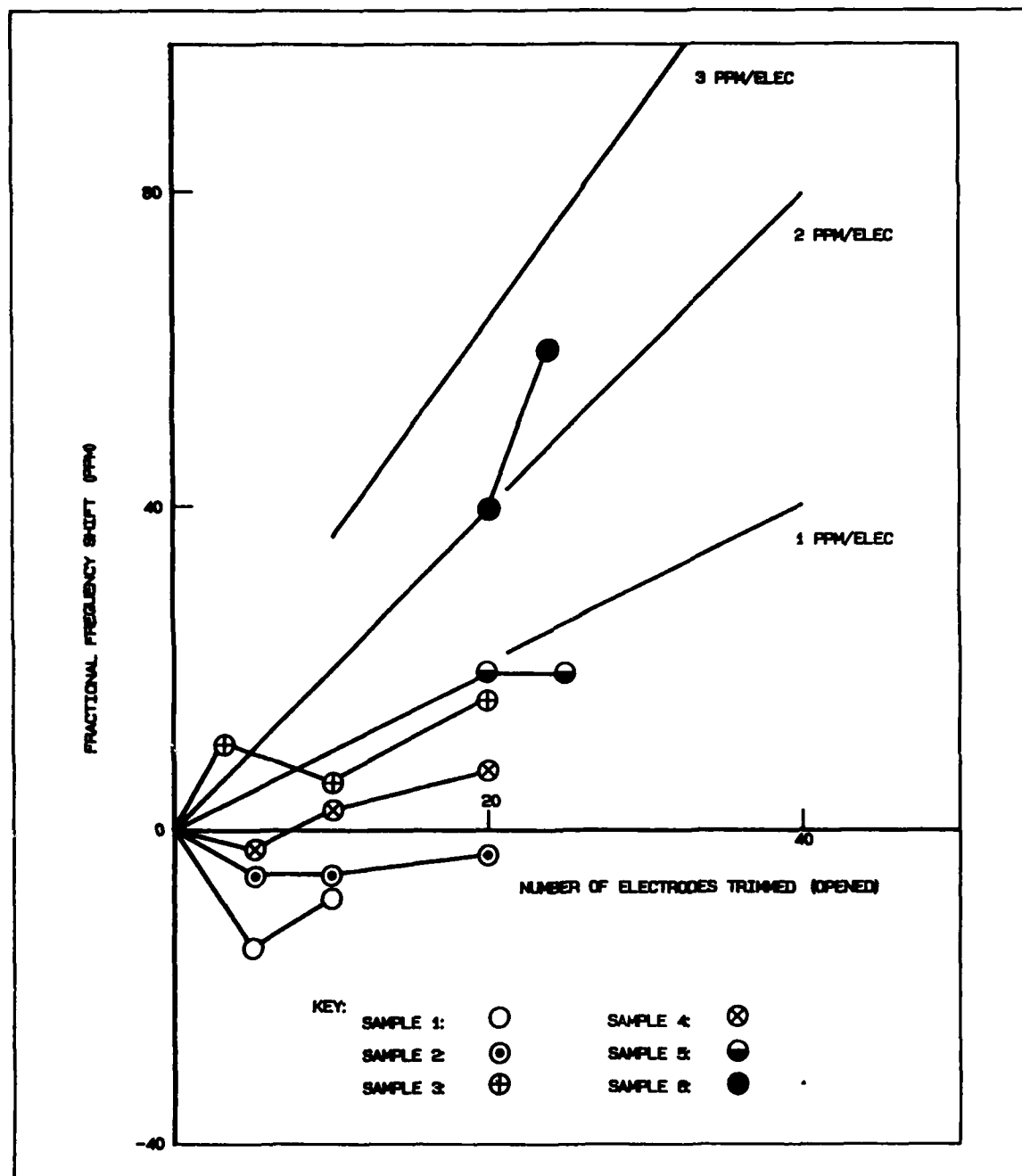


Figure 7.2. Fractional Frequency Shift as a Function of Opened Electrodes

## 8.0 CONCLUSIONS AND RECOMMENDATIONS

8.1 RAC Device. A review of the electrical data (Tables I and II, Appendix I) for the 10 RAC filters built during the Engineering Phase indicates that in some cases a large RMS phase error ( $9^\circ$ ) is still observed after application of the generic phase correction pattern. As a result, several RAC lines did not meet the required 25 dB time sidelobe specification (i.e. correlating against an ideal up-chirp matched filter) after a single correction. In addition, it was noted that several lines initially exhibited very large amplitude and phase distortion over the 60 MHz passband. The variations were, however, reduced to acceptable levels by subjecting the crystal to an additional surface etch using a normal solution of hydrofluoric acid.

Based on the above observation, it is concluded that the phase performance of the RAC lines can still not be predicted with a high degree of confidence. As a result, preliminary testing will still be required on the uncompensated crystal - an operation that is undesirable in the production phase. Therefore, an additional engineering effort will be directed toward further understanding the phase deviation characteristic and its dependence on the crystal's active surface state, both prior to processing and after the groove forming and rejuvenation step.

It is planned to measure the RAC phase response on the uncompensated crystal for at least six of the 18 Confirmatory Sample Phase filters. For several crystals, the entire surface will be uniformly ion beam etched prior to metallization and photolithographic processing of the transducer and reflective array configuration. Subsequent measurements are expected to indicate whether a surface pre-etch will improve both the magnitude of the phase amplitude response as well as provide an improved unit-to-unit passband characteristic. The wafers to be used on this phase of the program will be selected from the same boule of lithium niobate. Furthermore, careful tracking of the individual crystal die will be performed through the cleaning, the dry etch, and the oxygen enriched rejuvenation process steps. It is anticipated that at the end of the Confirmatory Sample Phase, where 18 additional devices will be fabricated, a good understanding of the reproducibility of the phase error response will have been obtained and an improved generic phase correction pattern can be generated for use on the pilot production units.

The RAC lines fabricated to date have all been phase compensated with a thin aluminum strip that is transferred to the crystal surface using a "lift-off" technique. This method will also be employed on the Confirmatory Sample Phase devices. For the devices to be fabricated during Pilot Production, the generic phase compensation pattern will be incorporated into the master photomask and will therefore be transferred to the crystal die along with the transducer and the reflective array configuration. Since this pattern will be comprised of a much thicker metal strip than what was previously employed using "lift-off", an evaluation must be performed to assure that the change in the surface acoustic wave velocity does not

adversely affect the phase compensation characteristic. The analysis will be performed during the Confirmatory Phase, and a sample device will be fabricated and evaluated using a thick pattern.

A key effort during the Engineering Phase was directed toward simplifying the existing RAC filter package. In particular, it was demonstrated that a nominal 50 dB feedthrough suppression level can be achieved without the notch placed in the crystal die between the input and output transducers and the accompanying septum machined into the housing frame. As a result, a more reliable device can be fabricated for operation over military environments. Furthermore, the manufacturing cost has been largely reduced since the crystal fabrication and package seal and rework steps are greatly simplified.

To date, only a small quantity of devices have been built employing the new housing design. In all cases, the measured feedthrough levels have been near the 50 dB value. Additional engineering tasks are planned to increase the margin by several dB above 50 dB. Specifically, experiments will be performed replacing the simple series inductors at both the input and output ports with transformers. Other planned experiments will employ modifications in the cover for the crystal cavity. For example, a grooved structure and also a selectively plated geometry using a high resistivity material will be considered. Both approaches are designed to attenuate and modify anomalous field patterns existing in the crystal cavity.

**8.2 Resonator Device.** A review of the data presented in Chapter 7 on the Trim Development and Evaluation effort for the resonator indicates that several activities have not been completed. In particular, wafer level yields have not been entirely established, and the final frequency trim technique using a small spot size laser beam has not been fully established.

The summary data of Table I and the associated histograms in Section 7.2 demonstrate that yields at the wafer level are strongly dependent on the degree of control possible for the deposition and photolithographic parameters using production equipment and processing practices. Additional wafers will be processed and analyzed before a definitive production oriented yield figure can be established. The engineering effort on the proposed trim technique has also not been completed. The samples tested so far have not provided sufficient information to 1.) demonstrate repeatability, 2.) establish a maximum frequency shift capability, and 3.) characterize the trim effect on the resonator's feedthrough suppression performance. As a result, additional engineering efforts on both the activities discussed above will continue during the Confirmatory Sample Phase. In particular, the following tasks are planned:

**Task 1: Wafer Level Yield Evaluation.** It is proposed to process an additional set of 2 x 2 inch wafers, each containing 50 individual resonator die. Pattern delineation will be accomplished using the existing photomask. The grooved depth for the reflective array will be selected based on the data analyzed

on previous wafers. The fabricated wafers will be probed for center frequency and subsequently analyzed again for groove depth variation, metallization thickness and stripe-to-gap width control. Actual yield data will be presented as a histogram depicting the number of yielded die per 20 kHz frequency interval.

Task 2: Laser Trim Development. Using die from wafers previously processed and evaluated, several devices will be assembled. A trim evaluation will be performed on both untuned and series tuned crystals. In order to fully understand the maximum achievable frequency shift and its dependence on feedthrough, the experiments must also be performed on several untuned resonators. Package size considerations, stringent control of distributed parasitic capacitance and the inherent close proximity of the input transducer relative to the output transducer, require the tuning elements at both ports to be similarly placed close to each other. It is suspected that their finite size introduces signal cross-coupling effects and, as a result, the device feedthrough level is largely controlled by these elements. Experimentation with untuned devices will eliminate this effect and will demonstrate clearly the dependence of maximum frequency shift on signal suppression.

APPENDIX A  
TEST DATA FOR ENGINEERING PHASE RAC FILTERS



TABLE I. ENGINEERING PHASE I RAC FILTER TEST DATA

Parameter	Units	#1		#2		#4		#5		#6	
Insertion Loss*	dB	37	36.5	39	38.5	40	38.5	39	40	40.5	39
Center Frequency	MHz	200.7	200.7	200.7	200.4	200.5	200.4	200.4	200.5	200.5	200.4
3 dB Bandwidth	MHz	60.2	60.2	60.2	60.7	60.5	60.5	60.5	60.9	60.5	60.5
F <sub>0</sub> Delay	sec	35.34	35.29	35.93	35.34	35.35	35.30	35.95	35.30	35.32	35.96
Dispersive Delay	sec	59.9	60.0	60.0	60.1	60.2	59.6	60.3	60.5	60.3	60.4
RMS Phase Deviation	Deg	19.7	9.0	6.1	10.0	8.1	8.9	3.4	8.7	14.9	3.7
Sidelobe Suppression**	dB	-	24	29	28.5	28.5	26	32	24.5	18	32
Feed-Through Supp.	dB			50				50		50	50
Spurious Echo Supp.	dB			-				-		-	-
VSMR***	-			1:3.3				1:2.8		1:2.8	1:2.5

\* Insertion loss values obtained by averaging over passband.

\*\* Sidelobe level when correlated against ideal up-chirp.

\*\*\* Measurements performed at f<sub>0</sub>.

TABLE II. ENGINEERING PHASE II RAC FILTER TEST DATA

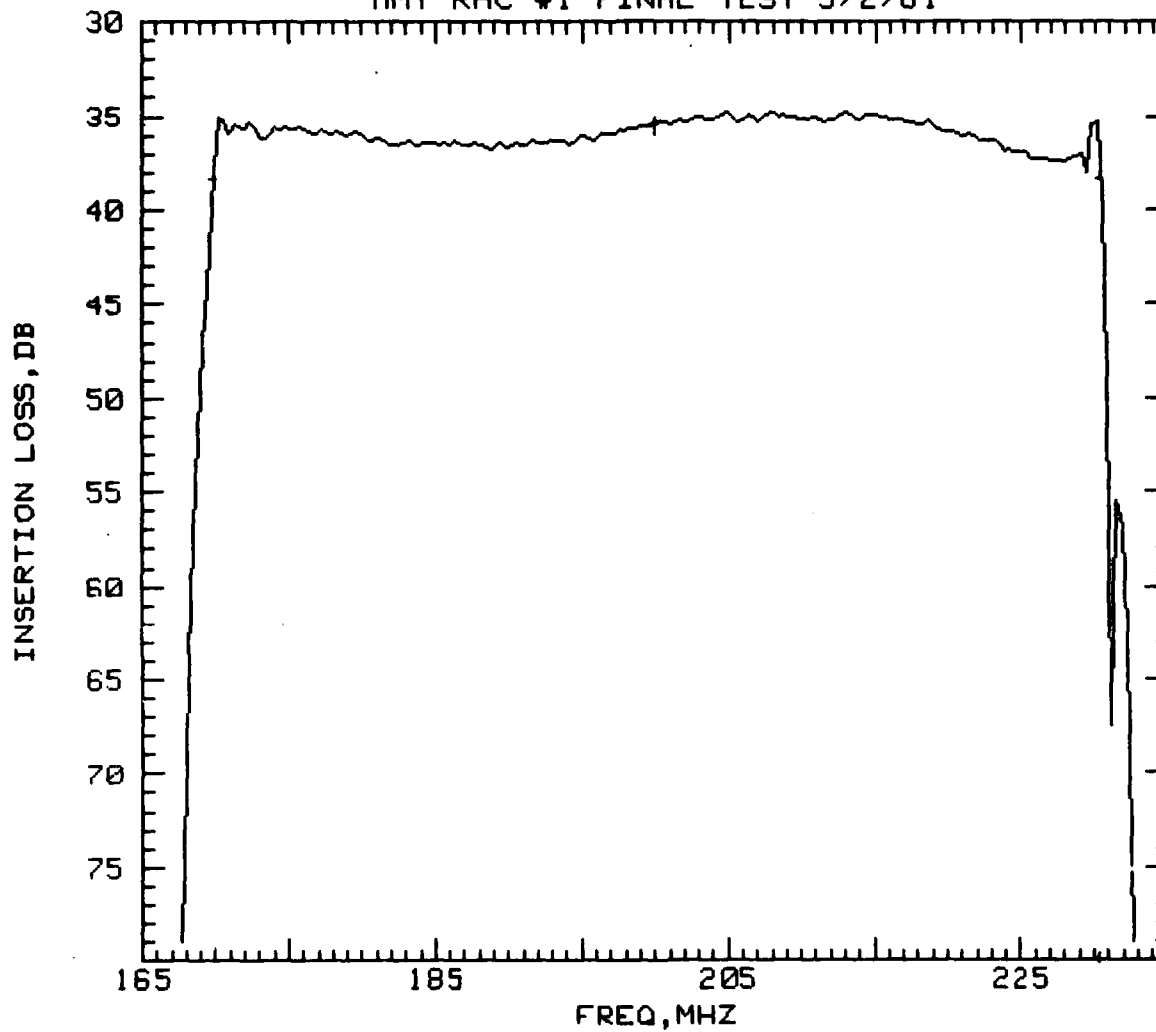
Parameter	Units	#8		#9		#10		#11		#12	
		1	2	1	2	1	2	1	2	1	2
Insertion Loss*	dB	36	36	36	37	35.5	36.0	37.5	36.0	36.5	36.0
Center Frequency	MHz	200.5	200.6	200.4	200.2	200.5	200.5	200.7	200.6	200.6	200.6
3 dB Bandwidth	MHz	60.7	60.9	60.7	60.6	61.0	61.1	60.8	60.9	61.0	61.1
F <sub>0</sub> Delay	sec	36.00	36.02	35.33	36.03	35.31	36.00	35.31	36.02	35.32	36.03
Dispersive Delay	sec	60.4	60.6	60.4	60.3	60.8	60.8	60.5	60.6	60.8	60.8
RMS Phase Deviation	Deg	14.8	2.8	4.3	4.5	17.7	2.8	15.0	8.7	7.7	3.6
Sidelobe Suppression**	dB	19	37	37	30	26	35	29	33	19	30
Feed-Through Supp.	dB	-	62	-	61	62	55	54	44	48	53
Spurious Echo Supp.	dB	-	65	-	65	65	70	60	60	55	60
VSWR***	-	1:7.3	1:7.0	1:5.0	1:5.2	1:6.0	1:5.3	1:5.8	1:5.7	1:5.5	1:5.7

\* Insertion loss value obtained by averaging over passband.

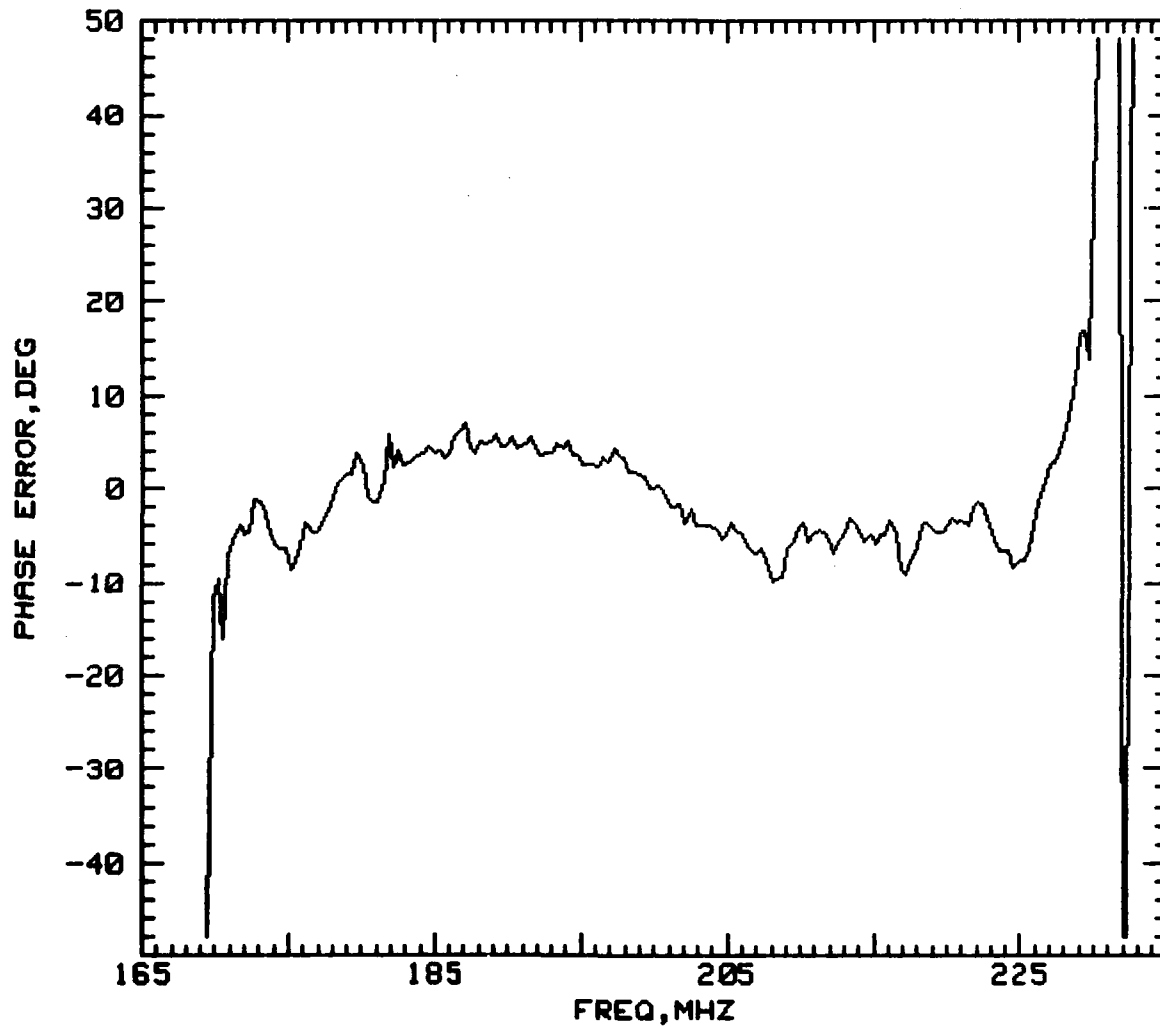
\*\* Sidelobe level when correlated against ideal up-chirp line.

\*\*\* Maximum measured value over passband.

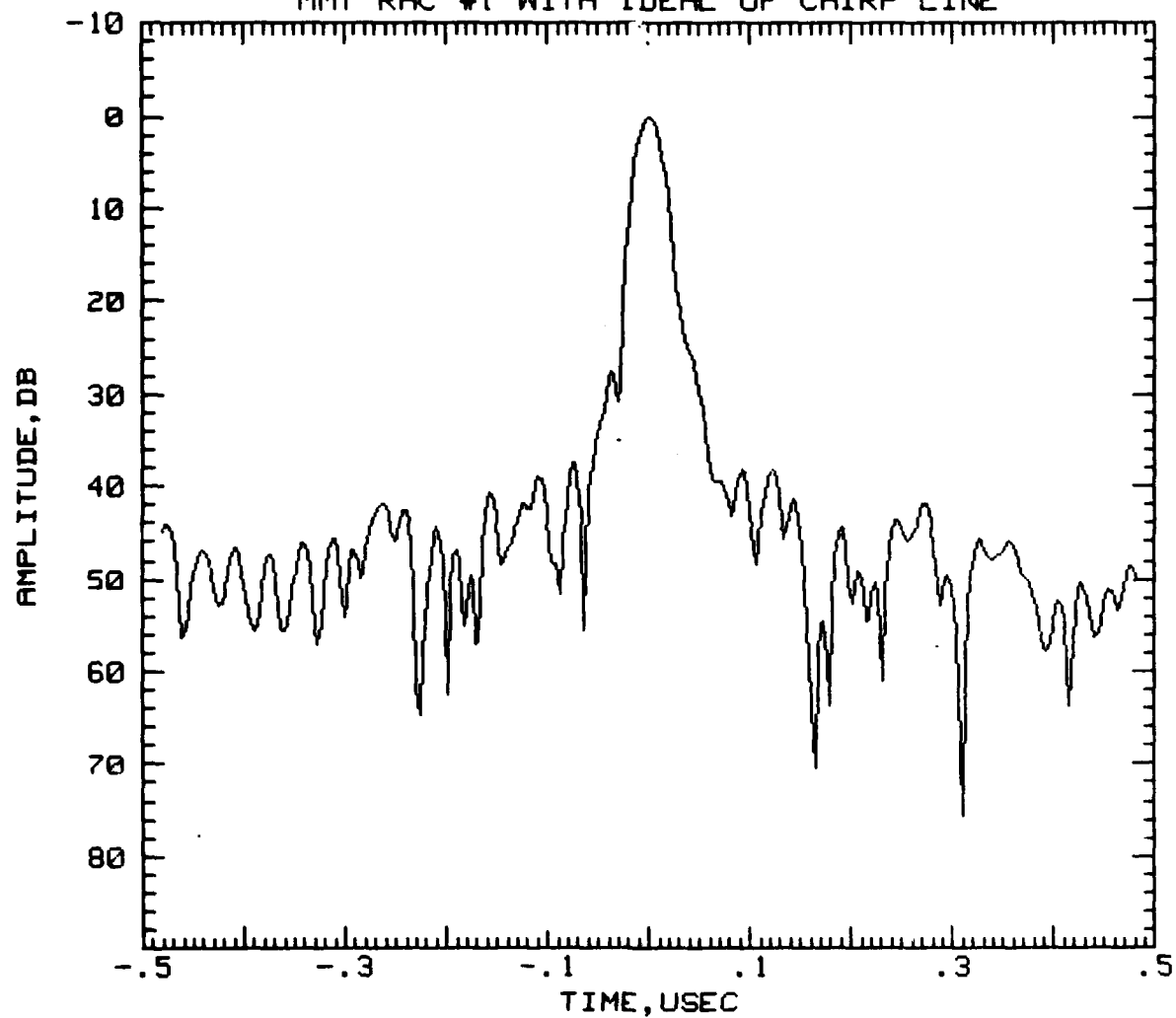
MINIMUM INSERTION LOSS= 34.76 DB AT F= 207.7 MHZ  
MMT RAC #1 FINAL TEST 5/2/81



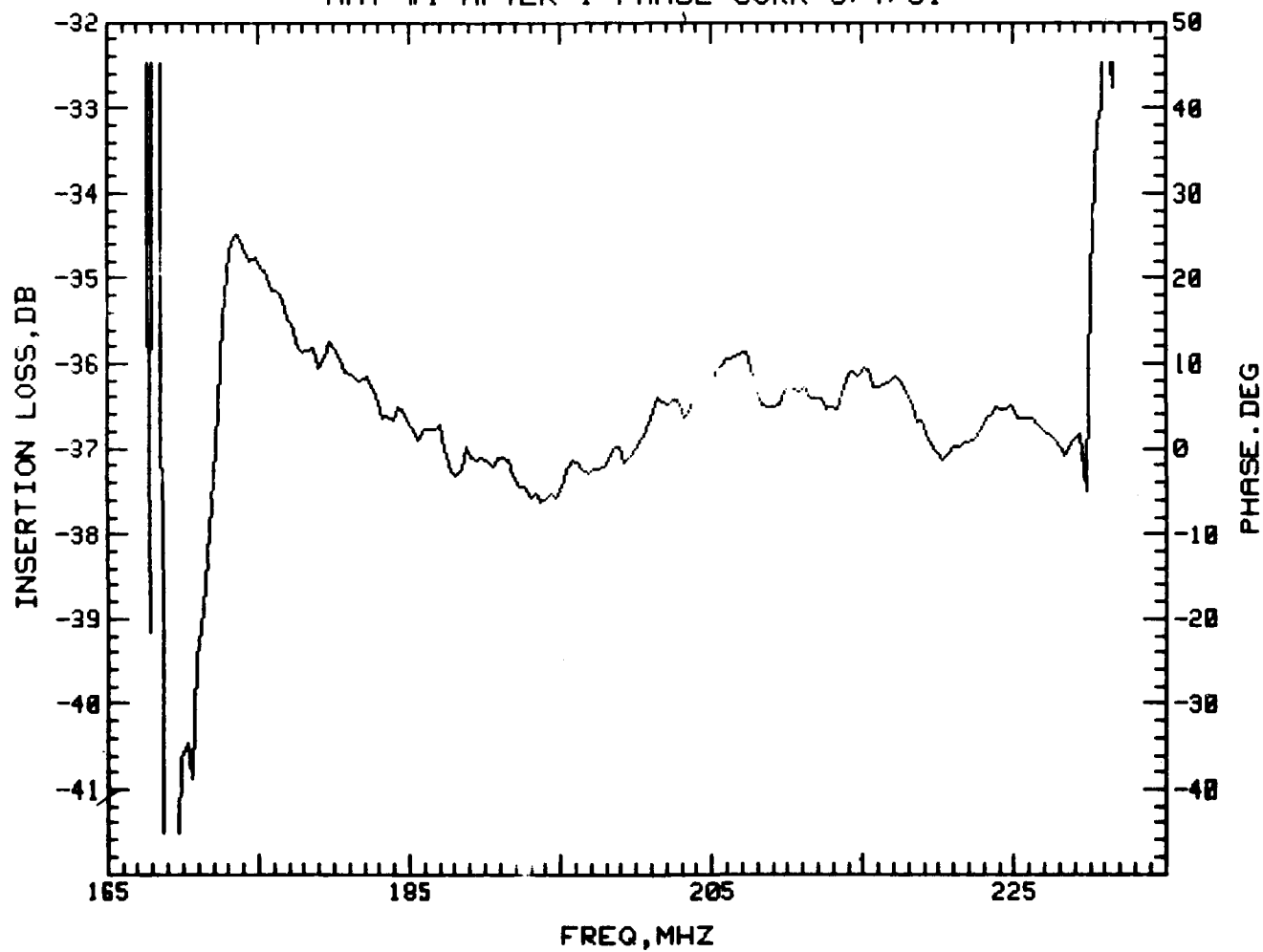
LINEAR      QUAD      RMS      F1      F2  
35.31590 -4.98041E-01      6.11      170.00      230.00  
MMTR1 RETUNED AFTER 2 PHASE CORR



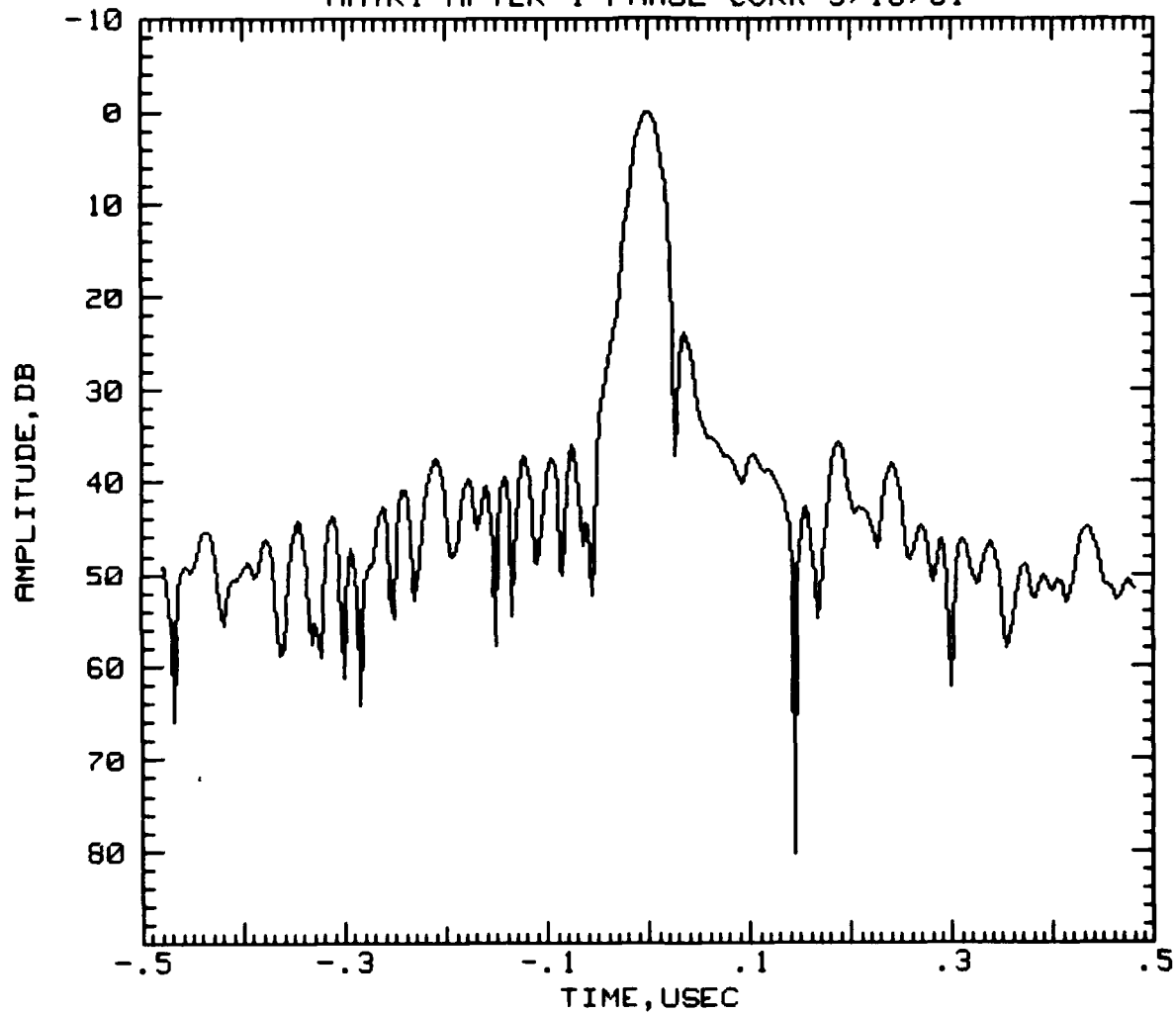
PEAK AMPLITUDE IS = 1.51367 ABSOLUTE  
SIGNAL TO NOISE RATIO IS= -1.29942714183 DB  
MMT RAC #1 WITH IDEAL UP CHIRP LINE



LINEAR      QUAD      RMS      F1      F2  
35.28990 -4.98243E-01      9.01      170.00      230.00  
MMT #1 AFTER 1 PHASE CORR 3/4/81



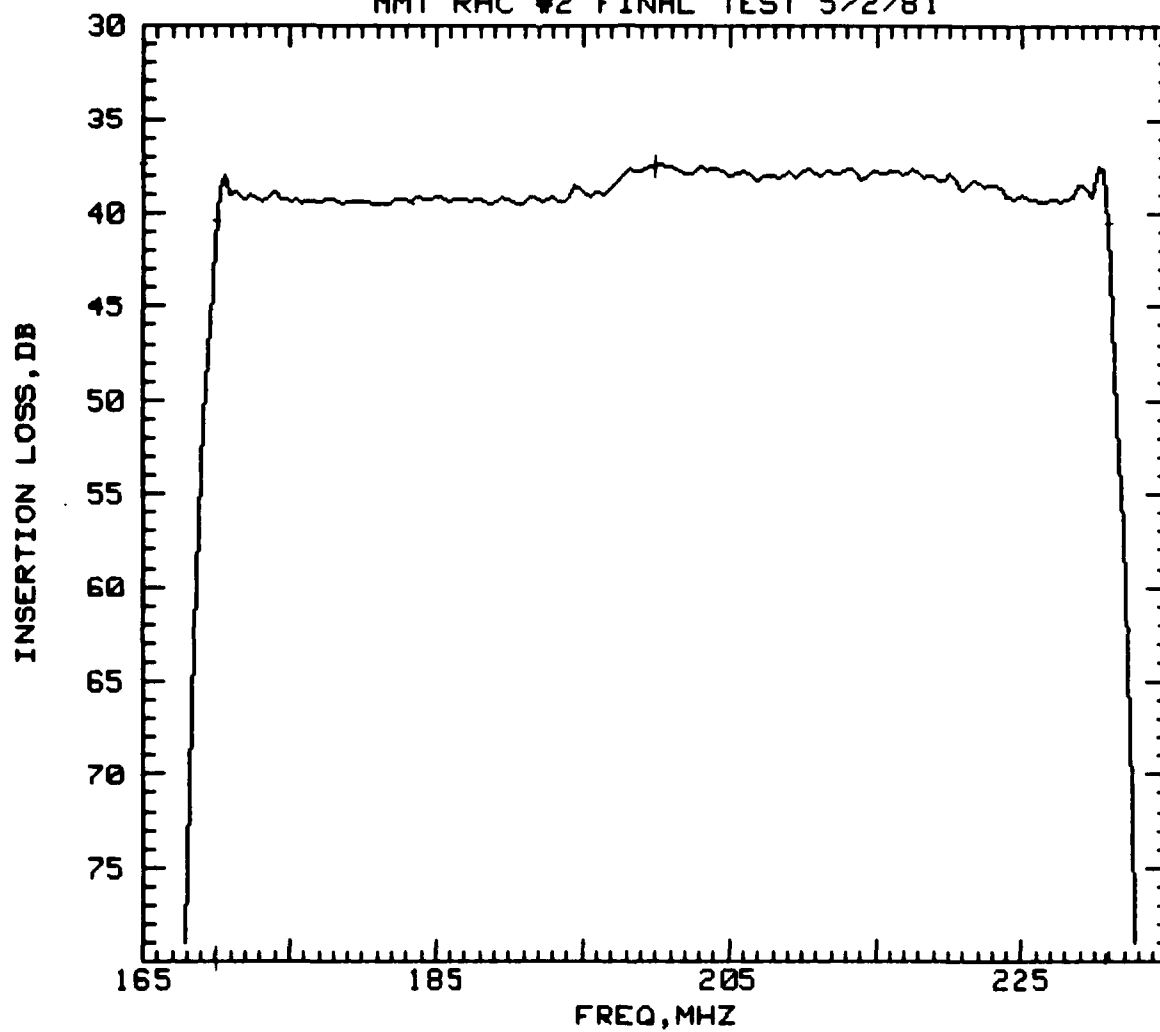
PEAK AMPLITUDE IS = 1.43759 ABSOLUTE  
SIGNAL TO NOISE RATIO IS= -1.58363015986 DB  
MMTR1 AFTER 1 PHASE CORR 3/18/81



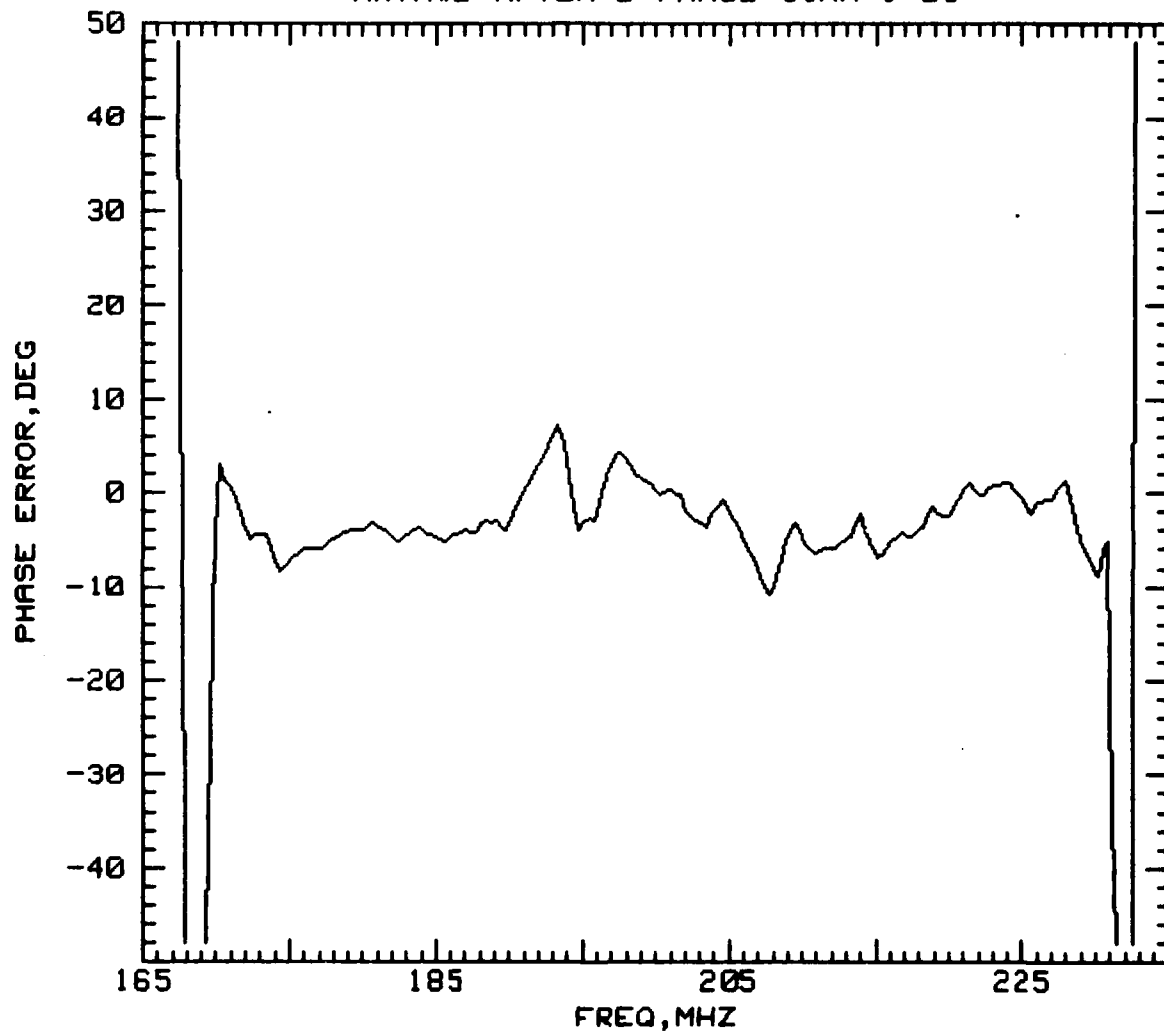
TEST DATA FOR S/N 2 RAC FILTER



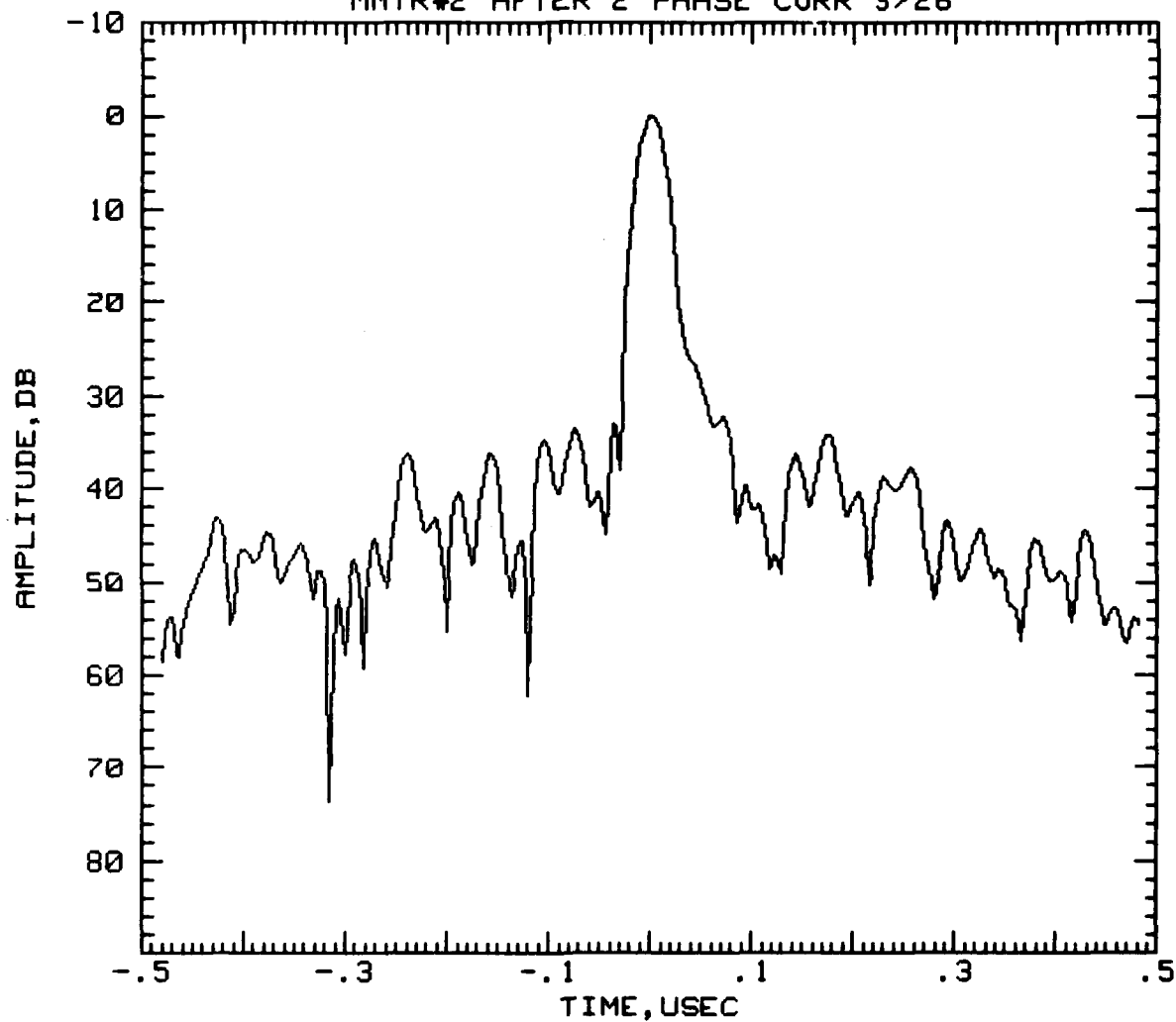
MINIMUM INSERTION LOSS= 37.42 DB AT F= 200.35 MHZ  
MMT RAC #2 FINAL TEST 5/2/81



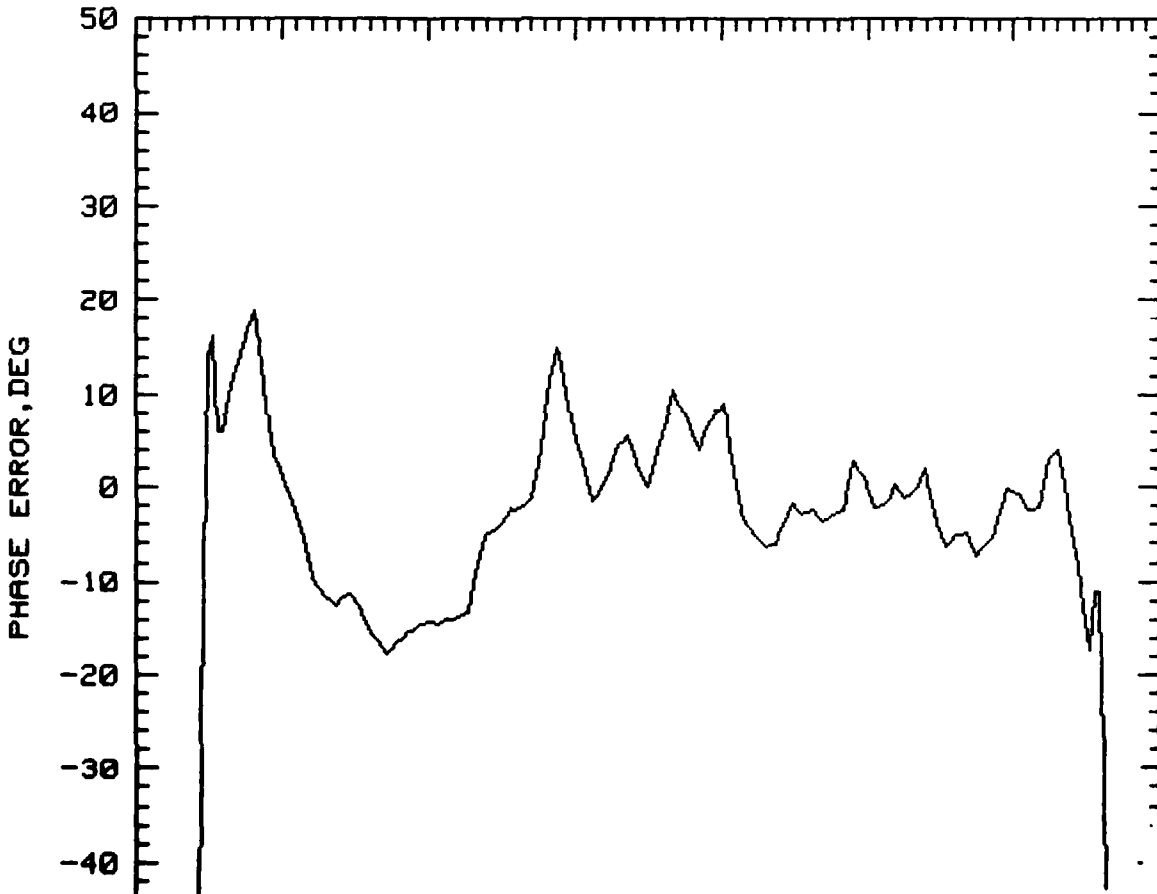
LINEAR      QUAD      RMS      F1      F2  
35.34751 -4.97903E-01      3.95      170.00      230.00  
MMTR#2 AFTER 2 PHASE CORR 3/25



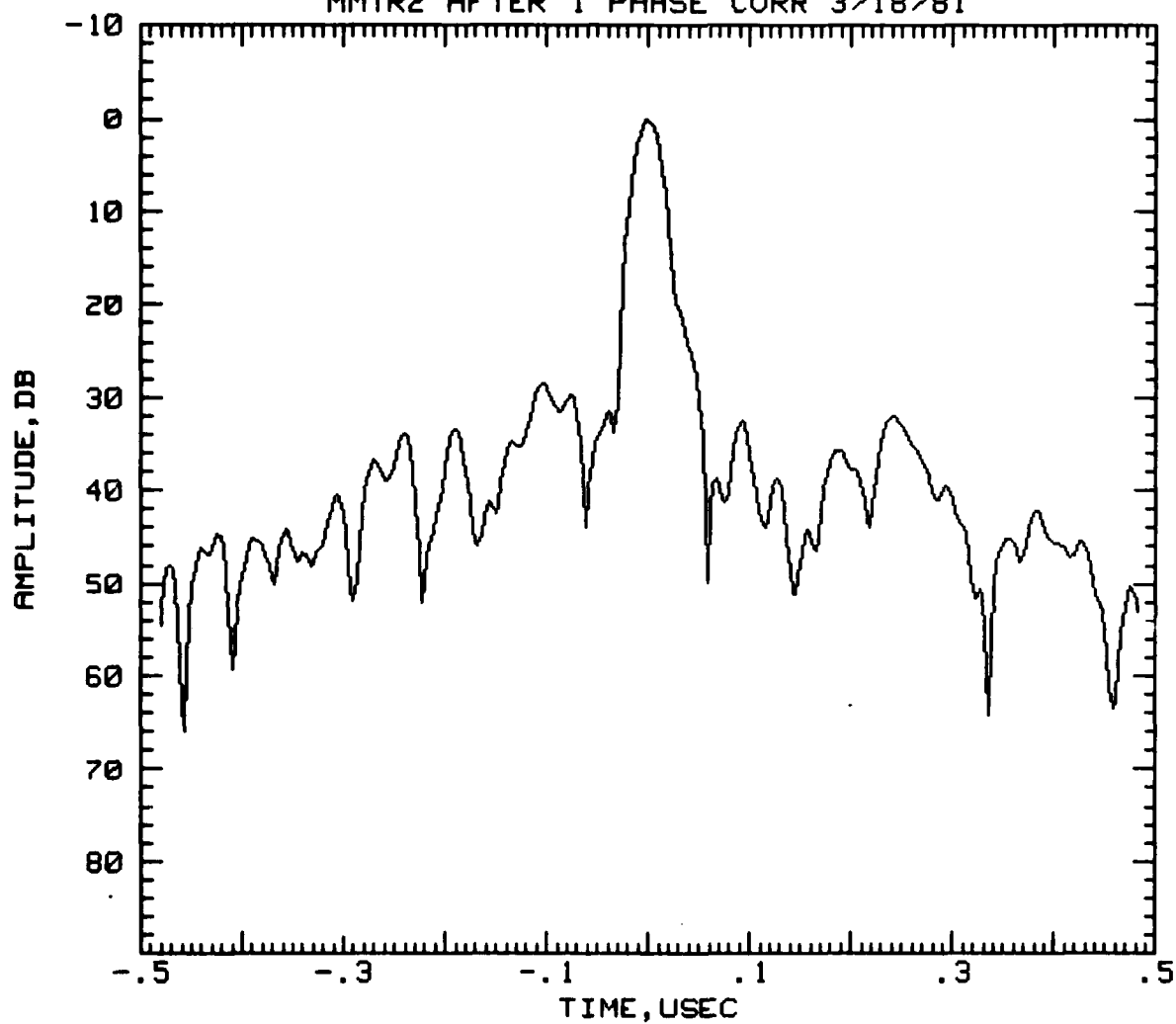
PEAK AMPLITUDE IS = .953778 ABSOLUTE  
SIGNAL TO NOISE RATIO IS= -1.56332697287 DB  
MMTR#2 AFTER 2 PHASE CORR 3/26



LINEAR	QUAD	RMS	F1	F2
35.34519	-4.97970E-01	8.12	170.00	230.00
MMT #2 AFTER 1 PHASE CORR 3/6/81				



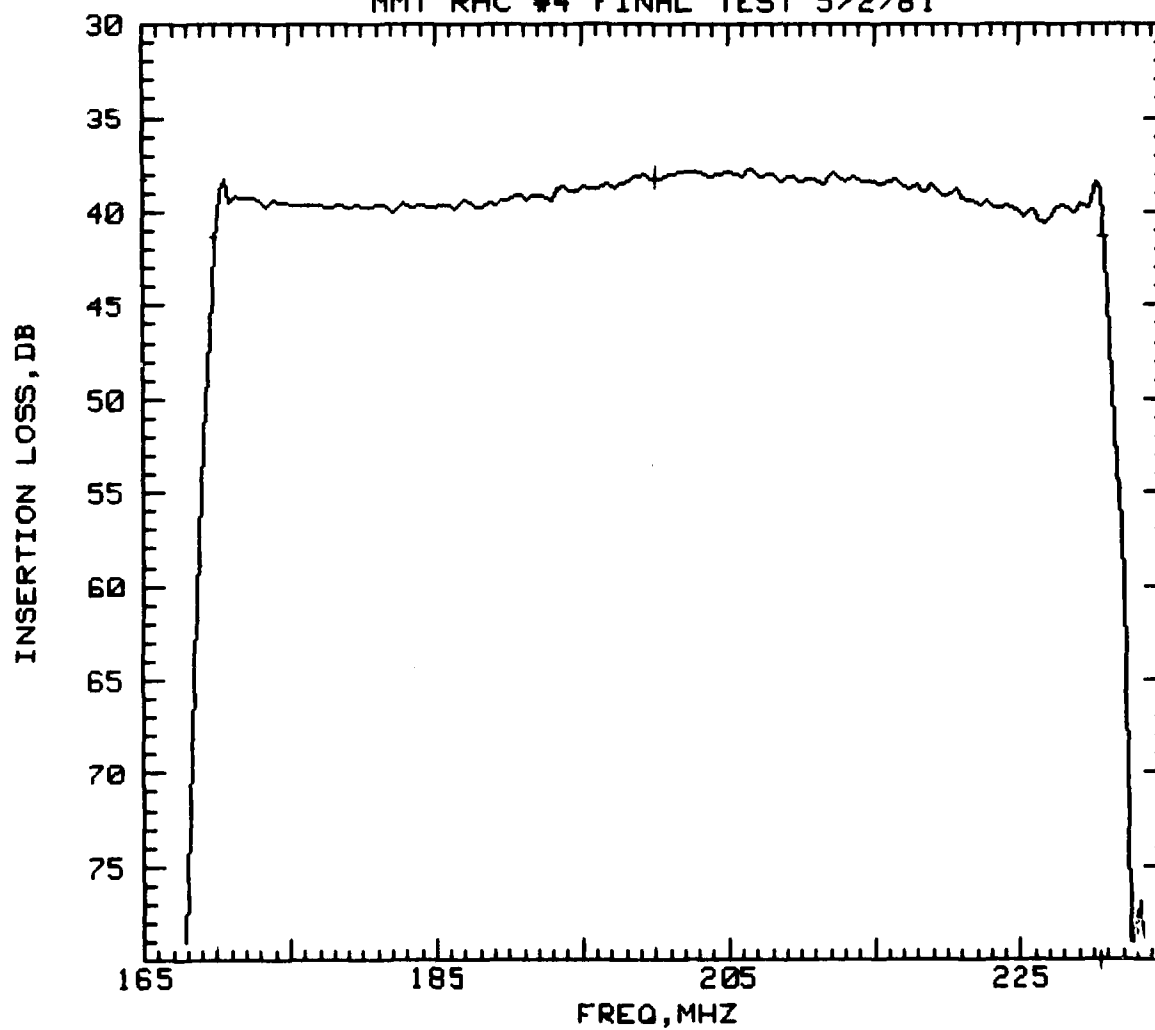
PEAK AMPLITUDE IS = .900274 ABSOLUTE  
SIGNAL TO NOISE RATIO IS= -1.70017119199 DB  
MMTR2 AFTER 1 PHASE CORR 3/18/81



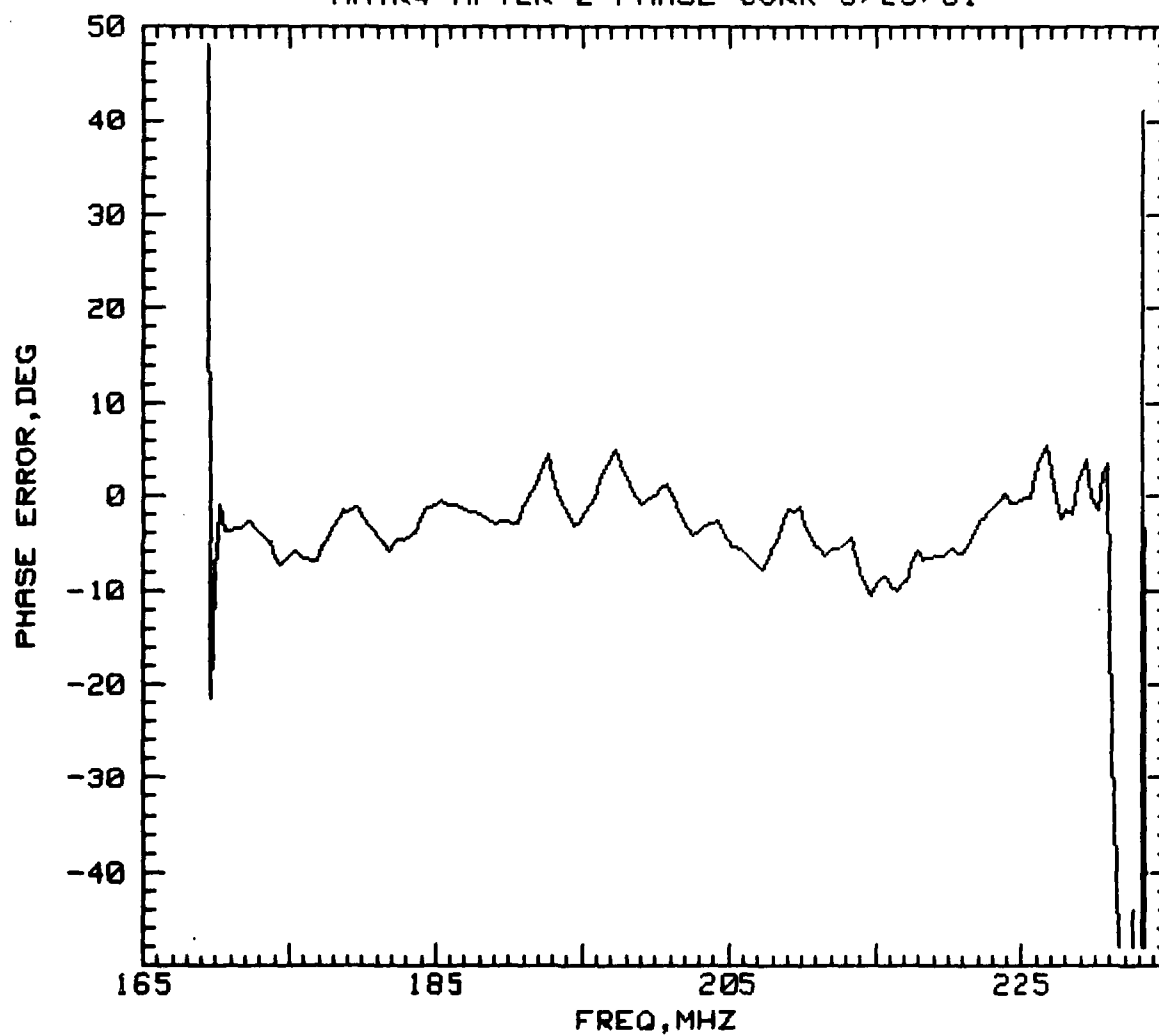
TEST DATA FOR S/N 4 RAC FILTER)

MINIMUM INSERTION LOSS= 37.76 DB AT F= 206.3 MHZ

MMT RAC #4 FINAL TEST 5/2/81

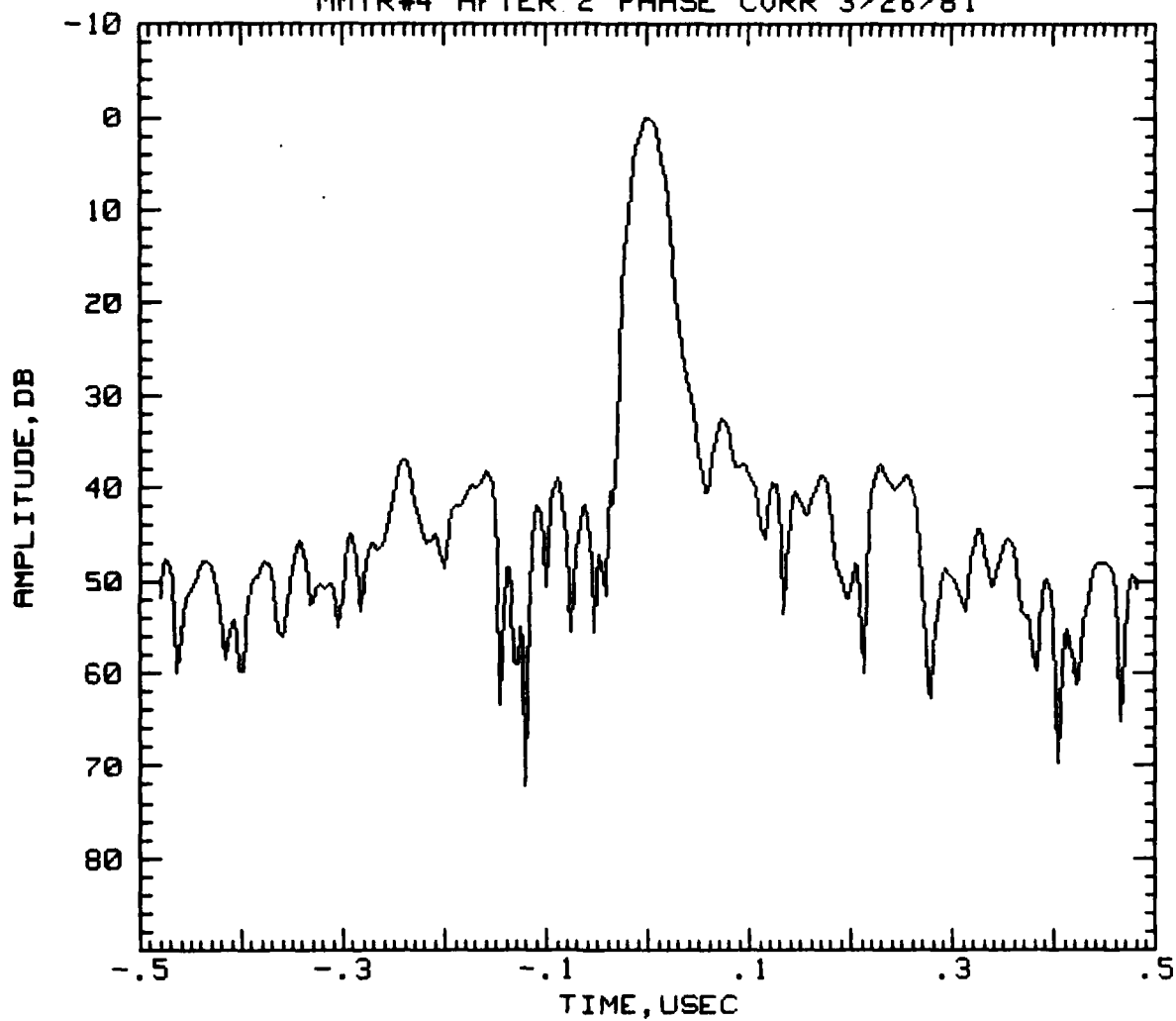


LINEAR      QUAD      RMS      F1      F2  
35.34181 -4.98076E-01      3.40      170.00      230.00  
MMTR4 AFTER 2 PHASE CORR 3/25/81

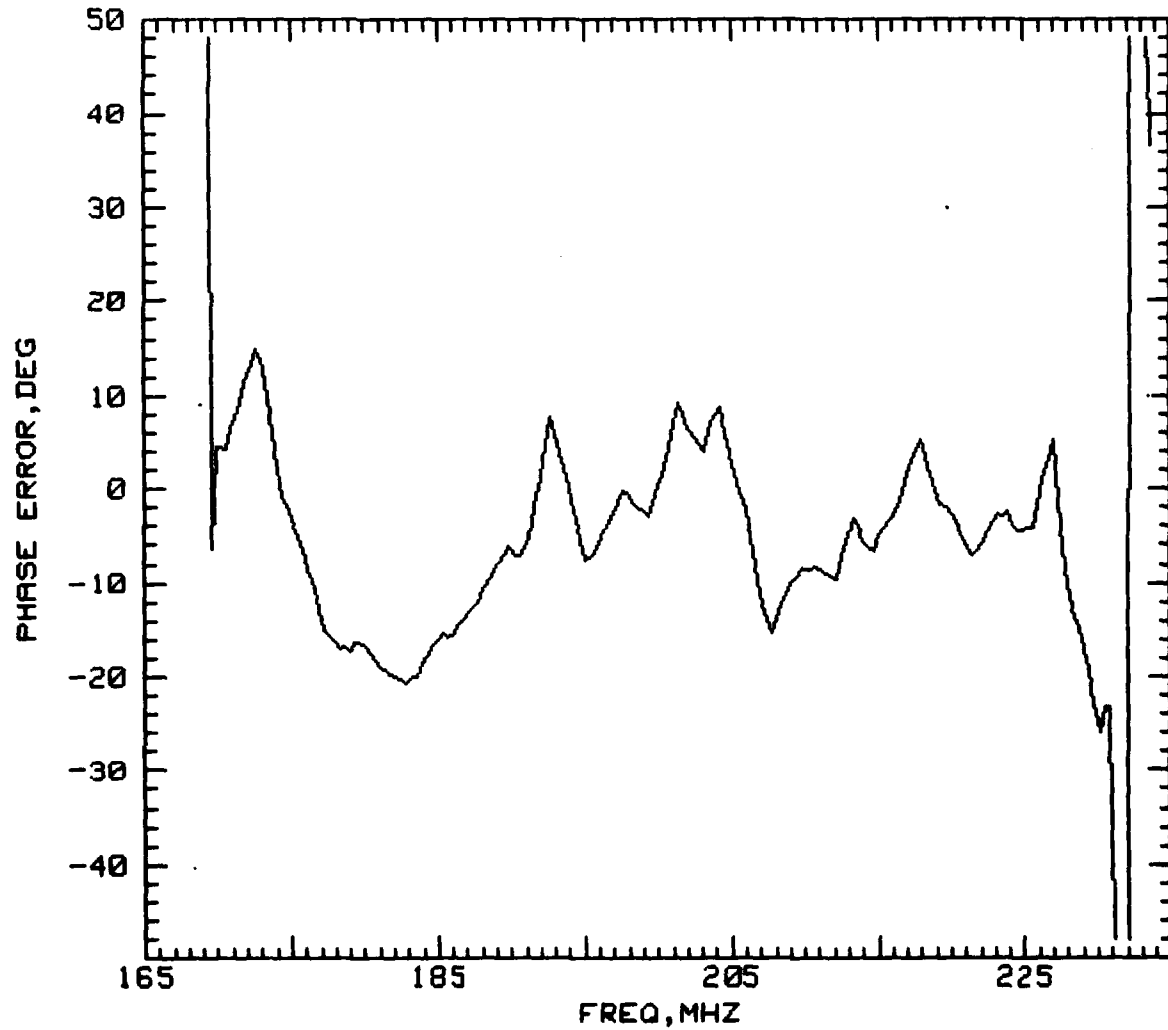




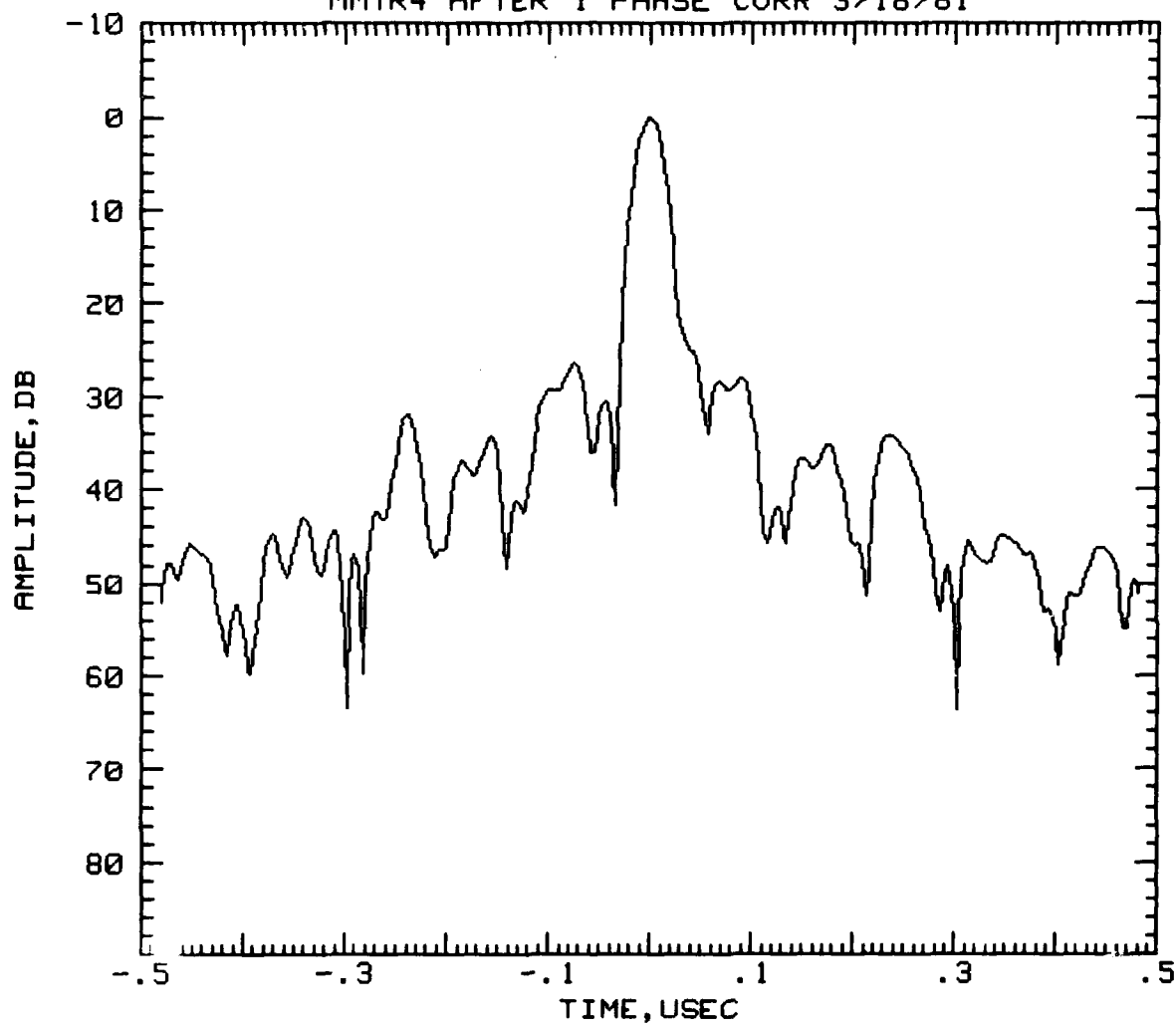
PEAK AMPLITUDE IS = 1.03797 ABSOLUTE  
SIGNAL TO NOISE RATIO IS= -1.28846642807 DB  
MMTR#4 AFTER 2 PHASE CORR 3/26/81



LINEAR      QUAD      RMS      F1      F2  
35.29643 -4.98270E-01      8.88      170.00      230.00  
MMT #4 AFTER 1 PHASE CORR 3/6/81

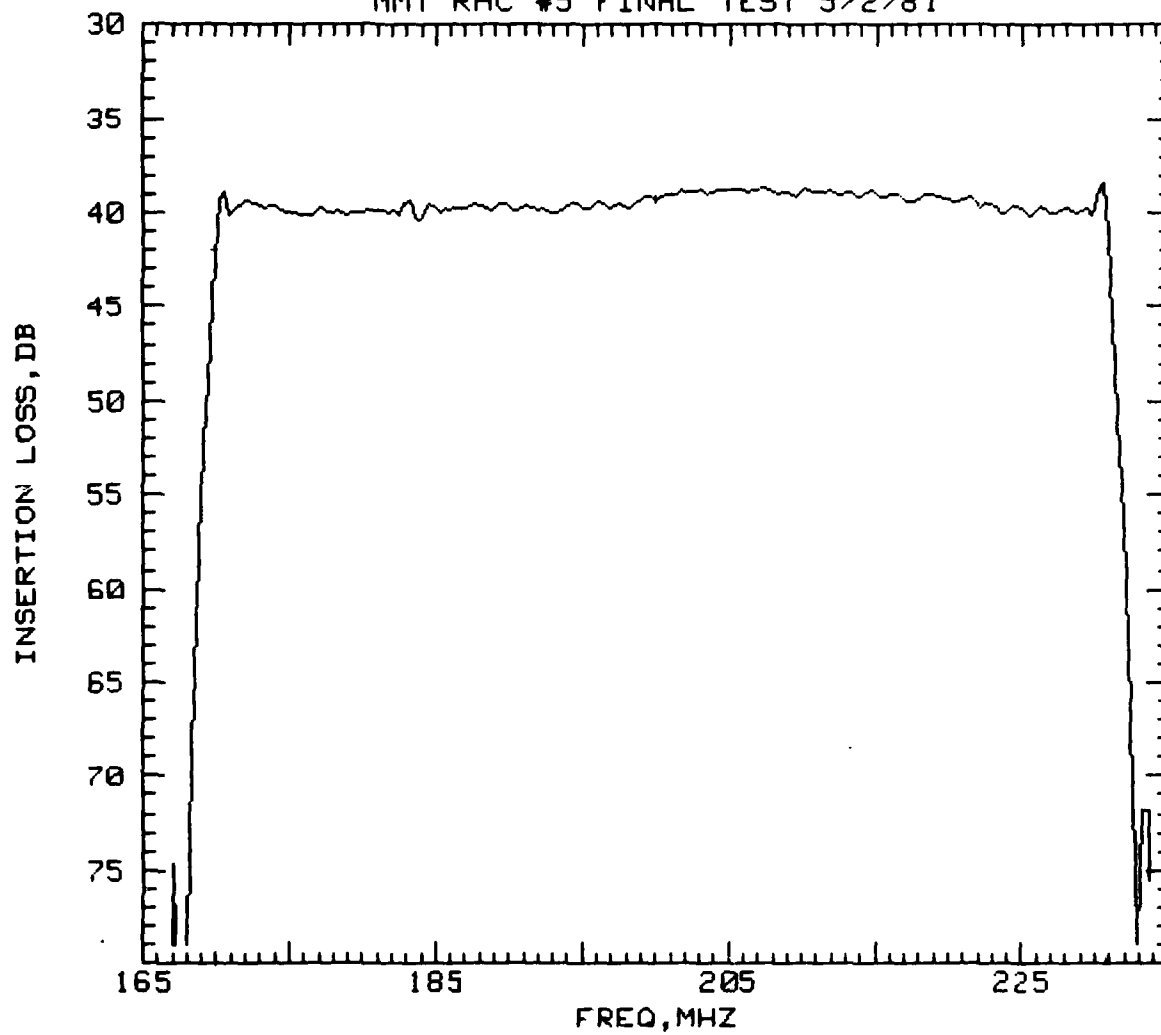


PEAK AMPLITUDE IS = .981859 ABSOLUTE  
SIGNAL TO NOISE RATIO IS= -1.33871560112 DB  
MMTR4 AFTER 1 PHASE CORR 3/18/81

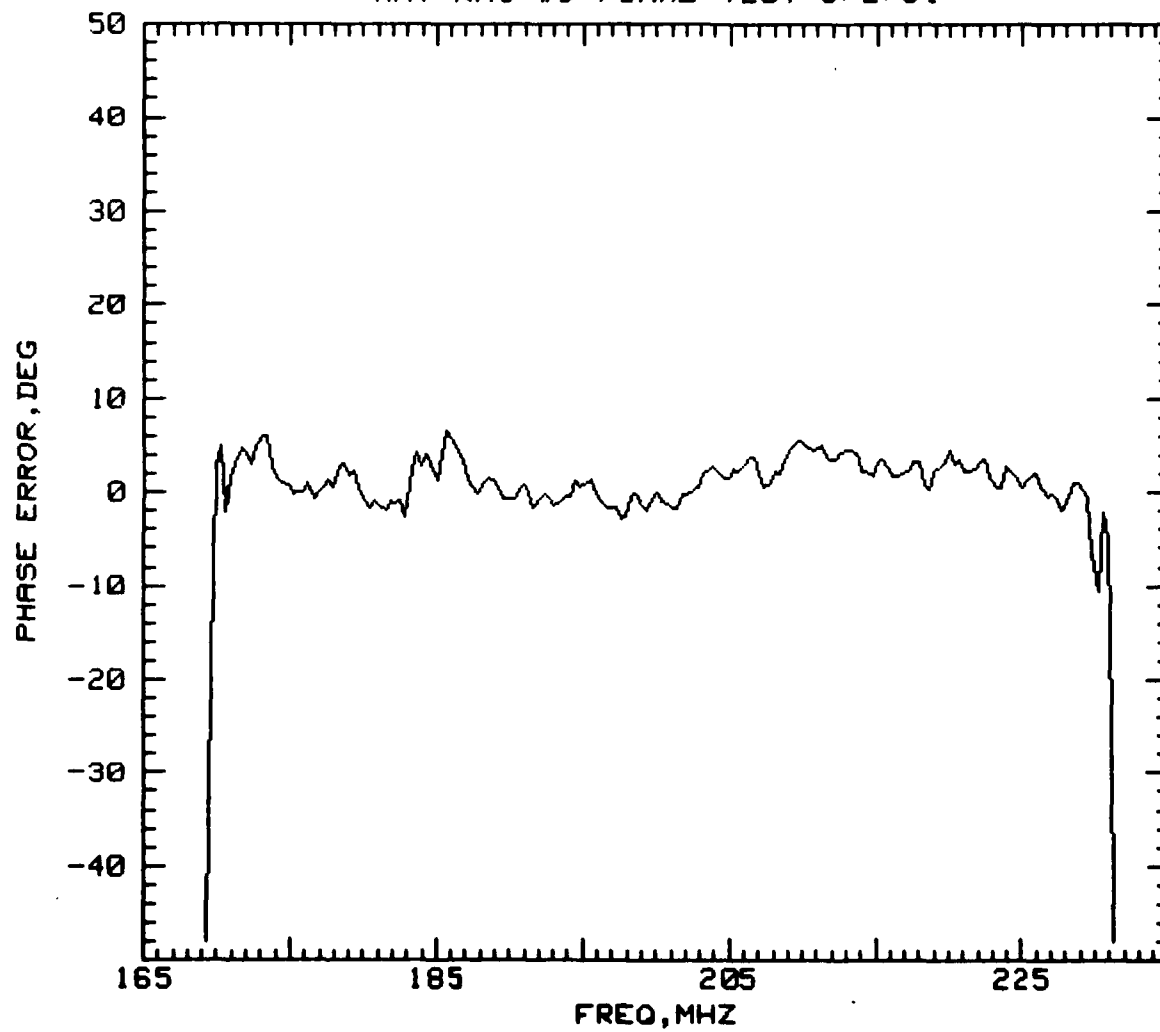


TEST DATA FOR S/N 5 RAC FILTER

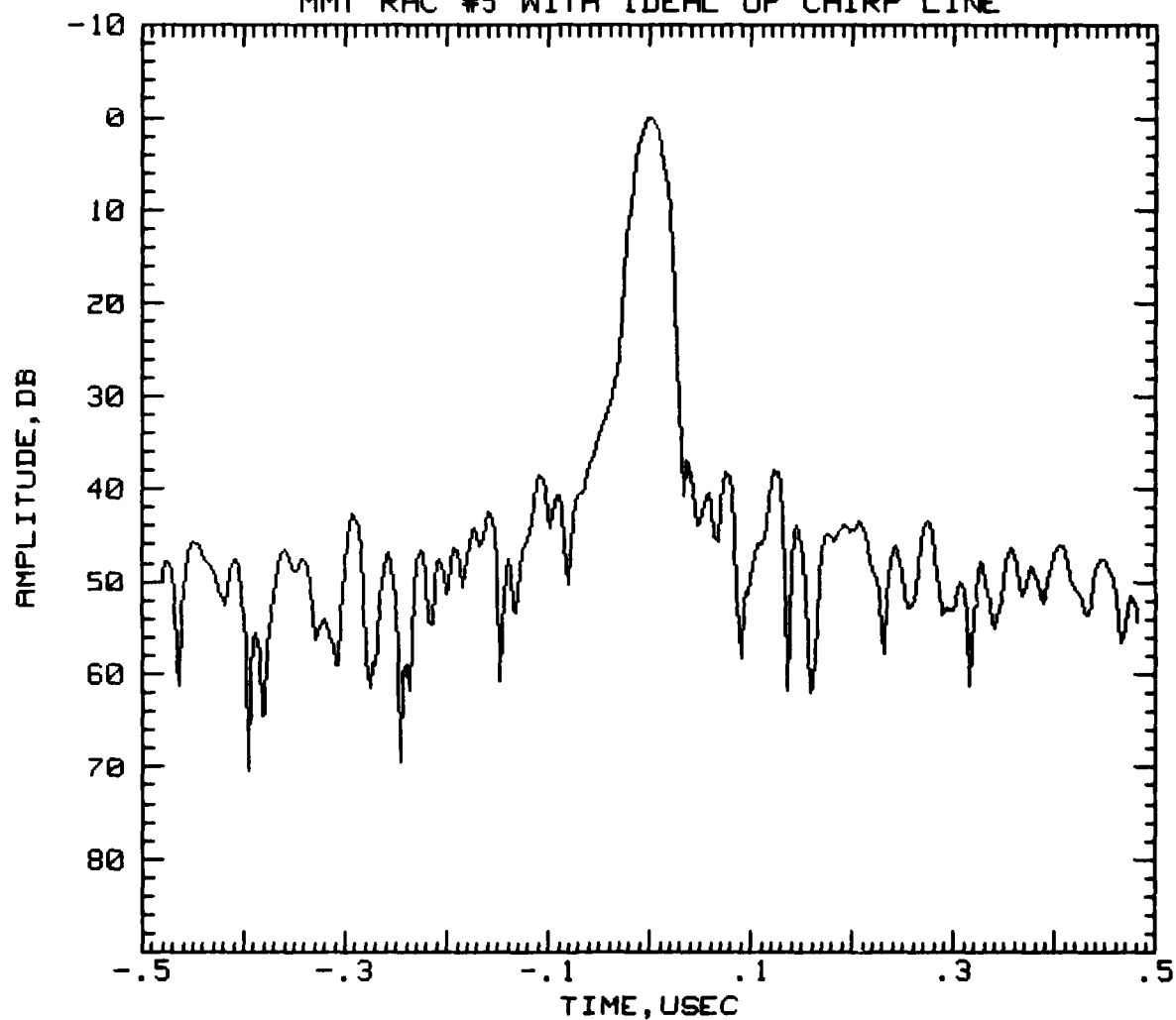
MINIMUM INSERTION LOSS= 38.36 DB AT F= 230.45 MHZ  
MMT RAC #5 FINAL TEST 5/2/81



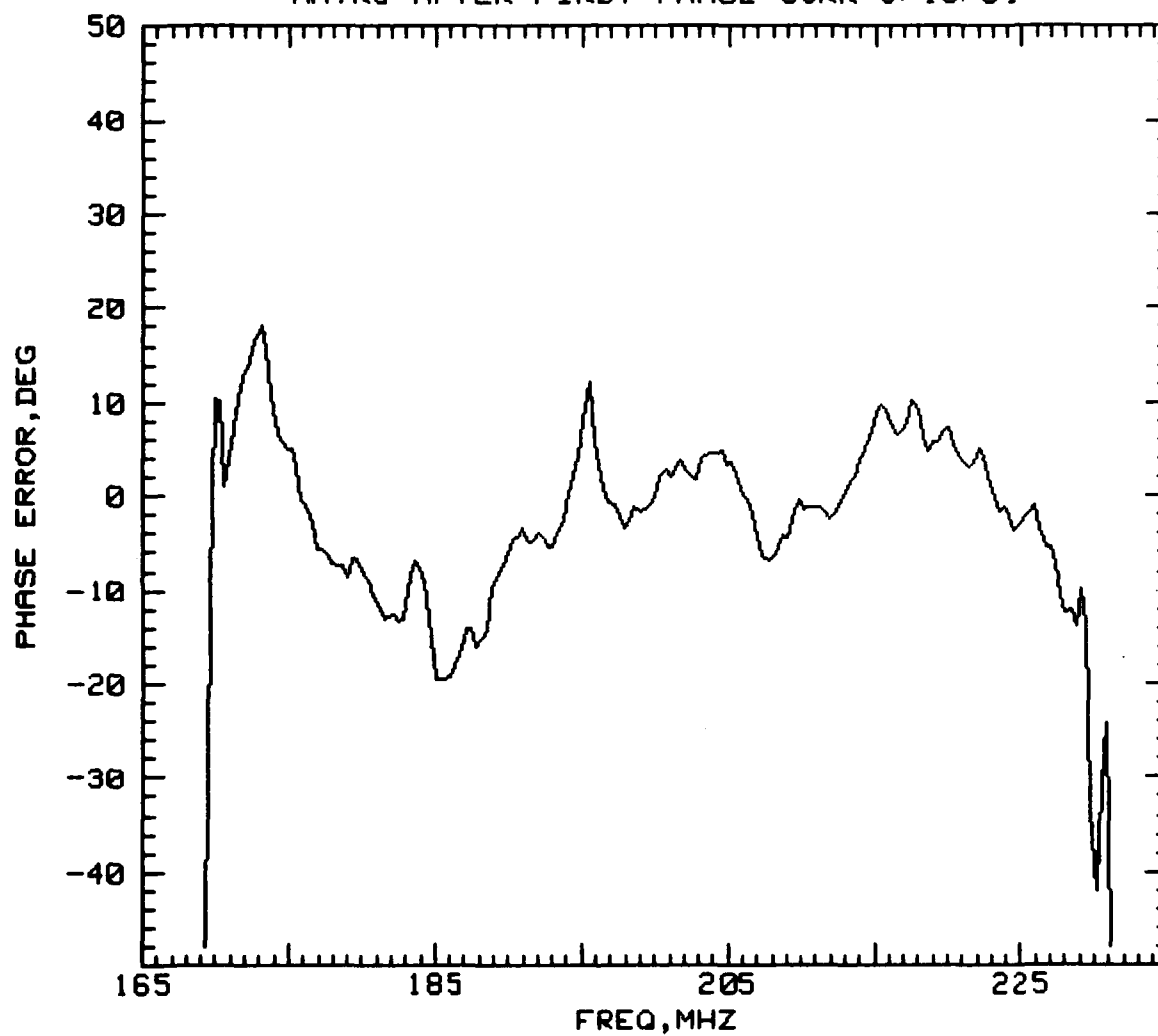
LINEAR      QUAD      RMS      F1      F2  
35.95821 -4.98165E-01      2.37      170.00      230.00  
MMT RAC #5 FINAL TEST 5/2/81



PEAK AMPLITUDE IS = .998298 ABSOLUTE  
SIGNAL TO NOISE RATIO IS= -1.32505825317 DB  
MMT RAC #5 WITH IDEAL UP CHIRP LINE



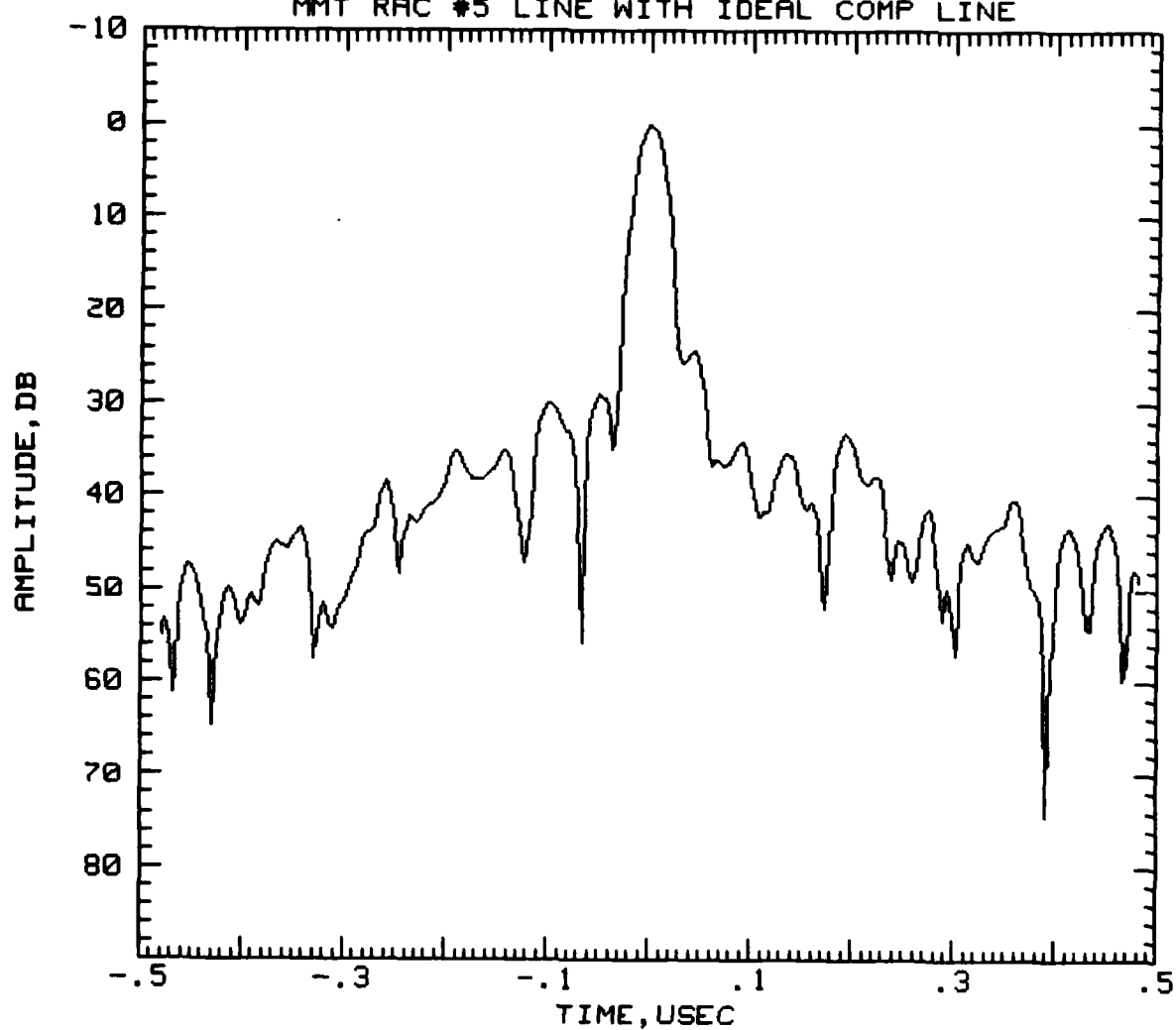
LINEAR      QUAD      RMS      F1      F2  
35.30150 -4.98224E-01      8.65      170.00      230.00  
MMTR5 AFTER FIRST PHASE CORR 3/18/81





PEAK AMPLITUDE IS = .931806 ABSOLUTE  
SIGNAL TO NOISE RATIO IS= -1.47394685866 DB

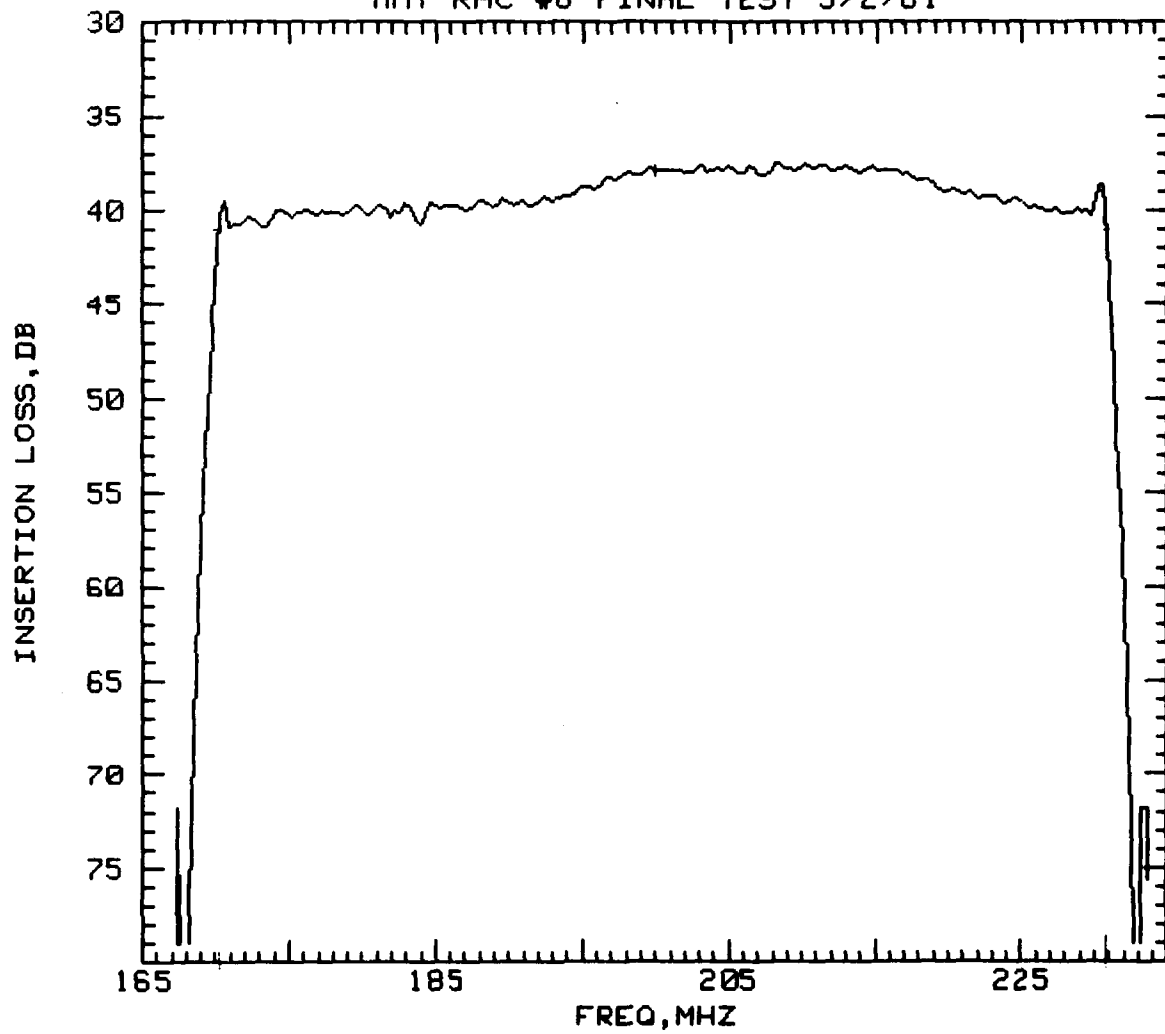
MMT RAC #5 LINE WITH IDEAL COMP LINE



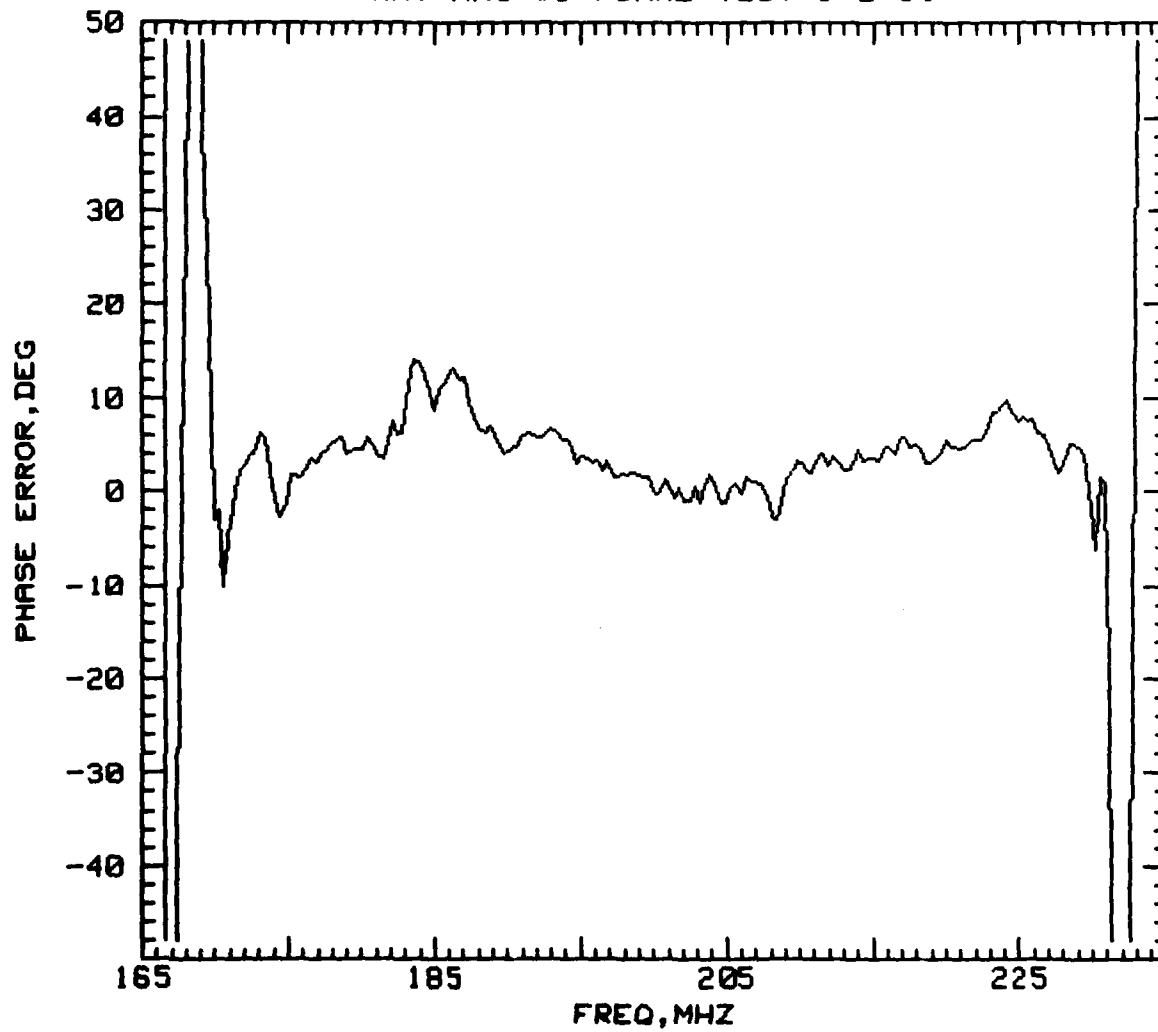
TEST DATA FOR S/N 6 RAC FILTER

MINIMUM INSERTION LOSS= 37.5 DB AT F= 208.05 MHZ

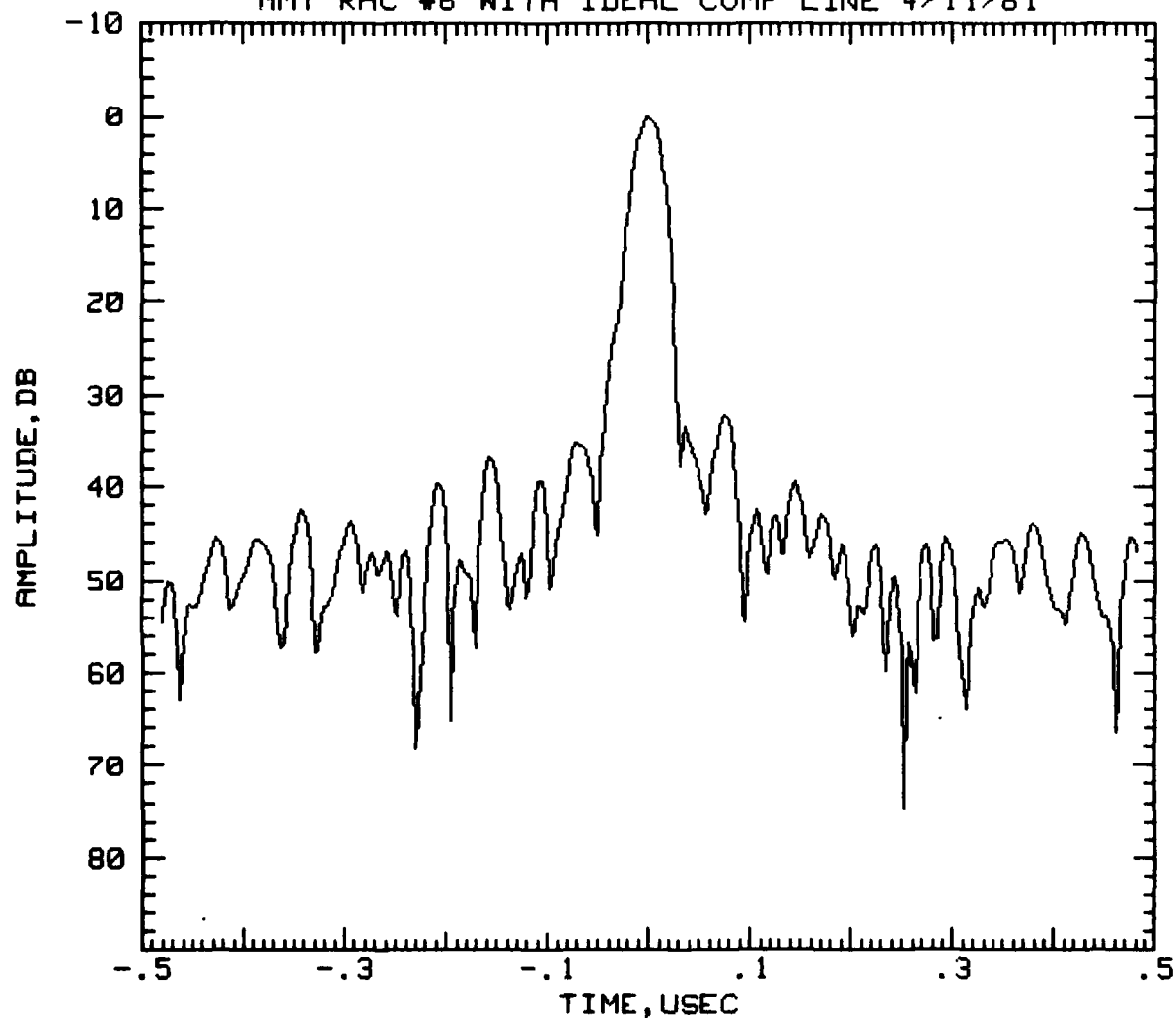
MMT RAC #6 FINAL TEST 5/2/81



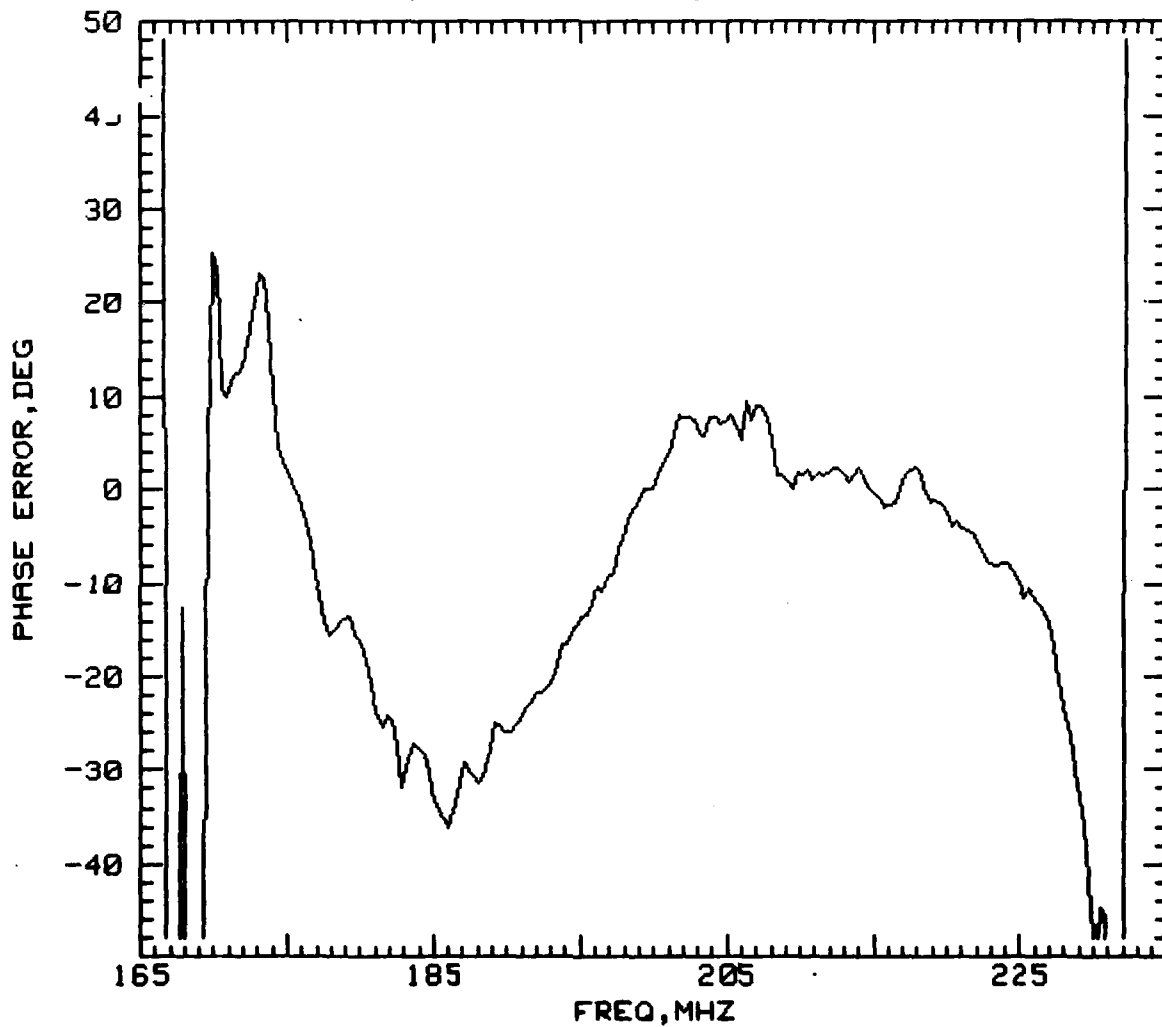
LINEAR      QUAD      RMS      F1      F2  
35.95902 -4.98168E-01      3.69      170.00      230.00  
NMT RAC #6 FINAL TEST 5/2/81



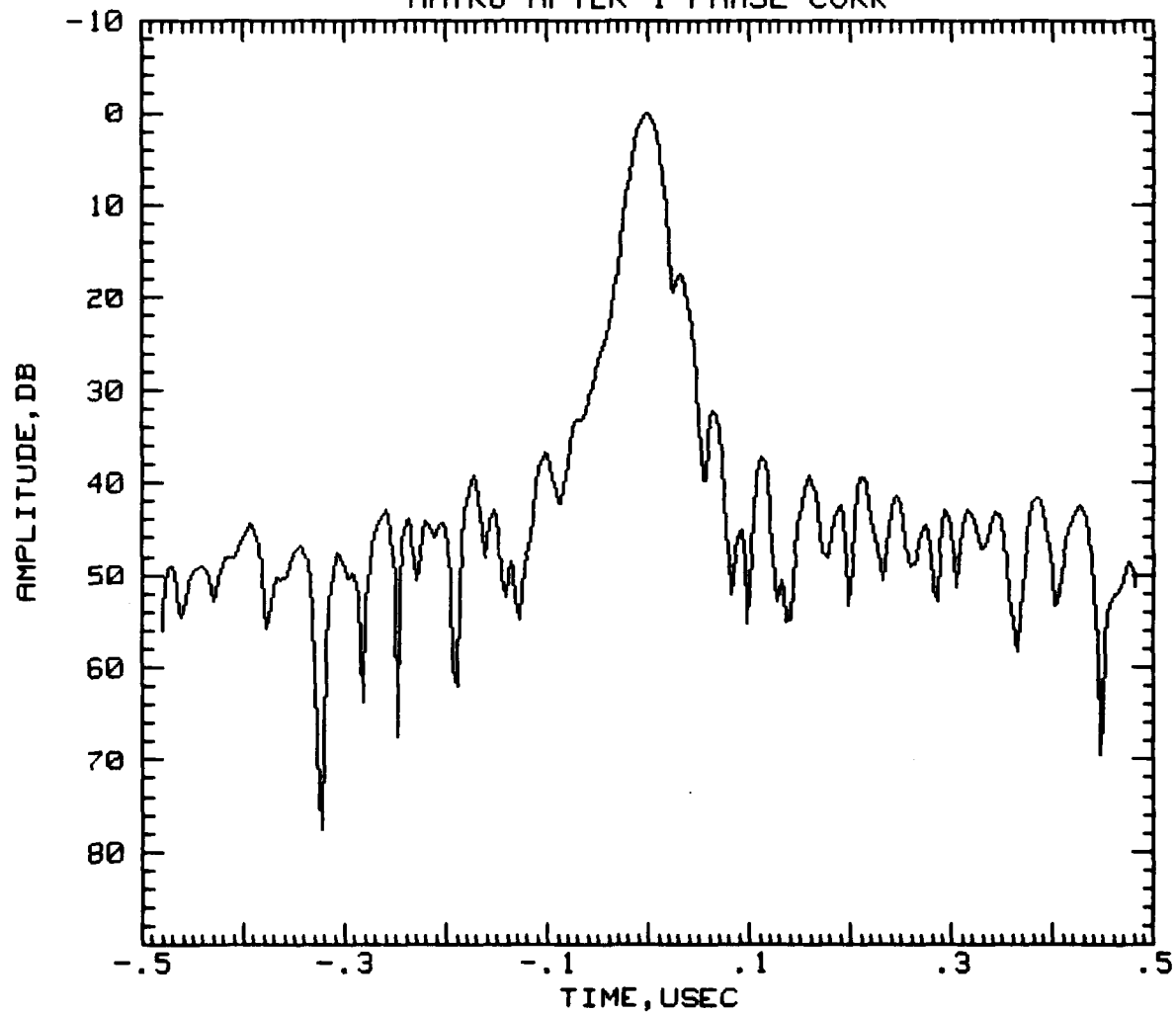
PEAK AMPLITUDE IS = .851422 ABSOLUTE  
SIGNAL TO NOISE RATIO IS= -1.42820399989 DB  
MMT RAC #6 WITH IDEAL COMP LINE 4/11/81



LINEAR      QUAD      RMS      F1      F2  
35.31177 -4.98169E-01      14.85      170.00      230.00  
MMTR6 AFTER 1 PHASE CORR(3/20/81)



PEAK AMPLITUDE IS = .899774 ABSOLUTE  
SIGNAL TO NOISE RATIO IS= -1.55690953455 DB  
MMTR6 AFTER 1 PHASE CORR

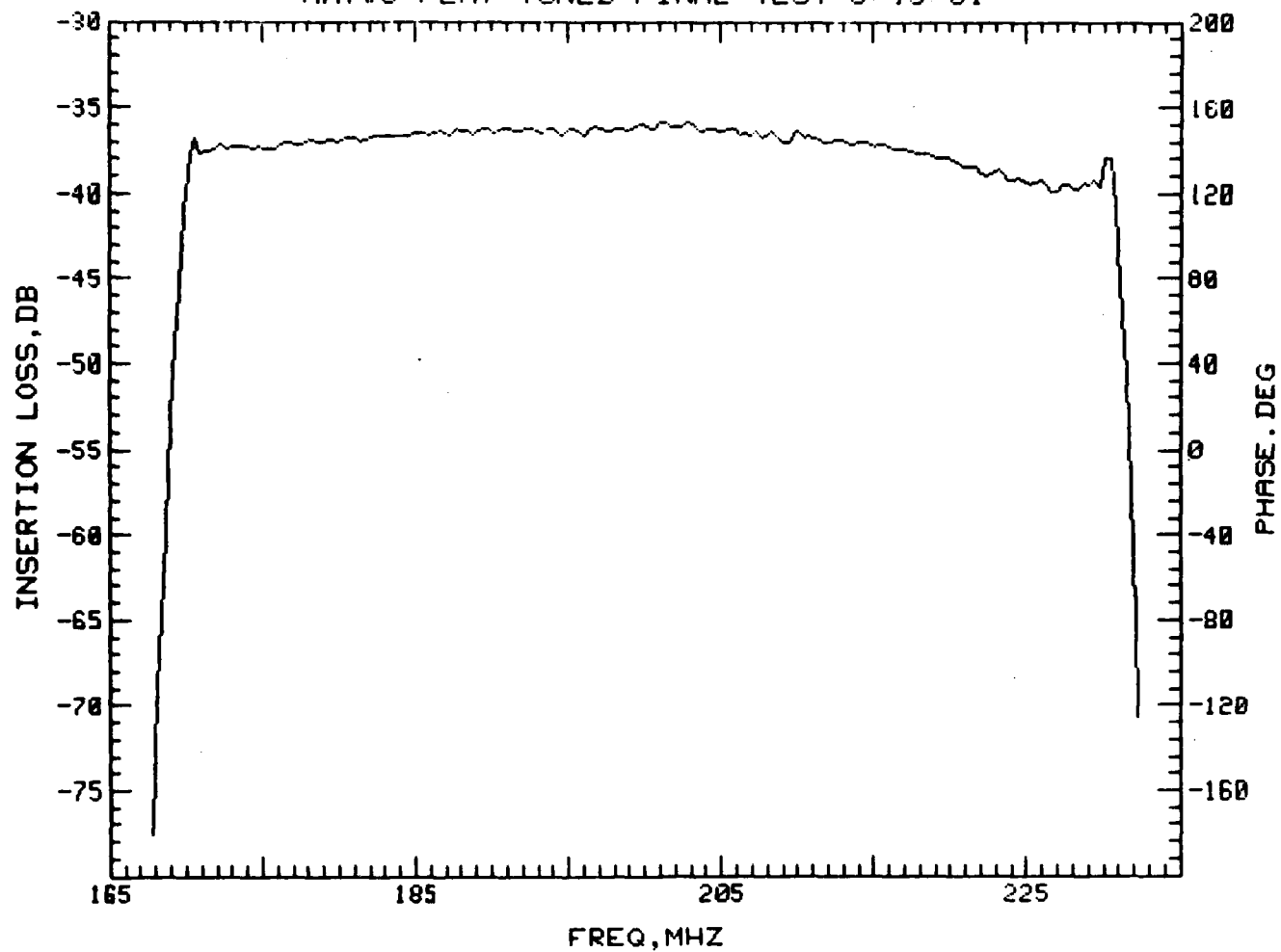


TEST DATA FOR S/N 8 RAC FILTER

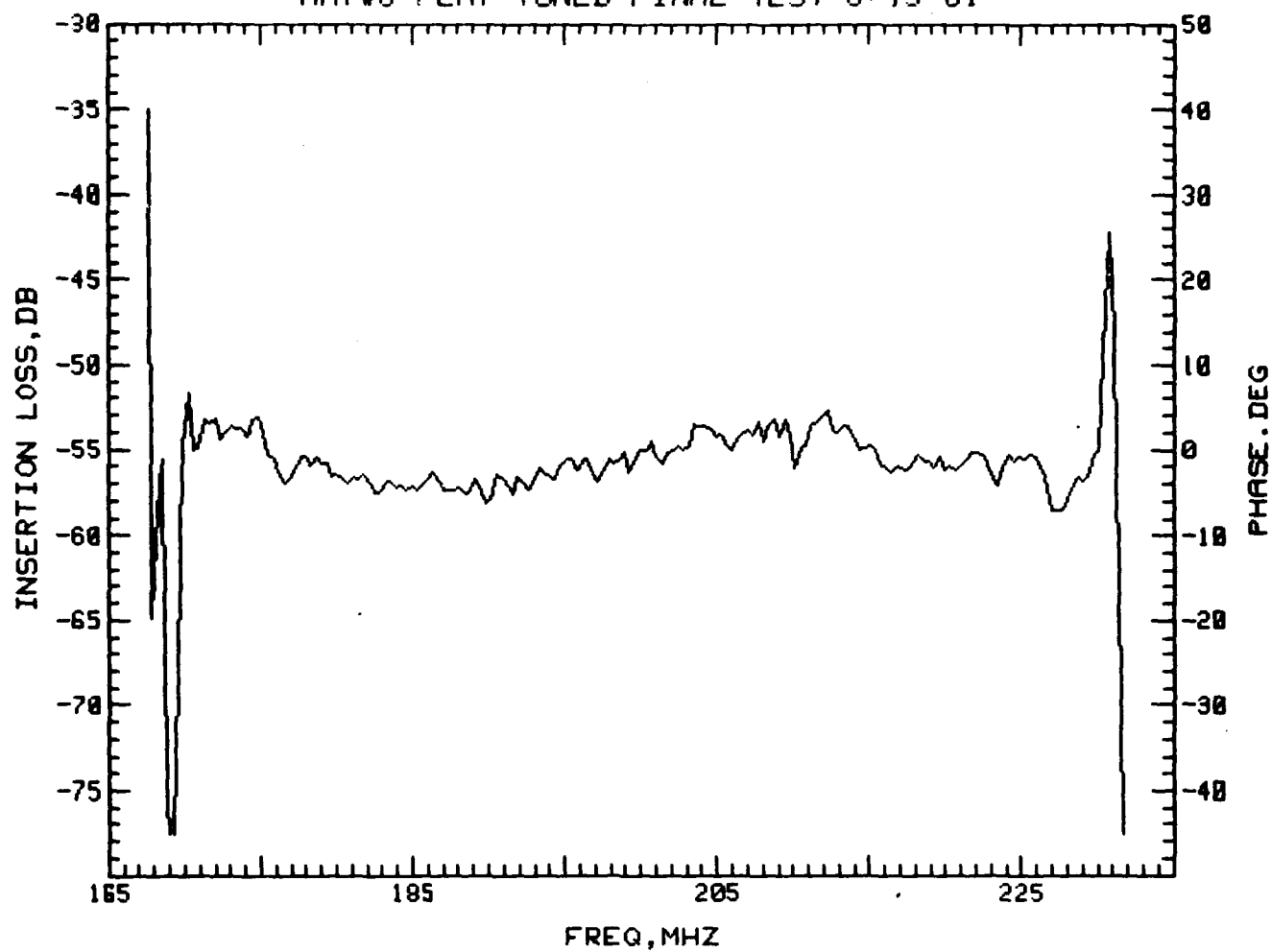


MINIMUM INSERTION LOSS= 35.9 DB AT F= 201.05 MHZ

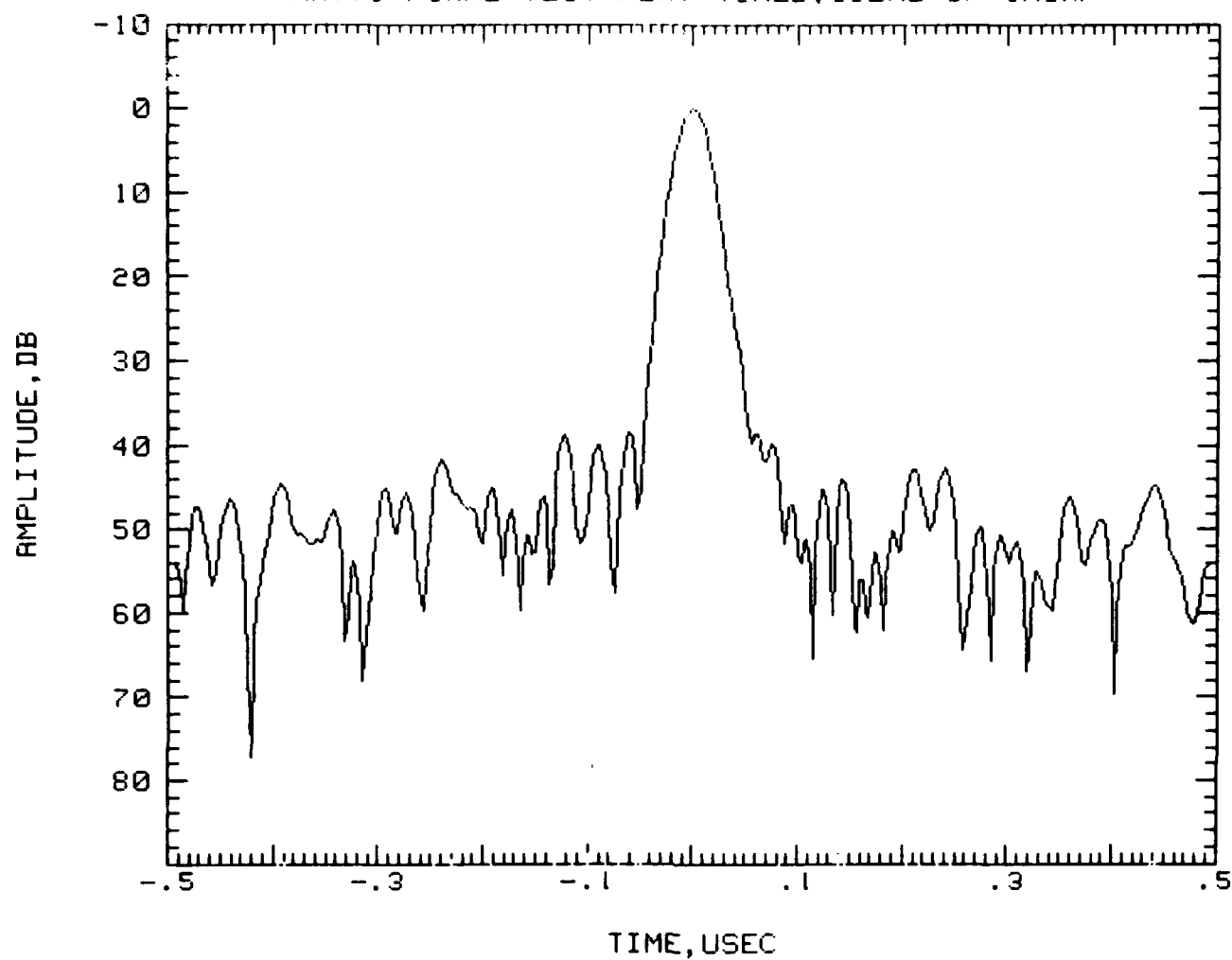
MMT#8 FLAT TUNED FINAL TEST 8/19/81



LINEAR      QUAD      RMS      F1      F2  
35.99934 -4.97970E-01      2.71      170.00      230.00  
MMT#8 FLAT TUNED FINAL TEST 8/19/81

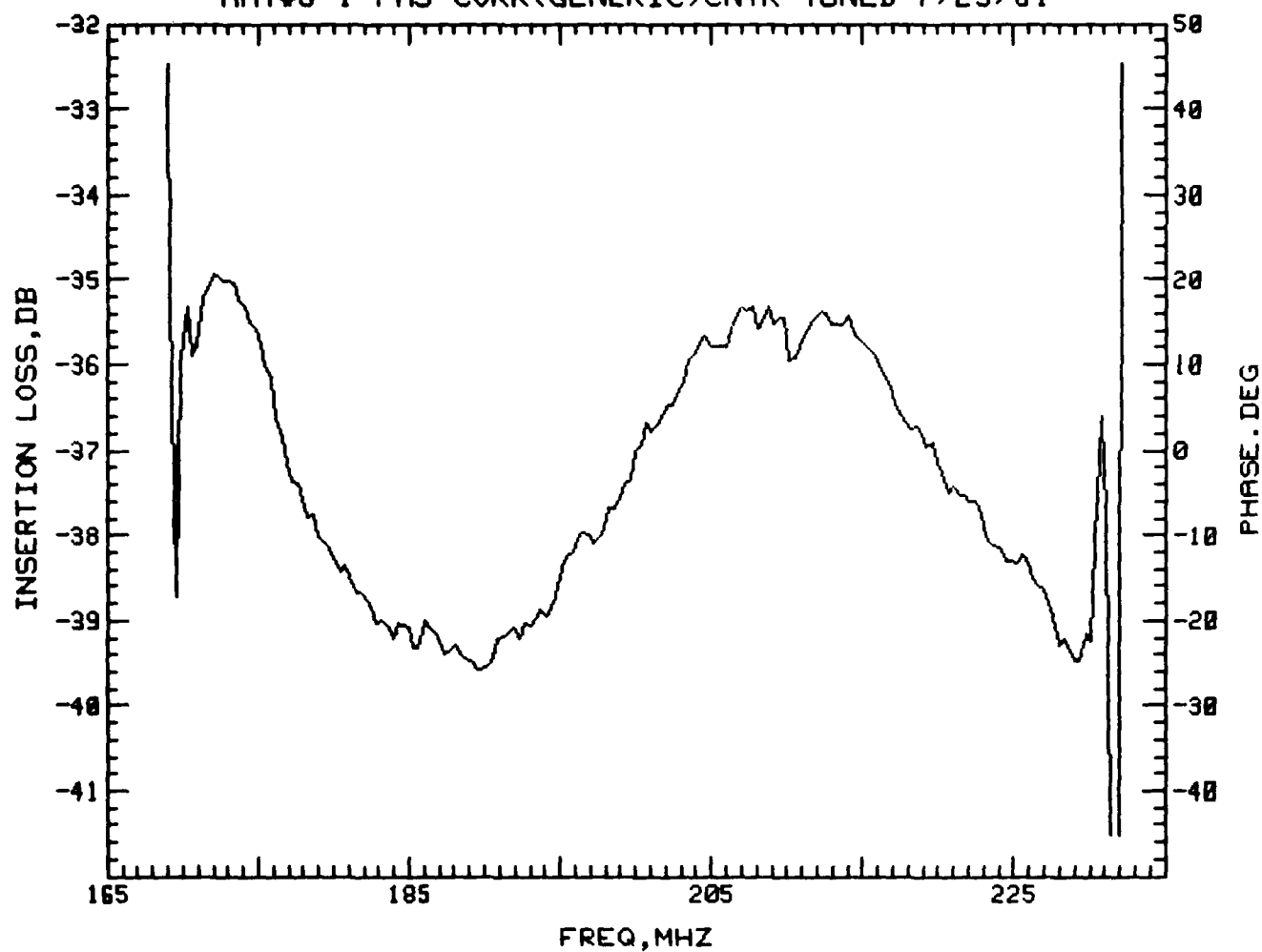


PEAK AMPLITUDE IS = 1.28873 ABSOLUTE  
SIGNAL TO NOISE RATIO IS= -1.0264127265 DB  
NMT#8 FINAL TEST FLAT TUNED; IDEAL UP-CHIRP



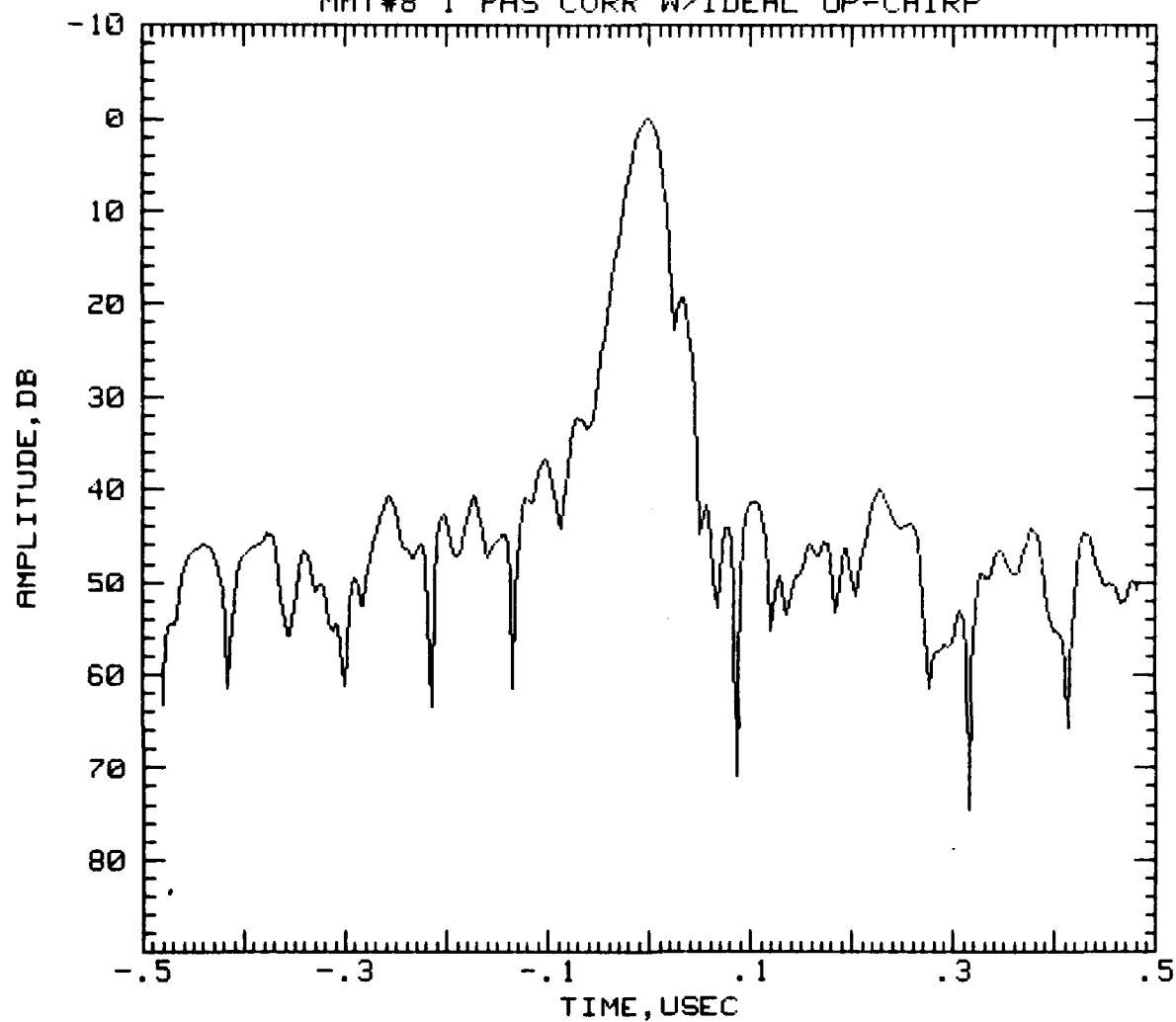
LINEAR QUAD RMS F1 F2  
36.00483 -4.97869E-01 14.78 170.00 230.00

MMT#8 1 PHS CORR(GENERIC)CNTR TUNED 7/29/81



PEAK AMPLITUDE IS = 1.67865 ABSOLUTE  
SIGNAL TO NOISE RATIO IS= -1.26152302312 DB

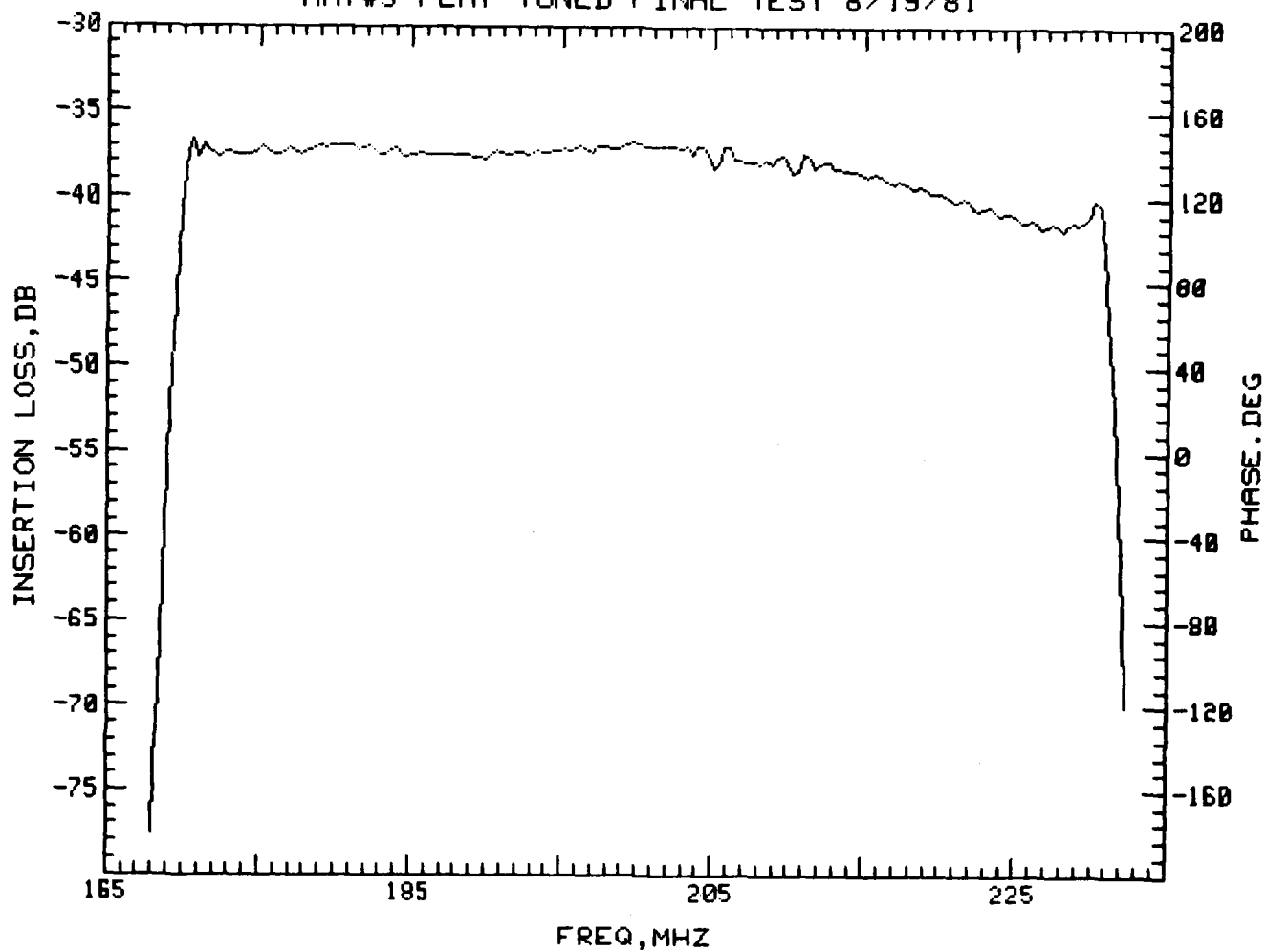
MMT#8 1 PHS CORR W/IDEAL UP-CHIRP



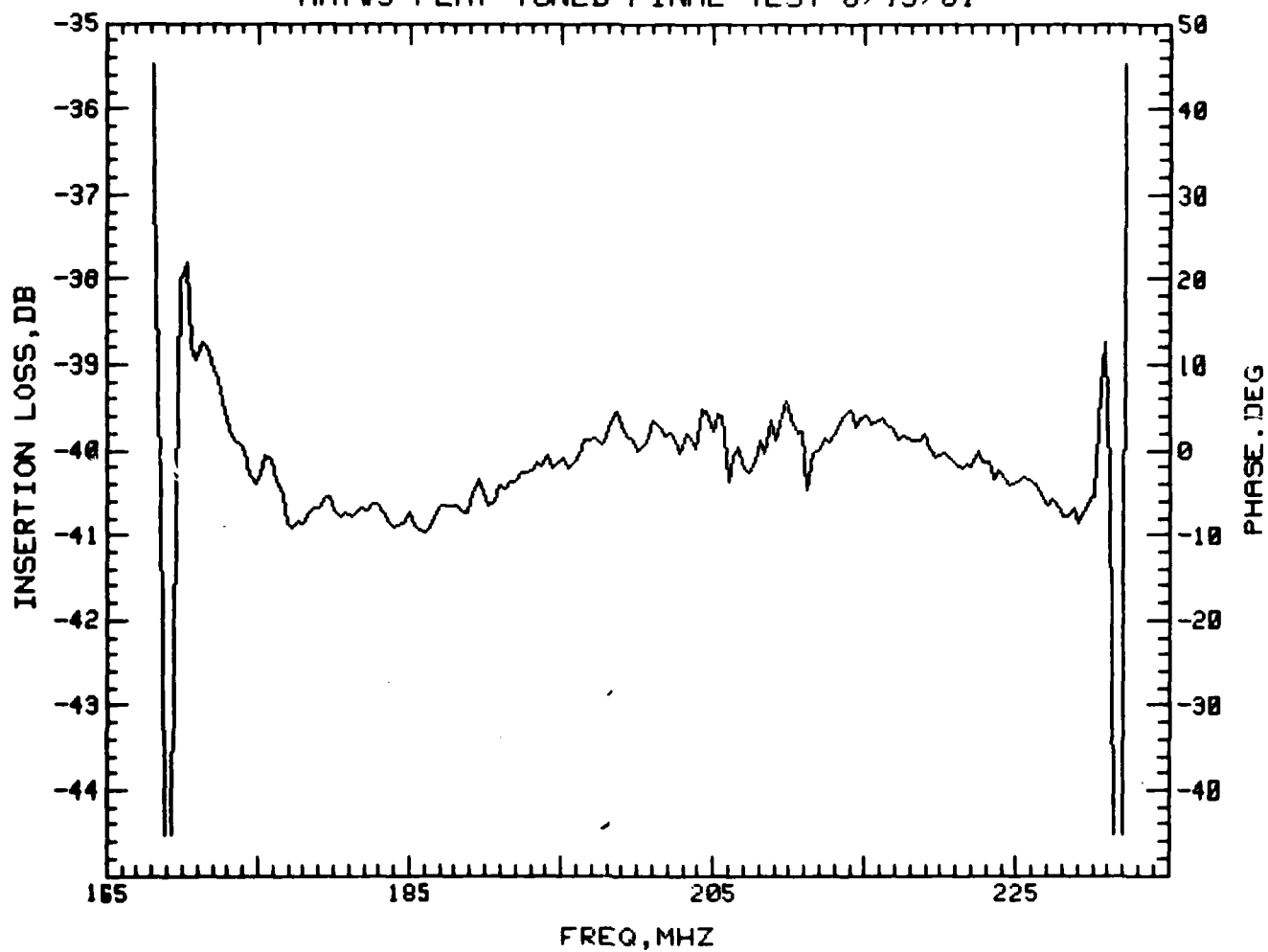
TEST DATA FOR S/N 9 RAC FILTER

MINIMUM INSERTION LOSS= 36.6 DB AT F= 170.6 MHZ

MMT#9 FLAT TUNED FINAL TEST 8/19/81



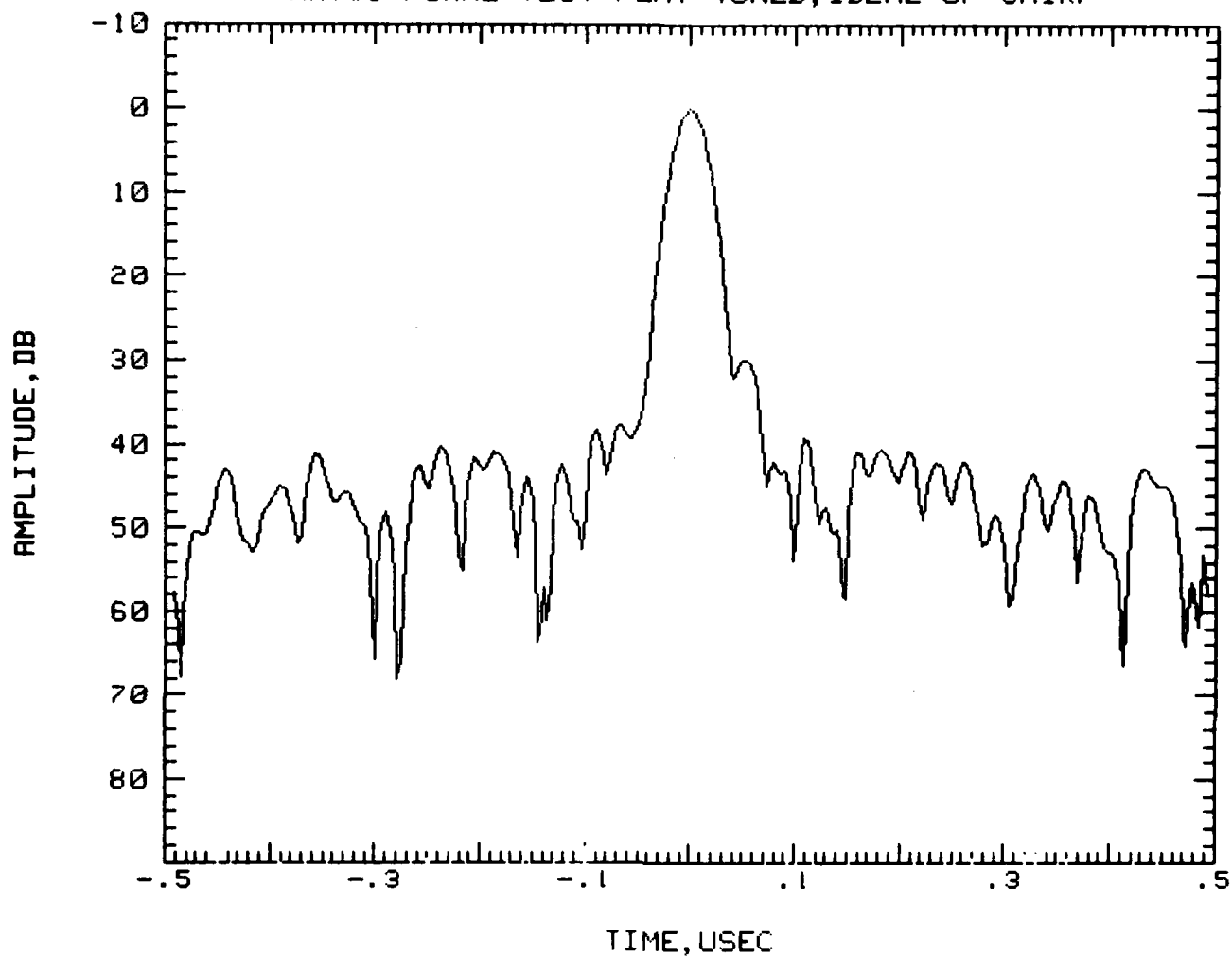
LINEAR      QUAD      RMS      F1      F2  
35.98222 -4.97979E-01      5.32      170.00      230.00  
MMT#9 FLAT TUNED FINAL TEST 8/19/81





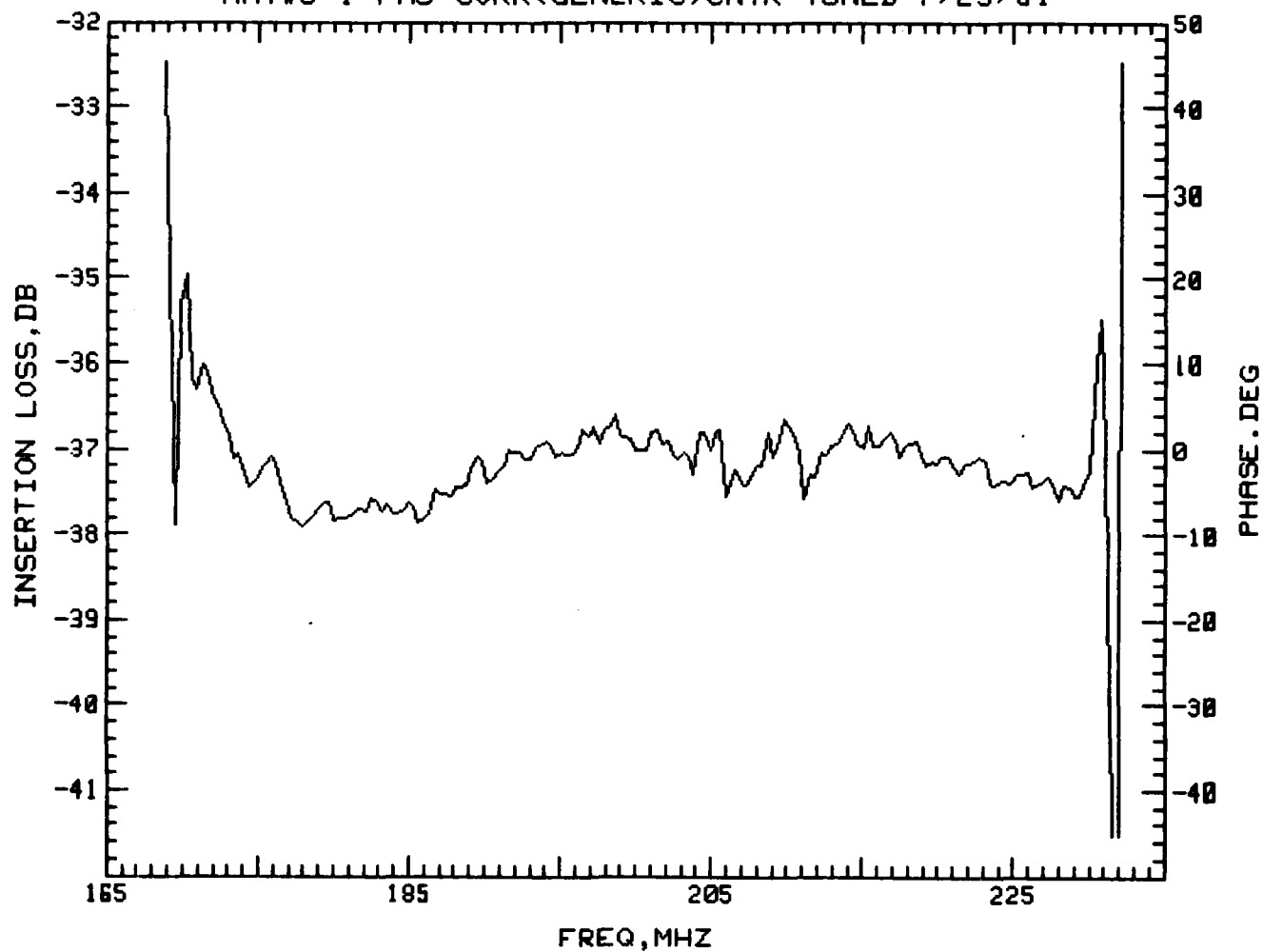
PEAK AMPLITUDE IS = 1.14386 ABSOLUTE  
SIGNAL TO NOISE RATIO IS= -1.1097173839 DB

MMT#9 FINAL TEST FLAT TUNED; IDEAL UP-CHIRP

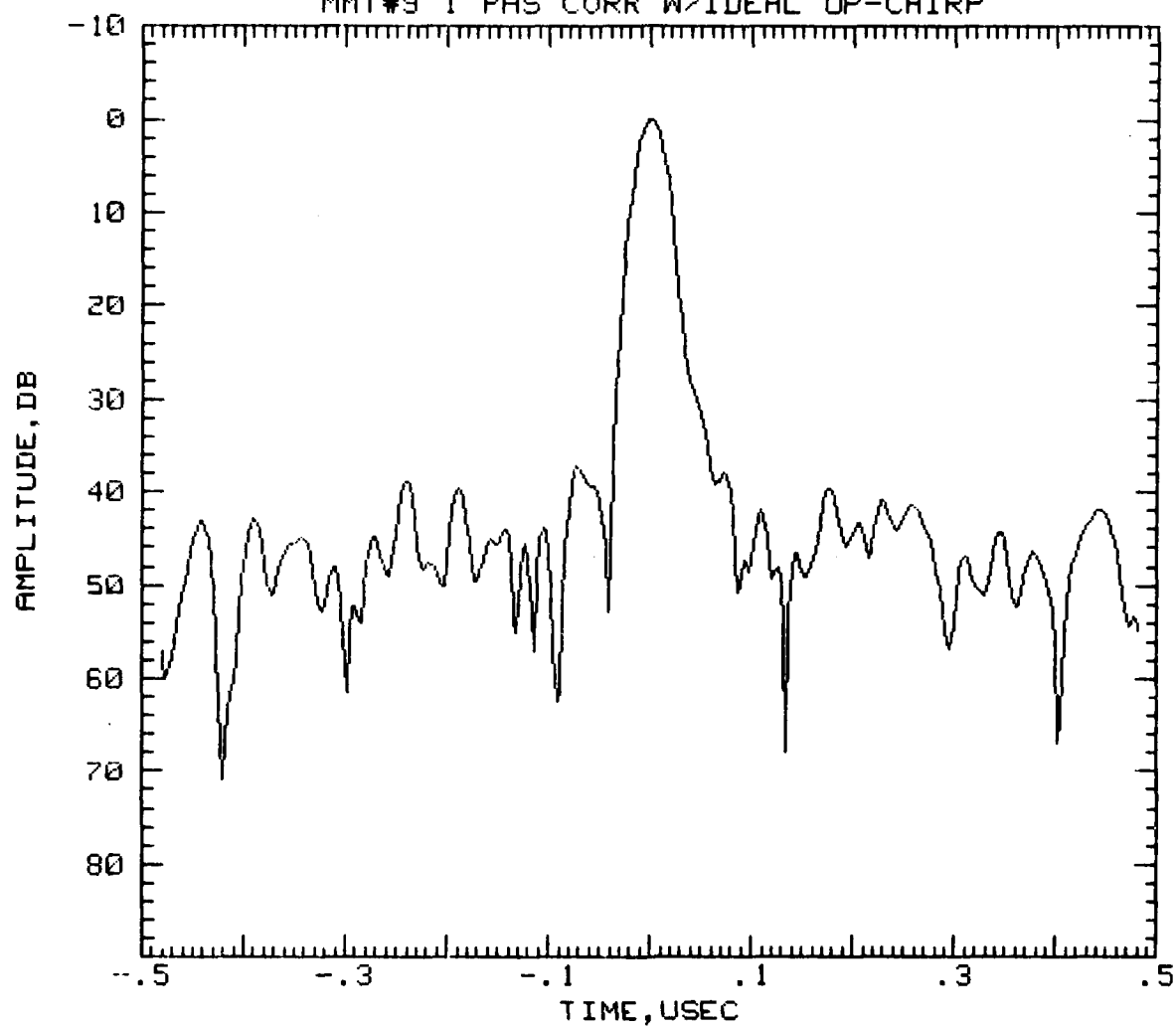


LINEAR      QUAD      RMS      F1      F2  
35.33255 -4.97903E-01      4.27      170.00      230.00

MMT#9 1 PHS CORR(GENERIC)CNTR TUNED 7/29/81



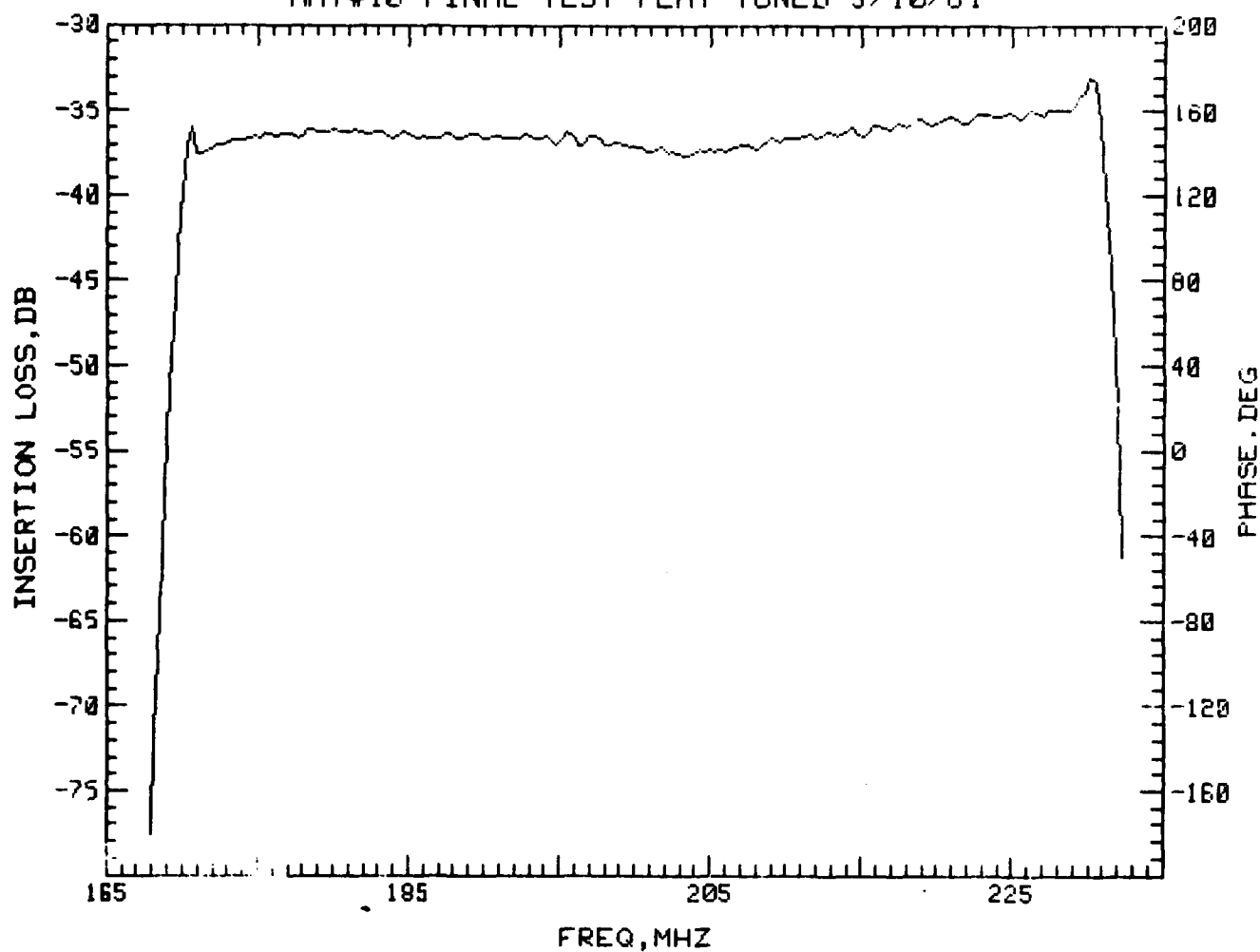
PEAK AMPLITUDE IS = 1.61425 ABSOLUTE  
SIGNAL TO NOISE RATIO IS= -.862527075827 DB  
MMT#9 1 PHS CORR W/IDEAL UP-CHIRP



TEST DATA FOR S/N 10 RAC FILTER

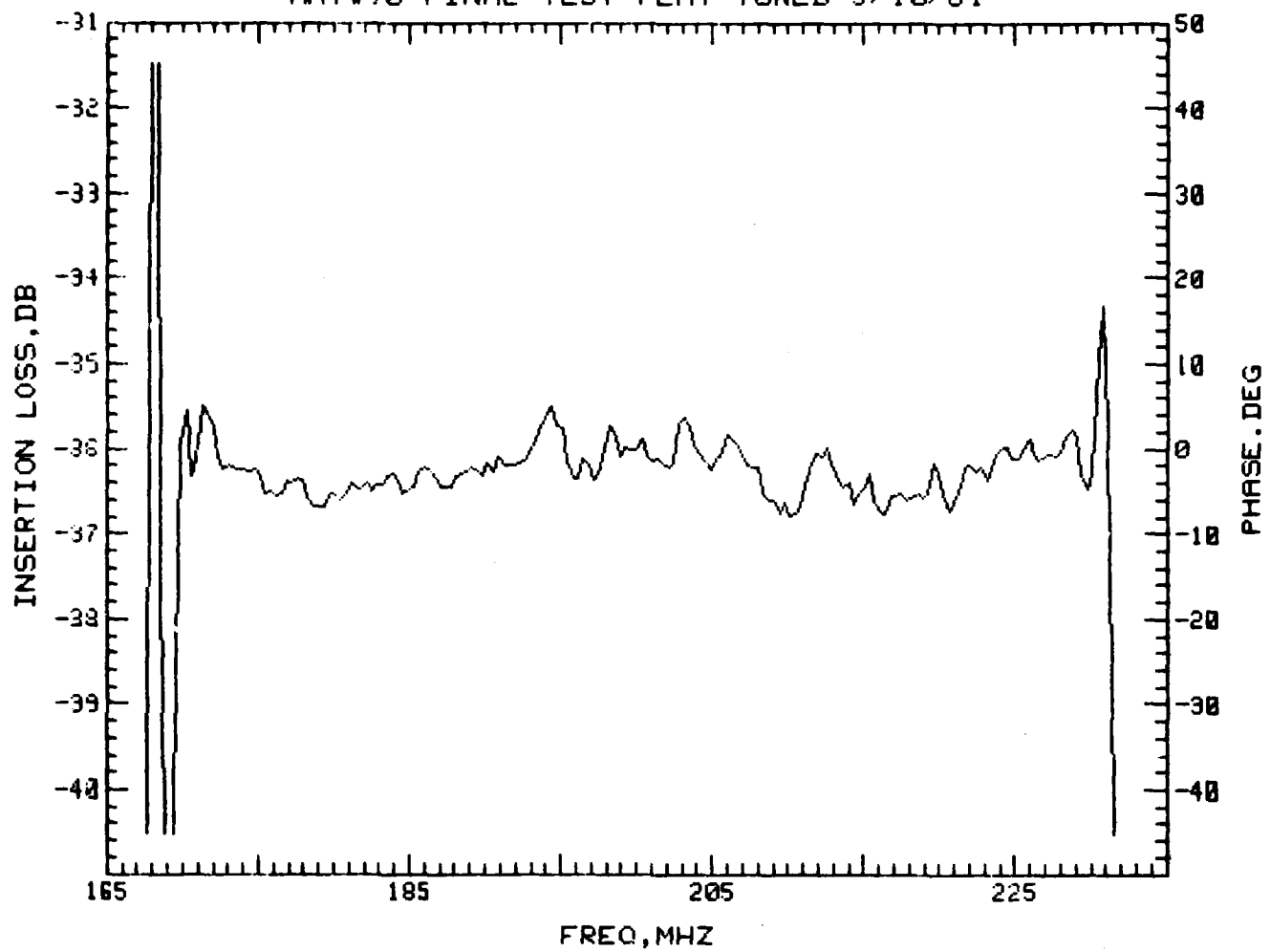
MINIMUM INSERTION LOSS= 33 DB AT F= 230.1 MHZ

MMT#10 FINAL TEST FLAT TUNED 9/10/81

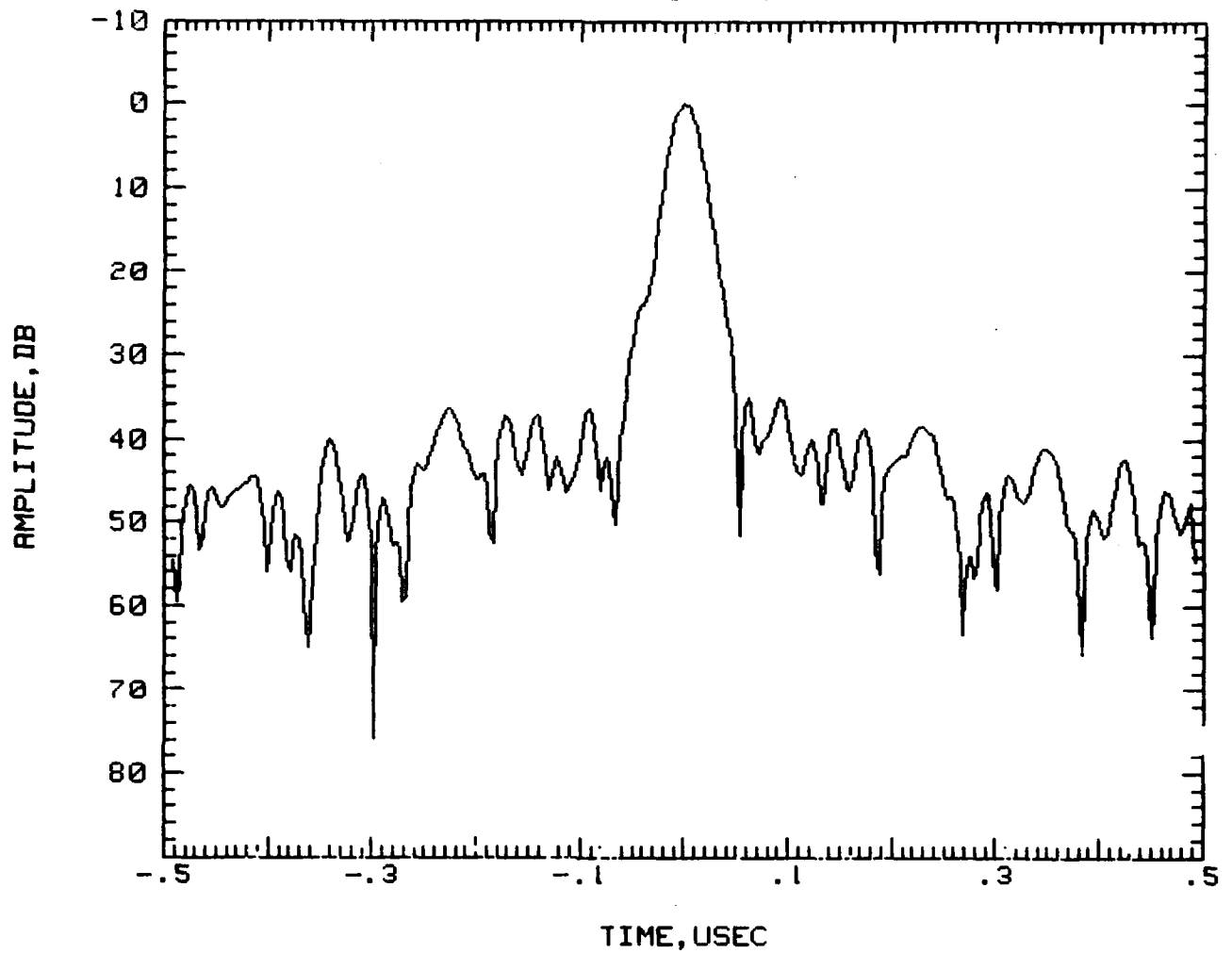


LINEAR      QUAD      RMS      F1      F2  
36.00824 -4.97925E-01      2.83      170.00      230.00

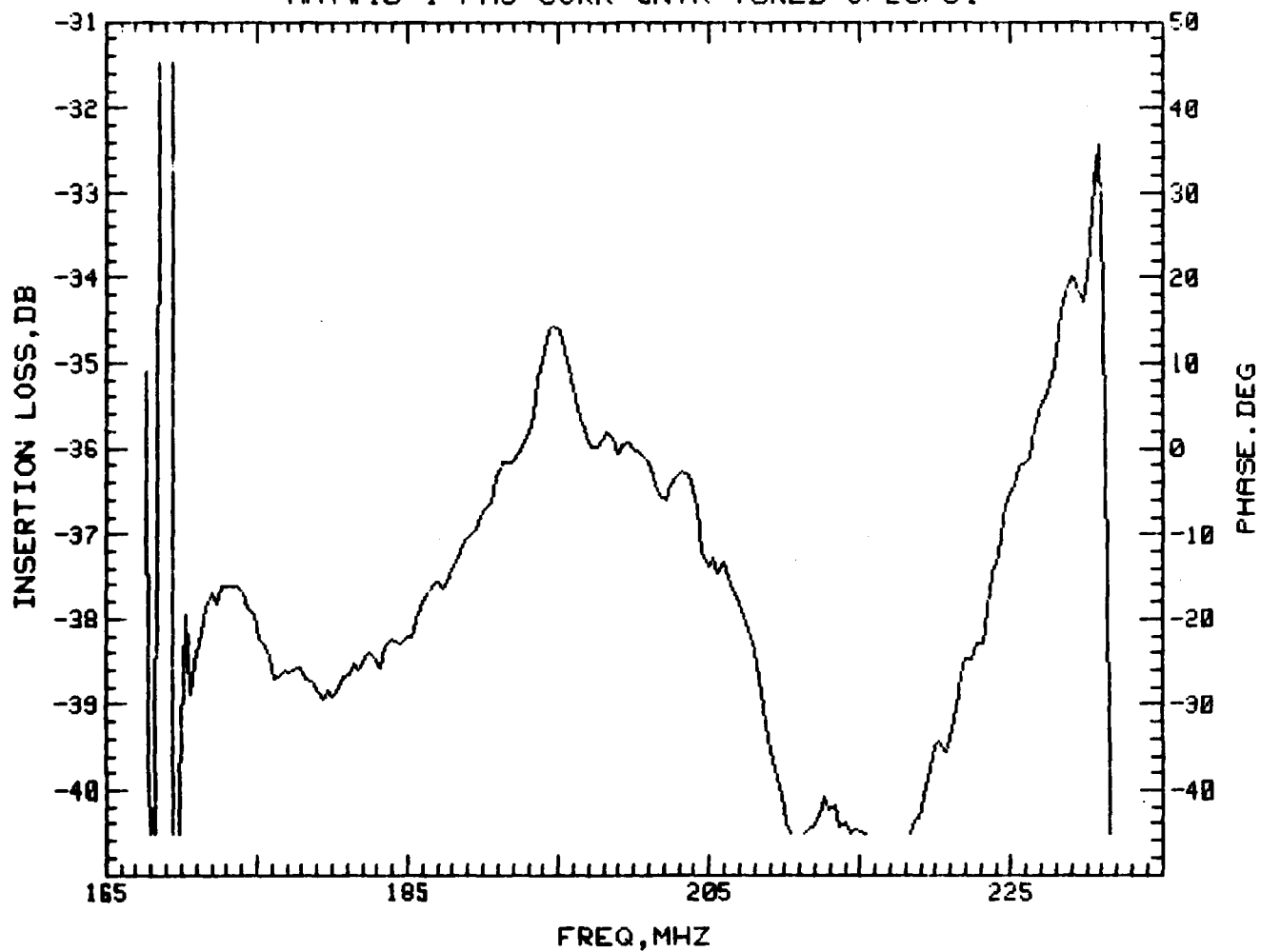
MMT#10 FINAL TEST FLAT TUNED 9/10/81



PEAK AMPLITUDE IS = 1.27694 ABSOLUTE  
SIGNAL TO NOISE RATIO IS= -1.83127123486 DB  
MMT#10 FINAL

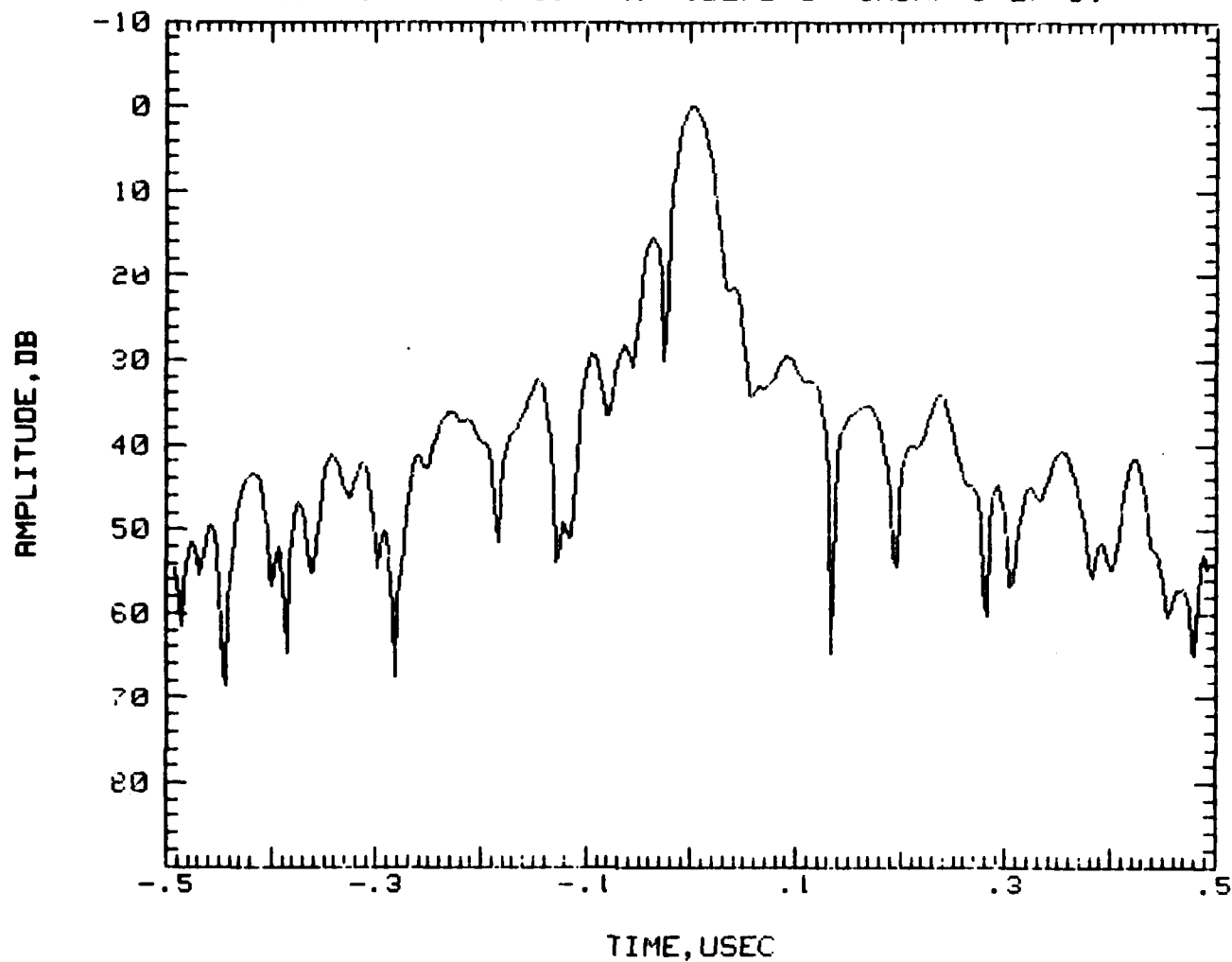


LINEAR      QUAD      RMS      F1      F2  
35.31212 -4.98228E-01      17.73      170.00      230.00  
MMT#10 1 PHS CORR CNTR TUNED 8/26/81



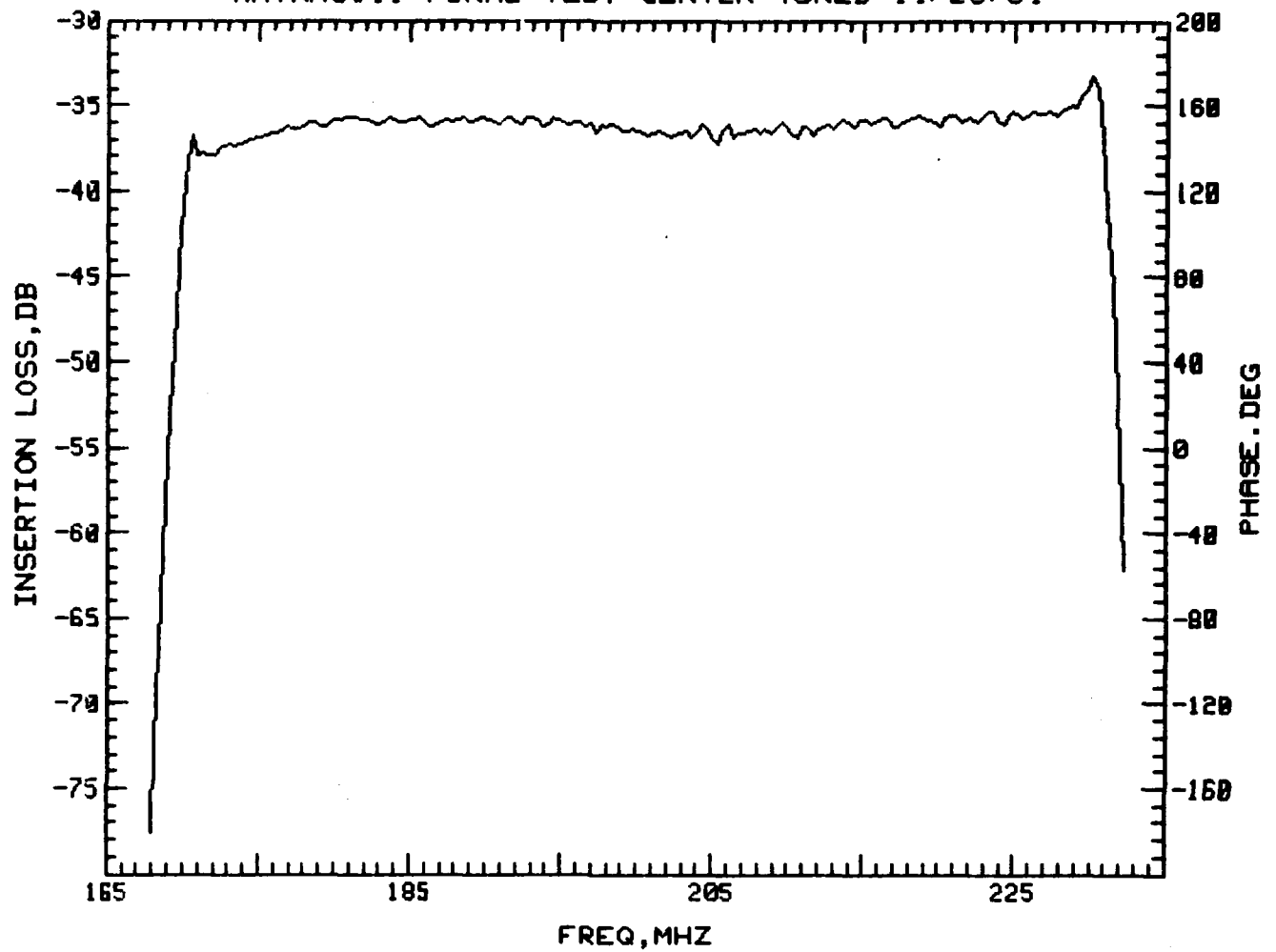


PEAK AMPLITUDE IS = 1.46616 ABSOLUTE  
SIGNAL TO NOISE RATIO IS= -2.01943340181 DB  
MNT#10 1 PHS CORR W/ IDEAL UP-CHIRP 8/27/81



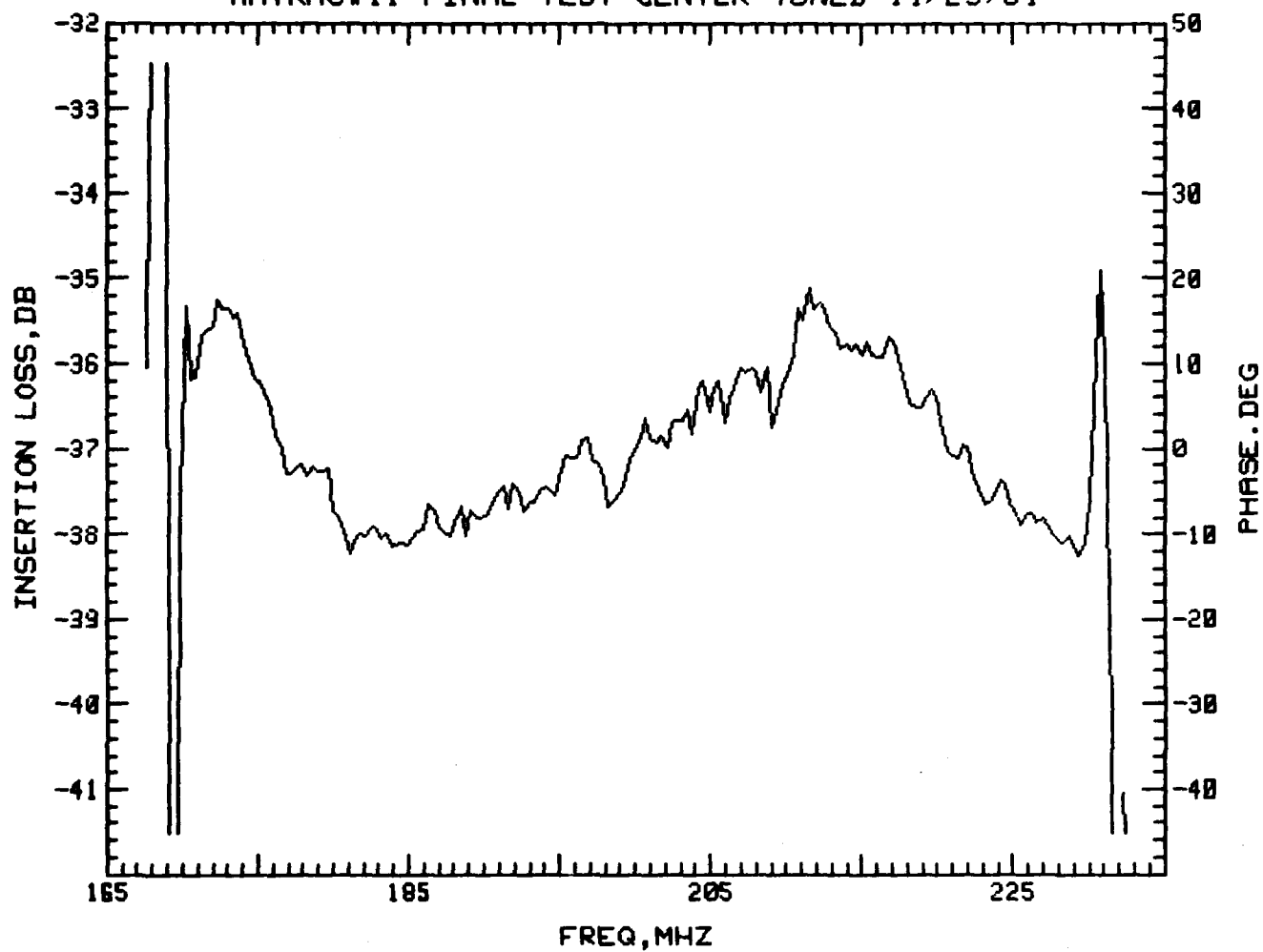
TEST DATA FOR S/N 11 RAC FILTER

MINIMUM INSERTION LOSS= 33.3 DB AT F= 230.1 MHZ  
NMTRAC#11 FINAL TEST CENTER TUNED 11/23/81

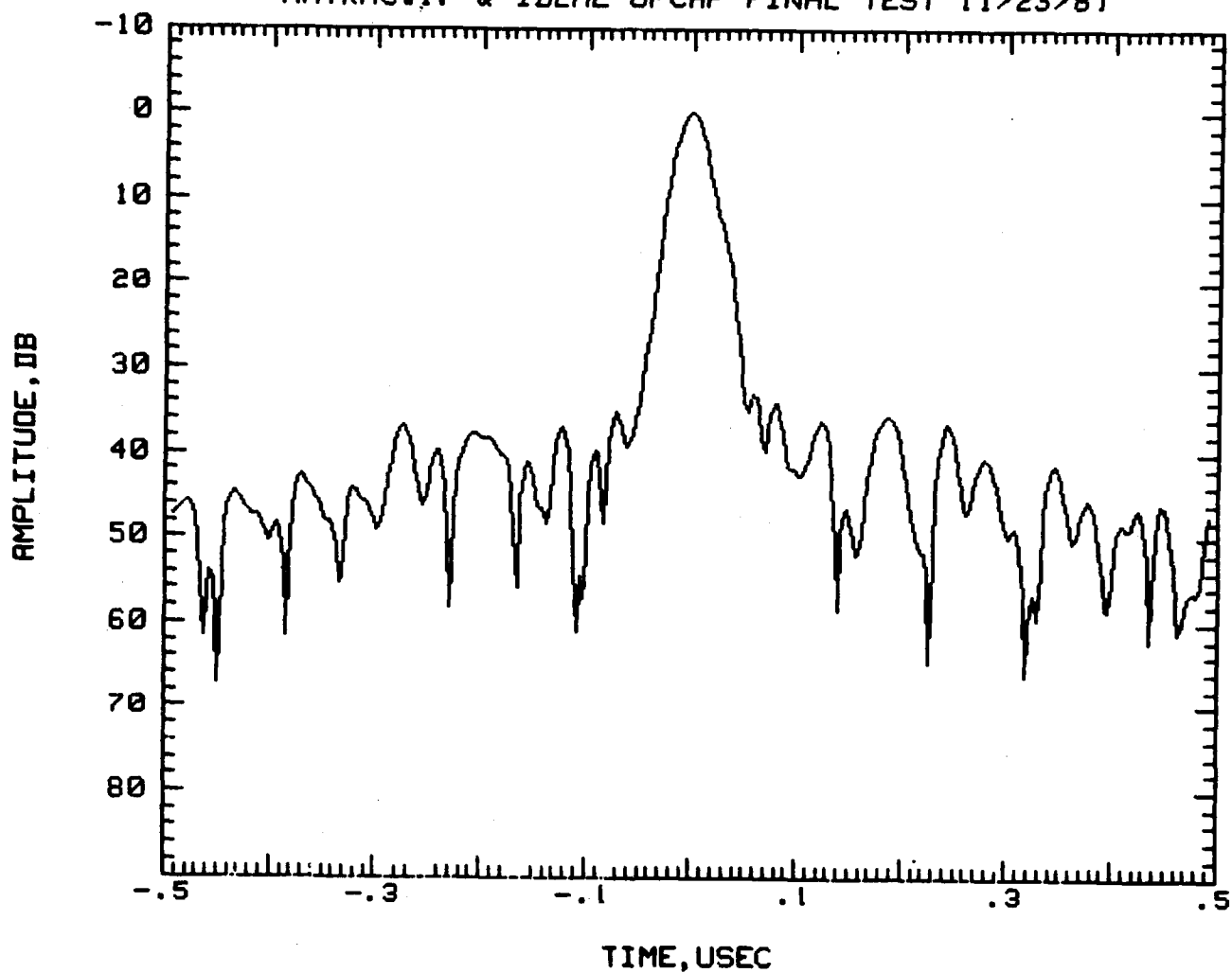


LINEAR      QUAD      RMS      F1      F2  
36.01764 -4.97671E-01      8.73      170.00      230.00

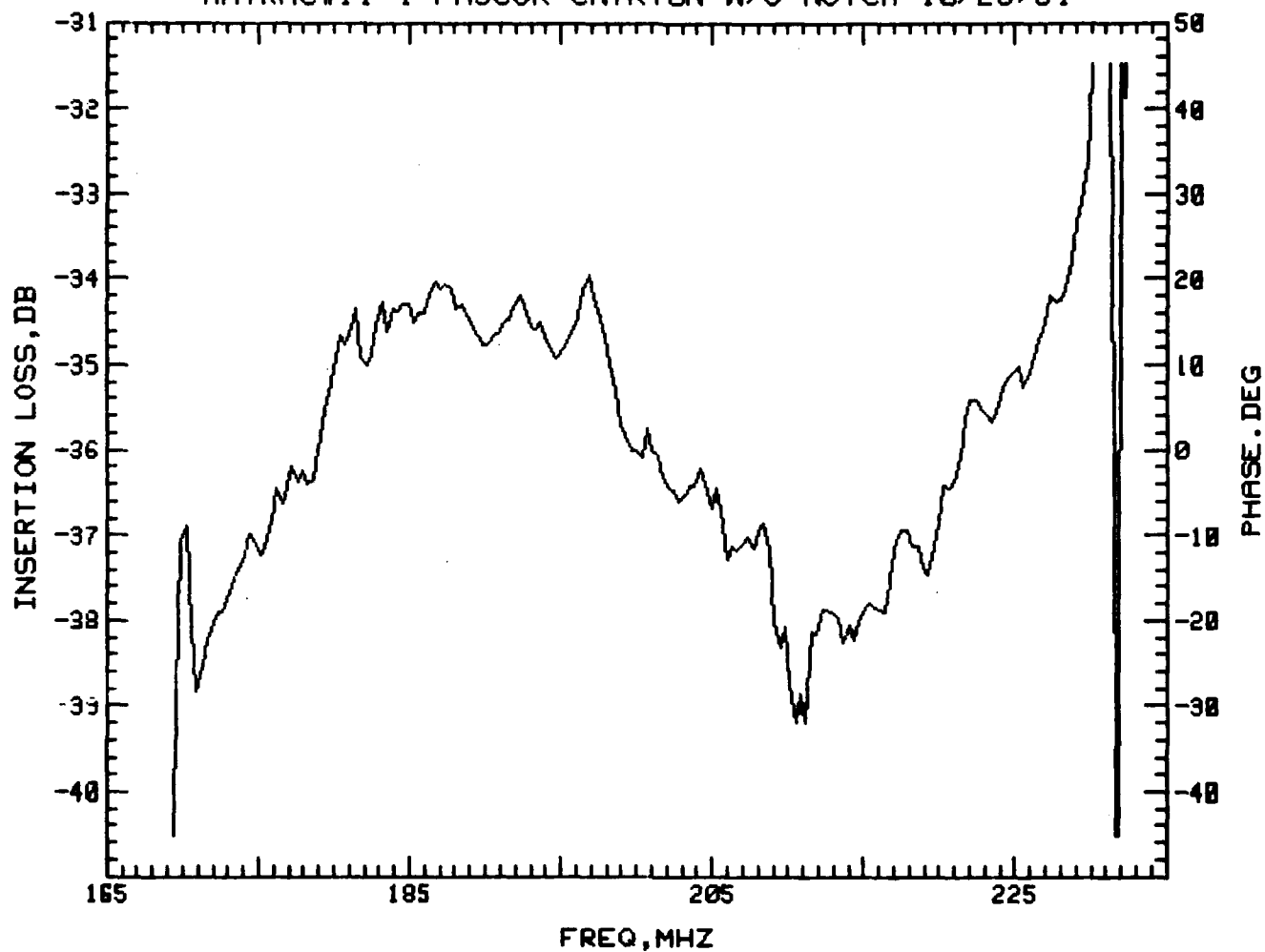
MMTRAC#11 FINAL TEST CENTER TUNED 11/23/81



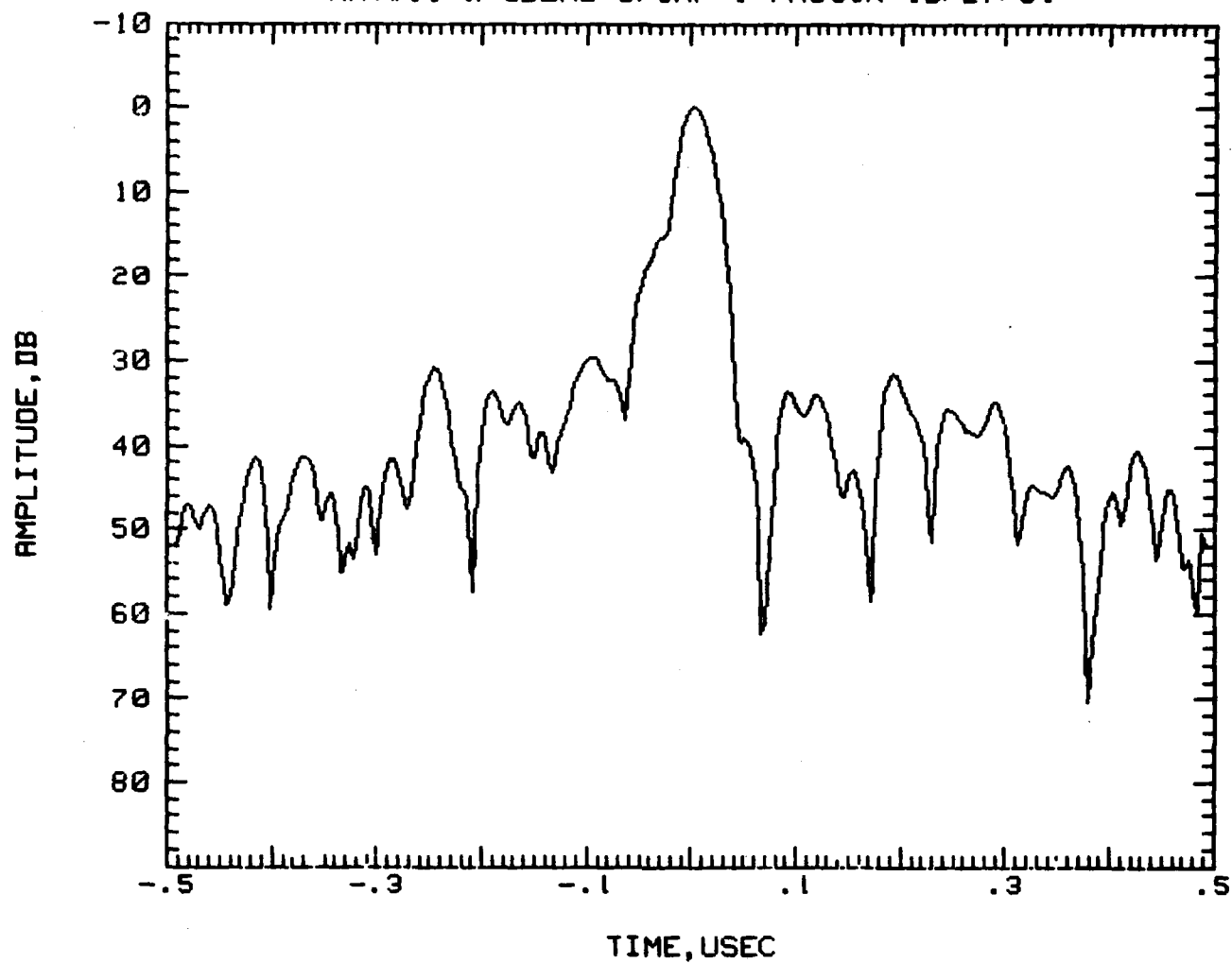
PEAK AMPLITUDE IS = 1.3168 ABSOLUTE  
SIGNAL TO NOISE RATIO IS= -1.62349562146 DB  
MMTRAC#11 & IDEAL UPCHP FINAL TEST 11/23/81



LINEAR      QUAD      RMS      F1      F2  
35.31105 -4.98005E-01      15.01      170.00      230.00  
MMTRAC#11 1 PHSCOR CNTRTUN W/O NOTCH 10/26/81



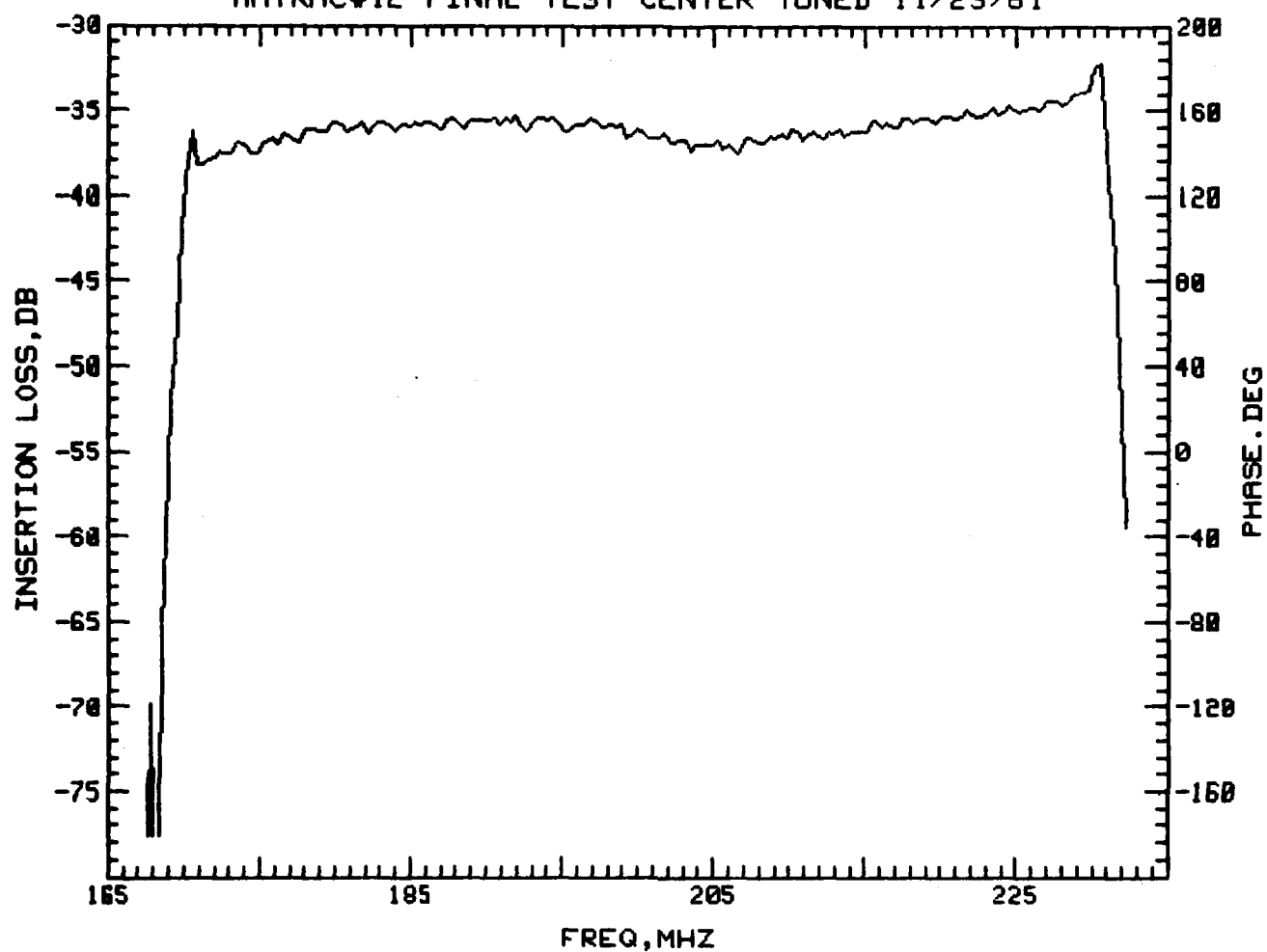
PEAK AMPLITUDE IS = 1.17574 ABSOLUTE  
SIGNAL TO NOISE RATIO IS= -1.99028537831 DB  
MMT#11 & IDEAL UPCHP 1 PHSCOR 10/27/81



TEST DATA FOR S/N 12 RAC FILTER

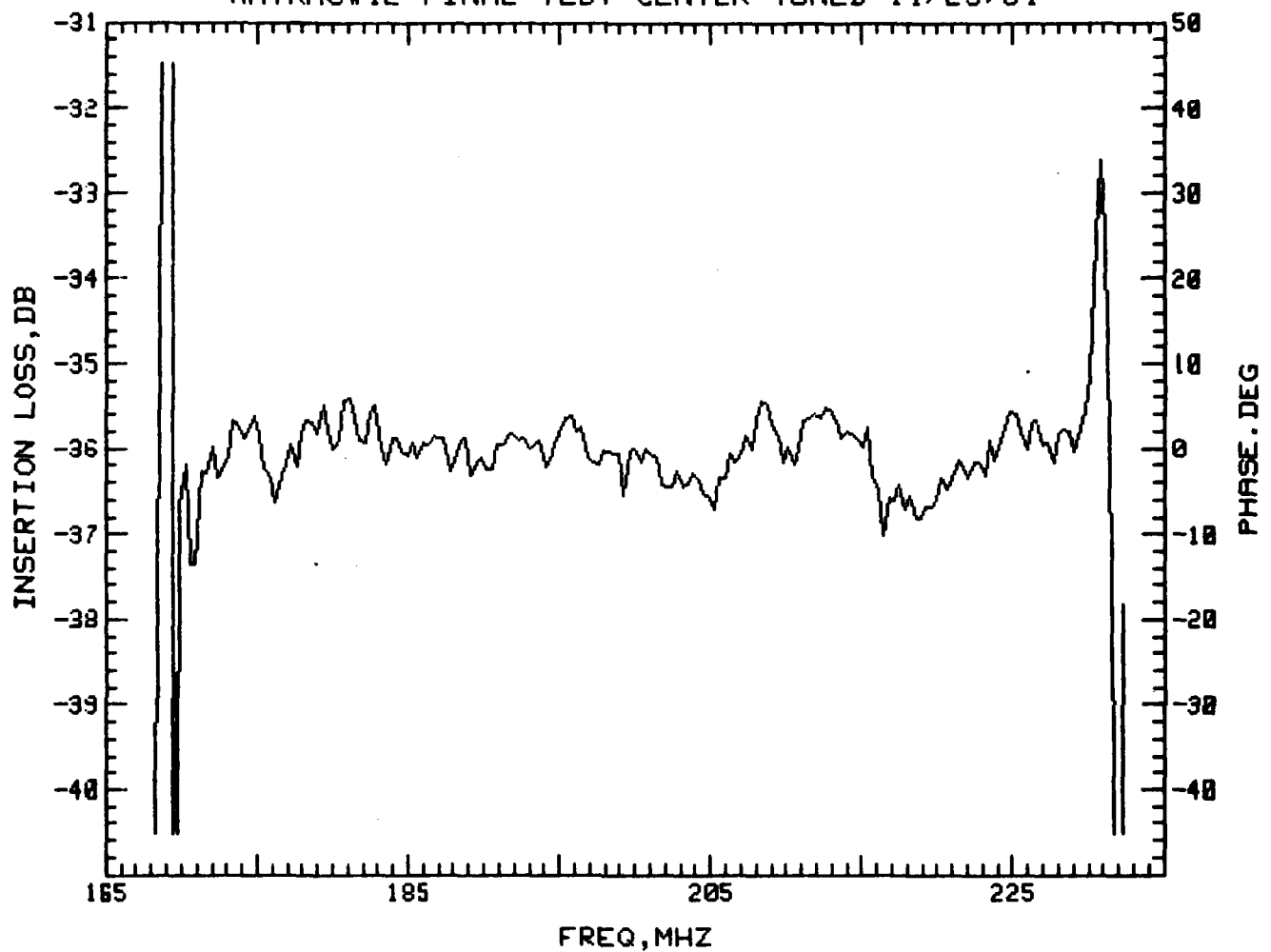


MINIMUM INSERTION LOSS= 32.3 DB AT F= 230.45 MHZ  
MMTRAC#12 FINAL TEST CENTER TUNED 11/23/81

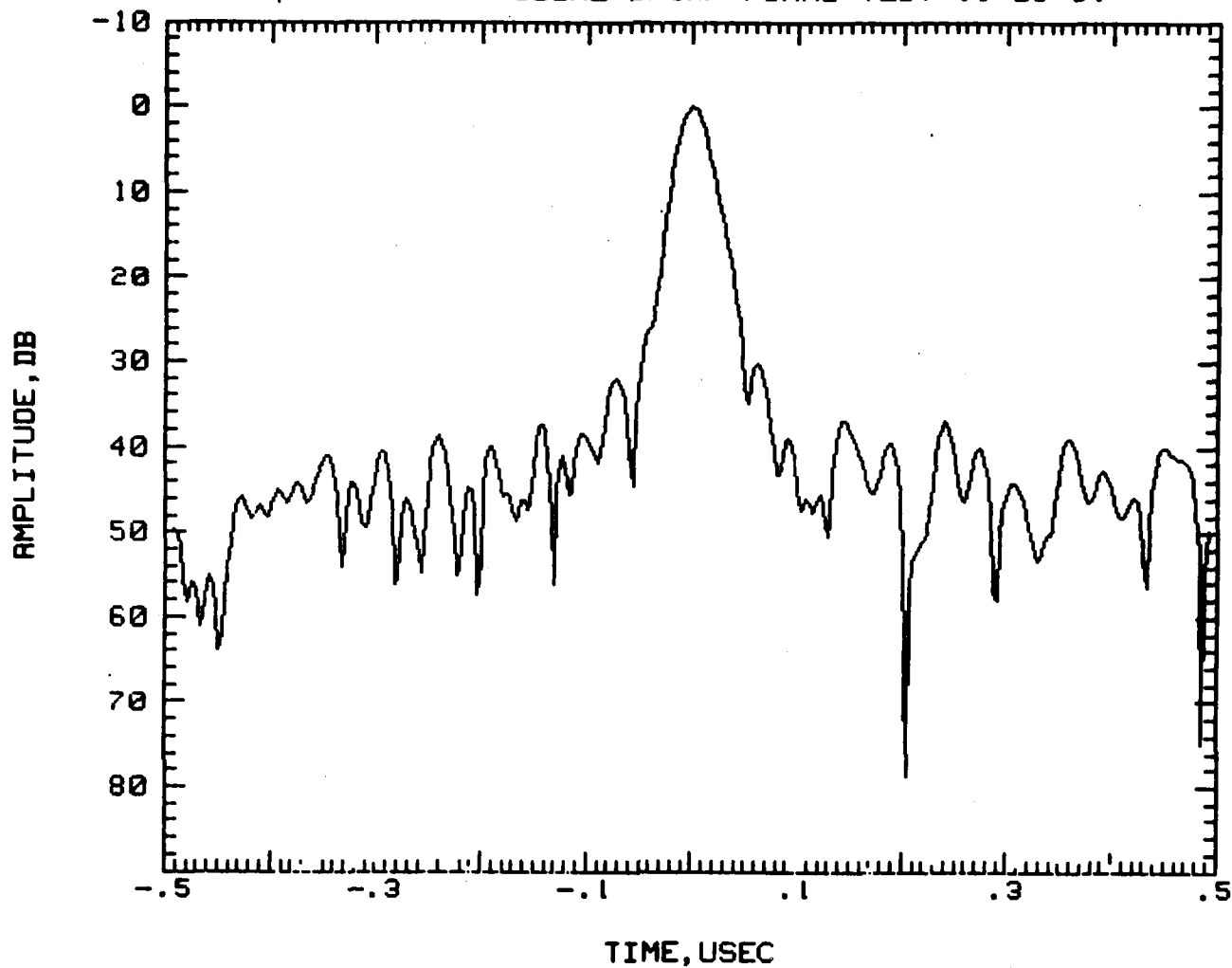


LINEAR      QUAD      RMS      F1      F2  
36.02631 -4.97841E-01      3.55      170.00      230.00

MMTRAC#12 FINAL TEST CENTER TUNED 11/23/81

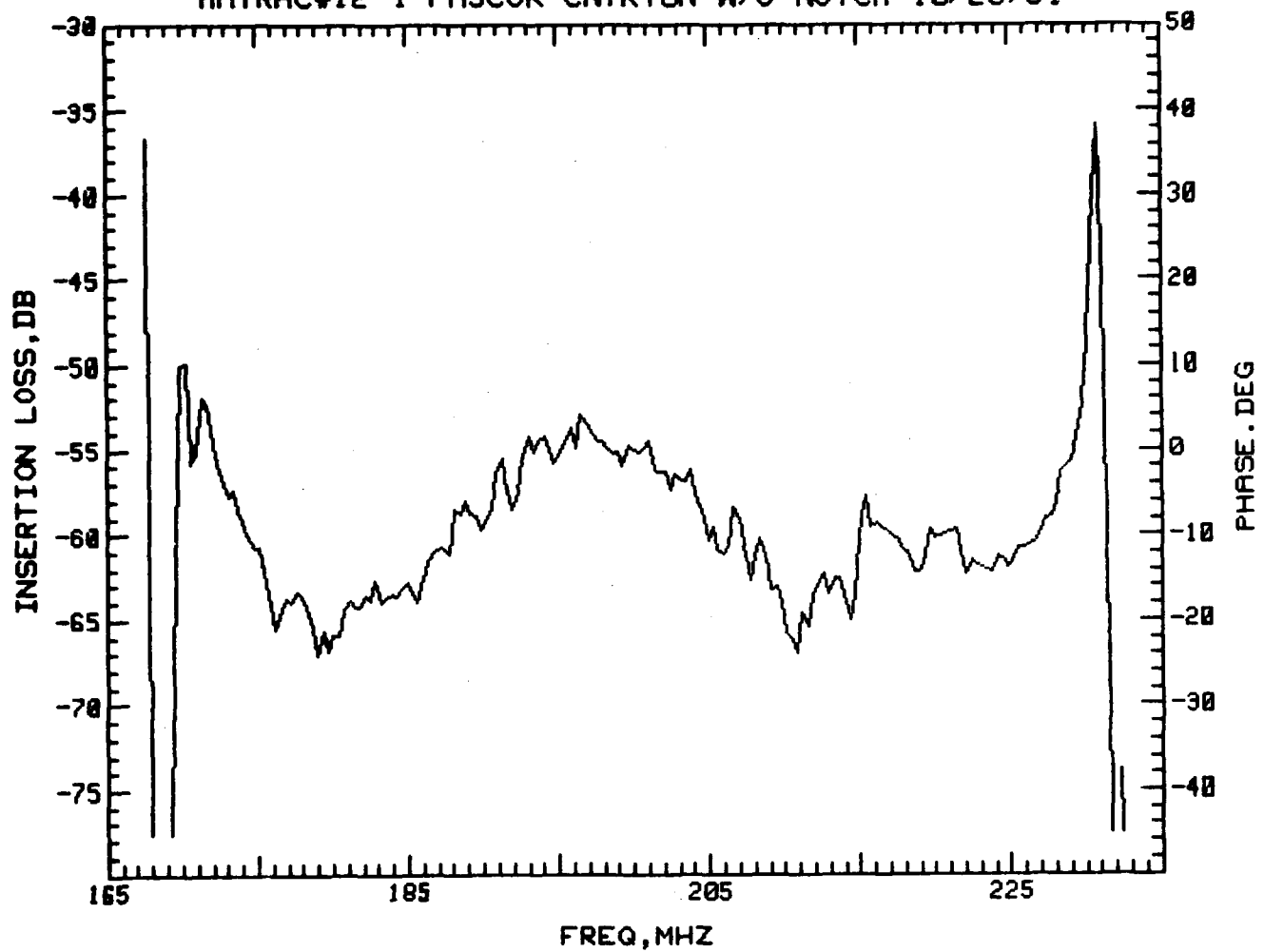


PEAK AMPLITUDE IS = 1.33844 ABSOLUTE  
SIGNAL TO NOISE RATIO IS= -1.68725686196 DB  
MMTRAC#12 & IDEAL UPCHP FINAL TEST 11/23/81

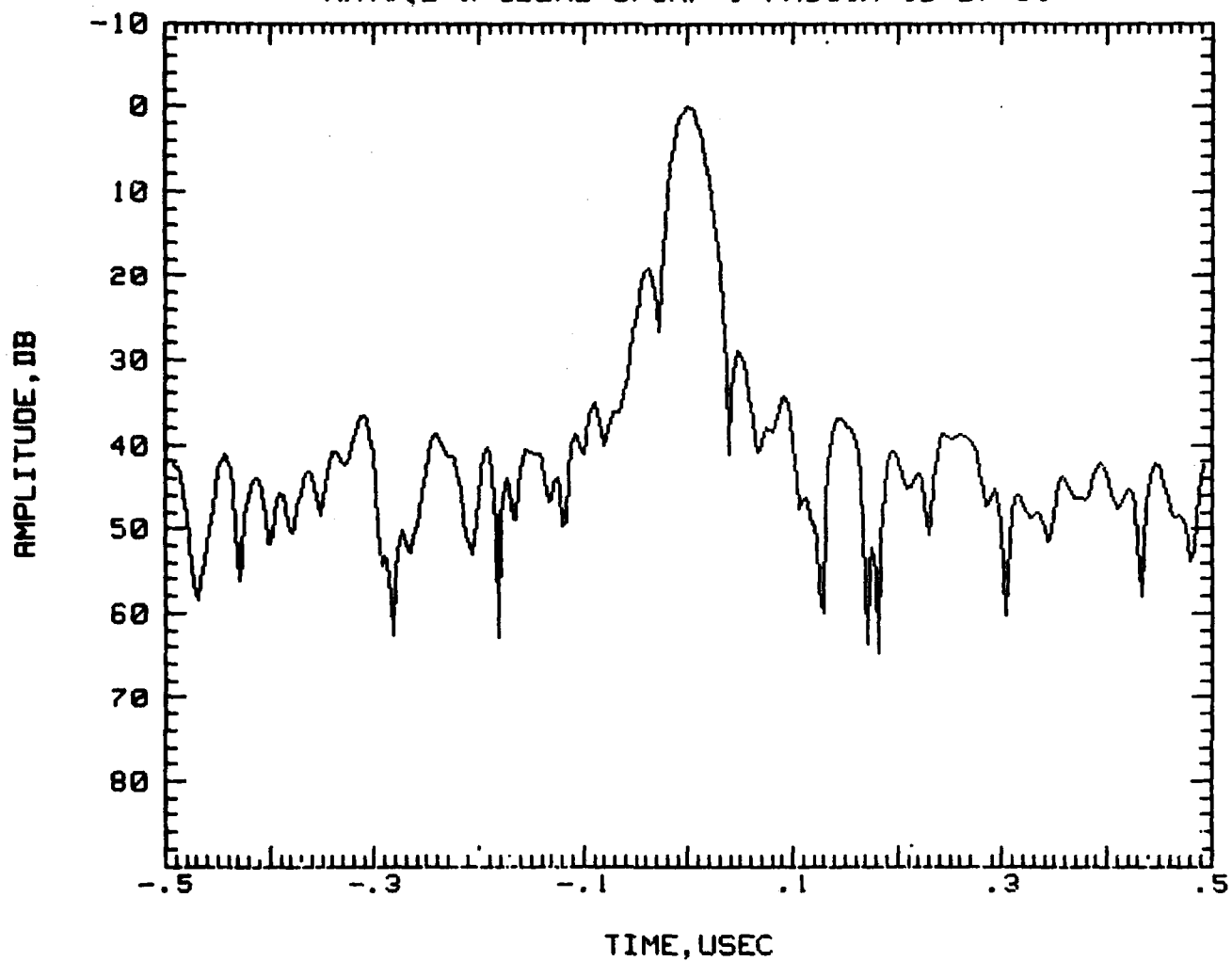


LINEAR      QUAD      RMS      F1      F2  
35.32152 -4.98151E-01      7.69      170.00      230.00

MMTRAC#12 1 PHSCOR CNTRTUN W/O NOTCH 10/26/81



PEAK AMPLITUDE IS = 1.26073 ABSOLUTE  
SIGNAL TO NOISE RATIO IS= -1.96413174005 DB  
MMT#12 & IDEAL UPCHP 1 PHSCOR 10/27/81



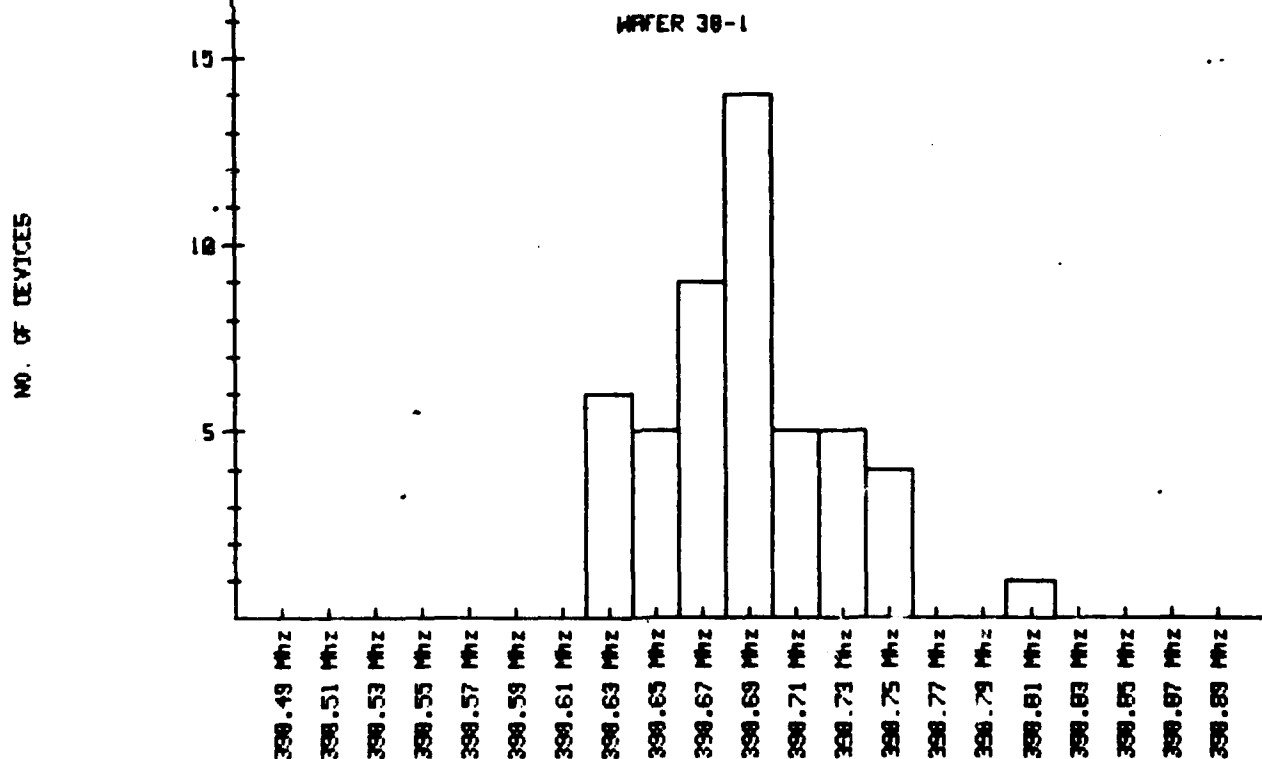
APPENDIX B

WAFER LEVEL FREQUENCY PROBE RESULTS FOR  
ENGINEERING PHASE RESONATORS

# WAFER#38-1

	A	B	C
1	398.721	398.692	398.746
2	398.687	398.664	398.745
3	398.743	398.681	398.733
4	398.732	398.681	398.703
5	398.712	398.692	398.727
6	398.733	398.654	398.689
7	398.714	398.663	398.667
8	398.676	398.633	398.682
9	398.692	398.628	398.687
10	398.720	398.627	398.661
11	398.681	398.625	398.658
12	398.689	398.644	398.668
13	398.699	398.661	398.674
14	398.695	398.638	398.703
15	398.681	398.638	398.657
16	398.672	398.652	0.000
17	398.759	0.000	398.804
% GOOD PARTS	AVRG CF (MHZ)		STND DEV (MHZ)
96.1	398.6874		.0381

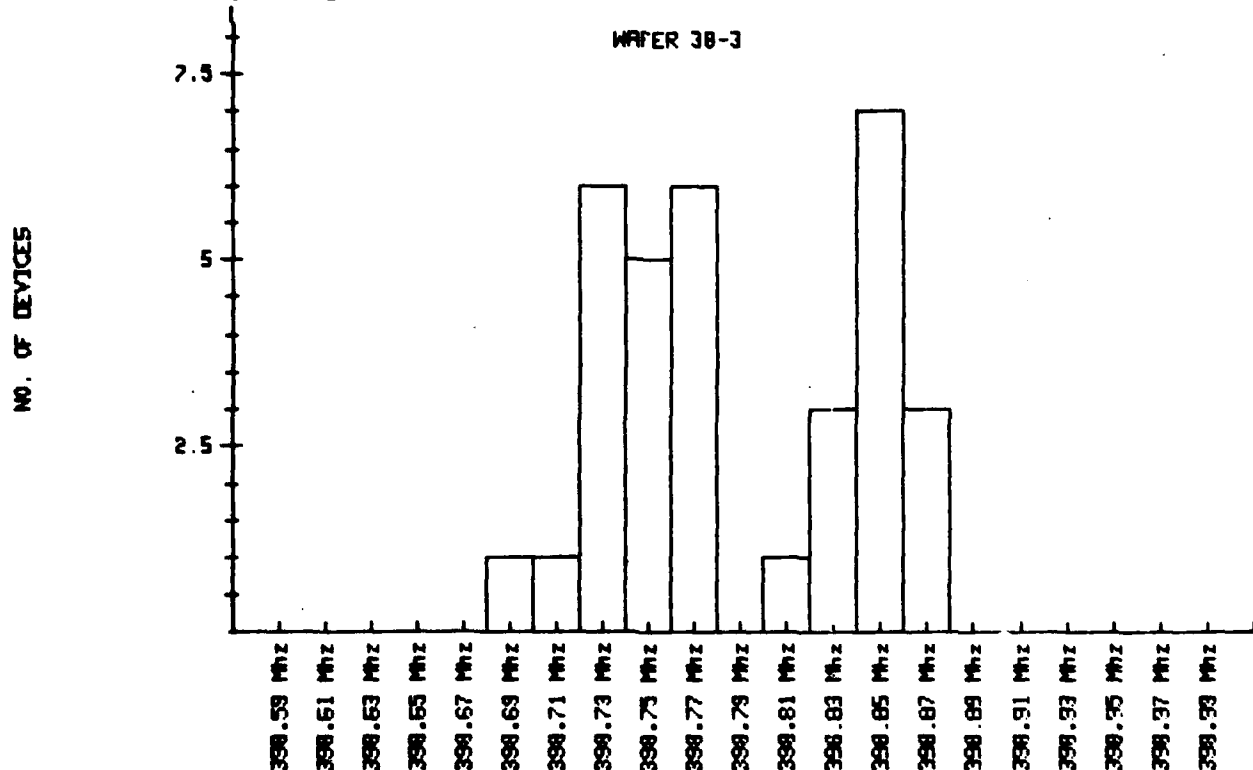
CENTER FREQ(Mhz)= 398.69  
WINDOW SPACING(Mhz)= .02



# WAFER 38-3

	A	B	C
1	0.000	0.000	0.000
2	0.000	398.732	398.750
3	0.000	398.754	398.737
4	0.000	0.000	398.737
5	0.000	398.807	0.000
6	0.000	398.772	398.692
7	398.874	398.731	398.702
8	0.000	0.000	398.839
9	398.842	398.728	0.000
10	398.865	398.746	398.733
11	398.842	398.847	398.746
12	398.851	398.828	0.000
13	398.851	398.767	398.764
14	398.825	398.770	398.779
15	398.864	0.000	398.776
16	398.849	398.751	0.000
17	398.854	0.000	0.000
% GOOD PARTS	AVRG CF (MHZ)	STND DEV (MHZ)	
64.7	398.7880	.0543	

CENTER FREQ(Mhz)= 398.79  
WINDOW SPACING(Mhz)= .02

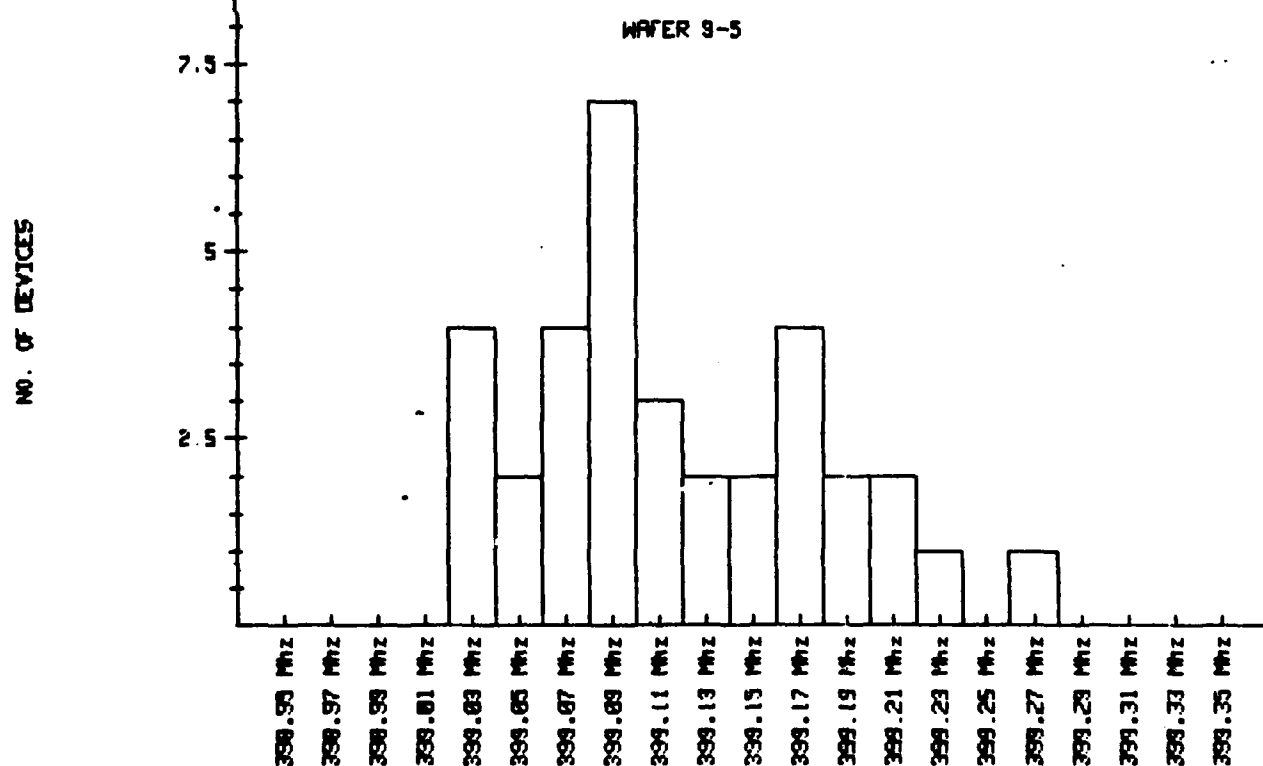




# WAFER 9.5

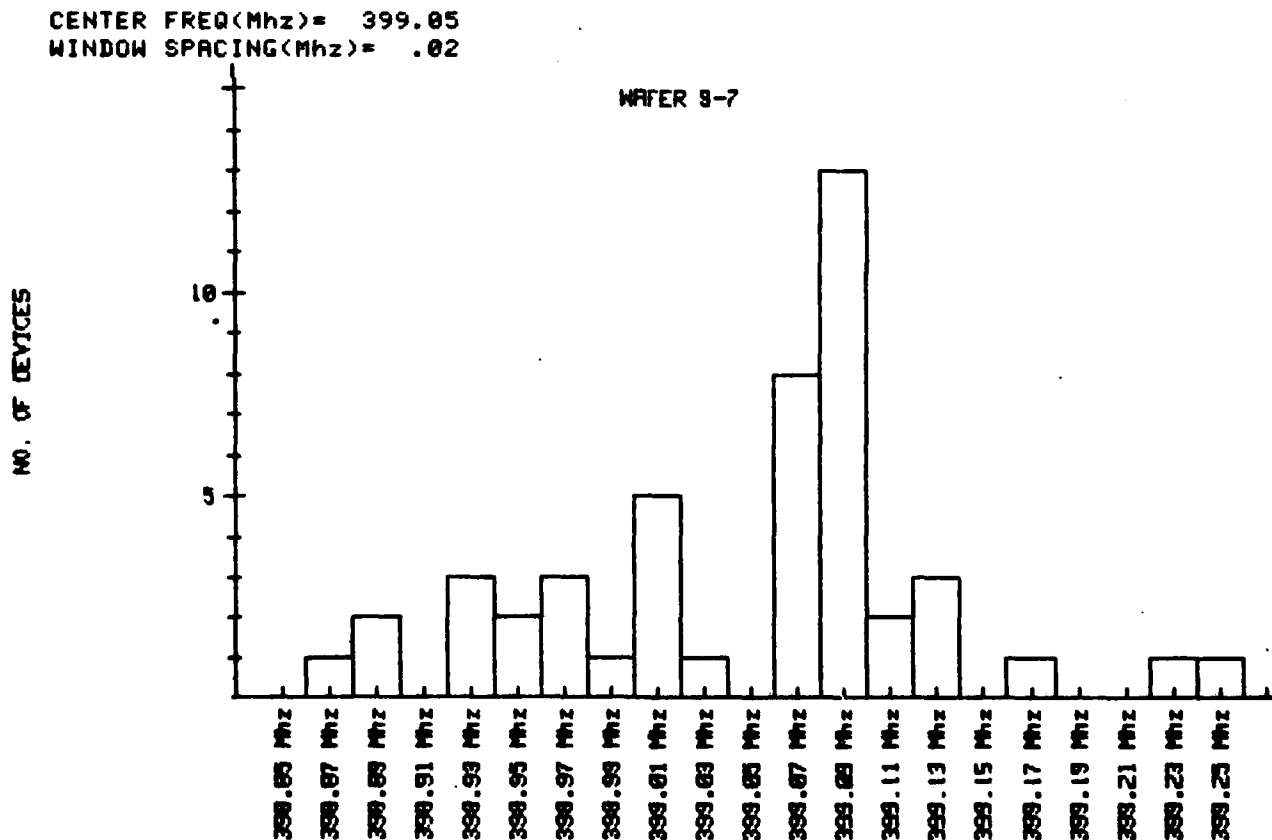
	A	B	C
1	0.000	0.000	399.471
2	0.000	0.000	399.722
3	0.000	0.000	399.276
4	399.191	0.000	399.177
5	399.117	399.088	399.167
6	399.097	399.062	399.133
7	0.000	399.031	399.115
8	399.084	399.056	399.097
9	0.000	399.074	399.085
10	0.000	399.062	399.055
11	399.109	399.169	399.032
12	0.000	399.202	399.035
13	399.161	399.080	399.039
14	399.158	399.095	399.095
15	399.152	399.191	399.130
16	399.218	399.233	0.000
17	0.000	0.000	0.000
% GOOD PARTS	AVRG CF (MHZ)	STND DEV (MHZ)	
70.6	399.1461	.1300	

CENTER FREQ(Mhz)= 399.15  
WINDOW SPACING(Mhz)= .02



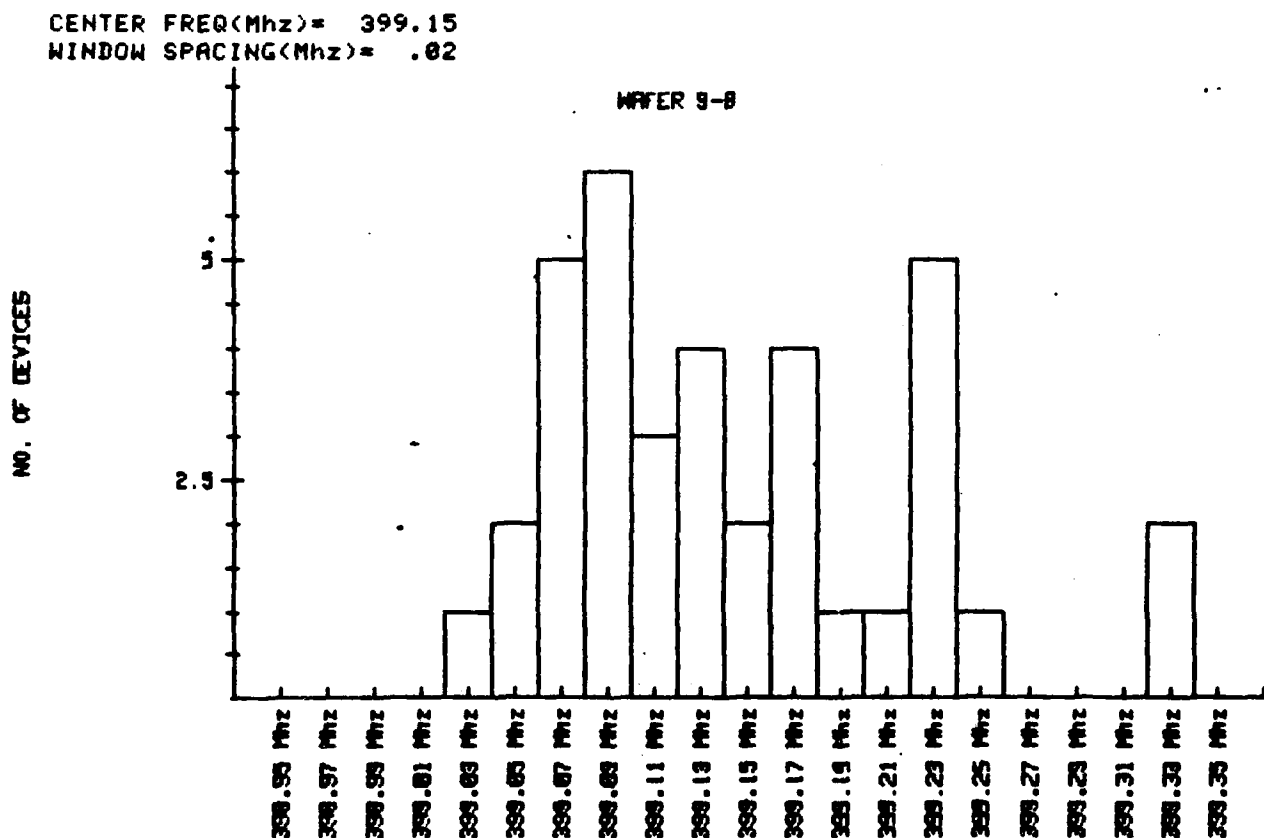
9.7

	A	B	C
1	399.179	0.000	399.243
2	0.000	399.228	0.000
3	399.092	398.947	399.075
4	399.082	398.928	399.088
5	399.005	398.969	399.103
6	399.020	398.952	399.068
7	399.010	398.930	399.066
8	399.027	398.962	399.076
9	399.124	398.940	0.000
10	399.082	398.980	399.062
11	399.098	398.885	399.066
12	399.071	398.877	399.070
13	399.095	398.895	399.092
14	399.003	398.982	399.094
15	399.089	399.012	399.086
16	399.121	399.093	399.100
17	399.120	399.088	399.132
% GOOD PARTS	AVRG CF (MHZ)	STND DEV (MHZ)	
92.2	399.0491	.0822	



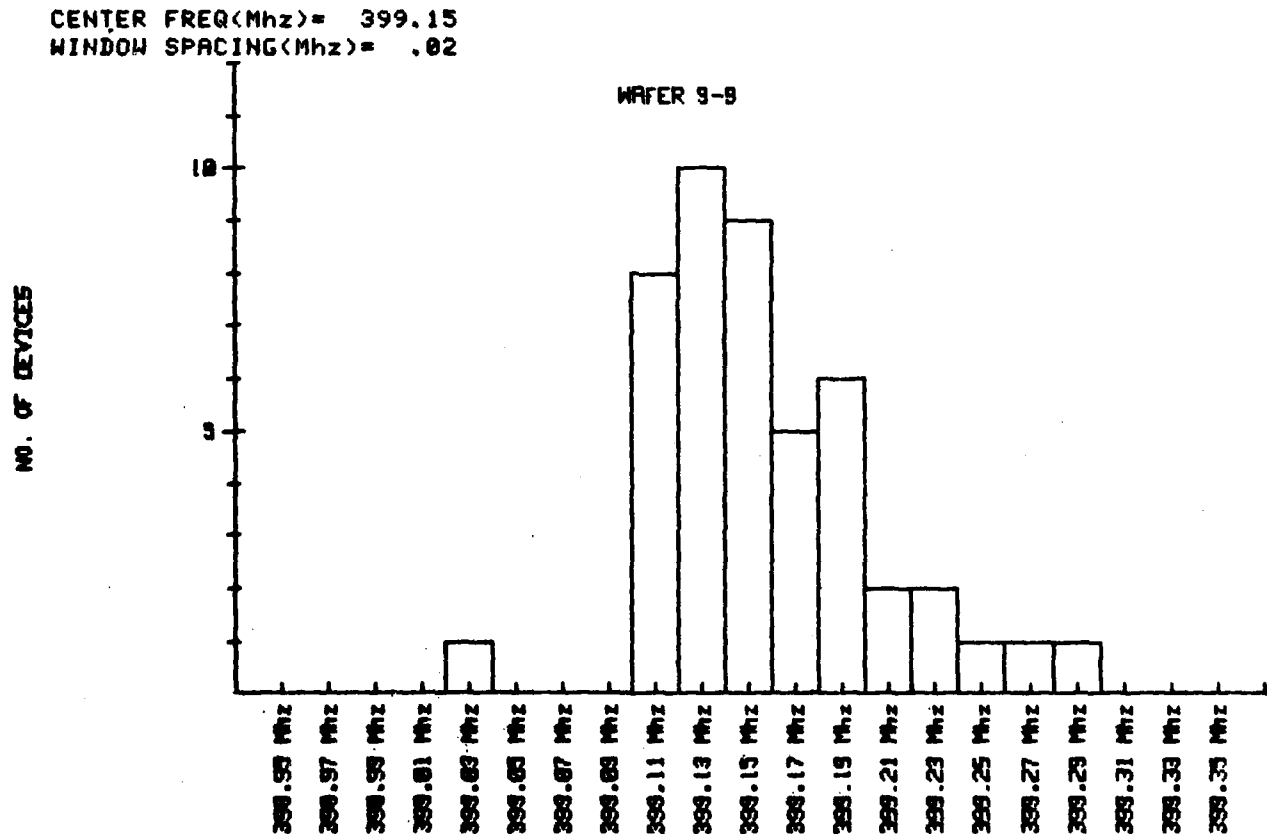
# WAFER 9-8

	A	B	C
1	0.000	399.326	0.000
2	399.173	399.111	0.000
3	399.240	399.127	399.148
4	399.238	399.075	399.094
5	399.227	399.099	399.096
6	399.197	399.066	399.075
7	399.171	399.047	399.072
8	0.000	399.070	399.096
9	399.173	399.096	399.166
10	399.230	399.089	399.113
11	399.237	0.000	0.000
12	399.243	399.058	399.137
13	399.457	399.040	399.122
14	0.000	0.000	399.147
15	0.000	0.000	399.106
16	0.000	0.000	399.127
17	0.000	399.333	399.209
% GOOD PARTS	AVRG CF (MHZ)		STND DEV (MHZ)
74.5	399.1534		.0896



# WAFER 9.9

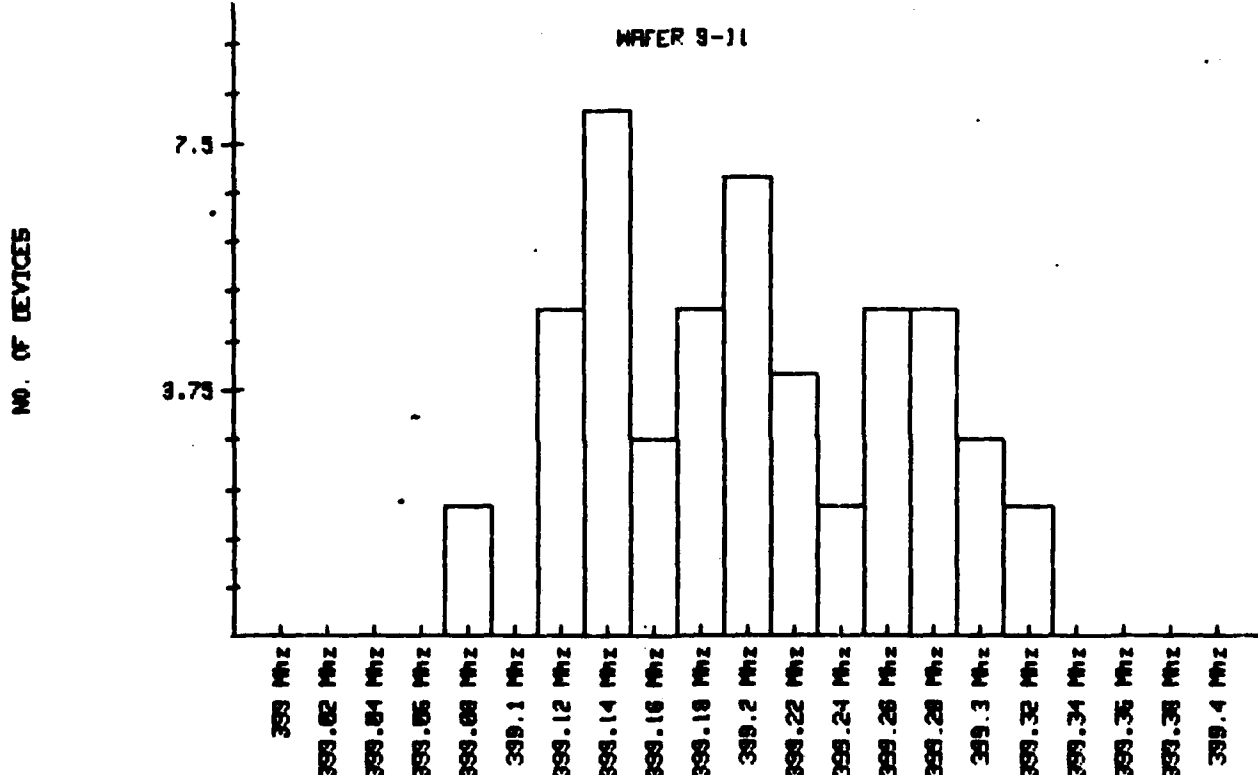
	A	B	C
1	399.252	0.000	399.298
2	399.147	399.198	399.195
3	399.145	399.227	399.154
4	399.129	399.207	399.120
5	399.106.	399.142	399.187
6	399.108	0.000	399.144
7	399.117	399.112	399.132
8	399.111	0.000	399.119
9	399.142	399.129	399.127
10	399.193	399.154	399.128
11	399.168	399.179	399.118
12	399.189	399.158	399.040
13	399.176	0.000	399.131
14	399.174	399.122	399.132
15	399.188	399.138	399.131
16	399.201	399.246	399.147
17	399.277	399.368	399.170
% GOOD PARTS	AVRG CF (MHZ)	STND DEV (MHZ)	
92.2	399.1636	.0584	



# WAFER 9.9

	A	B	C
1	399.326	399.252	399.263
2	399.216	399.216	399.305
3	399.150	399.134	399.318
4	399.153	399.141	399.284
5	399.159	399.183	399.273
6	399.180	399.228	399.277
7	399.195	399.270	399.272
8	399.139	399.301	399.283
9	399.135	399.300	399.231
10	399.129	399.263	399.210
11	399.137	399.254	399.214
12	399.120	399.236	399.203
13	399.167	399.209	399.206
14	399.116	399.179	399.193
15	399.089	399.173	399.195
16	399.083	399.148	399.125
17	399.123	399.145	399.172
% GOOD PARTS	AVRG CF (MHZ)	STND DEV (MHZ)	
100.0	399.2014	.0641	

CENTER FREQ(Mhz)= 399.2  
WINDOW SPACING(Mhz)= .02



## REFERENCES

1. W. D. Otto, H. M. Gerard, "On Rayleigh Wave Reflection from Groove at Oblique Incidence and an Empirical Model for Bulk Wave Scattering in RAC Devices", 1977 Ultrasonic Symposium Proceedings, Cat. #77CH1264-ISU, pp 596-601.
2. William J. Tanski, "SAW Resonators Utilizing Withdrawal Weighted Reflectors", IEEE Trans. Sonics and Ultrasonics, Vol. SU-26, No. 6, Nov. 1979.
3. L. A. Coldren, R. L. Rosenberg, "SAW Resonator Filter Overview: Design and Performance Tradeoffs", 1978 Ultrasonics Symposium Proceedings, IEEE Cat. #78CH1344-ISU, pp 422-432.
4. William J. Tanski, "High Q and GHz SAW Resonators", Op.at., pp 433-437.
5. William J. Tanski, "GHz SAW Resonators", 1979 Ultrasonics Symposium Proceedings, IEEE Cat. #79CH1482-9, pp 815-823.
6. H. A. Haus, "Modes in SAW Grating Resonators", J. Appl. Phys., Vol. 48, No. 12, pp 4955-4961, Dec. 1977.
7. William J. Tanski, "Surface Acoustic Wave Resonators on Quartz", IEEE Trans. on Sonics and Ultrasonics, Vol. SU-26, No. 20, pp 93-104, 1979.
8. Peter S. Cross, William R. Shreve, Tun Sein Tan, "Synchronous IDT SAW Resonators with Q above 10,000", 1979 Ultrasonics Symposium Proceedings, IEEE Cat. #79CH1482-9, pp 824-829.
9. R. D. Weglein, O. W. Otto, "Scattering Properties of Metallic Acoustic Surface Reflective Gratings", IEEE Ultrasonics Symposium Proceedings, Cat. #74CH0896-ISU, pp 205-207, Nov. 1974.
10. F. G. Marshall, E. G. S. Pange, "Mode Conversion in Surface Acoustic Wave Reflective Arrays", Electron. Lett. 10, pp 137-138, 1974.
11. R. Potter, "Surface Acoustic Wave Slanted Device Technology", IEEE Transactions on Sonics and Ultrasonics, SU-26, No. 6, pp 411-418, Nov. 1979.
12. C. N. Helmick, D. J. White, R. L. King, "Fine Tuning of Narrow-Band SAW Devices Using Dielectric Overlays", 1977 Ultrasonics Symposium Proceedings, IEEE Cat. #77CH1264-ISU, pp 659-663.
13. J. Wise, J. Schoenwald, E. Staples, "Impedance Characterization and Design of 2-Pole Hybrid SAW Resonator Filters", 1980 Ultrasonics Symposium Proceedings, IEEE Cat. #80CH1602-2, pp 200-203.

14. C. N. Helmick, D. J. White, "Observations of Aging and Temperature Effects on Dielectric-Coated SAW Devices", 1978 Ultrasonics Symposium Proceedings, IEEE Cat. #78CH1344-ISU, pp 580-585.
15. W. J. Tanski, "Surface Acoustic Wave Frequency Trimming of Resonant and Traveling-Wave Devices on Quartz", Applied Physics Letters, 39, No. 1, pp 40-42, July 1981.

ELECTRONICS TECHNOLOGY AND DEVICES LABORATORY  
CONTRACT DISTRIBUTION LIST

101 Defense Technical Information ATTN: DTIC-TCA Cameron Station (Bldg 5) 012 Alexandria, VA 22314	579 Cdr. PM Concept Analysis Centers Arlington Hall Station ATTN: DRCPM-CAC 001 Arlington, VA 22212
203 GIDEP Engineering & Support Dept TE Section PO Box 398 001 NORCO, CA 91760	Cdr. Night Vision & Electro-Optics ERADCOM ATTN: DELNV-D 001 Fort Belvoir, VA 22060602
205 Director Naval Research Laborator ATTN: Documents Library (TILD) 001 Washington, DC 20375	603 Cdr. Atmospheric Sciences Lab ERADCOM ATTN: DELAS-SY-S 001 White Sands Missile Range, NM 88002
301 Rome Air Development Center ATTN: Documents Library (TILD) 001 Griffiss AFB, NY 13441	607 Cdr. Harry Diamong Laboratories ATTN: DELHD-CO, TD (In Turn) 2800 Powder Mill road 001 Adelphi, Md 20783
437 Deputy for Science & Technology Office Asst Sec Army (R&D) 001 Washington, DC 20310	609 Cdr. ERADCOM ATTN: DRDEL-CG, CD, CS (In Turn) 2800 Powder Mill Road 001 Adelphi, MD 20783
438 DQDA (DAMA-ARZ-D/ Dr. F.D. Verderame 001 Washington, DC 20310	612 Cdr. ERADCOM ATTN: DRDEL-CT 2800 Powder Mill Road 001 Adelphi, MD 20783
482 Director US Army Materiel Sys Anal Actv ATTN: DRXSY-MP 001Aberdeen Proving Ground, MD 21005	680 Commander US Army Electronics R&D Command 000 Fort Monmouth, NJ 07703 1 DELET-M 1 DELEW-D 1 DELET-DD 1 DELSD-L (Tech Library) 2 DELSD-L-S (STINFO) 10 DELET-MA-M
563 Commander, DARCOM ATTN: DRCDE 5001 Eisenhower Avenue 001 Alexandria, VA 22333	681 Commander US Army Communications R&D Command ATTN: USMC-LNO 001 Fort Monmouth, NJ 07703
564 Cdr. US Army Signals Warfare Lab ATTN: DELSW-OS Vint Hill Farms Station 001 Warrenton, VA 22186	
705 Advisory Group on Electron Devices 201 Varick Street, 9th Floor 002 New York, NY 10014	



ELECTRONICS TECHNOLOGY AND DEVICES LABORATORY  
CONTRACT DISTRIBUTION LIST (Continued)

103	Code R123, Tech Library DCA Defense Comm Engrg Ctr 1800 Wiehle Ave 001 Reston, VA 22090	455	Commandant US Army Signal School ATTN: ATZH-CD 001 Fort Gordon, GA 30905
104	Defense Communciations Agency Technical Library Center Code 205 (P.A. Tolovi) 001 Washington, DC 20305	507	Cdr. AVRADCOM ATTN: DRSAB-E PO Box 209 001 St. Louis, MO 63166
206	Commander Naval Electronics Lab Center ATTN: Library 001 San Diego, CA 92152	517	Commander US Army Satellite Communications Agcy ATTN: DRCPP-SC-2 001 Fort Monmouth, NJ 07703
207	Cdr. Naval Surface Weapons Ctr White Oak Laboratory ATTN: Library Code WX-21 001 Silver Spring, MD 20910	518	TRI-TAC Office ATTN: TT-DA 001 Fort Monmouth, NJ 07703
314	Hq. Air Force Systems Command ATTN: DLCA Andrews Air Force Base 001 Washington, DC 20331	519	Cdr. US Army Avionics Lab AVRADCOM ATTN: DAVAA-D 001 Fort Monmouth, NJ 07703
403	Cdr. MICOM Redstone Scientific Info Center ATTN: Chief, Document Section 001 Redstone Arsenal, AL 35809	520	Project Manager, FIREFINDER ATTN: DRCPP-FF 001 Fort Monmouth, NJ 07703
407	Director Ballistic Missile Defense Advanced Technology Center ATTN: ATC-R, PO Box 1500 001 Huntsville, AL 35807	521	Commander Project Manager, SOTAS ATTN: DRCPP-STA 001 Fort Monmouth, NJ 07703
418	Commander HQ, Fort Huachuca ATTN: Technical Reference Div 001 Fort Huachuca, AZ 85613	531	Cdr. US Army Research Office ATTN: DRXRO-PH(Dr. Lontz) DRXRO-IP (In Trun PO Box 12211 001 Research Triangle Park, NC 27709
475	Cdr. Harry Diamond Laboratories ATTN: Dr. N. Berg/Branch 15200 2800 Powder Mill Road 001 Adelphi, MD 20783	604	Chief Ofc of Missile Electronic Warfare Electronic Warfare Lab, ERADCOM 001 White Sands Missile Range, NM 88002

ELECTRONICS TECHNOLOGY AND DEVICES LABORATORY  
CONTRACT DISTRIBUTION LIST (Continued)

606 Chief Intel Materiel Dev & Support Ofc Electronic Warfare Lab, ERADCOM 001 Fort Meade, MD 20755	Dr.J.S. Bryant OCD ATTN: DARD-ARP Washington, DC 20310
614 Edr. ERADCOM ATTN: DRDELL-LL-SB-AP (In Turn) 2800 Powder Mill Road 001 Adelphi, MD 27083	Dr. R. LaRosa Hazeltine Corporation Greenlawn, NT 11740
617 Cdr. ERADCOM ATTN: DRDEL-AQ 2800 Powder Mill Road 001 Adelphi, MD 20783	General Electric Co. Electronics Lab Electronics Park Syracuse, NY 13201 ATTN: Mr. S. Wanuga
619 Cdr. ERADCOM ATTN: DRDEL-PA-ILS-ED (In Turn) 2800 Powder Mill Road 001 Adelphi, MD 20783	RADC Deputy for Elec Technology ATTN: EEA (Dr. P. Carr) Hanscom AFB, MA 01731
701 MIT - Lincoln Laboratory ATTN: Mr. E. Stern PO Box 73 002 Lexington, MA 02173	Army Space Program Office ATTN: Maj. A.H. O'Brien 5001 Eisenhower Ave. Alexandria, VA 22333
703 NASA Scien & Tech Info Fac Baltimore/Washington Intl Airport 001 PO Box 8757, MD 21240	Mr. R. Bush CORC RADC Griffiss Air Force Base, NY 13440
704 National Bureau of Standards Bldg 225, RM A-331 ATTN: Mr. Leedy 001 Washington, DC 20231	Mr. G. Judd Hughes Aircraft Company Ground Systems Group 1901 W. Malvern Fullerton, CA 92634
707 TACTEC Batelle Memorial Institute 505 King Ave 001 Columbus, OH 43201	Commander, AFAL ATTN: Mr. W.J. Edwards, TEA Wright-Patterson AFB, OH 45433
Coordinated Science Laboratory University of Illinois Urbana, IL 61801 ATTN: Dr. Bill J. Hunsinger	Anderson Laboratories, Inc. 1280 Blue Hills Ave ATTN: Dr. A.A. Comparini Bloomfield, CN 06002

ELECTRONICS TECHNOLOGY AND DEVICES LABORATORY  
CONTRACT DISTRIBUTION LIST (Continued)

Mr. Henry Friedman  
RADC/OCTE  
Griffiss AFB, NY 13440

Cubic Corp  
9333 Balboa Ave  
MS 10-28  
San Diego, CA 92123  
ATTN: Dr. R.C. Badewitz

General Dynamics, Electronics Div  
PO Box 81127  
San Diego, CA 92138  
ATTN: Mr. T.A. Thiel

Texas Instruments, Inc.  
PO Box 5936  
13500 N. Central Expressway  
Dallas, TX 75222  
ATTN: Dr. Robert S. Wagers

Raytheon Company  
Research Division  
41 Spring St.  
Lexington, MA 02173  
ATTN: Dr. M.B. Schuler

Sperry Rand Research Center  
100 North Road  
Sudbury, MA 01776  
ATTN: Dr. H. Van De Vaart

Microwave Laboratory  
W.W. Hansen Laboratories of Physics  
Stanford University  
Stanford, CA 94305  
ATTN: Dr. H.J. Shaw

Westinghouse Electric Corp.  
Research & Development Center  
Beulah Road  
Pittsburgh, PA 15235  
ATTN: Dr. B. McAvoy

TRW  
Defense and Space Sys Group  
One Space Park  
Redondo Beach, CA 90278  
ATTN: Dr. R.S. Kagiwada

Dr. F. Cho  
Integrated Circuit Facility  
Motorola Government Electronics Division  
8201 East McDowell Road  
Scottsdale, AZ 85257

McGill University  
ATTN: G.W. Farnell  
Montreal 110, Canada

Advanced Technology Center, Inc.  
Subsidiary of LTV Aerospace Corp  
PO Box 6144  
Dallas, TX 75222  
ATTN: Mr. A.E. Sobey

United Aircraft Research Labs  
ATTN: Dr. Thomas W. Grudkowski  
East Hartford, CN 06108

Tektonix, Inc.  
PO Box 500  
Beaverton, OR 97007  
ATTN: Dr. T.M. Reeder  
MS50-362

Science Center  
Rockwell International  
Thousand Oaks, CA 91360  
ATTN: Dr. L.C. Lim

AMES Laboratory  
215 Reactor Bldg  
Iowa State University  
Ames, IA 50011  
ATTN: Dr. K. Lakin

ELECTRONICS TECHNOLOGY AND DEVICES LABORATORY  
CONTRACT DISTRIBUTION LIST (Continued)

SAWTEK, Inc.  
PO Box 7756  
2451 Shader Road  
Orlando FL 32854  
ATTN. Mr. S. Miller

Dr. R.C. Williamson  
Lincoln Laboratory - MIT  
PO Box 73  
Lexington, MA 02173

Dr. William R. Shreve  
HP Laboratories  
1501 Page Mill Road  
Palo Alto, CA 94304

D. Chrissotimos, Code 763  
National Aeronautics & Space Admin.  
Goodard Space Flight Center  
Greenbelt, MD 20771

Naval Research Laboratories  
Code 5237  
Washington, DC 20375  
ATTN: Dr. D. Webb

RF Monolithics  
4441 Sigma Rd  
Dallas, TX 75234  
ATTN: Mr. C.S. Hartmann

END